# Very Low Frequency Seismo-Acoustic Noise Below the Sea Floor (0.2 - 10 Hz)

by

Christopher Robert Bradley

B.S., University of New Mexico (1982)

Submitted in partial fulfillment of the
requirements for the degree of degree of

Doctor of Philosophy

at the

MASSACHUSETTS INSTITUTE OF TECHNOLOGY

and the

WOODS HOLE OCEANOGRAPHIC INSTITUTION

February 1994





Author .....
Joint Program in Marine Geology and Geophysics
Massachusetts Institute of Technology
Woods Hole Oceanographic Institution
December 13, 1993

Certified by ... .....
Ralph A. Stephen
Senior Scientist
Thesis Supervisor

Accepted by ..... .....
Marcia K. McNutt
Chairman, Joint Committee for Marine Geology and Geophysics

# Very Low Frequency Seismo-Acoustic Noise Below the Sea Floor (0.2 - 10 Hz)

by

Christopher Robert Bradley

Submitted to the Joint Program in Marine Geology and Geophysics
Massachusetts Institute of Technology
Woods Hole Oceanographic Institution
on December 13, 1993, in partial fulfillment of the
requirements for the degree of
Doctor of Philosophy

## Abstract

Ambient noise in the sea has been observed for over 100 years. Previous studies conclude that the primary source of microseisms is nonlinear interaction of surface gravity waves at the sea surface. Though this source relationship is generally accepted, the actual processes by which the wave generated acoustic noise in the water column couples and propagates to and along the sea floor are not well understood. In this thesis, the sources and propagation of sea floor and sub-sea floor microseismic noise between 0.2 and 10 $Hz$ are investigated. This thesis involves a combination of theoretical, observational and numerical analysis to probe the nature of the microseismic field in the Blake Bahama Basin.

Surface waves are the primary mechanism for noise propagation in the crust and fall into two separate groups depending on the relative wavelength/water depth ratio. Asymptotic analysis of the Sommerfeld integral in the complex ray parameter plane shows results that agree with previous findings by Strick (1959) and reveal two fundamental interface wave modes for short wavelength noise propagation in the crust: the Stoneley and pseudo-Rayleigh wave. For ocean sediments, where the shear wave velocity is less than the acoustic wave velocity of water, only the Stoneley interface wave can exist. For well consolidated sediments and basalt, the shear velocity exceeds the acoustic wave velocity of water and the pseudo-Rayleigh wave can also exist. Both interface waves propagate with retrograde elliptic motion at the sea floor and attenuate with depth into the crust, however the pseudo-Rayleigh wave travels along the interface with dispersion and attenuation and "leaks" energy into the water column for a half-space ocean over elastic crust model. For finite depth ocean models, the pseudo-Rayleigh wave is no longer leaky and approaches the Rayleigh wave velocity of the crust. The analysis shows that longer wavelength noise propagates as Rayleigh and Stoneley modes of the ocean+crust waveguide. These long wavelength modes are the fundamental mechanism for long range noise

propagation.

During the Low Frequency Acoustic Seismic Experiment (LFASE) a four-node, 12- channel borehole array (SEABASS) was deployed in the Blake Bahama Basin off the coast of eastern Florida (DSDP Hole 534B). This experiment is unique and is the first use of a borehole array to measure microseismic noise below the sea floor. Ambient background noise from a one week period is compared between an Ocean Bottom Seismometer (OBS) and SEABASS at sub-bottom depths of 10, 40, 70 and 100 meters below the sea floor. The 0.3 $Hz$ microseism peak is found to be nearly invariant with depth and has a power level of 65 and 75 $dB\ rel\ 1\ (nm/s^2)^2)/Hz$ for the vertical and horizontal components respectively. At 100 $m$ depth, the mean microseismic noise levels above 0.7 $Hz$ are 10 $dB$ and 15-20 $dB$ quieter for the vertical and horizontal components respectively. Most of this attenuation occurs in the upper 10 $m$ above 1.0 $Hz$, however higher modes in the spectra show narrow bandwidth variability in the noise field that is not monotonic with depth. Dispersion calculations show normal mode Stoneley waves below 0.7 $Hz$ and evidence of higher modes above 0.8 $Hz$. A strong correlation between noise levels in the borehole and local sea state conditions is observed along with clear observation of the nonlinear frequency doubling effect between ocean surface waves and microseisms. Particle motion analysis further verifies that noise propagates through the array as Rayleigh/Stoneley waves. Polarization direction indicates at least two sources; distant westerly swell during quiescent times and local surface waves due to a passing storm.

Above 1.0 $Hz$ the LFASE data shows little coherence and displays random polarization. Because of this, we believe scattered energy is a significant component of the noise field in the Blake Bahama Basin. A fully 3-D finite difference algorithm is used to model both surface and volume heterogeneities in the ocean crust. Numerical modeling of wave propagation for hard and soft bottom environments shows that heterogeneities on the order of a seismic wavelength radiate energy into the water column and convert acoustic waves in the water into small wavelength Stoneley waves observed at the borehole. Sea floor roughness is the most important elastic scattering feature of the ocean crust. Comparisons of 2D and 3D rough sea floor models show that out-of-plane effects necessitate the use of 3D methods. The out-of-plane energy that is present in the LFASE data comes from either heterogeneities in the source field (i.e. mixed gravity wave directions) or, equally likely, scattering of the source field from surface or volume heterogeneities in the sea floor.

Thesis Supervisor: Ralph A. Stephen
Title: Senior Scientist

# Acknowledgments

I once read in a thesis acknowledgments "Writing is not hard for me.", unfortunately I cannot make the same claim. I also once read in a thesis that the one cardinal rule for a thesis project is "...to never never never never give up...." This is advice I can claim to have heeded.

Writing acknowledgments are never easy. You are always afraid you may miss attributing due respect and appreciation to those who have made the task enjoyable and in fact possible. If I have overlooked anyone I apologize and thank them now regardless of their being named specifically.

I would like to thank my advisor, Ralph Stephen, for his encouragement and support while I worked on this project. I can truly say I appreciate all the time he has spent with me teaching me the art of doing good science and thinking through a problem. He never let me give; thank you. I would also like to thank the other members of my committee: Arthur Cheng, Henrik Schmidt, George Sutton, Steve Swift and Henry Dick (whose Geodynamics seminar allowed me to see the world and understand the ocean crust) for their helpful advice and enthusiasm. Tom Bolmer and Steve Swift also get special credit for being practical thinkers, good "advisors" and helpful friends during the "fire drill" times.

The friends have made in the Joint Program have made this experience not only survivable but in fact one of the most enjoyable of my life. Beyond the social, those who have made my scientific journey more pleasant include my office mates, Sarah Little, Carl Friedricks, Gary Jaroslow, Dan Lizarralde, Achangelo Sene, and especially Ted Charrette (whose family took me into their home my first two years at MIT) and fellow students, Cecile Wolfe, Joe LaCasce, Gail Christeson, Sarah Green and Carol Arnosti. Also the staff of the education office, particularly Jake, Abbie and Stella deserve credit for their generosity and warmth.

My family both natural and in-law have been an unquestioning support system during my tenure in graduate school. My parents have taught me the joy of learning and an appreciation of science and the beauty of the natural world. I cannot thank

them enough for their patience and support. Finally, I would like to thank my wife, Elise Ann Ralph. Outside of my committee, she has had the most influence on this thesis. I count myself a very fortunate man to have a sole mate with whom I can discuss every aspect of my life both social and academic.

This research was supported by Office of Naval Research grants N00014-89-C-0018, N00014-89-J-1012, N00014-90-C-0098, N00014-90-J-1493 and N00014-93-1-1352.

# Contents

# List of Figures

# Chapter 1

# Introduction

"Ocean noise" is not wholy a random or undesirable process. Urick (1986) defines ambient noise as a "prevailing, sustained background sound exclusive of momentary sound and self noise". Ocean noise is ubiquitous and is seen across frequencies from less than 0.01 $Hz$ to greater than $50,000$ $Hz$. Industrial (fishing, civil engineering and oil companies), military (naval acoustics and seismo-acoustic communication) and academic (seismology, acoustics and ocean engineering) applications in the ocean require knowledge of the mechanics of noise generation to fully understand measured data.

Between approximately 0.1 and 5.0 $Hz$ oceanic noise that is coupled to the crust is referred to as microseisms. The term "microseisms" should not be confused with "microseismicity". Microseisms are due to ocean waves, microseismicity and microearthquakes are due to minute stress releases in the earth's crust. Microseisms are regularly measured by ocean bottom and land seismometers and in most ocean basins reveal peak vertical displacements of $10^{-3}$ $cm$ between 0.1 and 0.5 $Hz$ (McCreery et al., 1993). To first order, absolute noise levels define the natural limitations of an experimental system at a site. Current debate over the location of ocean bottom seismometers as an extension of the world seismic network hinges on the behavior of noise within the oceanic crust (Sutton, 1990); since analysis of earthquakes and explosive source signals is limited by the ambient noise at a recording

station. Second order properties of ambient noise (i.e. particle motion, polarization and temporal behavior) can yield information about the propagation of sound in the ocean and sea bed and, more fundamentally, the creation of sound by fluid flow. So ambient ocean noise, despite the connotations from its name, is an important process and its analysis is key in determining both seismic system limitations and ocean and crust seismo-acoustic interaction.

This thesis is an investigation of ambient noise on and within the deep ocean crust. In particular, the infrasonic acoustic, $1 \rightarrow 20\ Hz$, (Urick, 1986) and very-low-frequency seismic, $0.1 \rightarrow 50\ Hz$, (Sutton, 1990b) bands are studied. In this chapter are given:

- a review of previous work into the source of microseismic energy,
- the objectives and contributions from the work in this thesis,
- and an outline of the remainder of the thesis.

The intent of the following section is to familiarize the reader with the long history of microseismic research and to bring current conceptions to light on microseism source mechanisms. Within the introduction of the subsequent chapters in this thesis additional articles are cited as they pertain to the subject of that chapter. In particular a review of ocean bottom microseism measurements is included in Chapter 3.

## 1.1 Historical Review

It has long been recognized that "microseisms" are closely related to sea state. Bertelli (1875) is cited by Milne (1883) as the father of microseismic research. Father Bertelli was the first to make systematic measurements of the sustained background noise at seismic stations throughout Italy. Milne, who coined the term "microseismic storm", found that locally high concentrations of microseismic energy measured at nearshore stations propagated inland and were sensed at inland stations after a time

delay. He was the first to recognize the traveling wave nature of microseisms and related the microseismic storms to the action of wind directly on the continent.

In the first half of this century many properties of microseisms were observed and catalogued. Microseismic noise was found to be related to atmospheric conditions (Laska, 1902) and correlated with surf on local coasts (Wiechert, 1905 and Gutenberg, 1910). Later several arguments put forth by Macelwane (1952), and Gilmore (1946) show that the majority of microseismic energy is generated at sea underneath large storm systems and propagates at approximately the Rayleigh interface wave velocity. Ramirez (1940) reviews the Navy's use of tripartite stations to correlate the particle motion of microseisms with the motion of low pressure cells at sea. Because of reflection and refraction of the storm microseisms along their travel path, the accuracy of location for a storm center via seismic methods was limited and the Navy discontinued the use of seismic stations as storm tracking centers.

Along with the observation that microseisms are temporally correlated with storms is the measured "double frequency" signature of microseisms first observed in the Mediterranean Sea by Imbo (1931). Imbo found that the frequency of the microseisms was twice that of the dominant ocean surface gravity wave period. Subsequent studies by Deacon (1947) (who measured microseisms and sea waves near the north coast of Cornwall) and Darbyshire (1950) found a similar 2 : 1 relationship in frequency. Darbyshire used frequency analysis to compare both microseism and ocean wave pressure data recorded during a storm in the North Atlantic and confirmed (1) that microseisms of different periods travel independently and (2) that each band of microseismic activity could be identified with a band of sea waves at 1/2 its frequency.

The first explanation to unite these two features of microseisms was published by Longuet-Higgins (1948;1950) who proposed a theory (based on theory by Miché, 1944) by which a standing wave in deep water could generate a second order acoustic wave. The standing wave, which can be regarded as a superposition of opposing propagating waves, imposes a fluctuating pressure distribution across the sea floor due to the nonlinear summation of its composite plane waves. To get his expres-

sion, Longuet-Higgins uses a perturbation expansion solution to the hydrodynamic equation. The first order term in the expansion describes the particle motion of the standing wave whereas the second order term describes the quadratic pressure response at the sea floor. This pressure response, $\bar{p}$, for an incompressible fluid at the sea floor is:

$$\frac{\bar{p} - p_o}{\rho} - g\,h = -2a_1\,a_2\,\sigma^2\,cos(2\sigma\,t), \tag{1.1}$$

where $p_o$ is atmospheric pressure, $\rho$ is the fluid density, $g\,h$ is the potential energy of a unit density fluid packet displaced a distance $h$ from the center of gravity, $a_1$, $a_2$ are the respective amplitudes of the opposing waves and $\sigma$ is the frequency of the waves. So equation ( 1.1) describes a process by which a pair of nonlinearly interacting gravity waves yields a pressure response at the sea floor of twice their frequency. Because strongly interacting waves travel with the storm center, Longuet-Higgins' theory was the first to encompass the two major observations from microseisms. Similarly, for standing waves on a compressible fluid the pressure response at the sea floor is:

$$\frac{\bar{p} - p_o}{\rho} - g\,h = -\frac{1}{2}\,a^2\,\sigma^2\,\frac{cos(2\sigma\,\frac{(z-h)}{c})}{cos(2\sigma\,\frac{h}{c})}\,cos(2\,\sigma\,t), \tag{1.2}$$

where $h$ is the water depth and $c$ is the compressional wave velocity of the fluid. There is a resonance or "organ pipe" mode possible when $cos(2\sigma\,\frac{h}{c}) \approx 0$. For a fixed ocean depth ($h$) and compressional wave speed ($c$), this corresponds to the following eigenfrequencies:

$$f_n = (n + 1/2)\pi\,\frac{c}{h}$$

implying that these frequencies should dominate the microseism spectrum. Data from Donn (1952) and others show that these modes do not necessarily dominate the microseism spectrum. Press and Ewing (1948;1952) discuss a different mechanism for the propagation of microseismic modes. They solve for the waveguide effect of the water column overlying the elastic sea floor. Press and Ewing and Tolstoy (1954) show that modes created in this waveguide have a horizontal phase velocity which asymptotically approaches the sea floor Rayleigh wave velocity and for an

infinite depth ocean the horizontal phase velocity corresponds to a true Stoneley wave. Press and Ewing suggest that microseisms are initiated by coupling between the ocean surface and atmosphere.

With the general acceptance of nonlinear wave-wave interaction as the source mechanism of microseisms came improvements on the theory by Hasselmann (1963) and later Hughes (1976) and Kadota and Labianca (1981). Using Lighthill's integral solution to the inhomogeneous hydrodynamic equation (Lighthill, 1952) Hasselmann showed that atmospheric fluctuations were an insignificant contributor to the noise field. He went on to show that seismic waves can be generated by random excitation fields of nonlinearly interacting gravity waves whose phase velocity matches the free modes of the elastic system (i.e. ocean/sea floor). He derives an expression in frequency and wavenumber for the equivalent pressure spectrum from a statistical distribution of directional surface gravity wave components. In an almost equivalent study, Hughes (1976) approximated the solution to the equations of motion for surface gravity waves using perturbation expansions. His solution is similar to Hasselmann's in form and inability to model the microseismic spectrum at frequencies above a few hertz. Kadota and Labianca (1981) have taken the perturbation expansions of Hasselmann and Hughes and corrected them for the fourth order statistical behavior of the gravity wave random field. They arrive at a more mathematically consistent theory for the sound pressure from nonlinearly interacting gravity waves and find that only the swell component of the gravity waves generates a pressure fluctuation.

In more recent studies, Kibblewhite and Ewans (1985) and Kibblewhite and Wu (1989) refined the expressions of one dimensional power spectra from Hasselmann and Hughes and compared them to microseismic records from the west coast of New Zealand. They found that the noise field from $0.1-5.0$ $Hz$ is controlled by nonlinear wave-wave interactions and that existing theories account for the observed spectra. In the latter paper, the authors derive expressions for the infrasonic spectra for a water layer overlying a solid half-space and include the effects of shear waves in the lower media. They conclude that a more complicated model with several layers is

required to explain the observed spectra. Both of these studies involve a microseism data set collected on land and cannot fully account for the propagation of seismic interface waves and modes within the water column and crust. A study of the propagation effects within a shallow water waveguide over a viscoelastic medium is presented in Schmidt and Kuperman (1988). They emphasize the importance of considering the propagation mechanisms when estimating the noise field source strength.

Most recently, Kibblewhite and Wu (1991) examine the two ways in which air flow can transfer energy into the water column: (1) directly at the air sea interface and (2) indirectly by exciting gravity waves which in turn interact nonlinearly and generate acoustic energy. They return to Lighthill's approach for (1) and compare it against the perturbation expansion methods used by Hasselmann and Hughes. Lighthill's integral solution includes quadrupole, dipole and monopole source terms corresponding to direct radiation of airflow turbulence, second order wave-wave interaction and first order pressure fluctuation respectively. They find that the direct radiation term is only significant during the early stages of sea development and that the use of the perturbation approximation is sufficient at low frequencies.

Cato (1991a;1991b) improved on Lighthill's theory by solving the hydrodynamic equations subject to a moving boundary condition between two fluid media of different density and sound speed. In contrast to Kibblewhite and Wu, Cato states that the direct radiation term can contribute significantly to the noise field. Lindstrom (1991) used Cato's development and extended it to include a stratified ocean against an elastic sea floor. Lindstrom finds that the direct radiation term can be ignored for water depths below approximately 400 m. In the frequency band between 0.1 and 0.7 $Hz$ Lindstrom reconfirms the importance of the orbital motion of wave-wave interaction at the sea surface by comparing his theory with ocean bottom data collected near the Chesapeake Bay.

Previous observations of microseisms at sea involved sea floor arrays and single sub-bottom seismic stations. The present study is the first to analyze the microseismic field at several depths below the sea floor simultaneously. It provides infor-

mation on the depth dependence of microseismic noise, on the propagation mechanisms (based in part on the polarization analysis and mean spectral behavior) and on the source of microseismic energy.

## 1.2 Objectives & Contributions

As with any seismic phenomenon, to understand microseisms we must define: the source, the mechanism by which the source is coupled to the ocean and ocean crust, and the process(es) by which the noise field propagates in the crust. The primary source mechanism has been well defined (as demonstrated by the literature review above) to be acoustic waves generated by the interaction of opposing surface gravity waves. The overall microseism spectrum is remakably uniform across the sea floor. This aspect of the microseismic field is investigated by Webb (1992) and he finds that the "equilibrium microseism spectrum" is created by a balance between the gravity wave source field and dissipation of energy into a waveguide formed by the ocean, crust and upper mantle.

Though the average microseism spectrum is fairly uniform, spatial variation of the spectrum can yield information about the geoacoustic properties of the crust. Layering within the sediments and basalt provide waveguides for the propagation of discrete modes. Roughness at the sea floor, whether it is at the fluid/solid boundary or the interface between the sediments and the basaltic bottom scatters microseismic noise. It may be possible in the future to invert for the sea floor roughness using the spatial correlation length of the noise field between seismometers placed on and within the sea floor crust (Liu, 1992). In this thesis the propagation of microseisms at and **below** the sea floor is investigated. The specific objectives are:

1. to review the theory of a spherical wave incident on the sea floor. This is done to clarify nomenclature for various propagation mechanisms over a broad band from 0.001 to 50 $Hz$. For example, at ultra-low-frequencies the ocean is a negligible component of the ocean-crust system and the sea floor elastic response can be explained by a free surface model (Rayleigh wave). In contrast,

at 50 $Hz$ the coupling between the sea floor and ocean permits the propagation of Stoneley and pseudo-Rayleigh waves without consideration of the ocean surface. At intermediate frequencies, like those in the microseism band, the ocean and sea floor create an efficient wave guide along which modes belonging to both Rayleigh and Stoneley branches propagate.

2. to describe the noise field within the Blake Bahama Basin as observed on an OBS and borehole array. We wish to determine the fundamental properties of the source and modes of propagation of the microseismic field. This study was motivated by the lack of any detailed information on ambient noise behavior observed simultaneously with depth below the sea floor. It was found that microseismic noise decays with depth below the sea floor but not necessarily linearly.

3. to model scattering of ambient noise energy by the method of finite differences. Interface waves predicted theoretically in Objective 1 and scattering observed during the analysis in Objective 2 were modeled. Finite differences has the advantage of including complete scattering effects from roughness and volume heterogeneities on the order of acoustic wavelengths. Scattering is proposed as the coupling mechanism of near vertical loading of the sea surface (ocean gravity wave interaction) into horizontally propagating modes at the sea floor (as hypothesized by Schreiner and Dorman, 1990). A detailed analysis of 2-D and 3-D models is required to evaluated the partitioning of energy into P-SV and SH modes of propagation.

The objectives listed above follow in a logical order. It is necessary to understand the theoretical behavior of seismo-acoustic wave propagation before analyzing data measured at the sea floor. The Sommerfeld integral was analyzed by the method of steepest descents in order to gain intuition about wave propagation in a fluid/solid system. Because interface waves are believed to propagate microseisms, Stoneley and pseudo-Rayleigh poles were the focus of the study. Though a multitude of previous authors have investigated the halfspace and waveguide problem (Pekeris,

1948; Ewing et al., 1957 and Tolstoy and Clay, 1987) we investigate the problem here in the complex ray parameter plane. We find closed form expressions for Rayleigh, Stoneley and pseudo-Rayleigh waves at the interface between a liquid layer and solid half-space. (A spin off of this analysis, is the identification of a pseudo-Rayleigh wave that can have a complex velocity whose real component is greater than the shear wave velocity of the solid. This wave may be of importance in studies of scattering from sea ice).

Data from the Low Frequency Acoustic Seismic Experiment (LFASE) confirmed the theory for nonlinear wave-wave interaction. This experiment was the first time a vertical array of geophones was deployed in an oceanic borehole. We were able to determine the near bottom depth dependence of noise within the ocean crust. We found that the microseism spectra were controlled qualitatively in both magnitude and directionality by local swell conditions. The LFASE data also show the presence of normal modes in the spectra. The depth dependence of noise at the site is not a simple monotonic function. Theoretical results from Chapter 2 show that in the microseism band higher modes are expected for a sediment structure like that at the Blake Bahama Basin. Particle motion and amplitude behavior at the site suggest a complicated local scattering mechanism. Short wavelength Stoneley modes are seen in the noise spectrum above 0.7 $Hz$ suggesting scattering from wavelength scale surface and volume heterogeneities. The finite difference modeling of Chapter 4 reveals complicated scattering both into the water column and into the sub-bottom. Even small scale heterogeneities can be significant.

The focus of Objective 3 was to study the scattering mechanisms that occur at volume and surface heterogeneities. We find that surface roughness is a more effective isotropic scatterer than similarly scaled volume heterogeneities. In tests between 2D and 3D models we find that 3D modeling is necessary to accurately include the effects of interface waves multiply scattering from sea floor roughness.

## 1.3 Outline

The remainder of this thesis is divided as follows: Chapter 2 is an analysis of the Sommerfeld integral representation of the acoustic field from a point source in a fluid incident on a solid boundary. Analysis will progress from the classical free-surface Rayleigh wave problem to an infinitely thick water layer over a half-space solid and finally to a liquid layer of variable thickness overlying a solid half-space. Chapter 3 contains the analysis of the Low Frequency Acoustic Seismic Experiment data. LFASE involved ocean bottom seismometers and a borehole array which measured vertical, horizontal and pressure components at DSDP site 534. The noise spectrum from the experiment is correlated with sea surface buoy data. Particle motion and directionality are computed to estimate scattering and interface wave modes for the LFASE data set. The results from different numerical scattering models are compared in chapter 4. Flat sea floors with "hard bottom" and "soft bottom" elastic properties are tested. We increase the complexity of the models from sea floor facets to volume heterogeneities to surface heterogeneities and estimate the scattering from two and three dimensional realizations of these models. Finally, chapter 5 lists the conclusions from this thesis and some suggested future work.

This research was supported by Office of Naval Research grants N00014-89-C-0018, N00014-89-J-1012, N00014-90-C-0098, N00014-90-J-1493 and N00014-93-1-1352.

# Chapter 2

# Surface Waves and Microseism Propagation

## 2.1 Introduction

In this chapter we address the interaction of an acoustic point source with the boundary between a fluid and elastic half-space. This problem is pertinent to the discussion of noise in the sea in that microseismic noise propagates in the ocean and sea floor primarily as guided modes within the water column and interface waves within the crust. This chapter is limited to a theoretical discussion of the Sommerfeld integral representation of an acoustic source interacting with the interface between a fluid half-space over an elastic half-space and a fluid layer over an elastic half-space.

Excellent reviews of acoustic observations in the sea measured by ocean bottom hydrophones and seismometers are presented in Urick (1986), Melton (1976) and Darbyshire (1960). More recent studies by Adair (1985) and Sutton and Barstow (1990) include reviews and results from noise measurements below the sea floor. Observed energy levels of ambient seismo-acoustic noise vary with environmental factors such as sea state and biologic and industrial activity. Originally, the term "microseism" referred to continental measurements of the continuous 0.1 - 0.3 $Hz$

seismic interface wave energy that could be directly related to ocean swell (Wilson and Press, 1952). Now, "microseisms" refers to ambient noise energy coupled to the sea floor and propagating in the ocean/crust waveguide between 0.05 and 5.0 Hz (Webb, 1992). The sources of microseisms and the mechanisms that convert gravity wave energy into acoustic noise in the sea are well understood (see literature review in Chapter 1).

In the latter half of this century many high quality experiments have gathered microseismic energy directly on the sea bed (see literature review in Chapter 3). Data gathered from various regions [North Pacific, (Latham and Sutton, 1966); Southern California, (Schreiner and Dorman, 1990); North Atlantic (Webb, 1992); South Pacific (Adair et al., 1986)] all indicate that microseismic energy arises from distant as well as nearby sources. One probable mode for noise propagation in the ocean crust is by interface waves trapped at the sea floor interface. Several authors find that low velocity sea floor sediments enhance the coupling of ambient acoustic noise into crustal seismic noise (Latham and Nowroozi, 1968; Schmidt and Kuperman, 1988; Sutton and Barstow; 1990; Schreiner and Dorman, 1990). Three-dimensional modeling of an acoustic point source interacting with a sea floor comprised of heterogeneous sediments shows that energy penetration into the sea floor induces volume scattering from velocity inhomogeneities and creates a strong interface wave field (Bradley and Stephen, 1993; and Chapter 4 of this thesis).

The above studies and observations indicate that a thorough understanding of the behavior of interface and guided waves as they move from the deep ocean, to shallow water and onto land is necessary for a complete understanding of microseisms. The purpose of this chapter is to define the possible interface wave mechanisms that apply in the microseism band by calculating the Sommerfeld integral solution to the elastic wave equation with asymptotic analysis. In particular, the range of Stoneley, Scholte, Rayleigh and pseudo-Rayleigh interface waves is investigated for a series of models with elastic parameters similar to both soft sediment and hard basement sea floors.

Ewing et al., (1957) provides an excellent review of the deterministic half-space

liquid over solid and liquid layer over half-space problem but do not treat the hard versus soft bottom interface problem or discuss in detail the behavior of the interface wave poles. It should also be noted here that Kuperman and Schmidt (1989) find a perturbation solution for rough surface scattering from horizontally stratified media and Liu (1992) combines the theories of Kuperman and Schmidt and Kuperman and Ingenito (1980) to express the scattered field from a statistically distributed source interacting with a rough surface analytically. The Liu results are important for modeling the noise field from various realizations of source and surface distributions and they represent the 'state of the art' for forward modeling of microseismic noise. Our goal in this chapter is to understand, in detail, the fundamental physics of the interaction of an acoustic source with the boundary between a fluid and solid.

Although this is a classical approach treated by many authors, we review it here in modern nomenclature (the complex ray parameter plane) for models pertinent to the sea floor ambient noise issue. Specific results from this chapter will be referred to in subsequent chapters for investigating the noise field in the Blake Bahama Basin.

## 2.2 Models

Several simple sea floor/crust models are constructed for the range of physical parameters illustrated in Figure (2.1). A point source is shown in Figure (2.1) along with several resultant waves that are excited as the incident energy interacts with a boundary between media. As the incident wave meets the boundary between the crust and the atmosphere illustrated in Figure (2.1), the wave is reflected off the free surface and interface wave modes are excited. For elastic waves this boundary can be treated as a free surface. When the incident wave interacts with the boundary between the fluid ocean and solid crust the wave reflects and transmits energy away, through, and along the boundary (see Figures 2.2 and 2.3).

The reference model (Case 1) is an elastic half-space. Conceptually we choose to model it as a zero depth ocean as shown in Figure (2.1) since we will be adding a finite depth ocean in subsequent models. The source is placed just below the free

surface of the solid. The interface wave solution for this model is known as the Rayleigh wave labeled "R" in the figure. Both "Hard Bottom" and "Soft Bottom" conditions are shown (the distinction between these conditions, defined below, is unimportant for the free surface problem; however, they are key for understanding the waves at a liquid/solid interface).

At the smallest seismic wavelengths, the ocean/crust mechanical system can be thought of as an infinite half-space liquid over an infinite half-space elastic solid, Case 2 (Figure 2.2). Though strong variations in the velocity of the water layer are known to exist (for example the Sound Fixing and Ranging (SOFAR) channel) and are important in the transmission of acoustic noise horizontally through the sea (e.g. the T-phase in earthquake seismology reported by Tolstoy and Ewing, 1950), we are primarily interested in the propagation mechanisms along the sea floor. Hence, for this analysis the water velocity, $\alpha_1$, is fixed. For a hard bottom crust, the acoustic cutoff frequency marks the transition from Rayleigh wave modes to water born modes. For and average ocean depth of 2.0 km the acoustic 1/4 wave cutoff is 0.19 Hz. Below this frequency normal modes in the water column are not supported.

The deep water ocean gravity wave dispersion relation ($\omega^2 = g\ k$) predicts that the surface gravity wave wavelengths are between 100 $m$ and 0.3 $m$ at the peak microseism frequencies between 0.05 and 5.0 $Hz$. Surface gravity wave energy decays exponentially with depth, so most ocean wave energy is coupled to the sea floor via nonlinearly generated acoustic waves (Longuet-Higgins, 1950). In the infragravity wave band, 0.001 - 0.05 $Hz$, ocean gravity waves have wavelengths on the order of the ocean depth and wave energy is directly coupled to the sea floor.

For the half-space liquid over half-space solid model, normal modes of the acoustic system are not excited, so the focus of this section will be strictly on the generation and propagation of interface waves along the sea floor. For crustal models with vertical gradients higher modes can exist and have been modeled numerically by several authors (e.g. Schmidt and Kuperman, 1988; and Schreiner and Dorman, 1990). There are two end member models for the ocean/crust system; "Hard

Bottom" where the shear velocity of the bottom is greater than the acoustic wave velocity of the water, and "Soft Bottom" where the shear wave velocity is less than the acoustic wave velocity of the water (see Figure 2.2).

Hard bottom conditions exist where the ocean lies over young ocean crust consisting of thinly sedimented basalt or over consolidated limestone and reefs. Soft bottom conditions exist where ocean sediment is comprised of unconsolidated mud and sand with thickness greater than or equal to the seismic wavelength. In the deep ocean, sediment depth can range from 0 km at ocean ridges to 0.5 km within abyssal basins. Near the continents, sediment thickness can range from 1.0 - 10.0 km on continental margins and up to 15 km in sedimentary basins like the Gulf of Mexico (Trehu et al., 1989).

It should be noted that it is possible for the compressional wave velocity of the solid to be less than that of the ocean. Kawahara (1984) and Frisk et al. (1980) both consider acoustic models with slow compressional wave sediments in the upper 10 m of the sea floor. Models compiled by Lavoie and O'Hara (1989) for Site 534B, where the LFASE data presented in Chapter 3 was collected, all have compressional wave velocity below the water velocity in the upper 60 m. This model is not considered in the thesis because the effect of a relatively thin slow P-wave layer in deep water and at frequencies below 5.0 Hz will only slightly effect the overall spectrum.

Two interface waves, the pseudo-Rayleigh and Stoneley waves (labeled "pR" and "S" in Figure 2.2), are created by the coupling of compressional and shear energy at the interface and their existence is dependent on the ratio of the material velocities and densities of the liquid/solid system. These two wave types are the focus of the analysis of Case 2.

For the third class of models (Case 3), the infinitely deep ocean is replaced with a liquid layer of finite depth H (Figure 2.3). This effectively introduces a free surface boundary condition permitting the propagation of normal modes through the waveguide created by the free surface, ocean and crust. We find the phase velocity limit for the fundamental mode to be the Rayleigh wave velocity of the solid and at high frequencies or deep water the lower limit is a true Stoneley wave (a

nondispersive, interface wave traveling along the interface between two elastic half-spaces or between acoustic and elastic half-spaces). The Stoneley interface wave at a fluid/solid half-space is also known as a "Scholte" wave. Note that neither Rayleigh or Stoneley waves propagate at the boundaries of solely acoustic media.

## 2.3 Theory

In this section we develop the theory for acoustic waves incident on a boundary between a liquid and an elastic solid and solve the boundary value problem through asymptotic analysis of the Sommerfeld integral. The Sommerfeld integral is an integral representation of a point source as an infinite sum of cylindrical waves. Section 2.3.1 begins with a derivation of the Sommerfeld integral in complex ray parameter space. We then make use of this integral solution to determine the behavior and existence of certain interface wave modes in section 2.4.

The analysis of the field from a point source interacting on a plane boundary between two homogeneous half-spaces in "welded" contact is referred to as Lamb's problem (Lamb, 1904; Aki and Richards, 1980, pg 193). For this study the upper medium (subscript 1) is either a vacuum or liquid. The lower medium (subscript 2) is an elastic solid. The material properties modeled are density ($\rho$), P-wave velocity ($\alpha$) and S-wave velocity ($\beta$). Three parameterized test cases involving different contrasts between these elastic parameters and different fluid depths will be analyzed; 1) Vacuum over elastic half-space, 2) Liquid half-space ($\beta_1 = 0$) over elastic half-space and 3) Liquid layer of variable thickness over elastic half-space. In the latter two cases, the soft bottom ($\alpha_2 > \alpha_1 > \beta_2$) and hard bottom ($\alpha_2 > \beta_2 > \alpha_1$) models are compared and examined. Surface wave pole locations, corresponding to zeros in the denominator of the reflection coefficient, are found for each of these test cases. Individual poles represent slownesses corresponding to Rayleigh, pseudo-Rayleigh and Stoneley waves traveling along the interface. These waves are believed to contribute significantly to the noise spectrum within and near the ocean crust (Schmidt and Kuperman, 1988).

By varying the water depth in test Case 3, we investigate the effects of ocean shoaling on the propagation of Rayleigh waves from shallow to deep water environments. The analysis shows the dominant modes of Rayleigh and Stoneley waves in the ocean crust with differing elasticity. Webb (1992) has argued for an equilibrium microseism spectrum resulting from a balance between dissipation in the upper mantle and excitation in the deep ocean waveguide.

### 2.3.1 Lamb's Problem

The analytic representation of an acoustic or elastic wave incident on the boundary between two homogeneous half-spaces is known as "Lamb's Problem". Lamb (1904) gave an exact solution to a similar problem involving a normal impulse on a free surface. Lamb's analysis presented the method for calculating the interaction of a point source with any general continuous planar boundary between two homogeneous media.

Aki and Richards (1980 Chapter 6), is used as a reference for the following development of reflection, refraction and interface wave generation at the boundary between two homogeneous media. Their nomenclature is used for the development of the Sommerfeld integral in terms of complex ray parameter (horizontal slowness). This coordinate system is convenient for post-critical incidence; the ray parameter region where interface waves are generated.

Consider the inhomogeneous wave equation for the propagation of a point source (with time dependence $e^{-i\omega t}$) in a homogeneous full-space with velocity $c$,

$$\frac{\partial^2 \phi}{\partial t^2} \; - \; c^2 \nabla^2 \phi \; = \; 4\pi c^2 \delta(\vec{x} - \vec{x_o}) \; e^{-i\omega t} \tag{2.1}$$

where $\phi$ is the displacement potential, $\omega$ the angular frequency in radians, $\delta(\vec{x} - \vec{x_o})$ a spatial delta function prescribing the source at $\vec{x_o} \; = \; x_o \, \hat{\imath} + y_o \, \hat{\jmath} + z_o \, \hat{k}$ and $t$ the time variable. The solution to equation ( 2.1) can be found by convolving the source term with the Green function solution to the wave equation. The Green function is the solution to:

$$\frac{\partial^2 G}{\partial t^2} - c^2 \nabla^2 G = \delta(\vec{x} - \vec{x_o})\, \delta(t - t_o),$$

where $G(\vec{x}, t; \vec{x_o}, t_o)$ is the field measured at a point $\vec{x}$ and time $t$ due to a unit impulse source at $\vec{x_o}$ initiated at time $t_o$. Assuming the point excitation occurs at the coordinate origin ($\vec{x_o} = 0$) and at the initiation time ($t_o = 0$), then the field measured at an observation point $\vec{x}$ is

$$G(\vec{x}, t) = \frac{1}{4\pi c^2} \frac{\delta(t - \frac{|\vec{x}|}{c})}{|\vec{x}|}. \tag{2.2}$$

Convolving equation ( 2.2) with the time dependent forcing function yields,

$$\phi(\vec{x}, t) = \frac{1}{|\vec{x}|}\, e^{i\omega(\frac{|\vec{x}|}{c} - t)}. \tag{2.3}$$

This is the solution to equation ( 2.1) and it represents a spherical wave propagating from the origin in an infinite homogeneous medium with speed $c$.

A second solution to equation ( 2.1) can be obtained via Fourier analysis. For this thesis the Fourier transform will be defined as in Aki and Richards (1980, pg 129), where the forward spatial and time transforms of an arbitrary function $f(x, t)$ are:

$$f(x,t) \rightarrow F(k_x, t) = \int_{-\infty}^{\infty} f(x,t) e^{-ik_x x} dx$$

and

$$f(x,t) \rightarrow F(x, \omega) = \int_{-\infty}^{\infty} f(x,t) e^{+i\omega t} dt.$$

The inverse transforms are:

$$F(k_x, t) \rightarrow f(x,t) = \frac{1}{2\pi} \int_{-\infty}^{\infty} f(k_x, t) e^{+ik_x x} dx$$

and

$$F(x, \omega) \rightarrow f(x,t) = \frac{1}{2\pi} \int_{-\infty}^{\infty} f(x, \omega) e^{-i\omega t} d\omega.$$

Using these definitions the forward spatial Fourier transform of equation ( 2.1) becomes,

$$-\omega^2 \Phi(\vec{k}, t) + |\vec{k}|^2 c^2 \Phi(\vec{k}, t) = 4\pi c^2\, e^{-i\omega t}. \tag{2.4}$$

where $\mid \vec{k} \mid^2 = {k_x}^2 + {k_y}^2 + {k_z}^2$ is the magnitude vector. The solution to equation ( 2.4) is then,

$$\Phi(\vec{k},t) = \frac{4\pi c^2}{\mid \vec{k} \mid^2 c^2 - \omega^2} e^{-i\omega t}. \tag{2.5}$$

Writing the triple inverse transform of equation ( 2.5) along all the wave number components $k_x, k_y$ and $k_z$ and equating to ( 2.3) we get,

$$\frac{1}{\mid \vec{x} \mid} e^{i\omega(\frac{\mid \vec{x} \mid}{c} - t)} = \frac{e^{-i\omega t}}{2\pi^2} \int_{-\infty}^{\infty}\int_{-\infty}^{\infty}\int_{-\infty}^{\infty} \frac{e^{i(k_x x + k_y y + k_z z)}}{\mid \vec{k} \mid^2 - \frac{\omega^2}{c^2}} dk_x dk_y dk_z. \tag{2.6}$$

Equation ( 2.6) is now the expression for a point acoustic source (left hand side of 2.6) as in infinite sum of plane waves over all $k_x$, $k_y$ and $k_z$. The phase velocity is arbitrary in the right hand side term in equation ( 2.6). An integration along $k_z$ is performed to remove the arbitrary phase velocity in the plane wave term, $e^{i(\vec{k}\cdot\vec{x} - \omega t)}$ where $\omega/k$ varies from 0 to $\infty$. So $k_z$ is extended to the complex plane and we integrate ( 2.6) along the real axis. This integration is done along with respect to $k_z$ since we will be analyzing the interaction of the point source with horizontal $(XY-plane)$ boundaries. The integrand has poles at $k_z = \pm(\omega^2/c^2 - {k_x}^2 - {k_y}^2)^{1/2}$ some of which lie on the real $k_z$-axis and and must be accounted for in the integration. The poles can be rotated off the axis to allow the integration path to remain on real $\vec{k}$. To rotate the poles off the real axis, a small imaginary component is added to $1/c$. This is equivalent to introducing a small amount of attenuation. Aki and Richards (1980) show that $Im\{1/c\}$ must be small and positive to agree with dispersion relations and physical radiation conditions. A complex velocity rotates the poles into the first and third quadrants of the complex plane. Integrating ( 2.6) first for $z > 0$ the result is the sum of the residues of $\phi$ for the $k_z$ poles:

$$\phi(\vec{x},t) = \frac{e^{-i\omega t}}{2\pi} \iint_{-\infty}^{\infty} \frac{e^{i(k_x x + k_y y) - \gamma z}}{\gamma} dk_x dk_y$$

and for $z < 0$,

$$\phi(\vec{x},t) = \frac{e^{-i\omega t}}{2\pi} \iint_{-\infty}^{\infty} \frac{e^{i(k_x x + k_y y) + \gamma z}}{\gamma} dk_x dk_y.$$

Now the spherically expanding wave can be expressed as an infinite sum of plane waves for all $z$:

$$\frac{1}{\mid \vec{x} \mid} e^{i\omega \frac{\mid \vec{x} \mid}{c}} = \frac{1}{2\pi} \iint_{-\infty}^{\infty} \frac{e^{ik_x x + ik_y y - \gamma \mid z \mid}}{\gamma} dk_x dk_y, \tag{2.7}$$

where $\gamma$ is complex and defined, $\gamma = ({k_x}^2 + {k_y}^2 - \frac{\omega^2}{c^2})^{1/2}$. The sign of $\gamma$ is chosen so the evaluation of equation ( 2.7) is bounded when $\mid z \mid \rightarrow \infty$, i.e. $Re\{\gamma\} > 0$. For a perfectly elastic medium $Re\{\gamma\} \geq 0$. Equation ( 2.7) is called the Weyl integral and is based in the Cartesian coordinate system.

Ultimately, we would like to integrate the wave equation over a single variable. We can make one more approximation without losing our ability to integrate over model variability in $z$, which is the assumption of radial symmetry. The point source can now be represented as a sum over cylindrical waves whose symmetry is about the $z - axis$. To derive this form of equation ( 2.7) a change of variables for $k_x$ and $k_y$ is needed. In the $k_x$ $k_y$ plane, a plane wave can be expressed in cylindrical coordinates:

$$k_x = k_r cos(\varphi')$$

$$k_y = k_r sin(\varphi')$$

where $k_r$ is normal to the wavefront in the $k_x$ $k_y$ plane and $\varphi'$ is is the relative angle between $k_r$ and $k_x$. Figure (2.4a) illustrates the wavenumber coordinate frame. Now $\gamma = ({k_r}^2 - \frac{\omega^2}{c^2})^{1/2}$, the area element defined by $dk_x$ and $dk_y$ becomes $dk_r$ $k_r d\varphi'$ and the horizontal wavenumber plane is defined by $0 \leq k_r < \infty$ and $0 \leq \varphi' < 2\pi$. Similarly, $x$ and $y$ are redefined as,

$$x = rcos(\varphi)$$

$$y = rsin(\varphi),$$

where $r$ is the range from the source and $\varphi$ is the azimuth (see Figure 2.4b). Equation ( 2.7) becomes:

$$\frac{1}{\mid \vec{x} \mid} e^{i\omega \frac{\mid \vec{x} \mid}{c}} = \frac{1}{2\pi} \int_0^{\infty} \int_0^{2\pi} \frac{k_r}{\gamma} e^{ik_r r cos(\varphi - \varphi') - \gamma \mid z \mid} d\varphi' dk_r, \tag{2.8}$$

Recognizing that $\int_0^{2\pi} e^{ik_r r cos(\varphi)} d\varphi = 2\pi\ J_o(k_r r)$, the $\varphi'$ integral can be replaced with a cylindrical Bessel function $J_o(k_r r)$. Equation ( 2.8) becomes:

$$\frac{1}{\mid \vec{x} \mid} e^{i\omega \frac{\mid \vec{x} \mid}{c}} = \frac{1}{2\pi} \int_0^{\infty} \frac{k_r\ J_o(k_r r)\ e^{-\gamma \mid z \mid}}{\gamma} dk_r, \tag{2.9}$$

where $i\gamma = (\frac{\omega^2}{c^2} - {k_r}^2)^{1/2}$ with $Re\{\gamma\} > 0$ ensuring exponential decay with $z$. Equation ( 2.9) is known as the Sommerfeld integral and expresses spherical waves from a point source at the origin as a sum of cylindrical waves in the horizontal wavenumber plane symmetric about the z-axis. These waves form a conical wavefront in 3-space. Figure (2.4c) illustrates the conical wavefront for a particular $k_r$, where $k_r = \frac{\omega\ sin\theta}{c}$ and $\theta$ is the angle the wavefront makes with the z-axis.

Expressing equation ( 2.9) in terms of horizontal slowness or ray parameter, $p = \frac{sin\theta}{c} = \frac{k_r}{\omega}$, and vertical slowness $\xi = \frac{cos\theta}{c} = (\frac{1}{c^2} - p^2)^{1/2}$ and adding back the time dependence, $e^{-i\omega t}$:

$$\frac{1}{R} e^{i\omega(\frac{R}{c} - t)} = i\omega\ e^{-i\omega t} \int_0^{\infty} \frac{p}{\xi} J_o(\omega p r)\ e^{i\omega\xi \mid z \mid} dp, \tag{2.10}$$

where, $i\gamma = (\frac{\omega^2}{c^2} - {k_r}^2)^{1/2} = \omega(c^{-2} - p^2)^{1/2} = \omega\xi$ and $Re\{\gamma\} > 0$.

There is an ambiguity in sign due to the complex function $\xi$. A branch cut defined by $\xi$ separates the two Riemann sheets; $Re\{\gamma\} > 0$; $Im\{\gamma\} > 0$ and $Re\{\gamma\} < 0$; $Im\{\gamma\} < 0$. The integration over $p$ should remain on the physically meaningful Riemann sheet on which $Im\{\xi\} \geq 0$ otherwise the wave will grow exponentially with $z$ as indicated by the $e^{i\omega\xi z}$ term in equation ( 2.10). For both equations ( 2.8) and ( 2.9) there can exist a $\gamma$ which is real and positive (e.g. when $\frac{\omega^2}{c^2} < {k_r}^2$). This yields inhomogeneous waves which decay exponentially with $\mid z \mid$ and travel along horizontal planes. These horizontally confined interface waves are discussed in detail in the next section.

## 2.4 Rayleigh, pseudo-Rayleigh and Stoneley Wave Pole Analysis

### 2.4.1 Case 1: Elastic Half-space

Equation ( 2.10) is a convenient way to express solutions to the wave equation for matching boundary conditions at horizontal interfaces between media, the most likely interface to encounter in a layered earth. Figure (2.1) illustrates the wave components arising from a spherical compressional wave impinging on the free surface of an elastic half-space, Case 1 in this analysis. The variables $\alpha$, $\beta$ and $\rho$ will be used as compressional velocity, shear velocity and density for the media respectively. The incident wave field is a spherical compressional wave represented by the compressional potential, $\phi_i(\vec{x},t)$. The resultant field after interaction with the boundary consists of a reflected compressional wave (represented by the compressional potential, $\phi_r(\vec{x},t)$) and a reflected shear wave (represented by the shear potential, $\psi_r(\vec{x},t)$. Note that the shear potential is actually a vector potential. In this symmetry case SH decouples from SV. The shear potential corresponding to SV is scalar). At the boundary there can be a coupling of both the compressional and shear potentials producing interface waves. The dominant interface wave for the elastic half-space problem is the Rayleigh wave which is generated from a coupling between the inhomogeneous portions of both $\phi_r$ and $\psi_r$. In this section I discuss how each of these waves arise from ( 2.10)

We make use of *Lamé's Theorem* which defines the scalar and vector potentials, $\phi$ and $\psi$, for the displacement field and allows us to separate the wave equation into its compressional and shear wave components (Aki and Richards, 1980, pp 68–70). Adopting a $z$-positive-down convention, the three body wave potential fields ,the incident field ($\phi_i$), the reflected compressional field ($\phi_r$), and the reflected shear wave field ($\psi_r$), are expressed as:

$$\phi_i \;=\; i\omega\, e^{-i\omega t} \int_0^\infty A\, \frac{p}{\xi} J_o(\omega p r)\; e^{i\omega\xi|z\,-\,h|} dp, \tag{2.11}$$

$$\phi_r \;=\; i\omega\; e^{-i\omega t} \int_0^\infty \; B_{fs}\; \frac{p}{\xi} J_o(\omega p r)\; e^{i\omega\xi(z\,+\,h)} dp, \tag{2.12}$$

$$\psi_r \;=\; i\omega\; e^{-i\omega t} \int_0^\infty \; D_{fs}\; \frac{p}{\xi} J_o(\omega p r)\; e^{i\omega(\xi h\,+\,\eta z)} dp, \tag{2.13}$$

where $h$ is the vertical coordinate of the point source below the interface. $A$ is the amplitude of the incident compressional wave potential. $B_{fs}$ and $D_{fs}$ are the amplitudes of the reflected compressional and shear wave field potentials. The reflected shear wave potential, $\psi_r$, involves the shear wave vertical slowness which is defined as:

$$\eta \;=\; (\frac{1}{\beta^2} \;-\; p^2)^{1/2}.$$

To convert the displacement potentials in equations ( 2.11 - 2.13) into the cylindrical displacements we use Lamé's Theorem. The radial and vertical displacements, $u_r$ and $u_z$ are defined as,

$$\begin{aligned} u_r \;&=\; \frac{\partial\phi}{\partial r} \;+\; \frac{\partial^2\psi}{\partial r \partial z} \\ u_z \;&=\; \frac{\partial\phi}{\partial z} \;-\; \frac{1}{r}\frac{\partial}{\partial r}(r\frac{\partial\psi}{\partial r}), \end{aligned} \tag{2.14}$$

and the tangential and normal stresses are

$$\begin{aligned} \tau_{zr} \;&=\; \mu(\frac{\partial u_z}{\partial r} \;+\; \frac{\partial u_r}{\partial z}) \\ \tau_{zz} \;&=\; \lambda\nabla u \;+\; 2\mu\frac{\partial u_z}{\partial z}. \end{aligned} \tag{2.15}$$

The free surface boundary conditions require that radial and normal stresses must go to zero at $z \;=\; 0$. We begin by rewriting equations ( 2.11), ( 2.12) and ( 2.13) to obtain expressions for the total P- and S-wave potentials,

$$\phi \;=\; \phi_i + \phi_r \;=\; \int_0^\infty \frac{p}{\xi}\,[A\; J_o(\omega p r)\; e^{i\omega\xi|z\,-\,h|} \;+\; B_{fs}\; J_o(\omega p r)\; e^{i\omega\xi(z\,+\,h)}]\; dp, \tag{2.16}$$

$$\psi \;=\; \int_0^\infty \frac{p}{\xi}\,[D_{fs}\; J_o(\omega p r)\; e^{i\omega(\xi h\,+\,\eta z)}]\; dp, \tag{2.17}$$

and then match the boundary conditions at the free surface. One other useful identity for simplifying the radial derivative terms in ( 2.14) and ( 2.15) involves the Bessel function,

$$\frac{dJ_o(\omega pr)}{dr} \;=\; -\omega p J_1(\omega pr).$$

From ( 2.14), ( 2.15), ( 2.16) and ( 2.17), we find that the free surface tangential stress condition ($\tau_{zr} = 0$) yields, at $z \;=\; 0$:

$$2i\mu\omega\xi \; A \;=\; 2i\mu\omega\xi \; B_{fs} \;-\; (2\mu\omega^2 p^2 - \omega^2\rho) \; D_{fs}. \tag{2.18}$$

The normal stress boundary condition ($\tau_{zz} = 0$) gives

$$(\rho\omega^2 - 2\mu\omega^2 p^2) \; A \;=\; 2i\mu\omega^3 p^2 \eta \; D_{fs} \;+\; (2\mu\omega^2 p^2 - \omega^2\rho) \; B_{fs} \tag{2.19}$$

Solving for $B_{fs}$ and $D_{fs}$ in terms of the incident wave amplitude the P-wave reflection coefficient for displacement potential is:

$$\frac{B_{fs}}{A} \;=\; \acute{P}\grave{P} \;=\; \left[\frac{4p^2\xi\eta \;-\; (2p^2 - \frac{1}{\beta^2})^2}{4p^2\xi\eta \;+\; (2p^2 - \frac{1}{\beta^2})^2}\right] \tag{2.20}$$

and the S-wave reflection coefficient for displacement potential is,

$$\frac{D_{fs}}{A} \;=\; \left(\frac{\beta}{\alpha i\omega p}\right) \acute{P}\grave{S} \;=\; \left(\frac{\beta}{\alpha i\omega p}\right) \left[\frac{4\frac{\alpha}{\beta}p\xi(\frac{1}{\beta^2} - 2p^2)}{4p^2\xi\eta \;+\; (2p^2 - \frac{1}{\beta^2})^2}\right] \tag{2.21}$$

where $\beta^2\rho$ has been substituted for $\mu$. $\acute{P}\grave{P}$ and $\acute{P}\grave{S}$ are the plane wave displacement reflection coefficients for the free surface and can be found in Aki and Richards equations 5.26 and 5.27. So the complete displacement potential expressions are

$$\phi_i \;=\; i\omega \; e^{-i\omega t} \int_0^\infty \left[\frac{p}{\xi} J_o(\omega pr) \; e^{i\omega\xi|z \;-\; h|}\right] dp, \tag{2.22}$$

$$\phi_r \;=\; i\omega \; e^{-i\omega t} \int_0^\infty \acute{P}\grave{P} \left[\frac{p}{\xi} J_o(\omega pr) \; e^{i\omega\xi(z \;+\; h)}\right] dp, \tag{2.23}$$

$$\psi_r \;=\; i\omega \; e^{-i\omega t} \int_0^\infty \frac{\beta}{i\omega p\alpha} \acute{P}\grave{S} \left[\frac{p}{\xi} J_o(\omega pr) \; e^{i\omega(\xi h \;+\; \eta z)}\right] dp. \tag{2.24}$$

The method of steepest descents and saddle point analysis is used to solve the integrals in equations ( 2.22 - 2.24) giving the solution for the compressional and

shear potentials at any ray parameter. The method is complicated however due to the presence of branch cuts and poles in the solution. References on this method can be found in Aki and Richards (1980), Bender and Orzag (1978), and Morse and Feshbach (1953). Simply stated, the method of steepest descents is an evaluation method for integrals along the real axis by altering the path of integration into the complex plane while conserving the value of the integral. Optimally, the integration path is altered so that only a comparatively short portion of the path is needed to evaluate the integral.

The Bessel function in ( 2.23 and 2.24) is rewritten as the sum of two zero order Hankel functions of the first and second kind:

$$J_o(\omega pr) \;=\; \frac{1}{2}\left[H_o{}^{(1)}(\omega pr) + H_o{}^{(2)}(\omega pr)\right]$$

and

$$H_o{}^{(2)}(\omega pr) \;=\; -H_o{}^{(1)}(-\omega pr).$$

This substitution permits integration over the entire real axis, $-\infty \leq p \geq \infty$. For large arguments where $\omega pr \;\geq\; 14$, the asymptotic expansion of $H_o{}^{(1)}$ is

$$H_o{}^{(1)}(\omega pr) \;=\; \sqrt{\frac{2}{\pi\omega pr}}e^{i\,(\omega pr - \frac{\pi}{4})}.$$

Equations ( 2.23) and ( 2.24) now can be written:

$$\phi_r \;\sim\; \sqrt{\frac{\omega}{2\pi r}}\, e^{i(\frac{\pi}{4}-\omega t)} \int_{-\infty}^{\infty} \acute{P}\grave{P}\frac{p^{1/2}}{\xi}\, e^{i\,\omega(pr\,+\,\xi(z\,+\,h))}dp, \tag{2.25}$$

$$\psi_r \;\sim\; \sqrt{\frac{\omega}{2\pi r}}\, e^{i(\frac{\pi}{4}-\omega t)} \int_{-\infty}^{\infty} \frac{\beta}{i\omega\alpha}\acute{P}\grave{S}\frac{p^{1/2}}{\xi}\, e^{i\,\omega(pr\,+\,\xi h\,+\,\eta z)}dp. \tag{2.26}$$

Note that neither of these approximations is accurate for the limit as $p \rightarrow 0$ (i.e. near normal incidence). However this study is concerned primarily with near critical incidence where the approximation is accurate. Both of these approximate forms can now be integrated for complex $p$. The branch points and cuts must be identified in the integrand expressions for $\xi$ and $\eta$. These branch cuts are located in

the first and third quadrants of the complex ray parameter plane (see Figure 2.5) and each separate a unique set of Riemann sheets (Hildebrand, 1976, Chapter 10, and Aki and Richards, 1980, Chapter 6). The square root power on $p^{1/2}$ indicates an additional branch cut is needed extending from the branch point at $p = 0$. This cut is shown lying just above the real axis in Figure (2.5). As mentioned, a second set of cuts are determined for $Im\{\xi\} = 0$, $Im\{\eta\} = 0$ and $Re\{p\} = 0$. For these cuts the definitions of $\xi$ and $\eta$ describe hyperbolas in the complex $p$ plane as shown in Figure (2.5). An integration path must now be chosen to evaluate the displacement potential while taking into account the branch points, cuts and poles of the integrand. We begin by solving the reflected P-wave potential.

Because of the location of the $p^{1/2}$ branch cut and the branch points at $p = 0$, $p = \pm\frac{1}{\alpha^2}$ and $p = \pm\frac{1}{\beta^2}$ the integration path must be deformed to lie just above the real axis for $Re\{p\} \leq 0$ and just below the real axis for $Re\{p\} > 0$ when the incident wave is at sub-critical incidence. To evaluate this integral analytically for all complex ray parameters, the method of steepest descents is employed.

The integrals in equations ( 2.25) and ( 2.26) have the form:

$$I(x) = \int_c F(\zeta) e^{xf(\zeta)}\, d\zeta$$

where for the reflected P-wave potential;

$$xf(\zeta) \rightarrow \omega\, f(p) = \omega\, i\, (pr + \xi\, (z + h)) \tag{2.27}$$

and

$$F(\zeta) \rightarrow F(p) = \sqrt{\frac{\omega}{2\pi r}}\, e^{i\,(\frac{\pi}{4} - \omega t)} \acute{P}\grave{P} \frac{p^{1/2}}{\xi} \tag{2.28}$$

Because $\omega$ is assumed large and positive the magnitude of ( 2.25) is primarily controlled by $e^{\omega Re\{f(p)\}}$. The value of the integral is then controlled by maxima in $f(p)$, or "saddle points" (Brekhovskikh, 1960, refers to these as "passage points"). This occurs when the first derivative of $f(p)$ is zero. For equation ( 2.27),

$$\frac{f(p)}{dp} = f'(p) = i\, (r - p\, (z + h)/\xi)$$

$$\frac{d^2 f(p)}{dp^2} = f''(p) = -i\, (\frac{z + h}{\alpha^2 \xi^3}).$$

The saddle point lies on the real axis for $p_s$ ($p_{saddle}$) satisfying $f'(p) = 0$. Now for the derivative of ( 2.27) to be zero this implies $r\xi = p\,(z + h)$ or alternatively expressed, $r\,\frac{cos(\theta)}{\alpha} = (z + h)\frac{sin(\theta)}{\alpha}$ (where the saddle point slowness is defined as $p_s = \frac{sin(\theta)}{\alpha}$). Figure (2.6a) shows this saddle point to be the reflected wave off the free surface. For the reflected wave potential the integration path must remain on a physically real Riemann sheet for large $p$, in this case $Im\{\eta\} \geq 0$ and $Im\{\xi\} \geq 0$. Figure (2.7) shows this path which is asymptotic to lines making an angle $\theta$ with the real axis. The steepest descents path is defined by the quantity

$$i\,(pr + \xi h + \eta z) = R_o/\alpha + \text{a positive imaginary number } (iX^2)$$

where $R_o = ((h+z)^2 + r^2)^{1/2}$. This insures that the exponential in equation (2.25) goes to zero as $\omega$ goes to $\infty$ when the path lies off the real axis. The steepest descents path must cross back across the real axis (i.e. $Im\{p\} < 0$ to $Im\{p\} > 0$) at $p_r = \frac{1}{\alpha sin(\theta)}$.

Similarly for the shear wave potential in equation ( 2.26)

$$xf(\zeta) \rightarrow \omega\, f(p) = \omega\, i\,(pr + \xi h + \eta z)$$

and

$$f'(p) = i\,(r - p(\frac{h}{\xi} - \frac{z}{\eta}))$$

and

$$F(\zeta) \rightarrow F(p) = \sqrt{\frac{\omega}{2\pi r}}\, e^{i\,(\frac{\pi}{4} - \omega t)} \frac{\beta}{i\,\omega\,\alpha} \acute{P}\grave{S} \frac{p^{-1/2}}{\xi}$$

when the incident angle, $\theta$, exceeds $\theta_c = sin^{-1}\frac{\beta}{\alpha}$. The shear wave saddle point shows that the most significant contribution is the converted shear wave reflection off the free surface where $r = \frac{sin(\theta)}{cos(\theta)}\,h + \frac{\beta\, sin(\theta)}{\alpha\, cos(\theta')}\,z$ and $\eta = \frac{cos(\theta')}{\beta}$. The definitions of $\theta$ and $\theta'$ can be seen in Figure (2.6).

The steepest descents path normally stays on the $Im\{\xi\} \geq 0$; $Im\{\eta\} \geq 0$ Riemann sheet, however to pass through the saddle point, the path must cross

the $\xi$ and $\eta$ branch cuts. This is facilitated by shifting the path to the $Im\{\xi\} < 0$; $Im\{\eta\} < 0$ Riemann sheet in the first quadrant, crossing the branch cuts and then completing the integration on the $Im\{\xi\} \geq 0$; $Im\{\eta\} \geq 0$ Riemann sheet in the fourth quadrant. Because there are no poles or singularities lying in the $Im\{\xi\} < 0$; $Im\{\eta\} < 0$ Riemann sheet the evaluation of the integral is straight forward.

As we increase the angle of incidence the saddle point moves toward but remains left of the $\xi$ branch cut. The integration path must be taken around the $\xi$ branch cut and while the most significant contribution is still at the saddle point, the integration path must also be taken around the $\eta$ branch cut whose contribution to the integral is interpreted as an inhomogeneous P-wave coupled to the free surface, propagating horizontally as a vertically polarized S-wave (SV-wave) then radiating back to the receiver as an inhomogeneous P-wave. The arrival of the P-pole is between the head-wave and wide angle reflection.

Poles of the integrand start to contribute to the resulting field at high incidence angles. For this model the most significant pole contribution is the free surface Rayleigh wave. When $p = \frac{1}{\alpha sin(\theta)} < \frac{1}{c_r}$ (where $p = \frac{1}{c_r}$ is the Rayleigh pole of 2.25) the steepest descents path crosses back across the real axis before the pole (see Figure 2.8) and the residue from the pole must be included in the solution of equation (2.25).

Poles in the denominator of $\acute{P}\grave{P}$ and $\acute{P}\grave{S}$ also exist on different non-physical Riemann sheets. Although the integration path may not lie on the Riemann sheet where the pole occurs, these poles can contribute to the integral if they lie near a branch cut when the incidence angle is large. Poles on non-physical Riemann sheets are called "leaky modes" because the waves they describe are not strictly trapped to the interface but instead "leak" energy away from the boundary (see Gilbert and Laster, 1962). In a later section we will find the pseudo-Rayleigh is one of these leaky waves and can have a significant effect at a fluid solid interface.

The zeros in the denominator of $\acute{P}\grave{P}$ and $\acute{P}\grave{S}$ correspond to roots of a third order

polynomial in $p^2$, so equating the denominator to zero and expanding:

$$p^6\ 16(\frac{\beta^2}{\alpha^2}\ -\ 1)\ -\ p^4\ (\frac{16}{\alpha^2}\ -\ \frac{24}{\beta^2})\ -\ p^2\ (\frac{8}{\beta^4})\ +\ \frac{1}{\beta^6}\ =\ 0. \qquad (2.29)$$

Equation ( 2.29) is called the Rayleigh period equation. Rayleigh (1887) showed that ( 2.29) has three roots and described in detail the particle motion associated with the one physically real root lying on the real axis. The remainder of this chapter concentrates on the evaluation of the residues in the reflected wave potential that give rise to surface coupled waves of the Rayleigh type.

The Rayleigh wave pole is found for the denominator of $\acute{P}\grave{P}$ graphically using a complex root pole finding program. In Figure (2.9) the value of the Rayleigh period equation or Rayleigh function, $R(p)$ is contoured in the complex $p-$plane. The values are computed for a solid half-space with $\alpha\ =\ 4.0\ km/s$, $\beta\ =\ 2.3\ km/s$ and density $\rho\ =\ 2.3\ gm/cc$; this model will be used as Model 1 for the elastic hard bottom sea floor. Equation ( 2.29) can be solved by standard root finding algorithms (Press et al, 1986) however, the graphical method introduced here is useful for observing the behavior of the period equation for the subsequent liquid half-space and liquid layer problems. In particular this method allows the visualization of all the separate physical and non-physical Riemann sheets and the poles that lie on them. The dotted contours mark the amplitude of the imaginary component of $R(p)$ and the solid contours the real amplitude. When the zero contours of both the real and imaginary component of $R(p)$ cross there is a pole of equation ( 2.25) and equation ( 2.26). In Figure (2.9) the Rayleigh pole is found at p=0.473 s/m on the real axis.

The real and imaginary amplitude of $R(p)$ are shown along a portion the positive real axis (i.e. a cross-section through Figure (2.9a) along the real axis) in Figure (2.9b). Because the Rayleigh pole is real the zero crossing between the real and imaginary components of $R(p)$ occurs along the $Re\{p\}$ axis. We can see from equation ( 2.29) that there are 3 roots of $p^2$. The first of these roots is the Rayleigh pole described above. The second root is also a real pole but is unphysical owing to the fact that it describes a wave propagating faster than the body wave (on the real sheet). The third root is discussed below.

Near $\frac{1}{\alpha}$ a separate pole can be found on the $Im\{\xi\} < 0;\ Im\{\eta\} > 0$ Riemann sheet corresponding to one of the leaky modes described earlier. For a shear wave source this pole is an important component for high incident angle reflections in very high Poisson's ration solids, like sea floor sediments. In a similar set of plots as those for the Rayleigh pole, this pole is shown in Figures (2.10a) and (2.10b). In order to isolate the pole from the P-wave velocity, a model with a large difference in compressional and shear wave slowness was used ($\alpha = 4.0\ km/s$, $\beta = 1.7\ km/s$). For this model the pole is located at a complex slowness of $p = 0.374 + 0.09\,i$ shown in Figure (2.10a). The real $p - axis$ plot in Figure (2.10b) shows no simultaneous crossings of the real and imaginary component of $R(p)$ along real $p$, however the real component of the pole is plotted on Figure (2.10b) and is aligned with a crossing of the real and imaginary component of $R(p)$. This pole is identified in Aki and Richards as the $P$-pole or the $\bar{P}$-pulse discussed by Gilbert and Laster (1962). As the Poisson's ratio is increased the $P$-pole migrates to the $\frac{1}{\alpha}$ branch point and represents a distortion of the compressional head wave generated by a shear wave reflection. However, at sufficient range from a compressional wave source, it is the Rayleigh pole which contains the most energy.

Figure (2.11) shows a summary of the computed Rayleigh velocities for the free surface problem for a range of velocities reflecting both hard and soft bottom conditions. The density was fixed at 2.4 and 2.7 gm/cc for soft and hard bottom conditions respectively. In Figure (2.11) a boundary between physical and "non-physical" models is drawn. In the non-physical regime the Lamé constant $\lambda$ is negative a physical impossibility. A line is drawn indicating a "Poisson Solid", i.e. $\alpha = \sqrt{3}\beta$. We see that for physical solids, the shear wave velocity is the most important parameter for controlling the Rayleigh wave velocity.

Recalling the expression for $\acute{P}\grave{P}$, we take its limit as $p$ approaches the pole at $\frac{1}{c_r}$. In the numerator, $4p^2\xi\eta \rightarrow (2p^2 - \frac{1}{\beta^2})^2$ as $p \rightarrow \frac{1}{c_r}$. $R(p)$ is defined as the denominator of $\acute{P}\grave{P}$ and the Taylor series expansion of $R(p)$ near $p = \frac{1}{c_r}$ is

$$R(p) = R(\frac{1}{c_r}) + \frac{\partial R(\frac{1}{c_r})}{\partial p}(p - \frac{1}{c_r}) + \frac{\partial^2 R(\frac{1}{c_r})}{\partial p^2}\frac{(p - \frac{1}{c_r})^2}{2!} + \cdots$$

$\acute{P}\grave{P}$ to first order then becomes

$$\lim_{p \to \frac{1}{c_r}} \acute{P}\grave{P} \sim \frac{8(\frac{1}{c_r})^2 \xi(\frac{1}{c_r}) \eta(\frac{1}{c_r})}{(p - \frac{1}{c_r})\ R'(\frac{1}{c_r})}$$

since $c_r < \beta < \alpha$ we can keep the numerator from being complex by factoring out $i$ in both $\xi$ and $\eta$. The expression for $\acute{P}\grave{P}$ shows there is a simple pole at $\frac{1}{c_r}$. The residue at $\frac{1}{c_r}$of the reflected P-wave potential becomes

$$\phi_r \sim -8A \sqrt{\frac{2\pi\ \omega}{c_r\ r}}\ e^{i\ (\frac{\pi}{4} - \omega t)} \frac{(\frac{1}{{c_r}^2} - \frac{1}{\beta^2})^{1/2}}{{c_r}^2\ R'(1/c_r)}\ e^{(\frac{i\omega r}{c_r} - \omega\ (\frac{1}{{c_r}^2} - \frac{1}{\alpha^2})^{1/2}\ (z\ +\ h))}. \quad (2.30)$$

Similarly, taking the limit of $\acute{P}\grave{S}$ we get

$$\lim_{p \to \frac{1}{c_r}} \acute{P}\grave{S} \sim \frac{-4\ \xi(\frac{1}{c_r})\ \frac{i}{\omega}\ (\frac{1}{\beta^2} - \frac{2}{{c_r}^2})}{(p - \frac{1}{c_r})\ R'(\frac{1}{c_r})}$$

As above we compute the residue for ( 2.26) and get

$$\psi_r \sim 4A \sqrt{\frac{2\pi\ \omega}{c_r\ r}}\ e^{i\ (\frac{\pi}{4} - \omega t)} \frac{(\frac{1}{\beta^2} - \frac{2}{{c_r}^2})}{\omega\ R'(1/c_r)}\ e^{(\frac{i\omega r}{c_r} - \omega\ (\frac{1}{{c_r}^2} - \frac{1}{\alpha^2})^{1/2} h\ -\ \omega\ (\frac{1}{{c_r}^2} - \frac{1}{\beta^2})^{1/2} z))}. \quad (2.31)$$

Using the definition for displacement given above (equation 2.14) the displacements in the radial and vertical directions for $r \gg 1$ show geometric spreading is dependent on $r^{-1/2}$ along with higher order terms in $r^{-3/2}$ and $r^{-5/2}$. The generalized displacement equations for Rayleigh waves are

$$u_r \simeq \frac{i\omega\eta'}{c_r}\ C \left[\frac{2}{{c_r}^2} e^{-\omega\xi' z} + (\frac{2}{{c_r}^2} - \frac{1}{\beta^2})\ e^{-\omega\eta' z}\right] e^{i\frac{\omega r}{c_r}}\ r^{-1/2} + \bigcirc r^{-3/2} \quad (2.32)$$

and

$$u_z \simeq \frac{\omega\eta'}{c_r}\ C \left[\frac{-2\xi'}{c_r} e^{-\omega\xi' z} + \frac{(\frac{2}{{c_r}^2} - \frac{1}{\beta^2})}{\eta'}\ e^{-\omega\eta' z}\right] e^{i\frac{\omega r}{c_r}}\ r^{-1/2} + \bigcirc r^{-5/2} \quad (2.33)$$

where $\xi' = (\frac{1}{{c_r}^2} - \frac{1}{\alpha^2})^{1/2}$, $\eta' = (\frac{1}{{c_r}^2} - \frac{1}{\beta^2})^{1/2}$ and

$$C = -4A \sqrt{\frac{2\pi\ \omega}{c_r}}\ \frac{1}{R'(1/c_r)}\ e^{i\ (\frac{\pi}{4} - \omega t)\ -\ \omega\ \xi' h}.$$

Along the boundary, $z = 0$, the displacements simplify to

$$u_r \sim i\ C_1\ \frac{2i\omega\eta'}{{c_r}^2}\ r^{-1/2}\ e^{i\frac{\omega r}{c_r}}$$

$$u_z \sim C_1 \frac{\omega}{c_r}\left(\frac{1}{\beta^2} - \frac{2}{{c_r}^2}\right) r^{-1/2}\, e^{i\frac{\omega r}{c_r}},$$

where

$$C_1 = 4A\sqrt{\frac{2\pi\,\omega}{c_r}}\,\frac{1}{c_r\,R'(1/c_r)}\,e^{i\,(\frac{\pi}{4}-\omega t)\,-\,\omega\,\xi' h}.$$

The $\frac{\pi}{2}$ phase shift implied from the above equations defines elliptic particle motion at the free surface. The relative sign between the radial and vertical motion determines whether the motion will be prograde or retrograde. At the free surface $u_r/u_z > 0$ and motion is retrograde. With depth, the particle motion becomes prograde as the SV component dominates with depth. Vertical motion is greater amplitude than horizontal motion for free surface Rayleigh waves ($u_r/u_z < 1$).

### 2.4.2 Case 2: Liquid Half-space over an Elastic Half-space

Figure 2.2 is an illustration of Case 2, liquid half-space over an elastic half-space for a "Hard Bottom" ($\alpha_2 > \beta_2 > \alpha_1$) and a "Soft Bottom" ($\alpha_2 > \alpha_1 > \beta_2$) model. The solid and liquid are connected along an interface with the liquid in the region $z < 0$ and the solid occupying $z > 0$. The material constants for the upper medium are velocity ($\alpha_1$) and density ($\rho_1$) of the liquid, and for the lower medium for the P- and S-wave velocities ($\alpha_2$ and $\beta_2$) and density of the elastic solid ($\rho_2$). Several body wave types are illustrated as rays for the two models. Surface waves for these models are illustrated as curls along the water/solid interface (labeled S and pR) and lateral or "headwaves" are shown as arrows along the boundary (labeled $H_\alpha$ and $H_\beta$). The displacement potentials in the two media are

$$\phi_i = i\omega\, e^{-i\omega t}\int_0^\infty A\,\frac{p}{\xi_1}J_o(\omega pr)\, e^{i\omega\xi_1|z\,-\,h|}dp, \tag{2.34}$$

$$\phi_r = i\omega\, e^{-i\omega t}\int_0^\infty B_{hs}\,\frac{p}{\xi_1}J_o(\omega pr)\, e^{-i\omega\xi_1(z\,+\,h)}dp, \tag{2.35}$$

$$\phi_t = i\omega\, e^{-i\omega t}\int_0^\infty C_{hs}\,\frac{p}{\xi_1}J_o(\omega pr)\, e^{i\omega(\xi_2 z\,-\,\xi_1 h)}dp, \tag{2.36}$$

$$\psi_t = i\omega\, e^{-i\omega t}\int_0^\infty D_{hs}\,\frac{p}{\xi_1}J_o(\omega pr)\, e^{i\omega(\eta_2 z\,-\,\xi_1 h)}dp, \tag{2.37}$$

where $h$ is the height of the source above the interface ($h < 0$). The transmitted P- and S-wave potentials are $\phi_t$ and $\psi_t$. Again we regroup the potentials into their respective media,

$$\phi_1 = \phi_i + \phi_r = \int_0^\infty \frac{p}{\xi_1} \left[A\, J_o(\omega p r)\, e^{i\omega\xi_1|z\,-\,h|} + B_{hs}\, J_o(\omega p r)\, e^{-i\omega\xi_1(z\,+\,h)}\right] dp, \tag{2.38}$$

$$\phi_2 = \int_0^\infty \frac{p}{\xi_1} \left[C_{hs}\, J_o(\omega p r)\, e^{i\omega(\xi_2 z\,-\,\xi_1 h)}\right] dp, \tag{2.39}$$

$$\psi_2 = \int_0^\infty \frac{p}{\xi_1} \left[D_{hs}\, J_o(\omega p r)\, e^{i\omega(\eta_2 z\,-\,\xi_1 h)}\right] dp, \tag{2.40}$$

The boundary conditions are continuity of normal displacement and stresses at $z = 0$ ($\tau_{zz_1} = \tau_{zz_2}$; $u_{z_1} = u_{z_2}$) and that the shear stress in the elastic half-space must go to zero at the boundary, $\tau_{zr_2} = 0$. These conditions respectively result in the equations;

$$-\rho_1\omega^2\, A = \rho_1\omega^2\, B_{hs} + (2\mu_2\omega^2 p^2 - \omega^2\rho_2)\, C_{hs} + 2i\mu_2\omega^3 p^2\eta\, D_{hs}. \tag{2.41}$$

$$i\omega\xi_1\, A = i\omega\xi_1\, B_{hs} + i\omega\xi_2\, C_{hs} + \omega^2 p^2\, D_{hs}, \tag{2.42}$$

$$2i\mu_2\omega\xi_2\, C_{hs} = -(2\mu_2\omega^2 p^2 - \omega^2\rho_2)\, D_{hs}, \tag{2.43}$$

From the above we solve for the P-wave reflection and transmission coefficients:

$$\frac{B_{hs}}{A} = \left[\frac{4p^2\xi_2\eta_2 + (\frac{1}{\beta_2{}^2} - 2p^2)^2 - \frac{\xi_2\rho_1}{\beta_2{}^4\xi_1\rho_2}}{4p^2\xi_2\eta_2 + (\frac{1}{\beta_2{}^2} - 2p^2)^2 + \frac{\xi_2\rho_1}{\beta_2{}^4\xi_1\rho_2}}\right], \tag{2.44}$$

and

$$\frac{C_{hs}}{A} = \left[\frac{2\frac{\rho_1\beta_2{}^2}{\rho_2}(\frac{1}{\beta_2{}^2} - 2p^2)}{4p^2\xi_2\eta_2 + (\frac{1}{\beta_2{}^2} - 2p^2)^2 + \frac{\xi_2\rho_1}{\beta_2{}^4\xi_1\rho_2}}\right]. \tag{2.45}$$

Similarly. the transmitted S-wave coefficient is:

$$\frac{D_{hs}}{A} = \left[\frac{-4i\frac{\rho_1\beta_2{}^2}{\rho_2\omega}\xi_2}{4p^2\xi_2\eta_2 + (\frac{1}{\beta_2{}^2} - 2p^2)^2 + \frac{\xi_2\rho_1}{\beta_2{}^4\xi_1\rho_2}}\right] \tag{2.46}$$

We leave the reflection coefficients in terms of displacement potential for conical waves and concentrate on the poles of equations ( 2.44), ( 2.45) and ( 2.46). The

coefficients above correspond exactly with similar expressions derived by Ewing et al. (1959) and Brekhovskikh (1960) which are derived in terms of complex wave number. We keep these expressions in terms of complex ray parameter to maintain continuity with Case 1.

In the same manner as the free surface problem, the reflected wave potential can be evaluated by the method of steepest descents. Using the same approximation to the Bessel function used previously, the complete expression is

$$\phi_r \simeq \sqrt{\frac{\omega}{2\pi r}}\, e^{i(\frac{\pi}{4}-\omega t)} \int_{-\infty}^{\infty} \left[ \frac{4p^2\xi_2\eta_2 + (\frac{1}{\beta_2{}^2} - 2p^2)^2 - \frac{\xi_2\rho_1}{\beta_2{}^4\xi_1\rho_2}}{4p^2\xi_2\eta_2 + (\frac{1}{\beta_2{}^2} - 2p^2)^2 + \frac{\xi_2\rho_1}{\beta_2{}^4\xi_1\rho_2}} \right] \frac{p^{1/2}}{\xi_1}\, e^{i\omega(pr-\xi_1(z+h))} dp. \tag{2.47}$$

### pseudo-Rayleigh and Stoneley Poles

A steepest descents path for incident angles less than the critical shear or compressional angles is shown in Figure (2.12) for a hard bottom model. In Figure (2.12) the pre-critical integration path follows the steepest descents path until it must cross the branch cuts for $\xi_2$, $\eta_2$ and $\xi_1$. Here the path first drops to the lowest Riemann sheet for all three branch cuts ($Im\{\xi_1\} < 0$, $Im\{\xi_2\} < 0$, and $Im\{\eta_2\} < 0$). In order to pass through the saddle point, the path crosses back across the branch cuts and moves onto the top Riemann sheet after passing through the saddle point. So for pre-critical incidence the only significant waveform for this path is the reflected P-wave. The poles shown on Figure (2.12) do not contribute to the solution until the incident wave is post-critical.

The steepest descents path for an incident angle greater than the shear critical angle is shown in Figure (2.13) for a hard bottom model. Integrating the reflected wave potential becomes much more complicated because of the presence of branch cuts and poles which now must be considered in the solution. We find that poles extant on both physical and unphysical Riemann sheets can represent the largest amplitude waveforms at sufficient range. A nomenclature is developed for the different Riemann sheets needed:

$$[Im\{\xi_1\} > 0;\ Im\{\xi_2\} > 0;\ Im\{\eta_2\} > 0] \iff (+\ +\ +) \text{ sheet}$$

$$[Im\{\xi_1\} < 0;\ Im\{\xi_2\} < 0;\ Im\{\eta_2\} < 0] \iff (\ -\ -\ -\ ) \text{ sheet}$$

$$[Im\{\xi_1\} < 0;\ Im\{\xi_2\} > 0;\ Im\{\eta_2\} > 0] \iff (\ -\ +\ +\ ) \text{ sheet}$$

$$[Im\{\xi_1\} > 0;\ Im\{\xi_2\} < 0;\ Im\{\eta_2\} > 0] \iff (\ +\ -\ +\ ) \text{ sheet}$$

$$[Im\{\xi_1\} > 0;\ Im\{\xi_2\} < 0;\ Im\{\eta_2\} < 0] \iff (\ +\ -\ -\ ) \text{ sheet.}$$

These are the five Riemann sheets needed to compute the reflected wave potential in the complex $p$-plane. For post critical reflection two major pole contributions are present for the hard bottom case. These contributions are from the pseudo-Rayleigh and Stoneley wave poles.

For angles greater than the shear critical angle, the saddle point lies on the real axis between the $\frac{1}{\beta_2}$ and $\frac{1}{\alpha_1}$ branch points. To evaluate this saddle point several Riemann sheets are needed. As illustrated in Figure (2.13) the integration begins on the $(\ +\ +\ +\ )$ sheet for the $Re\{p\} < 0$ plane while asymptotically following the steepest descents path. The path remains on the $(\ +\ +\ +\ )$ sheet, integrating around the $\xi_2$ and $\eta_2$ branch cuts to account for the P- and S-headwave contributions. The headwaves are schematically illustrated in Figure (2.2) as $H_\alpha$ and $H_\beta$. In order to pass through the saddle point, the path must drop to the $(\ +\ -\ -\ )$ sheet, cross below the $\xi_2$ and $\eta_2$ cuts and then cross back through these cuts into the first quadrant. The path then moves to the $(\ -\ +\ +\ )$ sheet to pass through the $\xi_1$ cut. As the path crosses the $\xi_1$ cut it moves back to the physically real Riemann sheet $(\ +\ +\ +\ )$ and passes through the saddle point. While integrating through these different Riemann sheets care must be taken to include any pole or branch cut contributions to the solution. As it turns out for hard bottom media, a complex conjugate pair of poles exists on the $(\ -\ +\ +\ )$ sheet, one of these poles is disregarded because the resulting wave grows exponentially with $r$, the other attenuates with $r$ and is the pseudo-Rayleigh pole (Strick, 1959). A second pole lies to the right of the $\frac{1}{\alpha_1}$ branch point on the real axis. This pole is known as the Stoneley wave pole (Stoneley, 1924; 1946). More recently, this pole has been referred to as the Scholte pole in reference to the extensive analysis of its properties done by Scholte (1942; 1948; 1949).

As Cagniard found in 1939 and Scholte subsequently clarified in 1948, the Rayleigh period equation (i.e. the denominator of 2.44, 2.45, and 2.46) for the liquid over solid half-space problem can have two real roots. The first root (found by Cagniard) exists on the ( + + + ) sheet only when the liquid medium has an extremely low density, e.g. atmospheric density. In this case Cagniard defined the wave as a pseudo-Rayleigh wave because of its similar velocity and particle motion to the true free surface Rayleigh wave. Scholte commented that this root becomes unimportant and disappears for a liquid density greater than atmospheric. Roever and Vining (1959 part I) and Strick (1959 parts II and III) observed experimentally and discussed theoretically, that the pseudo-Rayleigh pole does not in fact vanish. Instead it moves to the ( − + + ) Riemann sheet as the density of the upper medium is increased.

The plots shown in Figure (2.14) show the location of this root for a zero density liquid over a hard bottom ($\alpha_1 = 1.5$, $\rho_1 = 0.0$, $\alpha_2 = 4.0$, $\beta_2 = 2.3$, $\rho_2 = 2.3$) and is a view of the complex $p$ plane with contours of the magnitude of the Rayleigh period equation. Dotted contours indicate the magnitude of the imaginary component and solid contours specify the real component. The vertical dashed lines mark the $1/\alpha_2$, $1/\beta_2$ and $1/\alpha_1$ slownesses. A cross section through the complex $p$-plane along the real axis and shows the real and imaginary components of the amplitude of R(p) in the lower plot of Figure (2.14). The pseudo-Rayleigh pole appears on both the ( + + + ) and ( - + + ) sheets at the identical location and is real and matches the Rayleigh wave velocity of the elastic solid for a zero density fluid half-space over elastic half-space (compare with results in Figure 2.9). When the fluid density is nonzero, the pseudo-Rayleigh pole only appears on the ( − + + ) sheet and has taken on an imaginary component (Figure 2.15 upper plot). As a result it no longer lies along the $Re\{p\}$-axis (Figure 2.15 lower plot).

The pseudo-Rayleigh velocity is greater than $\alpha_1$ but less than $\beta_2$ and matches the Rayleigh wave velocity of the solid when $\rho_1 \rightarrow 0$. The exponential terms in equations ( 2.38, 2.39, 2.40) reveal that the wave propagates as a traveling wave in the liquid (since $\xi_1$ is real) and attenuates away from the interface in the solid (because $\xi_2$

and $\eta_2$ are positive imaginary). Figure (2.15) shows the pseudo-Rayleigh complex conjugate pair labeled as an open circle in the $(Re\{p\} > 0, Im\{p\} < 0)$ quadrant. This pole is unphysical since it represents a wave which will grow exponentially with range.

A second pole falls on the real $p$-axis and lies to the right of the $1/\alpha_1$ branch point for hard bottom cases or right of the $1/\beta_2$ branch point for soft bottom cases. This pole occurs on the physical ( + + + ) sheet and is the Stoneley pole. Figure (2.16) shows the poles location for hard bottom model 1. Like the Rayleigh and pseudo-Rayleigh poles the particle motion of these poles results from the coupling of P- and SV-waves at the sea floor. Like the Rayleigh pole for the free surface, the displacement potentials are computed by evaluating the residues at the poles. Assuming a physical problem like that illustrated in Figure (2.2), the transmitted P and S displacement potentials are:

$$\phi_t \simeq -2A\sqrt{\frac{2\pi\omega}{c\,r}}\, e^{i(\frac{\pi}{4}-\omega t)} \left[\frac{\xi_2'\beta_2{}^2\,(2\frac{\beta_2{}^2}{c^2} - 1)}{R'(\frac{1}{c})}\right] e^{\frac{i\omega r}{c} - \omega\xi_1' h - \omega\xi_2' z}. \qquad (2.48)$$

and

$$\psi_t \simeq -4A\sqrt{\frac{2\pi\omega}{c\,r}}\, e^{i(\frac{\pi}{4}-\omega t)} \left[\frac{\xi_2'\beta_2{}^2\,(2\frac{\beta_2{}^2}{c^2} - 1)}{\omega\xi_1\, R'(\frac{1}{c})}\right] e^{\frac{i\omega r}{c} - \omega\xi_2' h - \omega\eta_2' z}. \qquad (2.49)$$

And the reflected P-wave displacement potential is

$$\phi_r \simeq -2A\sqrt{\frac{2\pi\omega}{c\,r}}\, e^{i(\frac{\pi}{4}-\omega t)} \left[\frac{(2\frac{\beta_2}{c^2} - 1)^2}{\xi'\, R'(\frac{1}{c})}\right] e^{\frac{i\omega r}{c} - \omega\xi_1'(z+h)}. \qquad (2.50)$$

where $c$ is either the Stoneley or pseudo-Rayleigh pole, $\xi_1' = (\frac{1}{c^2} - \frac{1}{\alpha_1{}^2})^{1/2} = i\xi_1$, $\xi_2' = (\frac{1}{c^2} - \frac{1}{\alpha_2{}^2})^{1/2} = i\xi_2$, and $\eta_2' = (\frac{1}{c^2} - \frac{1}{\beta_2{}^2})^{1/2} = i\eta_2$. Both the pseudo-Rayleigh and Stoneley wave propagate with retrograde elliptic motion at the interface like the free surface Rayleigh wave.

### Summary of pseudo-Rayleigh and Stoneley Poles

The differences and similarities between pseudo-Rayleigh and Stoneley waves are summarized here. Though both the pseudo-Rayleigh and Stoneley wave propagate

with different velocities and lie on separate Riemann sheets they are associated with each other and with the free surface Rayleigh wave.

Adding a water layer effectively reduces the vertical displacement. In contrast to free surface Rayleigh waves, the ratio $\mid \frac{u_r}{u_z} \mid$ is greater than unity for both pseudo-Rayleigh and Stoneley waves in soft bottom conditions. This effect should be seen in oceanic measurements at and below the sea floor. The data presented in chapter 3 confirms this analytic observation.

We show the effect of the water layer on the transition from Rayleigh to pseudo-Rayleigh and Stoneley waves for both hard and soft bottom models. In Figure (2.17) are plotted both the real (solid lines) and imaginary (dashed lines) amplitude of $R(p)$ for a hard bottom on the physical Riemann sheet ($\alpha_1 = 1.5,\ \alpha_2 = 4.0,\ \beta_2 = 2.3,\ \rho_2 = 2.3$). The Rayleigh pole and pseudo-Rayleigh pole ("pR") are identical for a zero density fluid. For $\rho_1 > 0$ the Rayleigh pole leaves the physical Riemann sheet, becomes the pseudo-Rayleigh pole on the ( $-$ $+$ $+$ ) sheet and the Stoneley pole appears ("St") near $1/\alpha_1$. The Stoneley pole moves to the right for increasing fluid density. The imaginary component of $R(p)$ for $p > 1/\alpha_1$ is zero and the real zero crossing traces the same path between $p = 1/\alpha_2 \rightarrow 1/\alpha_1$ and for the entire range of densities (0, .1, .5, 1 $gm/cc$).

The poles for the soft bottom model ($\alpha_1 = 1.5,\ \alpha_2 = 2.0,\ \beta_2 = 1.0,\ \rho_2 = 1.7$) are illustrated in Figure (2.18). The real pole remains a Stoneley wave and matches the free surface Rayleigh wave speed when $\rho_1 = 0$. The imaginary component of the pseudo-Rayleigh pole becomes very small, remains on the ( $-$ $+$ $+$ ) sheet and is located near $p = 1/\beta_2$. This pole is not considered in the solution because the ( $-$ $+$ $+$ ) sheet is not needed for integrating the Sommerfeld equation in soft bottom media.

Third we examine the relative importance of pseudo-Rayleigh and Stoneley waves. Though the Stoneley wave is the most important interface wave at long ranges, significant pseudo-Rayleigh displacements are possible when the source and receiver are near each other (Strick, 1959). The pseudo-Rayleigh pole was found for several realistic media whose P- and S-wave velocities were varied by 0.1 km/s

from 4.0 to 2.05 km/s and from 2.3 to 1.0 km/s respectively. The poles are shown in Figure (2.19) with the poles for $\beta_2 = 2.3, 1.7, 1.3$ km/s underlined. Referring back to Figure (2.16), we see drawn the real and imaginary contours for $R(p)$ when $\beta_2 = 1.2$ km/s from which we can tell that there is no pseudo-Rayleigh zero crossing on the ( + + + ) sheet.

When the S-wave velocity is near 1.7 km/s, the pseudo-Rayleigh pole is left of $\frac{1}{\beta_2}$ and remains so for soft bottom conditions. Between $\beta_2 = 1.7$ and 1.5 km/s the $\eta_2$ branch cut is still left of the $\xi_1$ cut and the integration path must still use the ( − + + ) Riemann sheet. As a result the contribution of the pole describes a radially attenuating interface wave propagating slightly faster than the shear velocity in the lower medium and leaking energy in both directions away from the interface. Lower attenuation in range is also associated with the pseudo-Rayleigh wave for $\beta_2 < 1.7$ km/s since the imaginary component is shrinking.

We see a similar behavior in the pseudo-Rayleigh pole as $\rho_2$ is varied from 2.24 to 0.48 gm/cc. The pole is tracked in Figure (2.20) with the poles at $\rho_2$=0.48, 0.96 and 2.24 underlined. When $\frac{\rho_2}{\rho_1} < 1$ the pseudo-Rayleigh pole lies to the left of the S-wave slowness and therefore the pseudo-Rayleigh wave propagates faster than the shear wave velocity of the solid half-space. This is a new and previously unreported result.

Fourth, compare our results with Strick (1959). Strick finds that, for a soft bottom, the pseudo-Rayleigh pole still exists but that it has moved to a different Riemann sheet. He points out that the contribution of this pole is a distortion of a rapidly attenuating shear head wave. In our analysis soft bottom conditions mean that the $\eta_2$ branch cut moves right of the $\xi_1$ branch cut and the path no longer requires the ( − + + ) sheet. However the pole remains on the ( − + + ) sheet and as a result the pseudo-Rayleigh pole should show up as a leaky mode at approximately the shear headwave velocity. The contribution of the pseudo-Rayleigh pole is negligible for soft bottom models.

Figures (2.19) and (2.20) show that the pseudo-Rayleigh pole occurs at slightly greater than the S-wave velocity for a limited range of realistic media. Strick

(1959) first showed that pseudo-Rayleigh waves are only important for media with $\beta_2 > \alpha_1$ because, from his analysis method, the pole dropped to a lower Riemann sheet. In our analysis it is the integration path that leaves the pseudo-Rayleigh pole Riemann sheet, because the $\eta_2$ branch cut moves to the right of the $\xi_1$ cut and there is no longer a need for the ( $-$ $+$ $+$ ) sheet. For hard bottom media pseudo-Rayleigh waves can exist for a wide range of $\frac{\rho_2}{\rho_1} < 1$. These waves could be found at water/ice boundaries or other fluid/solid hard bottom boundaries with similar density contrasts.

### 2.4.3 Case 3: Liquid Layer over an Elastic Half-space

Figure (2.3) is an illustration of Case 3: a liquid layer of variable thickness over an elastic half-space with hard and soft bottom properties. Traditionally, this problem is solved using normal mode analysis for the system with finite layer thickness. However, the asymptotic method is used here to provide continuity with the previous cases (a ray model). We will look in detail at the first and second modes of interface wave propagation. The change in pole location with changing water depth and velocity contrast across the interface is directly related to the conversion of continental crust Rayleigh waves (Case 1) into normal mode Rayleigh waves and Stoneley waves (Case 2) observed in the ocean crust (e.g. moving from conditions illustrated in Figures 2.1 to 2.3). The development below follows similar analysis by Tolstoy (1952), Biot (1952) and Ewing et al., (1957).

The model has a source buried a distance $h$ below the interface in the elastic solid (i.e. the source is at $z = H + h$). The water has a depth $H$ and the coordinate origin is at the free surface of the water with $z$ positive downward and range $r$ increasing to the right (see Figure 2.3). Displacement potentials in the two media are

$$\phi_i = A\, i\omega\, e^{-i\omega t} \int_0^\infty \frac{p}{\xi_2} J_o(\omega p r)\, e^{-i\omega\xi_2(z\, -\, (H+h))} dp, \tag{2.51}$$

$$\phi_r = i\omega\, e^{-i\omega t} \int_0^\infty B_{ll}\, \frac{p}{\xi_2} J_o(\omega p r)\, e^{i\omega\xi_2(z\, +\, h)} dp, \tag{2.52}$$

$$\phi_t = i\omega\, e^{-i\omega t} \int_0^\infty C_{ll}\, \frac{p}{\xi_2} J_o(\omega p r)\, e^{-i\omega(\xi_1 z\, -\, \xi_2 h)} dp, \tag{2.53}$$

$$\psi_r \;=\; i\omega\, e^{-i\omega t} \int_0^\infty D_{ll}\, \frac{p}{\xi_2} J_o(\omega p r)\; e^{i\omega(\eta_2 z \,+\, \xi_2 h)} dp. \tag{2.54}$$

where $B_{ll}$, $C_{ll}$ and $D_{ll}$ are the reflected P-, transmitted P- and reflected S-wave coefficients respectively for a liquid-layer/solid-half-space.

The boundary conditions for this model are slightly more complicated since there is a free surface on the water as well as the boundary between the liquid and the solid. These boundary conditions are;

$$\phi_1 \;=\; 0 \quad at \;\; z \;=\; 0, \tag{2.55}$$

$$u_{z_1} \;=\; u_{z_2} \;\; at \;\; z \;=\; H, \tag{2.56}$$

$$\tau_{zr_2} \;=\; 0 \;\; at \;\; z \;=\; H, \tag{2.57}$$

$$\tau_{zz_1} \;=\; \tau_{zz_2} \;\; at \;\; z \;=\; H. \tag{2.58}$$

As before we group the potentials for media 1 and media 2.

$$\phi_2 \;=\; \phi_i + \phi_r \;=$$

$$\int_0^\infty \tfrac{p}{\xi_2} \left[A\; J_o(\omega p r)\; e^{-i\omega\xi_2(z \,-\, (H+h))} \;+\; B_{ll}\; J_o(\omega p r)\; e^{i\omega\xi_2(z \,+\, h)}\right] dp, \tag{2.59}$$

$$\phi_1 \;=\; \int_0^\infty \frac{p}{\xi_2} \left[C_{ll}\; J_o(\omega p r)\; e^{-i\omega(\xi_1 z \,-\, \xi_2 h)}\right] dp, \tag{2.60}$$

$$\psi_2 \;=\; \int_0^\infty \frac{p}{\xi_2} \left[D_{ll}\; J_o(\omega p r)\; e^{i\omega(\eta_2 z \,+\, \xi_2 h)}\right] dp. \tag{2.61}$$

Now from ( 2.55), the free surface is satisfied by

$$\phi_1 \;=\; C\; J_o(\omega p r) sin(\omega\xi_1 z) e^{i\omega\xi_2 h} \tag{2.62}$$

and from continuity of normal displacements and stresses (boundary conditions 2.56 and 2.58)

$$2i\omega\xi_2\; A \;=$$

$$i\omega\xi_2\; B_{ll}\; e^{i\omega\xi_2 H} \,-\, \omega\xi_1\; C_{ll}\; cos(\omega\xi_1 H) \;+\; \omega^2 p^2\; D_{ll}\; e^{i\omega\eta_2 H} \tag{2.63}$$

and

$$-(2\mu_2\omega^2 p^2 - \omega^2 p^2) A =$$

$$(2\mu_2\omega^2 p^2 - \omega^2 p^2) B_{ll} + \omega^2\rho_1 sin(\omega\xi_1 H) C_{ll} + 2\mu_2 i\omega\eta_2\omega^2 p^2 D_{ll} e^{i\omega\eta_2 H}. \tag{2.64}$$

Finally, forcing the shear stresses to vanish in the water column ( 2.57) yields

$$2\mu_2 i\omega\xi_2\ A\ =$$
$$2\mu_2 i\omega\xi_2\ B_{ll}\ e^{i\omega\xi_2 H}\ +\ (2\mu_2\omega^2 p^2 - \omega^2 p^2)\ D_{ll}\ e^{i\omega\eta_2 H}. \qquad (2.65)$$

We are still interested in the poles of equations ( 2.59, 2.60 and 2.61). The denominator of the reflection and transmission coefficients is

$$(\frac{1}{\beta^2}\ -\ 2p^2)^2\ +\ 4p^2\xi_2\eta_2\ -\ \frac{\xi_2\rho_1}{\beta^4\xi_1\rho_2}\ tan\left[\omega H(\frac{1}{{\alpha_1}^2}\ -\ p^2)^{1/2}\right],\quad p\ <\ \frac{1}{\alpha_1}$$

$$(\frac{1}{\beta^2}\ -\ 2p^2)^2\ +\ 4p^2\xi_2\eta_2\ -\ \frac{\xi_2\rho_1}{\beta^4\xi_1\rho_2}\ tanh\left[\omega H(\frac{1}{{\alpha_1}^2}\ -\ p^2)^{1/2}\right],\quad p\ >\ \frac{1}{\alpha_1}. \qquad (2.66)$$

The roots of ( 2.66) define the interface wave modes that exist for a particular model. Schermann (1945) proved that there are $n$ finite real roots to equation ( 2.66). In the remainder of this section we will be concerned with the fundamental and first few of these $n$ roots computed for an ocean sea floor model. The same method of root finding employed above is used for the liquid layer problem.

Equation ( 2.66) describes the normal mode branch for Rayleigh waves (Tolstoy, 1954). This is not precisely the same phenomenon we investigated for Case 2. These modes are dispersive owing to the frequency term contained in the arguments to the *tan* and *tanh* functions. However, like the interface waves of Case 2, they propagate by coupling energy on either side of the interface.

In order to relate the analysis from Case 2 to Case 3 we address limiting cases. First consider $p\ <\ \frac{1}{\alpha_1}$, which is the case for Stoneley wave propagation. If the argument to $tanh(wH\xi_1)$ becomes large (say $>$ 5) the denominator becomes equivalent to that for Case 2 (see equation 2.44). This is equivalent to assuming the wavelength is small relative to the liquid depth. Hence, for deep water and high frequencies the interface wave excited is the classical Stoneley wave - a nondispersive surface wave propagating along the interface between two infinite half-spaces. For a perfect waveguide, the acoustic mode cutoff frequency determines the transition from water born modes and interface waves and as discussed previously, for a 2.0

km depth ocean this frequency is ~0.19 Hz. Below this frequency modes in the water column cannot exist and the Case 2 is an appropriate model. Although the sea floor properties effect the modal cutoff frequencies, the acoustic modes within the water column are the dominant feature of most ocean noise spectra (see Orcutt et al., 1992). Additionally, at high frequencies and incidence angles near the Rayleigh angle the free surface reflection is negligible (i.e. returns the seafloor many wavelengths away) and the problem can be treated as in Case 2.

Second, consider $p > \frac{1}{\alpha_1}$. The higher modes for equation ( 2.66) approach the Rayleigh wave speed of the elastic solid as $\omega H \rightarrow 0$. This Rayleigh wave mode differs from the complex pseudo-Rayleigh wave investigated previously and is real and propagates as waveguided modes. The limiting group velocity of the modes is the Rayleigh wave velocity.

Third, for the case where $\omega H \xi_1 = \frac{\pi}{4}$ the leaky pseudo-Rayleigh wave can propagate. This limiting case creates an interface wave that propagates as the pseudo-Rayleigh wave found in Case 2.

### Summary of Normal Modes and Application to LFASE

In Figure (2.21) the complex velocity plane is shown for modes 1 and 2 of a hard bottom model with a water depth wavelength ratio ($H/\lambda$) of 0.5. Figure (2.22) is the same model with $H/\lambda = 2$. These correspond to water depths of 750 and 3000m respectively if the source frequency is 1 Hz. We can see from Figure (2.22) that there are four modes and that mode 1 lies just below the water velocity and propagates as a part of the Stoneley wave branch ($p > \frac{1}{\alpha_1}$). As the water layer thickens mode 1 approaches the two half-space Stoneley wave velocity and the higher modes converge to the Rayleigh wave velocity. Also, the limits on the higher mode velocities must be $\alpha_1 < c_R < \beta_2$. In contrast, if the model has a soft bottom then there is only one fundamental mode possible the Stoneley mode.

In chapter 3 data analyzed from the Low-Frequency Acoustic-Seismic Experiment at DSDP Hole 534B are presented along with a review of the experimental method. Analysis indicates that two or more interface wave modes are seen in the

data.

Lavoie and O'Hara (1989) compiled a detailed velocity-depth table for Site 534. The data for P- and S-wave velocities is plotted in Figure (2.23). As a simple application of the analysis in Case 3, several half-space velocity models were analyzed whose elastic wave velocities were chosen from the 534B data set. Each liquid-layer/solid model had a fixed velocity ratio determined by the velocities seen at a depth in 534B. This simplified model was used to determine the frequencies at which a second mode propagates. Figure (2.24) is a summary of the phase velocity of the first and second modes for 10 separate Case 3 models. In each model the P- and S-wave velocities were computed by averaging the data set values down to the depth indicated along the right hand axis. Although energy propagates at the group velocity, phase velocities are useful to identify modes and have been the basis of the analysis of this chapter and we believe it may provide insight into the water born modes at Site 534B. (A more accurate approach is to compute phase and group velocities for models containing continuous velocity gradients and discrete layering with depth (e.g. Gomberg and Masters, 1984; Schmidt and Jensen, 1984). This has been left as a task for future work.)

The scales are not linear in Figure (2.24). The vertical axis reflects the $\beta_2/\alpha_1$ ratio (left side) and the depth in 534B at which the velocity for the model is chosen (right side). The velocities used at specific depths are averages of the compressional and shear velocities down to that depth. The H/lambda number is the ratio of the water depth to water wavelength. The contour values indicate the normal mode propagation velocity. Mode 1 is shown as solid contours and mode 2 is shown as dotted contours. The water depth is ~5000 m at 534B, and Figure (2.24) shows that for any combination of compressional and shear wave velocities found in the upper 1.7 km of sediments the frequency of the wave must be greater than 0.3 Hz for more than a single mode to propagate. In chapter 3 we will see that 0.3 Hz is the fundamental mode seen in the LFASE data.

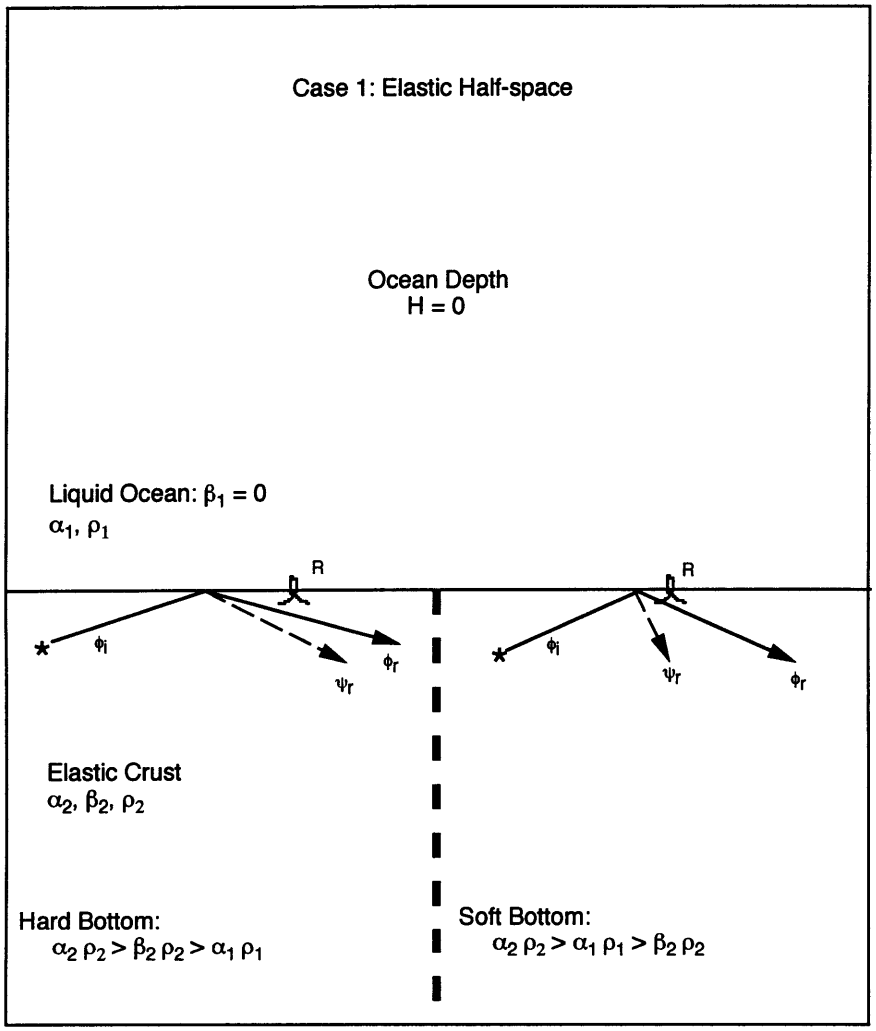


Figure 2-1: Model of elastic half-space. Ocean depth is zero and the point source is $h$ below the free surface. The source initiates a direct compressional wave $\phi_i$ which then interacts with the free surface to creates two body waves, the reflected P-wave ($\phi_r$) and S-wave ($\psi_r$), and a free surface Rayleigh wave ($R$). Two scenarios are illustrated: a hard bottom solid where $\alpha_2 > \beta_2 > \alpha_1$, and a soft bottom solid where $\alpha_2 > \alpha_1 > \beta_2$. For this model these definitions of "hard" and "soft" bottom are meaningless in the absence of a water column.

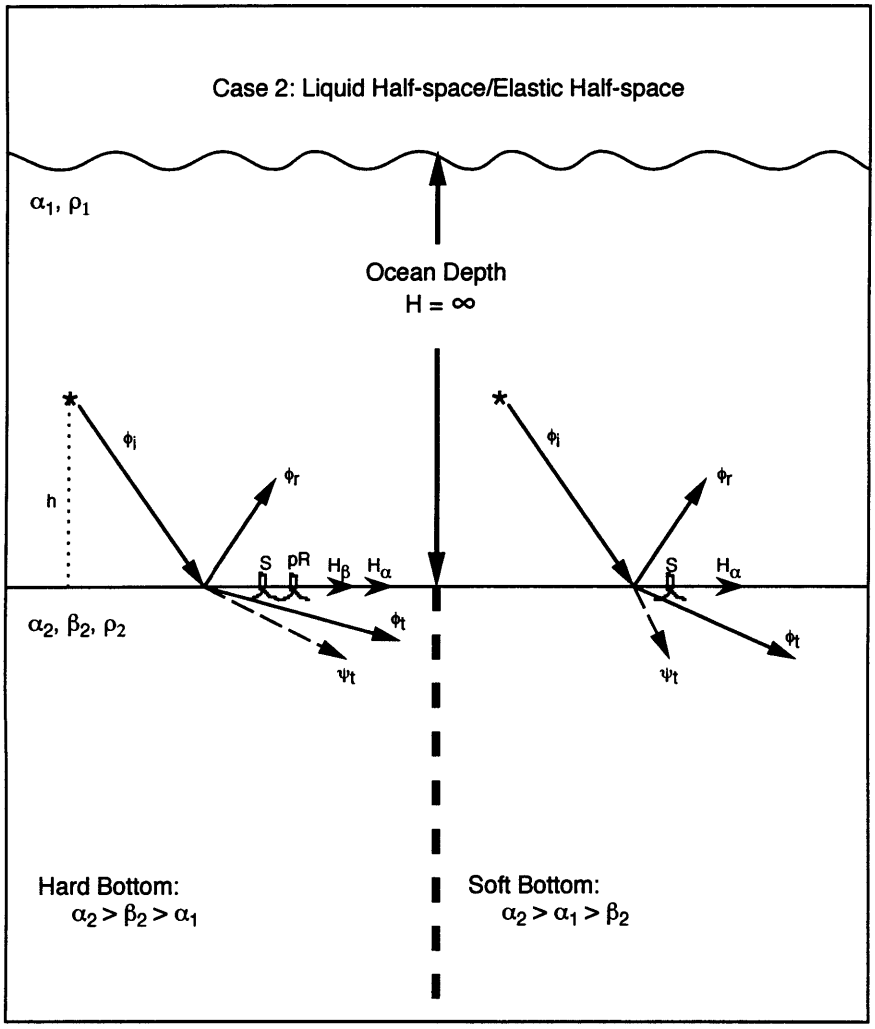


Figure 2-2: Model for half-space liquid over an elastic half-space solid. Ocean depth is $\infty$ and the point source is $h$ above the sea floor. The source initiates a direct compressional wave $\phi_i$ which then interacts with the sea floor to create three body waves, the reflected P-wave ($\phi_r$), the transmitted P-wave ($\phi_t$) and the transmitted S-wave ($\psi_t$). For the hard bottom case two potential interface waves are created: the pseudo-Rayleigh wave ($pR$) and the Stoneley wave ($S$). (Headwaves $H_\alpha$ and $H_\beta$ are only measureable in the upper medium.)

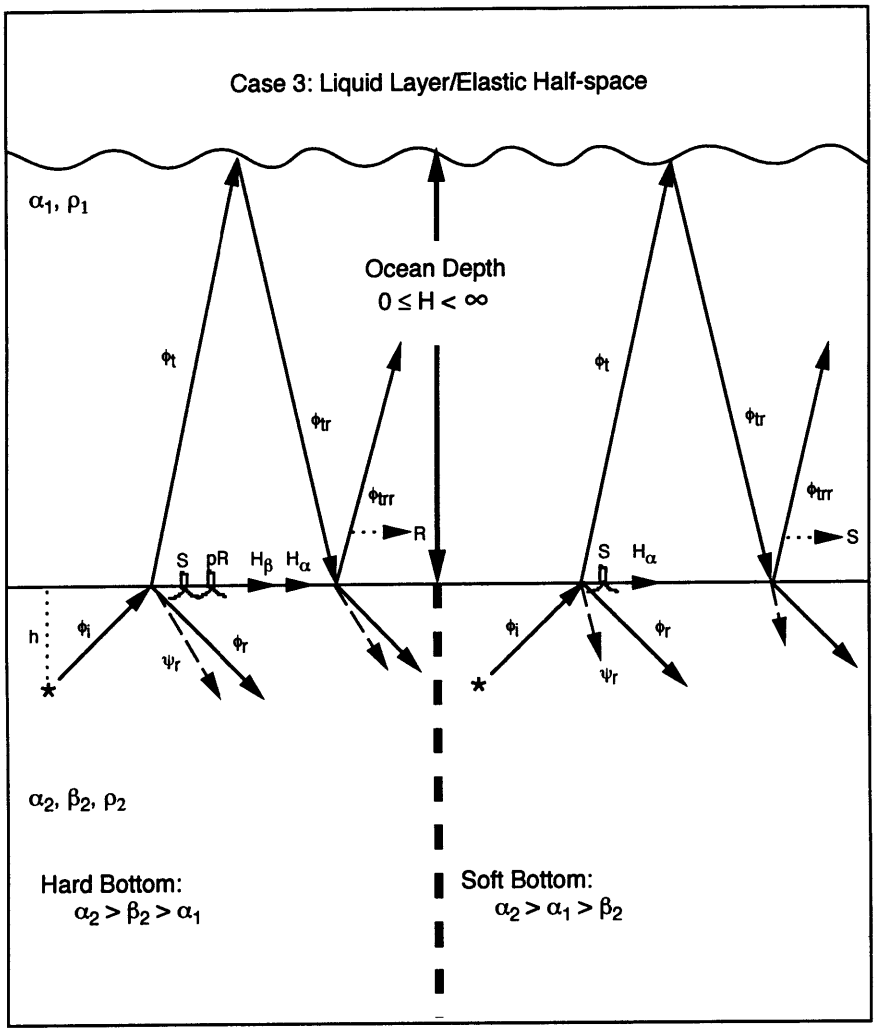


Figure 2-3: Model for liquid layer over an elastic half-space. Ocean depth is varied from 0 to $\infty$. For the hard bottom case two potential interface waves are created: the pseudo-Rayleigh wave ($R$) and the Stoneley wave ($S$). For the soft bottom case the shear headwave is not possible and the pseudo-Rayleigh wave becomes unphysical. Modes of the ocean layer are possible as shown by the multiple reflections $\phi_{tr}$. For soft bottoms these are leaky modes. (Headwaves $H_\alpha$ and $H_\beta$ are only measureable in the upper medium.)

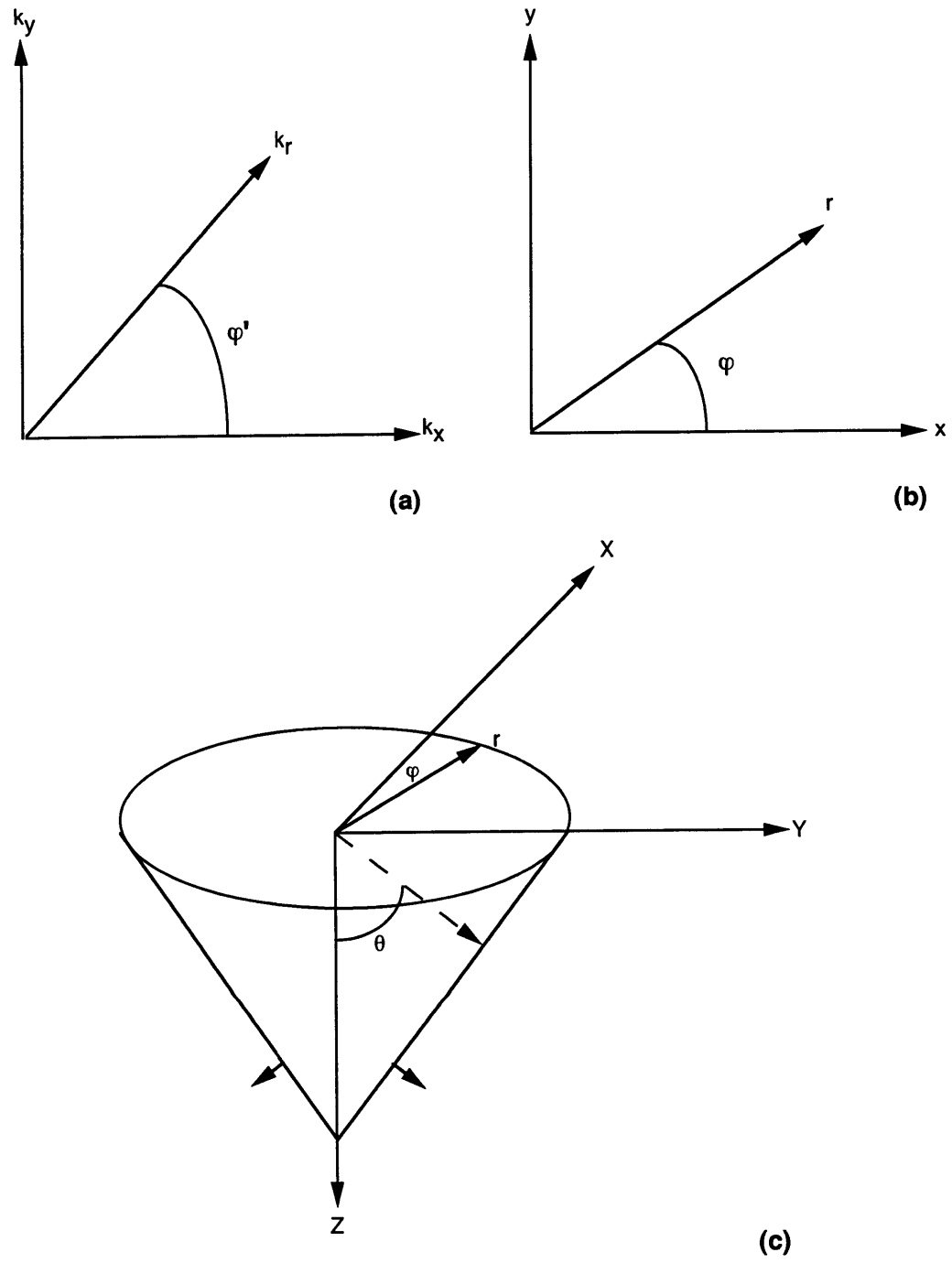


Figure 2-4: (a) Wavenumber coordinate frame. $k_x$ and $k_y$ are the Cartesian wavenumber coordinates in the $x-$ and $y-direction$ and $k_r$ is the wavenumber in cylindrically symmetric coordinates. (b) Spatial coordinate frame. $r$ is the range coordinate. (c) An illustration of a cylindrical wave propagating at angle $\theta$ with respect to the $z-axis$. The wave has propagated out to range $r = x\ cos(\phi')$.

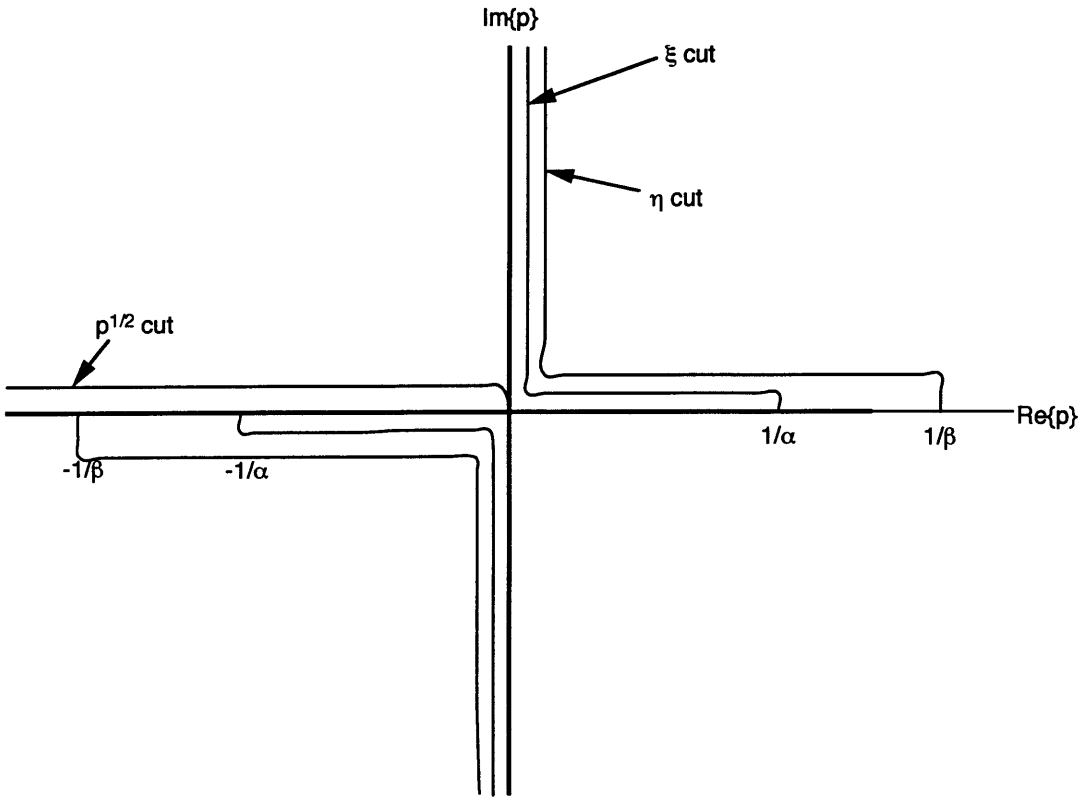


Figure 2-5: Complex ray parameter plane. $Re\{p\}$ is plotted along the abscissa and $Im\{p\}$ is plotted along the ordinate. Three branch cuts are shown: the $p^{1/2}$, the $\xi$, and $\eta$ cuts.

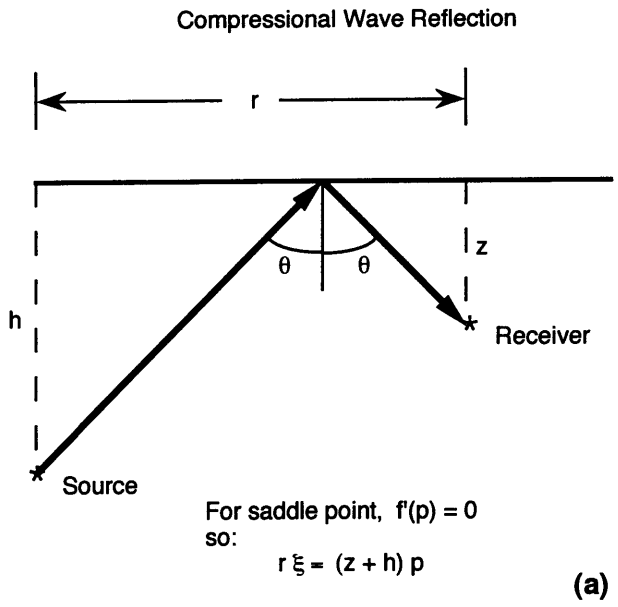


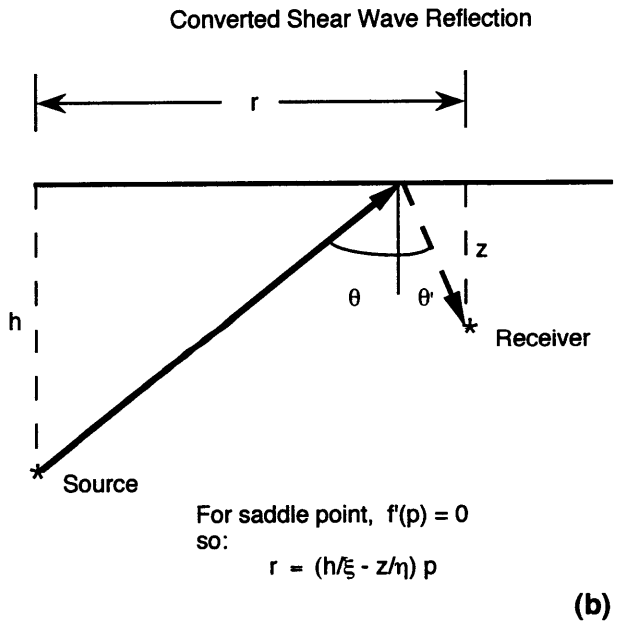


Figure 2-6: Free surface reflection of a point source. (a) Ray diagram of the compressional wave reflection from a point source at depth $h$ to a receiver at depth $z$. The incidence angle $\theta$ is equal to the reflected angle. (b) Ray diagram of the converted shear wave reflection from a point source at depth $h$ to a receiver at depth $z$. The incidence angle $\theta$ is larger than the reflected angle $\theta'$.

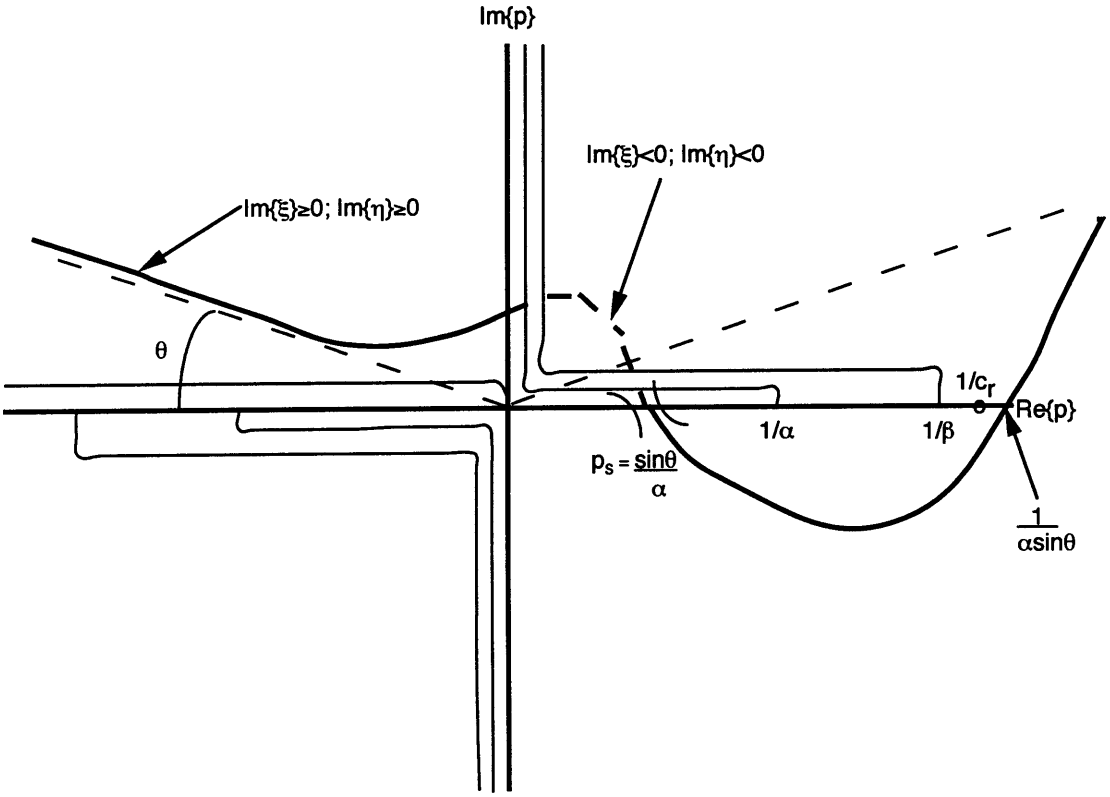


Figure 2-7: Integration path in the complex ray parameter plane for a point source impinging on the free surface of an elastic half space at pre-critical incidence. Branch cuts are identified in Figure (2.5) and the branch points along the positive real $p-axis$ are labeled $1/\alpha$ and $1/\beta$. The path occupies two Riemann sheets indicated by the heavy solid and dashed line. The reflected compressional wave is represented by the saddle point crossing at $p_s = \frac{sin(\theta)}{\alpha}$.

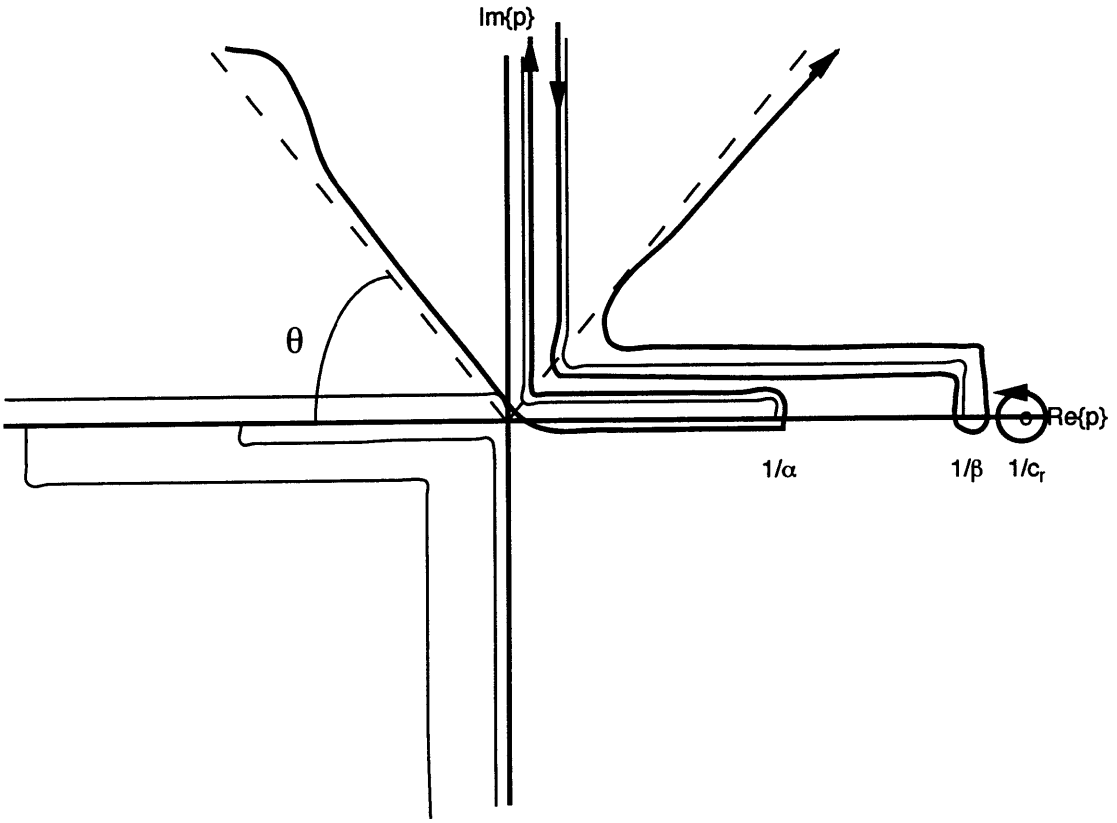


Figure 2-8: Integration path in the complex ray parameter plane for a point source impinging on the free surface of an elastic half space at post-critical incidence ($sin(\theta) > 1/\beta$). Branch cuts are identified in Figure (2.5) and the branch points along the positive real $p-axis$ are labeled $1/\alpha$ and $1/\beta$. The path occupies ( + + + ) and follows the heavy solid curved line. The Rayleigh pole ($1/c_r$) is included in the solution through a separate integration circuit.

Figure (2.9a)

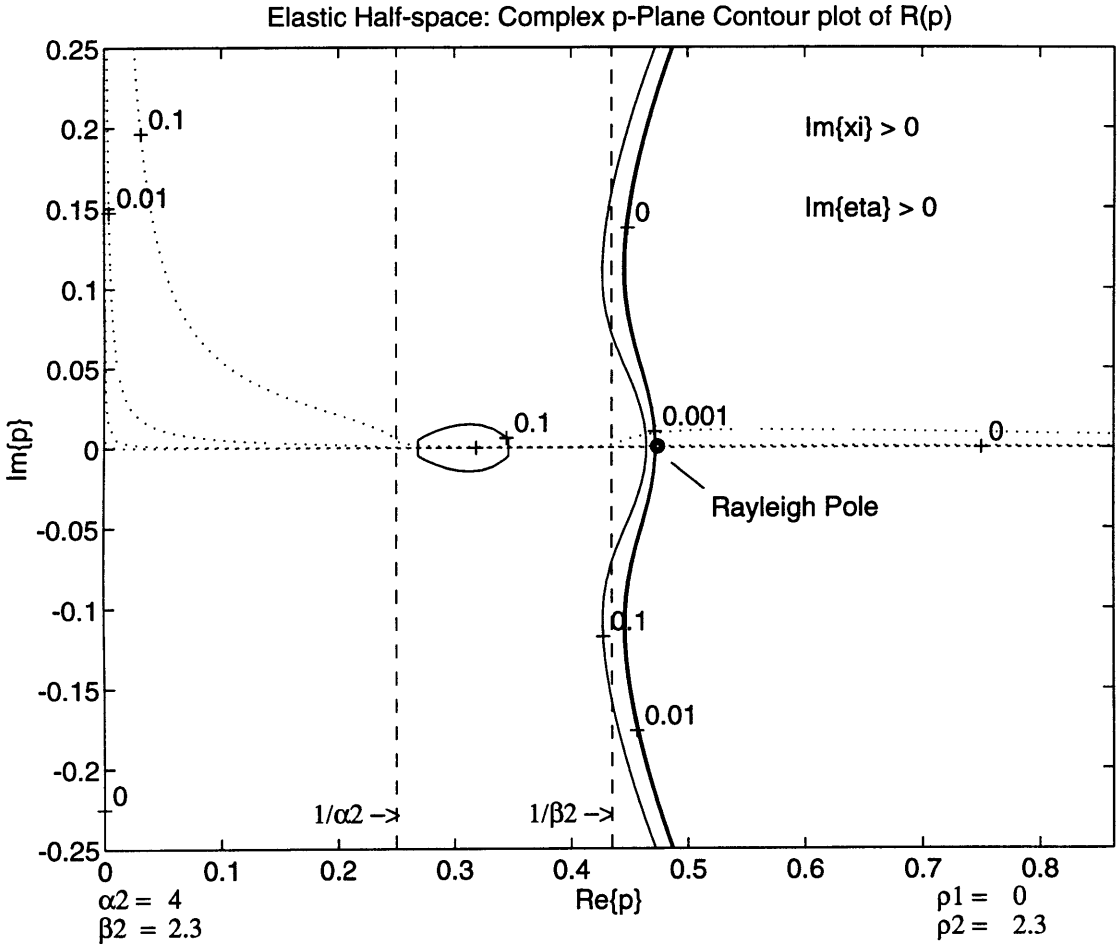


Figure 2-9: Magnitude of the real (solid contours) and imaginary (dotted contours) component plotted in the complex ray parameter plane for $Im\{\xi\} > 0$; $Im\{\eta\} > 0$ (contours are for 0.1, 0.01, 0.001, 0.0). The Rayleigh pole is located where the zero contours of the real and imaginary component cross. The dashed lines show $p_{\alpha_2}$ and $p_{\beta_2}$ of the solid. (b) Real and imaginary amplitudes of the Rayleigh period equation ($R(p)$) for real $p$. The pole is real and therefore the free surface Rayleigh wave propagates without attenuation or dispersion.

Figure (2.9b)

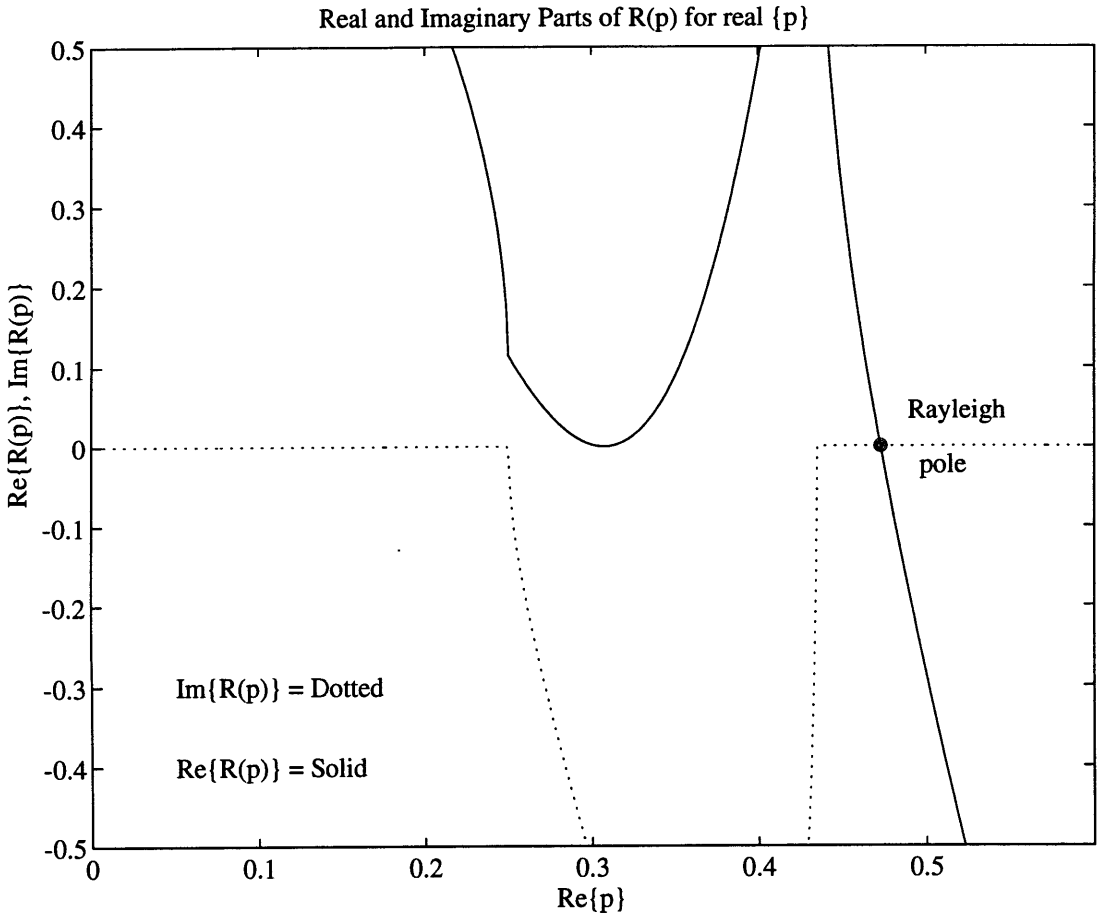
Real and Imaginary Parts of R(p) for real {p}
Re{R(p)}, Im{R(p)}
Re{p}
Rayleigh
pole
Im{R(p)} = Dotted
Re{R(p)} = Solid
0.5
0.4
0.3
0.2
0.1
0
-0.1
-0.2
-0.3
-0.4
-0.5
0
0.1
0.2
0.3
0.4
0.5

Figure (2.10a)

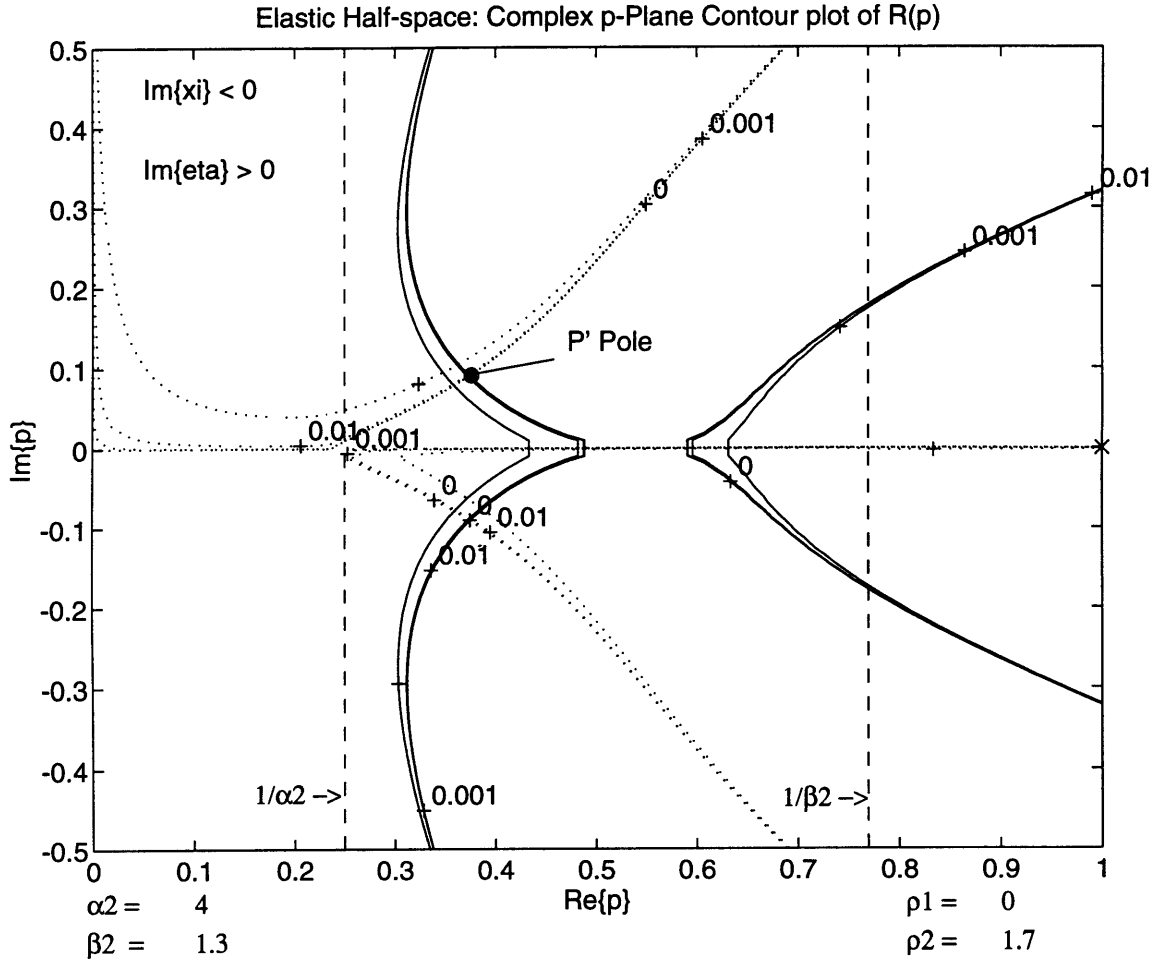


Figure 2-10: The $P'$ pole in the complex ray parameter plane. (a) Real (solid contours) and imaginary (dotted contours) component plotted for the $Im\{\xi\} > 0$; $Im\{\eta\} < 0$ Riemann sheet (contours are for 0.1, 0.01, 0.001, 0.0). The $P'$ pole is located at $p = 0.374 + 0.09i\ s/m$. The dashed lines show the compressional and shear slownesses of the solid. (b) Real and imaginary amplitudes of the Rayleigh period equation $R(p)$ for real $p$. The real component of $P'$ is shown.

Figure (2.10b)

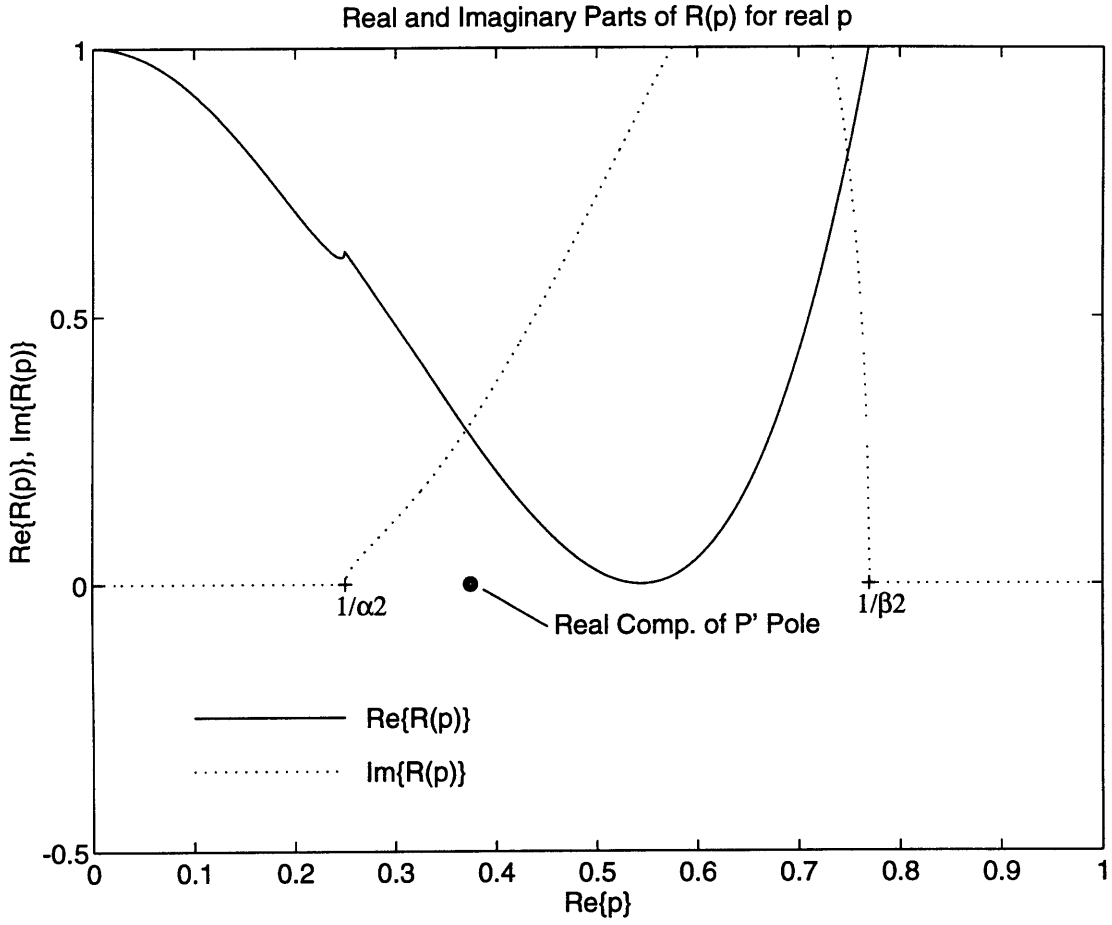
Real and Imaginary Parts of R(p) for real p
Re{R(p)}, Im{R(p)}
Re{p}
1
0.5
0
-0.5
0
0.1
0.2
0.3
0.4
0.5
0.6
0.7
0.8
0.9
1
1/α2
1/β2
Real Comp. of P' Pole
Re{R(p)}
Im{R(p)}

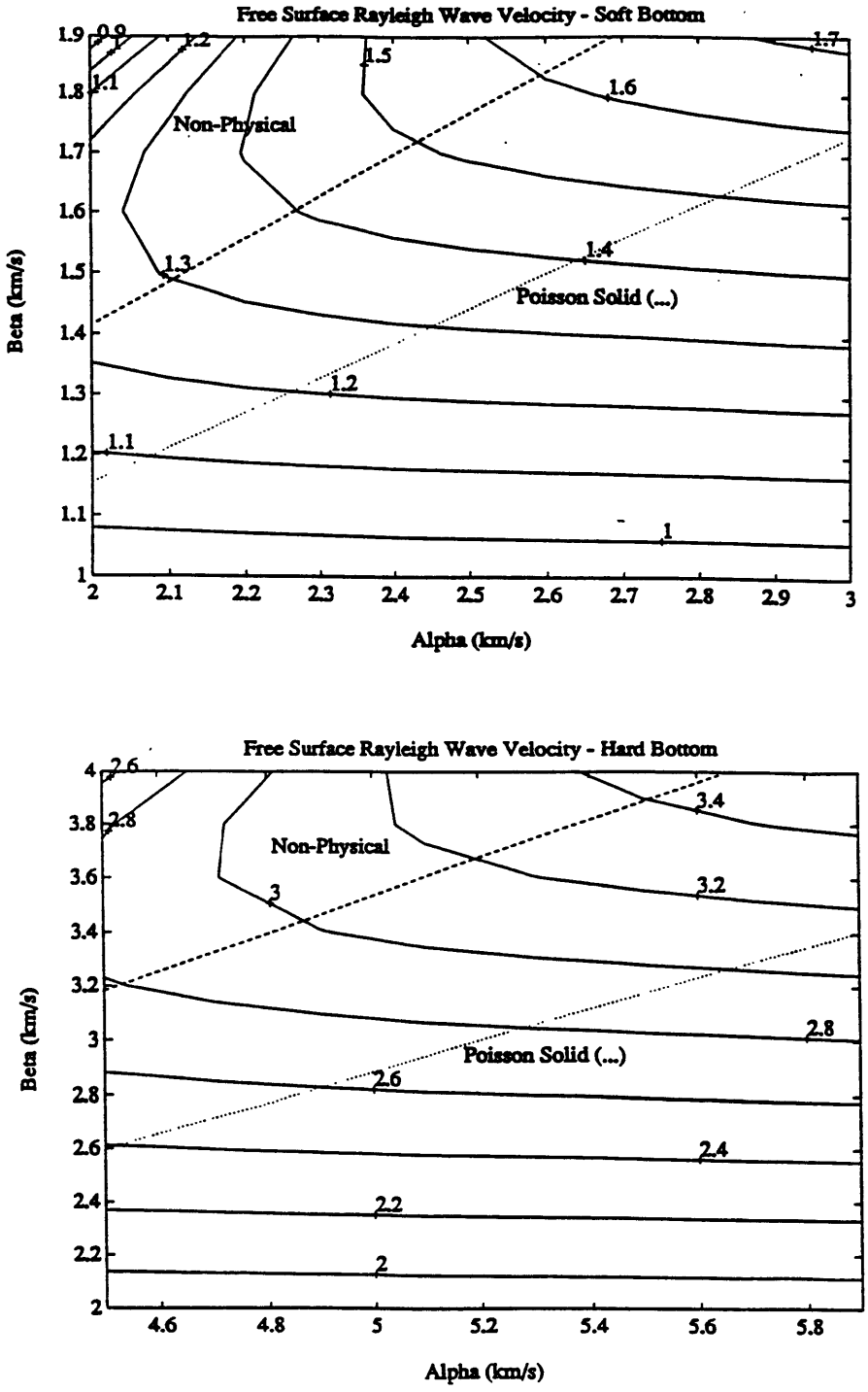


Figure 2-11: Summary of Rayleigh wave velocities for a range of compressional and shear velocities. The upper plot shows contours of Rayleigh waves for a low shear modulus and the upper plot for higher shear modulus. Dashed lines indicate the boundary between physical and non-physical elastic media (i.e. $\lambda \leq 0$) and dotted lines indicate a Poisson solid.

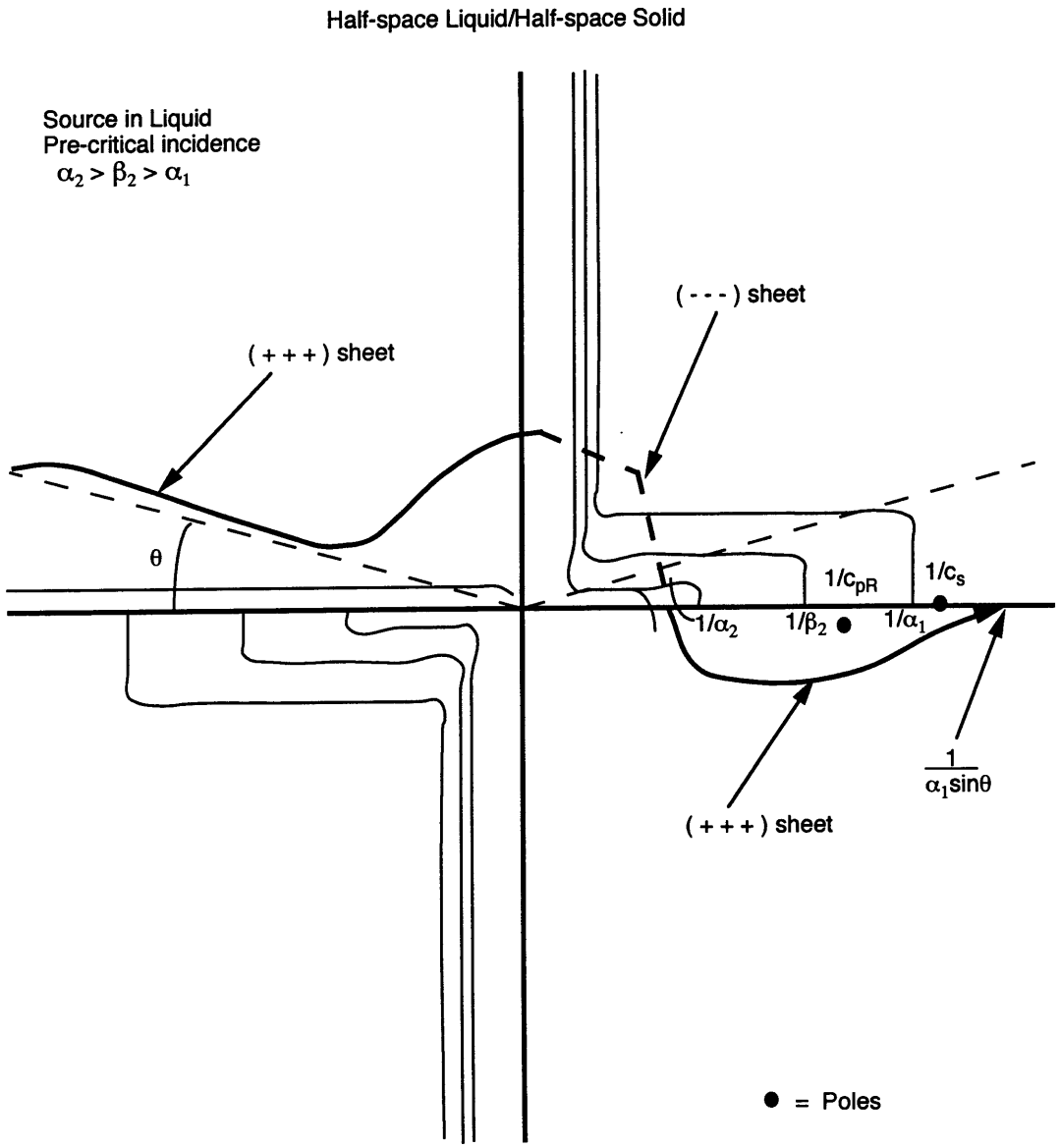


Figure 2-12: Integration path for a liquid half-space over elastic half space at pre-critical incidence. The path occupies two Riemann sheets as indicated by the heavy solid and dashed curved lines. The pseudo-Rayleigh pole ($1/c_{pR}$) and Stoneley pole ($1/c_s$) are shown.

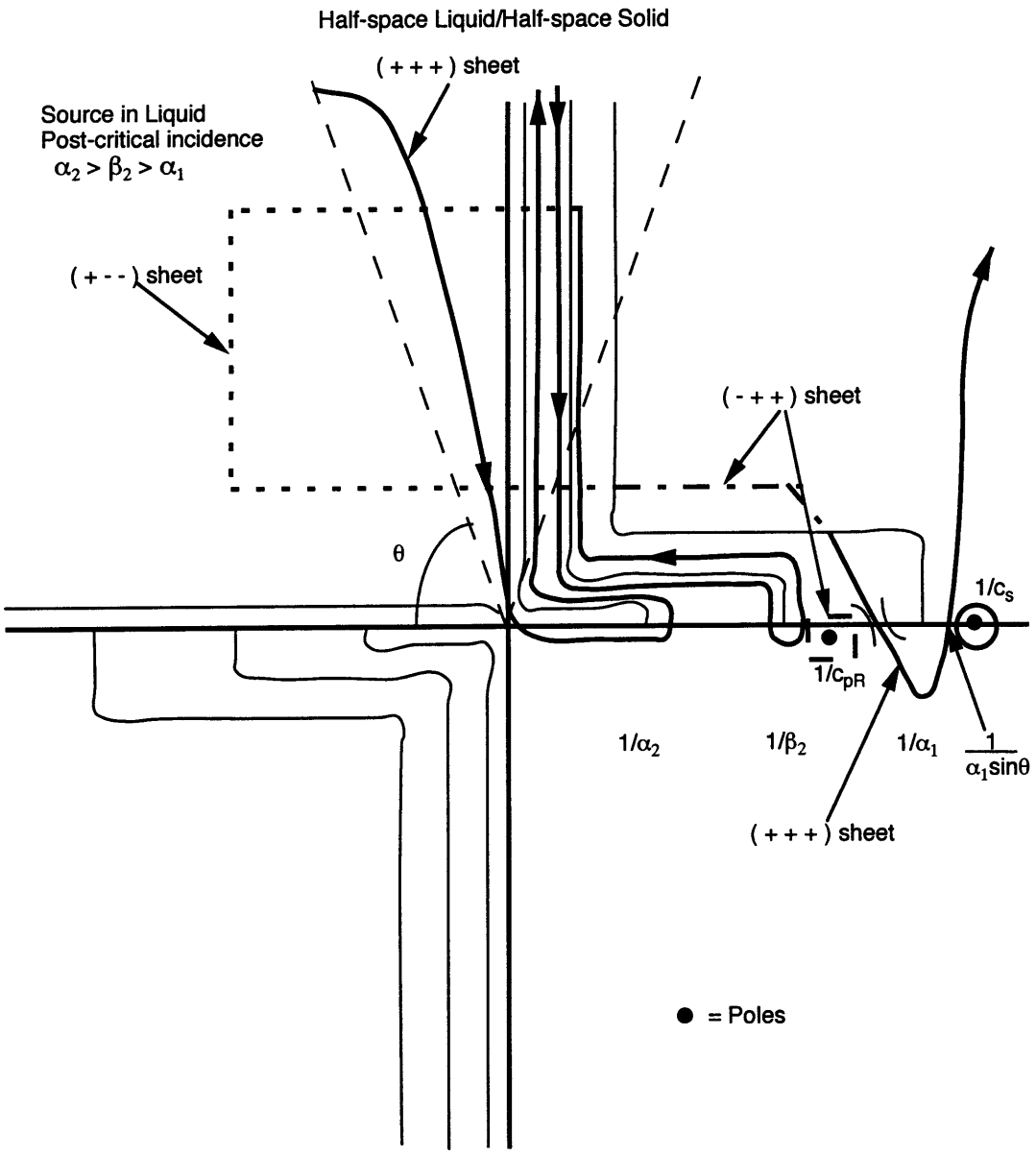


Figure 2-13: Integration path for a liquid half-space over a hard elastic half space at post-critical incidence for shear waves. The path occupies three Riemann sheets as indicated by the heavy solid and dashed curved lines. The pseudo-Rayleigh pole ($1/c_{pR}$) and Stoneley pole ($1/c_s$) are shown. Contributions from both the pseudo-Rayleigh and Stoneley pole must be included for post-critical incidence.

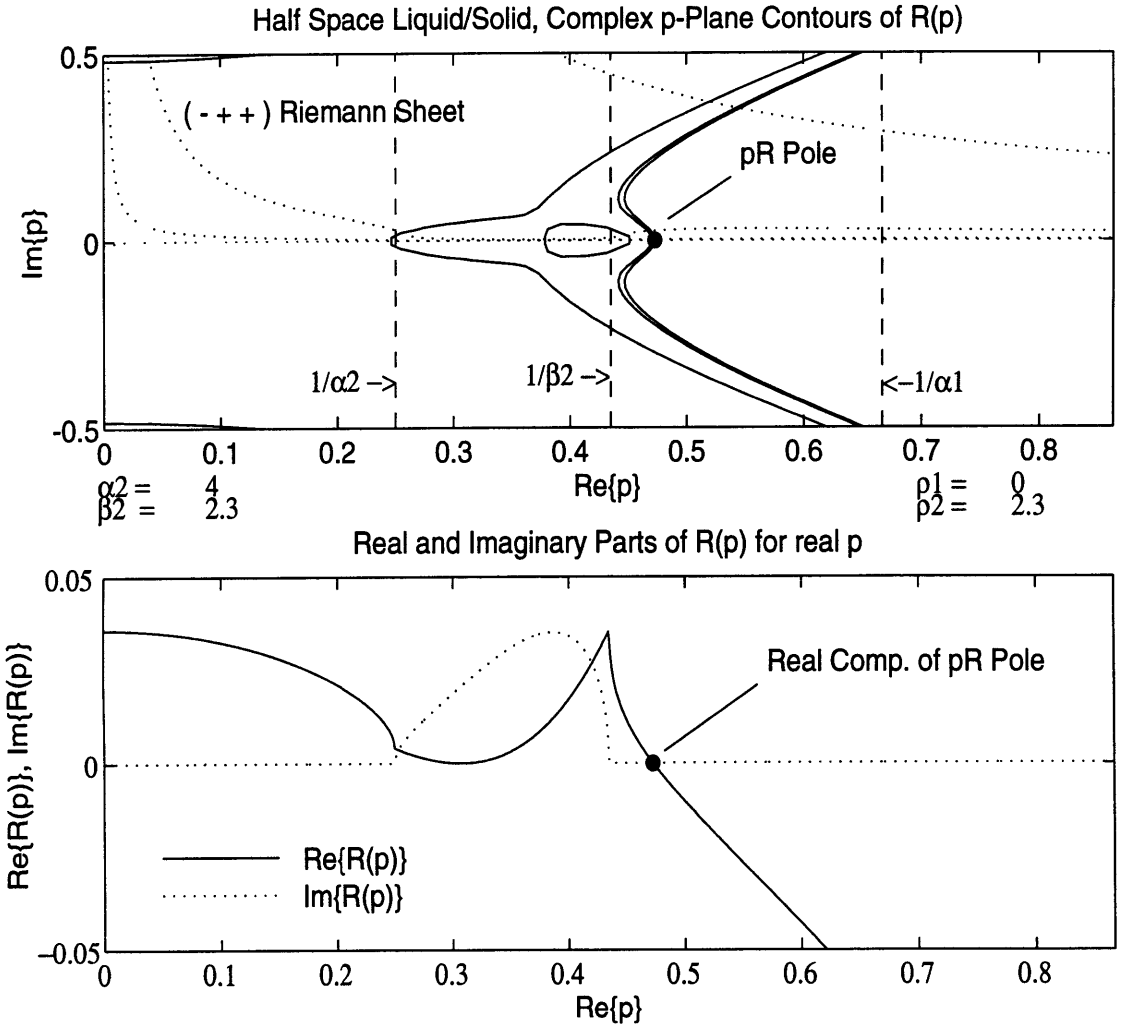


Figure 2-14: Contour plot of $R(p)$ for a zero density liquid half-space over an elastic half-space. The real (solid contours) and imaginary (dotted contours) components are plotted for ( − + + ) (contours are for 0.1, 0.01, 0.001, 0.0). The pseudo-Rayleigh pole is located where the zero contours of the real and imaginary component intersect. The lower plot shows the real and imaginary amplitudes of $R(p)$ for real $p$ and the location of the real component of the pseudo-Rayleigh pole.

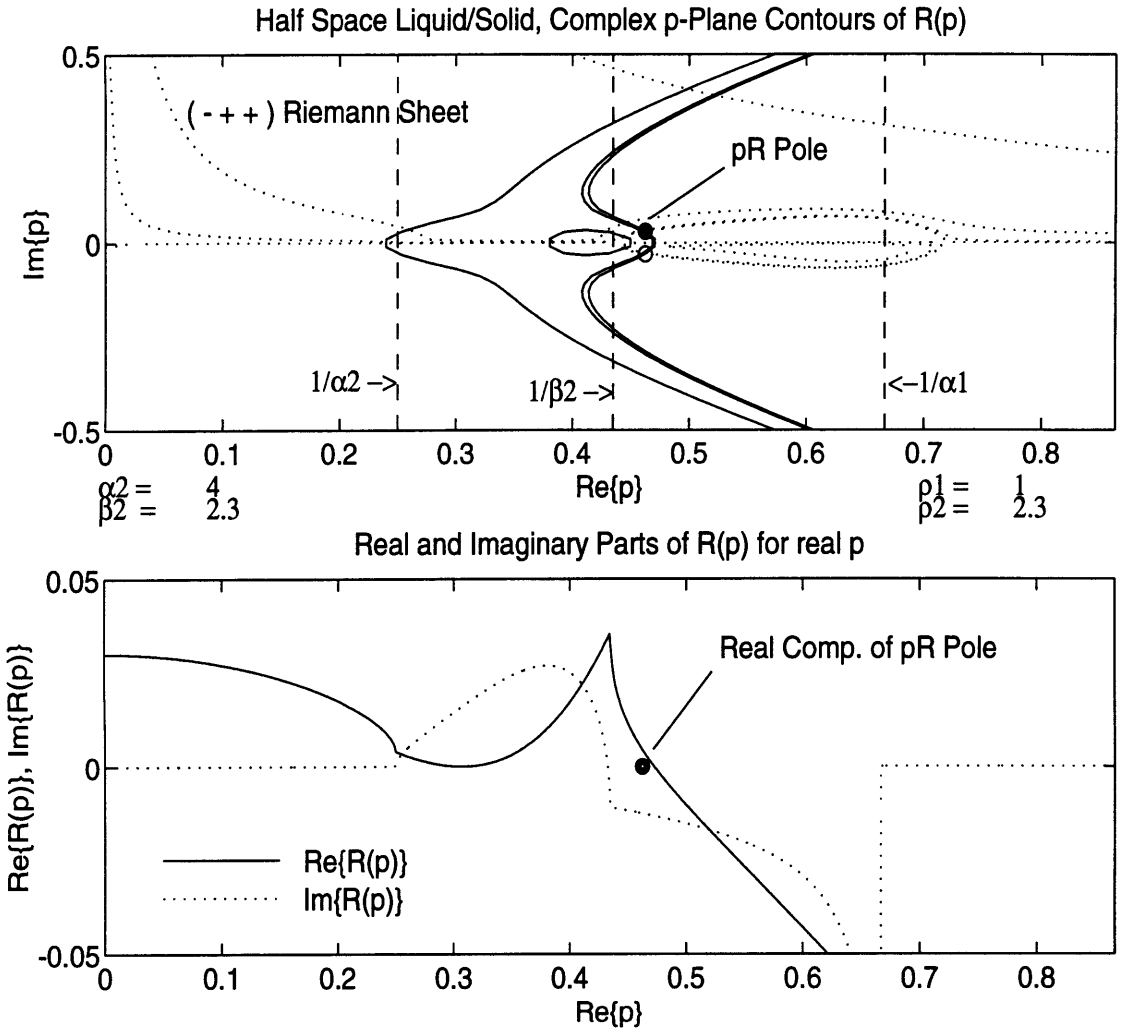


Figure 2-15: Contour plot of $R(p)$ for a unit density liquid half-space over an elastic half-space. The real (solid contours) and imaginary (dotted contours) component are plotted for ( $-$ $+$ $+$ ) (contours are for 0.1, 0.01, 0.001, 0.0). The pseudo-Rayleigh pole is at $p = 0.463 + 0.03i$ $s/m$ (the complex conjugate is shown as the open circle). The lower plot shows the real and imaginary amplitudes of $R(p)$ for real $p$ and the location of the real component of the pseudo-Rayleigh pole. The pseudo-Rayleigh pole is complex and therefore propagates with attenuation and dispersion.

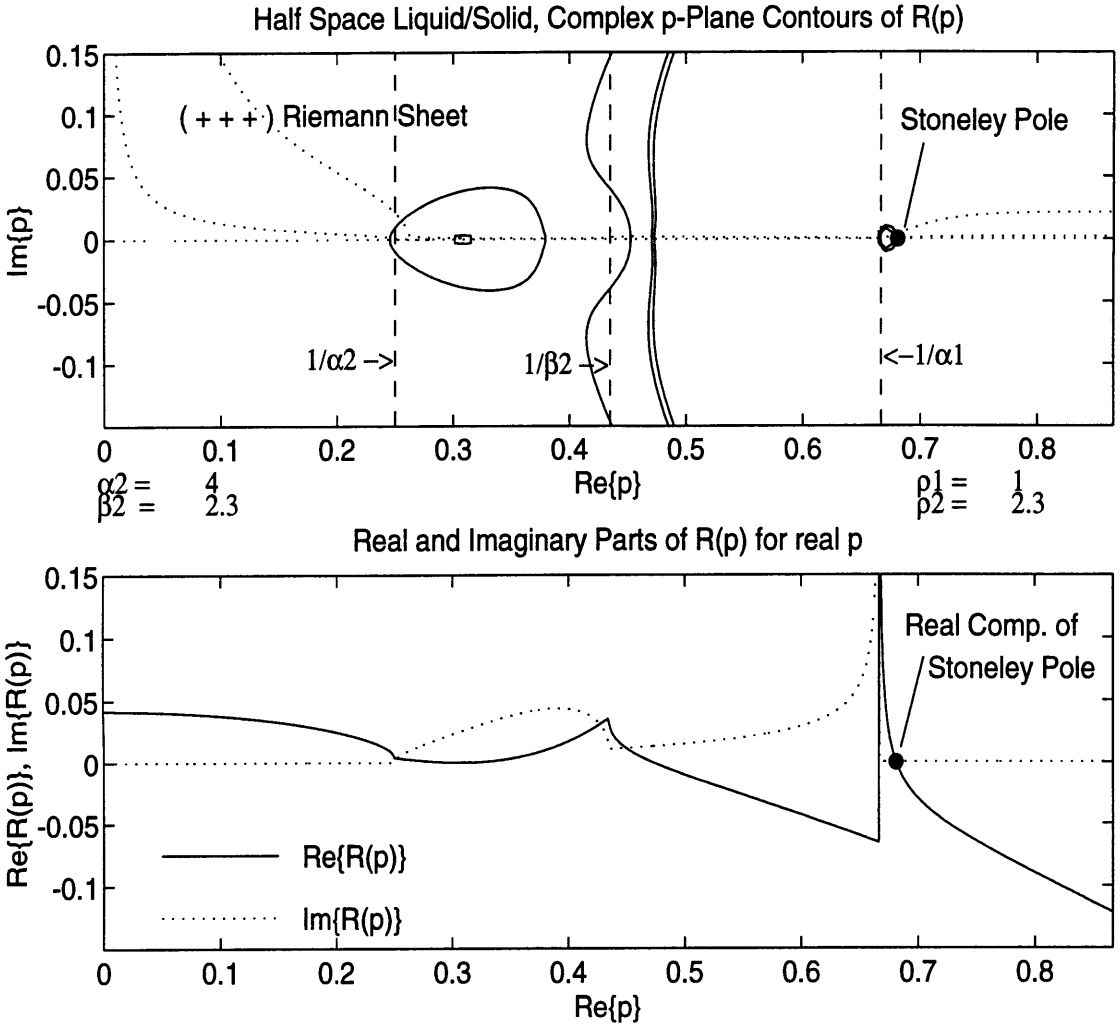


Figure 2-16: Contour plot of $R(p)$ for a unit density liquid half-space over an elastic half-space. The real (solid contours) and imaginary (dotted contours) component are plotted for ( + + + ) (contours are for 0.1, 0.01, 0.001, 0.0). The Stoneley pole is shown. The lower figure plots real and imaginary amplitudes of $R(p)$ and shows that only the Stoneley pole exists on the physical Riemann sheet.

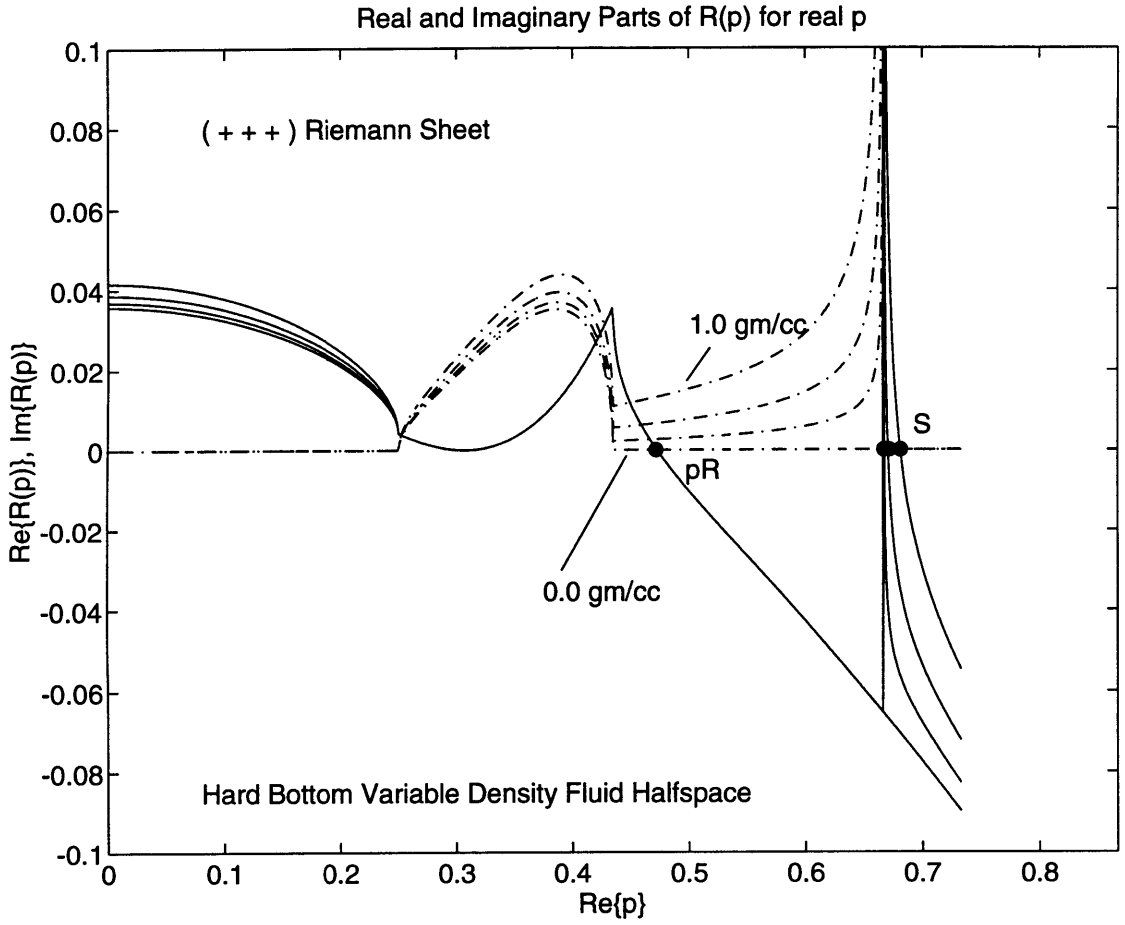


Figure 2-17: Magnitudes of the real and imaginary portions of the Rayleigh period equation for a variable density liquid half-space over an hard bottom elastic half-space for ( + + + ). The fluid density has values of 1.0, 0.5 0.1 and 0.0 $gm/cc$ in a model with $\alpha_1 = 1.5$, $\alpha_2 = 4.0$, $\beta_2 = 2.3\ km/s$ and $\rho_2 = 2.3\ gm/cc$. For $\rho_1 \geq 0$, the Stoneley pole appears and the Rayleigh/pseudo-Rayleigh pole leaves the physical Riemann sheet.

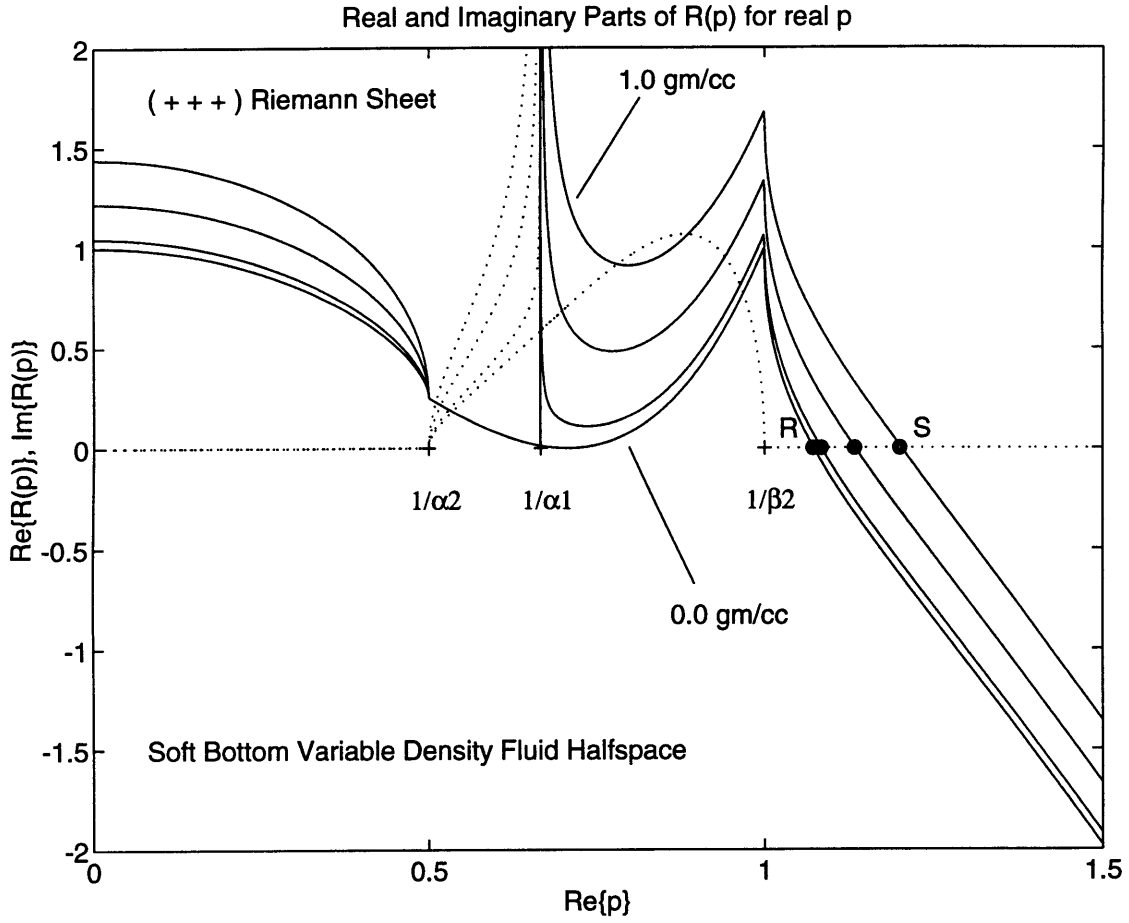


Figure 2-18: Magnitudes of the real and imaginary portions of the Rayleigh period equation for a variable density liquid half-space over an soft bottom elastic half-space for ( + + + ). The fluid density has values of 1.0, 0.5 0.1 and 0.0 $gm/cc$ in a model with $\alpha_1 = 1.5$, $\alpha_2 = 2.0$, $\beta_2 = 1.0$ $km/s$ and $\rho_2 = 1.7$ $gm/cc$. The Stoneley pole appears to the right of $p = 1/\beta_2$ and merges with the Rayleigh pole as $\rho_1 \rightarrow 0$. The pseudo-Rayleigh pole exists on ( − + + ) very near $1/\beta_2$.

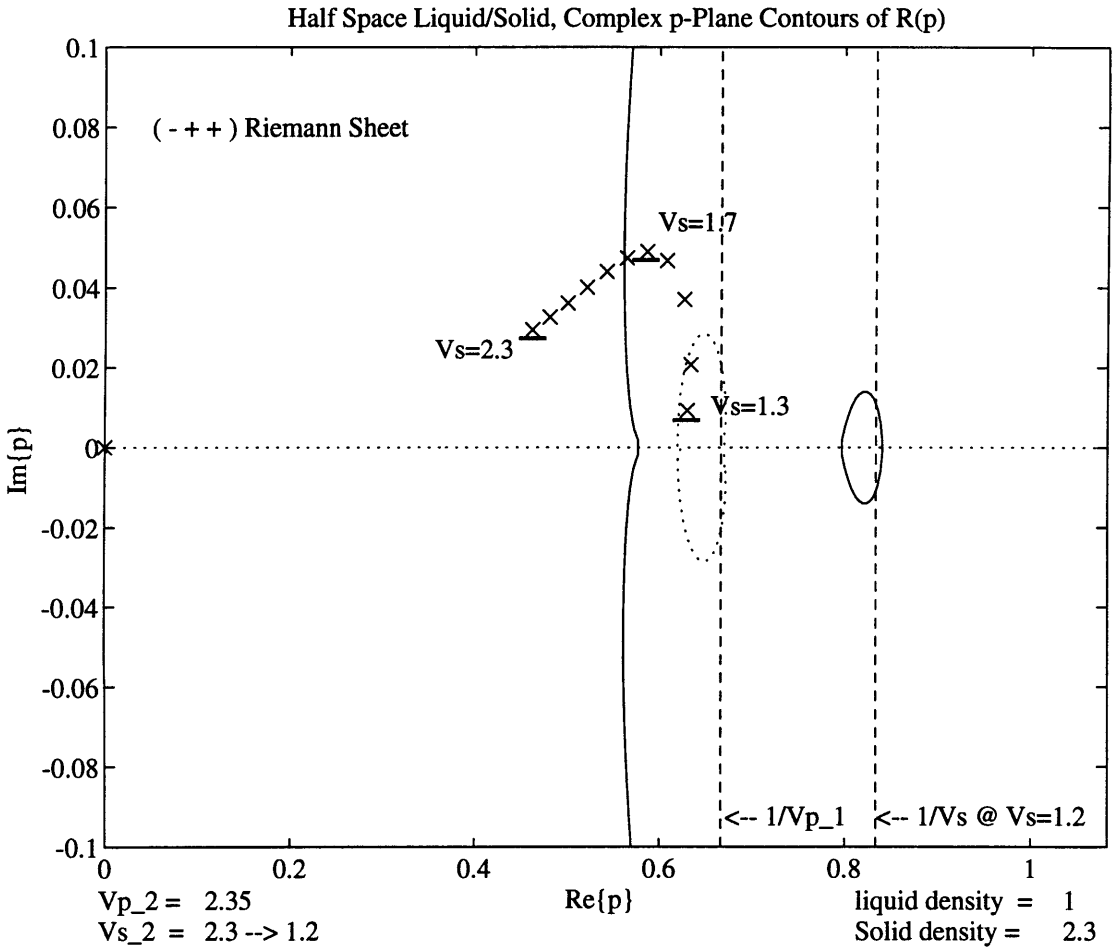


Figure 2-19: Complex ray parameter plane on the ( − + + ) Riemann sheet for half-space liquid/solid. The shear velocity of the solid is varied from 2.3 to 1.2 $km/s$ and the corresponding pseudo-Rayleigh poles ($\underline{X}$) evaluated.

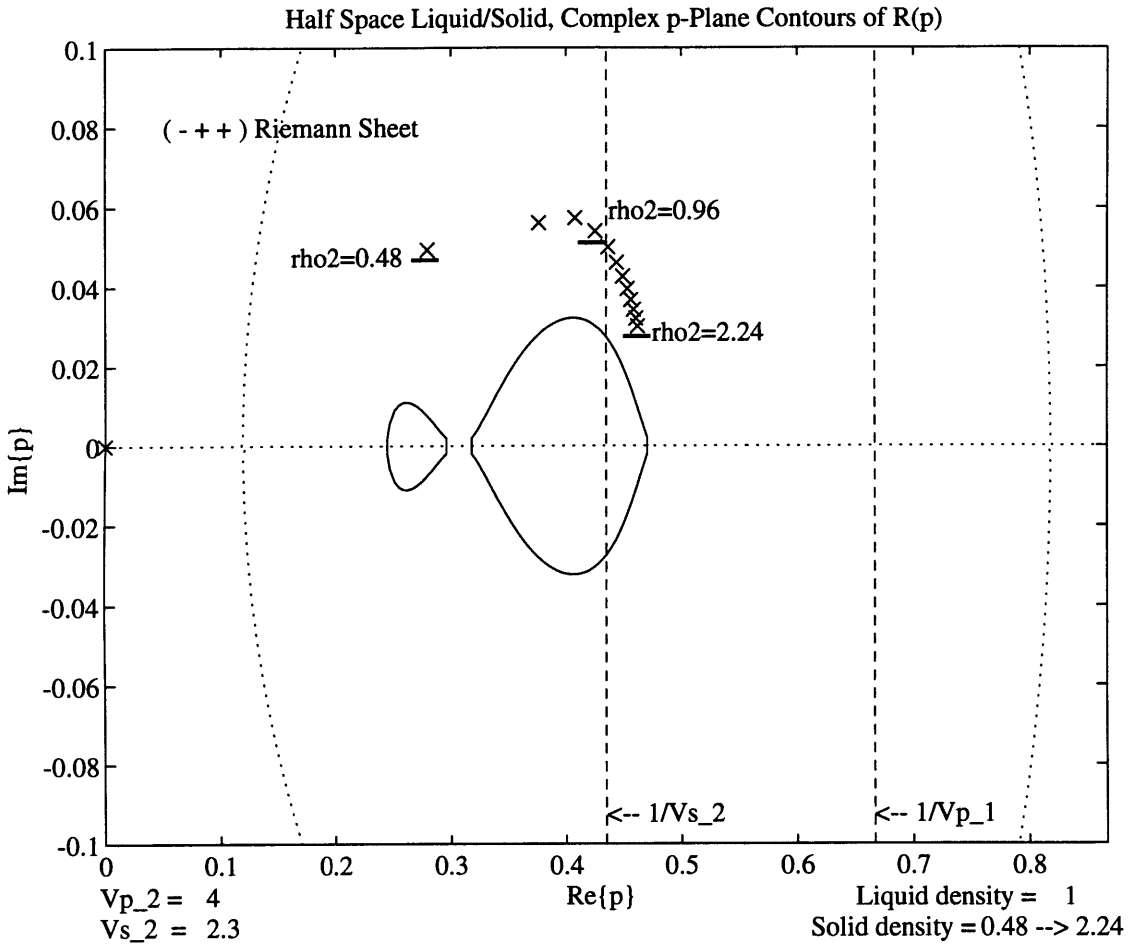


Figure 2-20: Complex ray parameter plane on the ( − + + ) Riemann sheet for half-space liquid/solid hard bottom model model. The density of the solid is varied from 0.48 to 2.24 $gm/cc$ and the corresponding pseudo-Rayleigh poles evaluated.

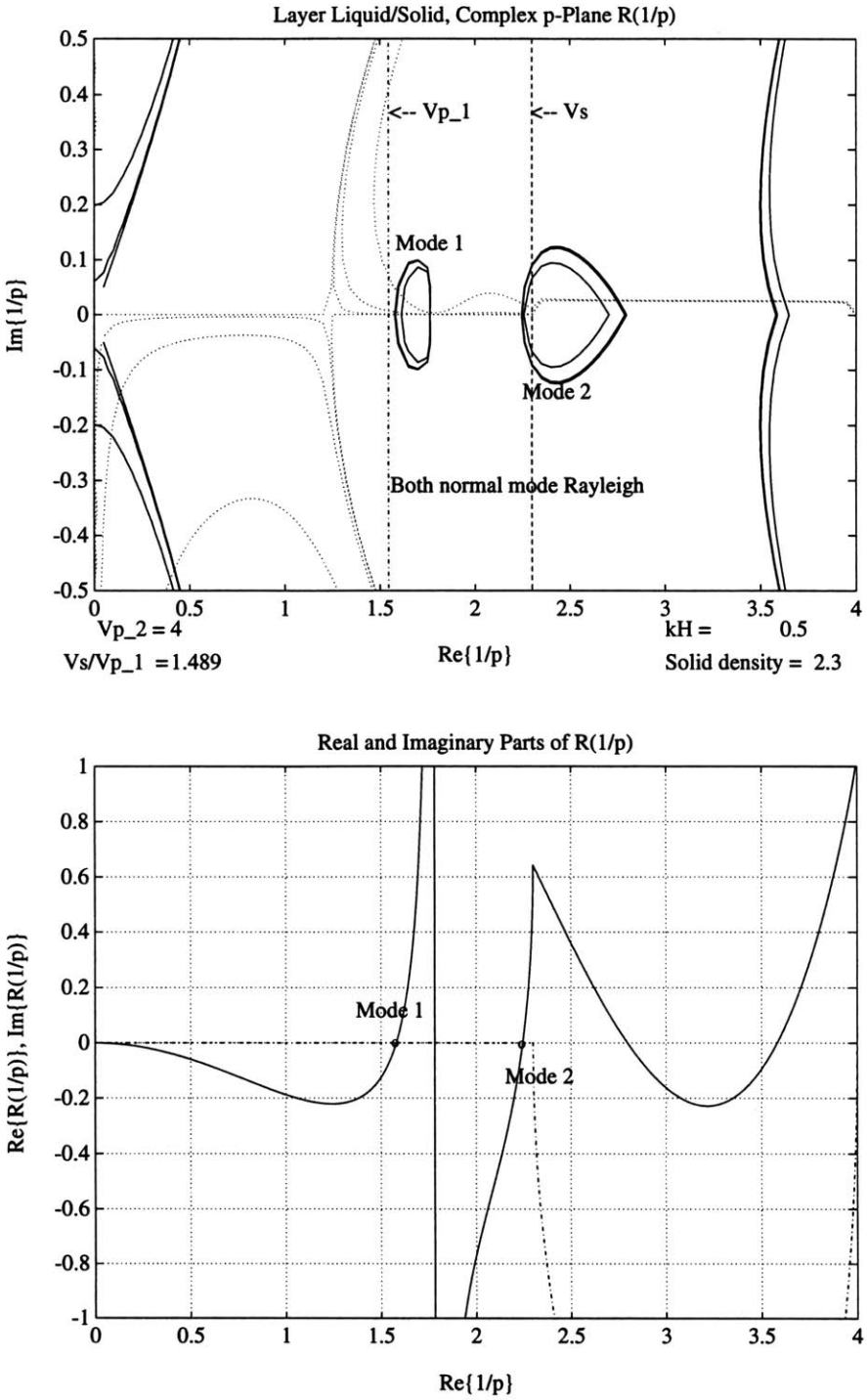


Figure 2-21: Liquid layer over elastic half-space model complex ray parameter plots for shallow water ($H/\lambda = 0.5$). Modes 1 and 2 are shown for a hard bottom model and both are members of the normal mode Rayleigh wave branch.

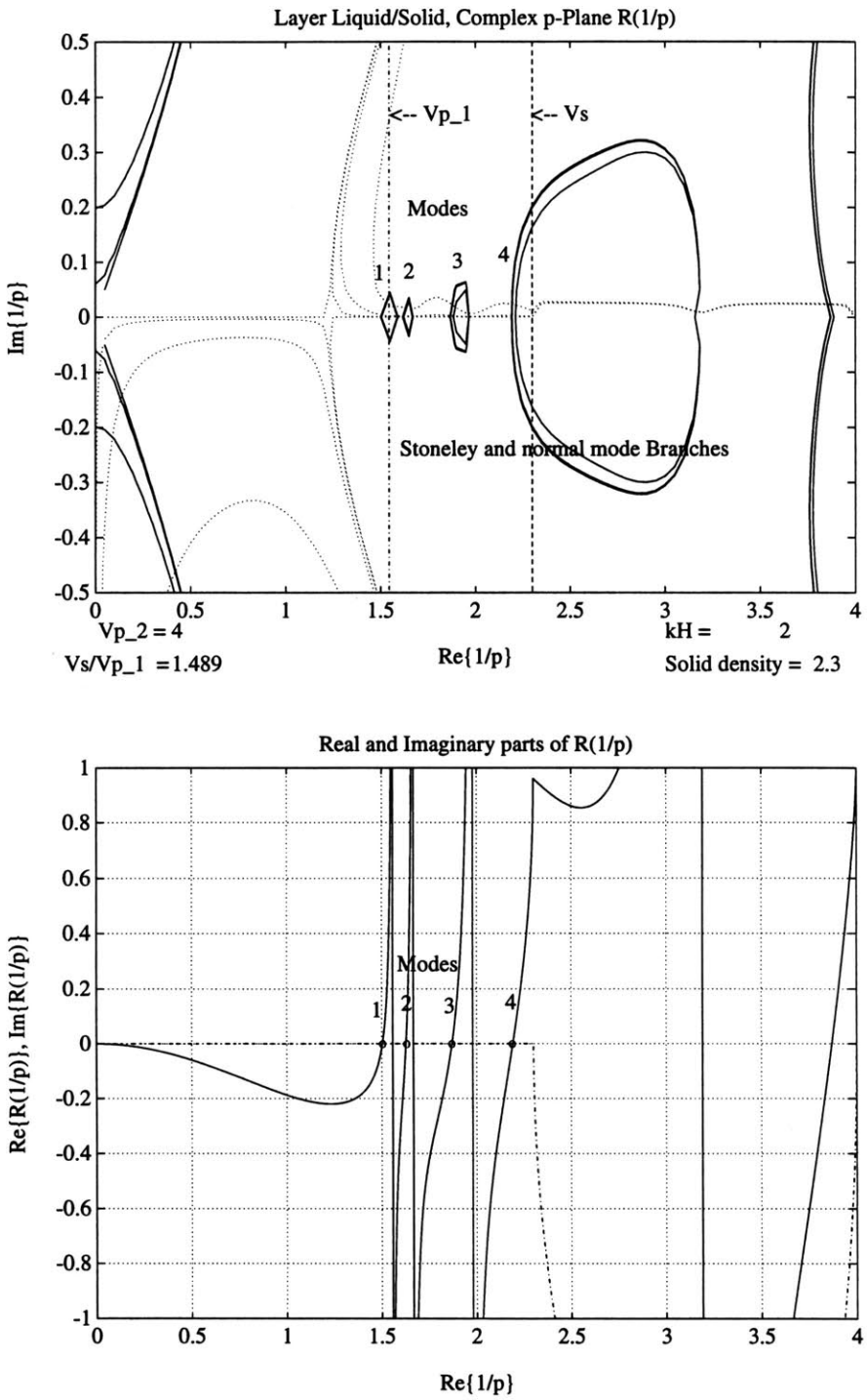


Figure 2-22: Liquid layer over elastic half-space model complex ray parameter plots for deep water ($H/\lambda = 2.0$). Modes 1, 2, 3 and 4 are shown for a hard bottom model. Mode 1 is part of the Stoneley mode branch ($p < 1/\alpha_1$) and the other three are part of the Rayleigh wave branch.

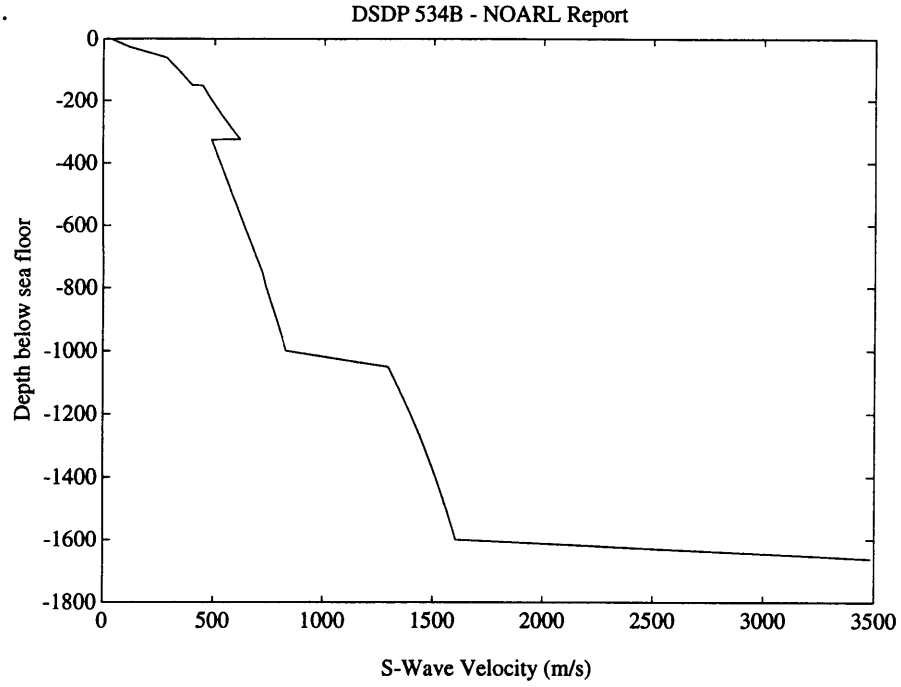


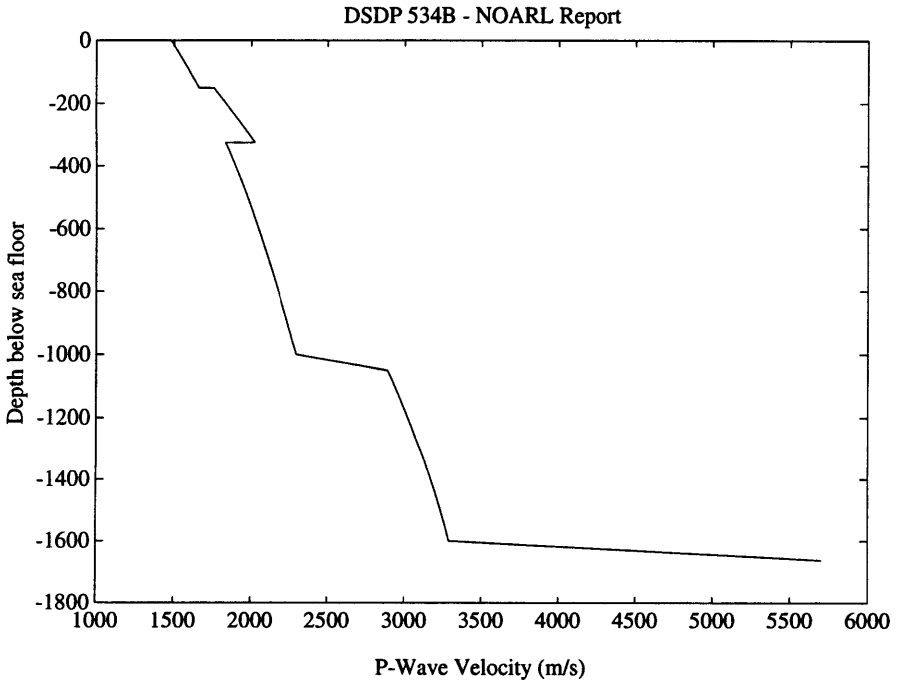


Figure 2-23: Shear and compressional wave velocities in the upper 1600 $m$ of sediments at the Low Frequency Acoustic Seismic Experiment Site 534B in the Blake Bahama Basin.

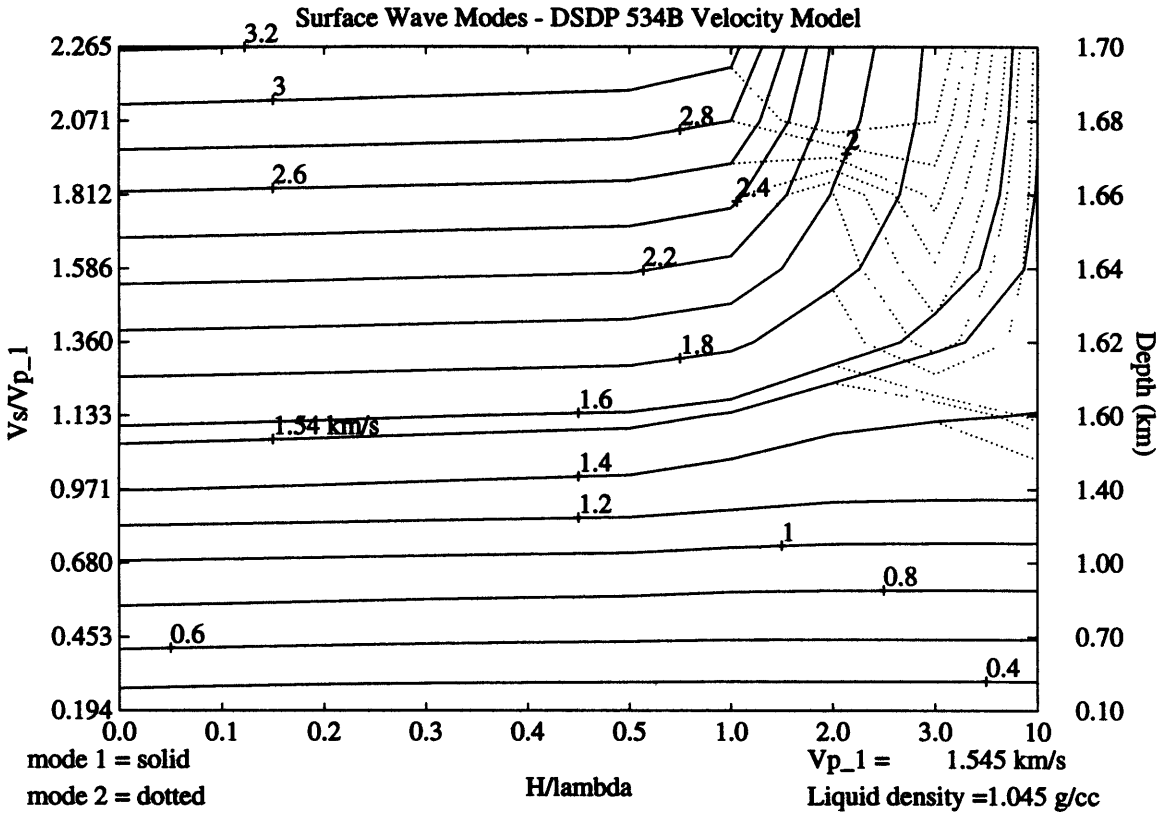


Figure 2-24: Contours of the first two modes predicted at the LFASE Site based on a 5 *km* deep ocean over half-space model. The solid lines are the fundamental mode and dotted lines indicate the second mode. $Vs/Vp_1$ (left hand axis) is the ratio of the average shear velocity in the bottom (averaged to the depth shown on the right hand axis) to the water velocity. The average compressional velocity is used in the calculation but is not labeled on the plot. H/lambda is the water layer thickness in wavelengths.

# Chapter 3

# The Low-Frequency Acoustic Seismic Experiment

## 3.1 Introduction

The Low Frequency Acoustic Seismic Experiment (LFASE) was designed to measure low frequency ($2 - 50\ Hz$) seismo-acoustic noise at and below the sea floor of the Blake Bahama Basin. The Seafloor Borehole Array Seismic System (SEABASS) in DSDP Hole 534B ($28°21'N$, $75°23'W$), measured vertical and horizontal ground velocity and borehole pressure at four depths below the sea floor (Stephen et al., 1993). Figure (3.1) shows the location of the wellbore at 4971 $m$ depth off the eastern Florida coast. Additionally, a sea floor array of twelve OBS instruments was located within a few kilometers of the hole and a vertical array of hydrophones was also placed in the water column. The simultaneous recording at multiple depths combined with sea floor seismometers and water column measurements provide a nearly ideal natural laboratory for exploring the ambient noise field. This unique experiment is the first attempt to measure noise at several depths above and below the sea floor simultaneously.

The experiment was conducted between August 7, 1989 and September 10, 1989 and consisted of two phases: an active shooting phase and a passive ambient noise

recording phase. During the active portion, the USNS Lynch and R/V Melville remained on site, conducting far and near offset controlled source experiments (i.e. explosives and airguns). For a discussion of this phase of the experiment see Stephen et al., (1993) and Spiess et al., (1992). The passive phase began late on August 17 when the ships left the site, leaving the borehole package and OBS's to autonomously record the ambient noise field. The passive phase lasted approximately one week from August 18 to August 25 ( the "noise week"). This chapter focuses on a description of very-low- and low-frequency ($0.1 - 10\ Hz$) ambient noise, its sources and its propagation mechanisms.

Previous studies of deep ocean ambient noise propose that the noise near the microseism peak ($0.1 - 0.4\ Hz$) propagates as trapped long wavelength fundamental mode Rayleigh waves of the crust+ocean mechanical system (Latham and Sutton, 1966, Latham and Nowroozi, 1968, Adair, 1985, Webb, 1992). Our observations suggest that microseismic energy also propagates by higher order Rayleigh modes and interface Stoneley waves excited by local heterogeneities. Besides these general properties, the microseismic field varies temporally and is correlated with sea state directly above the experiment site. Below we summarize some features that the LFASE data exhibit:

- The energy in the microseism peak at $0.3\ Hz$, does not vary with depth, maintaining a vertical acceleration power level near 65 $dB\ rel\ 1\ (nm/s^2)^2/Hz$ and an RMS horizontal ($\sqrt{transverse^2 + radial^2}$) power level of 75 $dB\ rel\ 1\ (nm/s^2)^2/Hz$. The average value of the microseism peak over the "noise week" varied less than 2 $dB$ between the sea floor OBS and the SEABASS sensor 100 $m$ below the sea floor. Temporal changes in the power of the microseism peak are correlated with changes in the swell caused by a storm that passed over the experiment site.

- In general, there is a monotonic decrease in noise energy with depth between 1.0 and 15 $Hz$. In this band the average vertical and horizontal spectral energy drops 10 and 15 $dB$ respectively over 100 $m$ depth.

- Between 0.3 and 0.4 $Hz$, the ratio of the (vertical)/(RMS-horizontal) components remains fixed with depth, indicative of a single long wavelength mode. At higher frequencies the (vertical)/(RMS-horizontal) particle motion ratio is variable with depth, a feature consistent with the presence of separate interface and guided wave modes. We also find similar horizontal noise levels on both the sea floor OBS and the uppermost SEABASS geophone. This supports the supposition that the horizontal noise levels on the OBS are 'real' and are not accentuated by poor coupling.

- Several other narrow bandwidth "modes" or features in the LFASE data are also associated with the local sea state and swell. These modes, which are not simple line spectra, have energy centered near 0.75, 1.2, and 2.1 $Hz$. Unlike the microseism peak, the modes are depth dependent, although not in a simple linear way. By examining particle motion in section 3.5.3 we find that the dominant azimuth of the motion agrees with the microseism peaks before and after the passage of a storm but is omnidirectional while the storm is nearby. These modes are strong evidence for discrete modes within the water column and sediments.

Using multiple window spectral analysis (Chave et al., 1987) we have been able to resolve the microseism peak along an oceanic borehole array for the first time and determine the depth dependence of noise below the sea floor at four simultaneously instrumented depths. Chapter 2 reviewed the theoretical and experimental observations for interface waves at the sea floor. In this chapter a short review of previous observations of deep sea microseisms on and within the sea floor is first presented. Next, the time series analysis of the data is described and a summary of the analysis results presented. Particle motion and polarization results are discussed leading to conclusions about the source and mode of propagation of noise in the basin. Finally, conclusions about the nature and sources of microseisms and seismo-acoustic noise between $0.1 - 15.0$ $Hz$ are presented based on dispersion curves, the computed spectral levels and particle motion polarization.

## 3.2 Previous Work

Longuet-Higgins (1950) presented the classic theoretical study of microseism generation, showing that microseism levels were controlled by wave-wave interaction at the sea surface. Longuet-Higgins cites work by Miche (1944) who found that the second order solution to gravity waves interacting at the sea surface did not attenuate with depth in the ocean but instead excited acoustic waves in the water; and he concludes that this acoustic radiation can effectively drive the sea floor at all ocean depths. Longuet-Higgins estimates the possible vertical displacements of the sea floor due to a 2000 $km$ wide storm at the surface to be $10^{-6}$ $m$. This value is now known to be within an order of magnitude of observations. In a later application of Miche's solution, Hasselmann (1963) finds that the probable mode of propagation in the bottom for this energy is via interface waves trapped at the water/solid interface. He also finds that microseisms are generated by only the Fourier components whose phase velocities match the free modes of the ocean/sea floor elastic system. Hasselmann compares his theoretical calculations with a data set compiled by Haubrich et al., (1963) and found partial agreement. The discrepancies between his theory and Haubrich's data he attributes to the near field source of the data. Haubrich's data was collected only 1/3 of a wavelength from the microseism source, a suite of breaking waves along the coastline 16 $km$ away.

At the Ocean Bottom Seismic System (OBSS) site off the coast of Northern California, ambient noise was reported between $0.002 - 0.4$ $Hz$ by Sutton and Barstow (1990). Coherent energy between 0.1 and 0.15 $Hz$ lead Sutton and Barstow to conclude that microseisms in this band are fundamental mode Rayleigh waves. Pressure and vertical displacement are highly correlated and have relative phase difference of $\pi$ radians which matches theoretical values for Rayleigh waves between 0.1 and 0.4 $Hz$. They conclude the double frequency microseisms in this band are due to waves from distant sources but are created by nonlinear wave interaction near the OBSS rather than at the storm center. During the passage of the two storms, noise levels in the $0.2-0.4$ $Hz$ band varied 20 $dB$ and were found to be related to local sea

state. Below 0.1 $Hz$ they find the noise level is related to the passage of two distant storms in the North Pacific. In this frequency band, the ratio of pressure to vertical velocity corresponds to that of higher mode Rayleigh waves excited by local wind waves. An earlier analysis of this same data set by Latham and Nowroozi (1968) showed that the ratio of horizontal and vertical particle motion in the frequency band $0.1 - 0.2$ $Hz$ agreed with model results for fundamental Rayleigh modes. The particle motions were compared with numerically calculated Rayleigh waves for a model containing 650 $m$ of sediment overlying basement.

An experiment involving a sea floor array of ocean bottom seismometers off the Southern California coast is described in Schreiner and Dorman (1990). An accurate sediment velocity model from a previous study (Sauter et al., 1986) was used to model the modes seen within a sediment pond in deep water off the coast of Southern California. An array of OBS's was deployed in a "minimum redundancy" grid with inter-element spacings of $8 - 156$ $m$ and spatial coherencies were computed between 0.06 and 10 $Hz$. The ambient noise was found to propagate as fundamental mode Rayleigh waves between 0.06 and 0.8 $Hz$. Between 0.8 and 4.0 $Hz$, higher mode Rayleigh/Stoneley/Scholte waves comprised the remainder of the noise field. Their Q mode studies showed the energy was scattered into the sediments within $20km$ of the array. In a follow up study (Dorman and Schreiner, submitted), the spectral ratios between horizontal and vertical components of the array are used to constrain the particular bandwidth and relative contribution of each mode to the noise field. Using the coherency length scale and spectral ratios, they find that noise does not necessarily decrease monotonically with depth. Higher modes within the sediments can create narrow band high amplitude signals at depth if sensors are placed at modal antinodes.

There are relatively few measurements of noise in oceanic boreholes. Stephen et al. (1987) studied VLF ambient noise in DSDP Hole 418 ($25.0^0N, 68.0^0W$) in the Western North Atlantic at five sequential depths below the sea floor and into basement rock (41, 81, 230, 330 and 430 meters). Using a single triaxial borehole sonde, they found that ambient noise levels between 5 and 50 $Hz$ were not directly

proportional to depth below the sea floor and may be a function of local geology and clamping. Noise seen at Hole 418 was isotropic and showed no distinct polarization.

Carter et al. (1984), using the Ocean Subbottom Seismometer (OSS) in Hole 494A off the Western Guatemalan coast, found that the ambient $10 - 20\ Hz$ noise levels at 194 $m$ below the sea floor were similar to the levels seen on an OBS located within 200 $m$ of the borehole. In the $2 - 10\ Hz$ band the downhole instrument measured noise levels 3 to 8 $dB$ below the OBS levels. The authors attribute the larger surface response to interface waves trapped at the water/sediment interface ($\leq 5\ Hz$) and shear wave noise ($7 - 10\ Hz$) which they expect to be greater due to the low shear modulus at the interface.

Duennebier et al. (1986; 1987), reported on noise levels measured by the OSS IV in a borehole near the Hokkaido trench (DSDP Hole 581C; $42.9^{o}N, 159.8^{o}E$). Noise levels observed 378 $m$ below the sea floor (22 $m$ sub-basement) were extremely quiet between 4 and 15 $Hz$; between 2 and 20 $Hz$, OSS IV noise levels were 20 $dB$ below the OBS's. Storms (wave breaking), shipping and biologic sources are the major influences on noise above 5 $Hz$; below 5 $Hz$, the noise is controlled by local sea state. The observation of a saturation spectrum between 0.5 and 5 $Hz$ on both the OBS and OSS systems for two separate storms indicates that coastal wave reflection is not as important as local nonlinear wave-wave interaction for noise generation. This bandwidth has been identified with wind driven gravity waves in the most commonly saturated portion of the ocean wave spectrum in deep water. McCreery et al. (1993) have coined the term "Holu" (the Hawaiian word for deep water) spectrum for this band.

The above studies using the OSS do not discuss the behavior of the spectra below 1 $Hz$ and particularly noise at the microseism peak near 0.2 $Hz$. The Marine Seismic System (MSS), a permanent borehole seismometer like the OSS (Hyndman, Salisbury et al., 1984 and Adair et al., 1984) was placed in DSDP borehole 395A on the Mid-Atlantic Ridge and rested unclamped at 516 $m$ sub-basement (600 $m$ below the sea floor). Electronic and least count noise were present below 0.3 $Hz$ and transients contaminated the spectrum above 2.2 $Hz$. Between 0.3 and 2.2 $Hz$ the noise

field was stationary on a time scale of 1 hour but was found to vary over greater time scales (order 10 hrs.). The MSS recorded noise levels near 60 $dB\ rel\ 1\ (nm/s^2)^2/Hz$ between 0.2 and 0.4 $Hz$, which are approximately the same levels as is seen at shallow depth by the OSS. During the MSS experiment, OBS noise levels were +10 $dB$ at 0.2 $Hz$ to +28 $dB$ at 2.2 $Hz$ above the borehole readings. Adair et al. (1984) conclude that the difference in noise level between the sea floor OBS and the downhole instrument is consistent with the theory that the microseismic energy is propagating as low velocity Stoneley modes which decay exponentially with distance from the ocean bottom.

Employing a triaxial version of the MSS, Adair et al. (1986) and Adair (1985) present borehole seismic data from DSDP Hole 595B. This experiment known as the "Ngendei Experiment" was designed to test the usefulness of borehole emplacement of seismic sensors in the ocean. The location was chosen close to the Tonga-Kermadec Trench in order to measure earthquakes and microseisms in the deep oceanic basement. In contrast to the conclusions made about the data observed by the MSS previously, Adair developed an ocean noise model and finds that in general, Stoneley modes are not excited, rather the primary mode of microseism propagation is by trapped fundamental mode Rayleigh waves along the whole ocean/sea floor crust mechanical system.

## 3.3 The LFASE Data

### 3.3.1 The SEABASS and OBS Data

SEABASS consisted of a vertical array of four individual satellites each containing a triaxial cluster of 4.5 $Hz$ seismometers. Each satellite has a locking arm with a clamping capability of over 140 lbs lateral force against the wellbore casing. The satellites were clamped at sub-bottom depths of 10 , 40 , 70 and 100 meters. Since the locking arm of the 40 $m$ seismometer failed, the data from this depth is unreliable.

As described in Orcutt et al. (1985), the OBS contains a triaxial set of 1 $Hz$ (Mark L4-3D) seismometers. (Riedesel et al. (1990) found that the L4 was able to accurately measure the microseism peak at 0.16 $Hz$ if used in conjunction with low noise amplifiers.) While twelve OBS stations were provided for the LFASE experiment, only two of the OBS's recorded meaningful information. Of these two, OBS "KAREN" recorded reliably and was free of the data "tears" and "spikes" that plagued the other OBS with usable noise records (Sereno, 1989). OBS "KAREN" was located within 100 m laterally of 534B. It was extremely fortuitous that the problem free OBS was so near the borehole. In effect, this OBS became the fifth node of the borehole array, placed at the sea floor. Because of its lower intrinsic frequency response, KAREN's spectra also became the reference spectra with which to test the accuracy of the lowest frequencies computed for the SEABASS spectra.

A 15 element vertical hydrophone array was deployed above the sea floor by the USNS Lynch during the active phase of the experiment. The array had an aperture of 500 $m$ with a 30 $m$ spacing between elements. The array was successfully deployed and recovered on site, however no data that overlapped in time with the passive noise phase of the experiment was recovered from the array.

The week of August 18 through August 25 was chosen for the ambient noise data analysis because it was the most uniformly recorded; this week will be termed the "noise week". Table (3.1) lists the time windows greater than 180 seconds that

were acquired during the noise recording phase from OBS Karen and SEABASS. SEABASS acquired either 10, 360, or 1200 second records every hour from 17 August 16:00 through 25 August 05:00 (a detailed review of the LFASE recording operations is contained in Bolmer et al., 1991). In all, over 200 Mbytes of sea floor data from SEABASS were successfully collected and analyzed for this thesis. OBS noise windows were uniformly 480 seconds long, at 12 hour intervals. In Table (3.1) the righthand column of the table indicates the eleven windows for which data was recorded simultaneously between the OBS and SEABASS instruments. If there was any overlap between the windows a "Y" is indicated in this column. In all, seventy-four 360 $s$ windows and eight 1200 $s$ SEABASS windows were analyzed to compute the average spectra of the microseism field and temporal noise evolution below 15 $Hz$ for the noise week. 10 $s$ windows were omitted for the study of frequencies below 1 $Hz$ but were used to identify temporal trends in the spectra over the week (Stephen et al., 1993.).

### 3.3.2 External Buoy and Ocean Wave Modeling Data

In addition to the LFASE data, information from the Fleet Numerical Oceanography Center's Global Spectral Ocean Wave Model (GSOWM) and data from NOAA "waverider" deep water pitch and roll buoys were used as a monitor of the sea state and barometric conditions during the LFASE noise week.

GSOWM numerically forecasts significant wave height and direction over the world's oceans (Clancy et al., 1986) in real time. A discrete set of wave energy spectra are estimated over a $2.5^o$ by $2.5^o$ spherical grid which in the North and South Atlantic extends from $77.5^oN$ to $72.5^oS$. Since GSOWM is a deep water forecasting tool, the model estimates are computed only at grid points off the continental shelf. The five nearest grid points are located at $(25^oN, 70^oW)$, $(27.5^oN, 70^oW)$, $(30^oN, 70^oW)$, $(32.5^oN, 70^oW)$ and $(35^oN, 70^oW)$ and are shown with respect to the LFASE borehole (Site 534B) location in Figure (3.1).

The spectra are binned in 24 directional bins (at $15^o$ spacing) and 15 frequency

bins with periods of : 3.24, 4.80, 6.32, 7.50, 8.57, 9.73, 10.91, 12.40, 13.85, 15.00, 16.40, 18.00, 20.00, 22.50 and 25.70 seconds. At each grid point, calculations are also made for wind vector; sea height, direction and period; and swell height direction and period. The GSOWM model discriminates between local seas and swell by comparing the surface gravity wave phase velocity with local wind velocity. The swell calculation is made for waves with phase velocities that are too large to be driven by local winds.

The NOAA Data Buoy Center (NDBC) maintains a system of automated buoys throughout the Northern Hemisphere. These "waverider" buoys collect both meteorological and oceanographic data which is telecommunicated to U.S. operational centers for use in real time forecasting and then archived by NDBC. Data from buoys number 41006, 41009 and 41010 were used to monitor the fine scale wave energy history near Hole 534B.

Figure (3.1) shows the location of Hole 534 relative to the GSOWM grid points and the NOAA buoys, along with the bathymetry. Buoys 41006 and 41010 are moored in deep water (over 500 $m$); the depth at buoy 41009 is under 100 $m$ of water and is considered shallow because it is on the order of the wind wave wavelength (LeMehaute, 1976). The nearest GSOWM grid points all lie 6° East of the borehole along longitude 70° W and in the deeper water off the continental rise.

## 3.4 Frequency and Particle Motion: Methods

There are three basic processing considerations for calculating spectra and particle motion from electromechanically recorded earth motion.

- Identifying stationary and nonstationary processes (i.e. continuous and transient signal);
- Choosing an accurate spectral estimation method;
- Estimating the theoretical system limits and correcting for the known transfer function of the electromechanical pick-up with the system amplifiers;

In the following subsections we will review the methods used for calculating the spectra and particle motion polarization. These methods form the core of the processing used on the LFASE data. Transients are first mentioned. Then the multiple window spectral analysis method is described. System limits are computed based on a consideration of the instrument dynamic range, transfer function and the natural ambient noise level. The last subsection (3.4.4) discusses the spectral matrix method of calculating particle motion polarization.

### 3.4.1 Transients

Outside of the electrical and mechanical limits of the seismometers, care must be taken to ensure that nonstationary events do not bias the spectral estimate of the noise sample. Both the OBS data and the borehole array data contained natural and electronic artifacts. The spectra and timing of these artifacts have been analyzed and catalogued and both electronic and biologic origins for the transients have been identified. For the most part, the transients were avoided during the spectral analysis. Since the majority of the energy in these transients lies above 15.0 Hz, they are beyond the scope of this thesis and will not be discussed further.

### 3.4.2 Spectral Analysis

Ambient noise is usually considered a stationary, Gaussian distributed stochastic process. However the measurement of ambient noise involves a finite, discrete sampling of this process for a time period over which its behavior may not be completely stationary. To obtain reliable spectral estimates of a continuous process from finite time series requires a time weighting function which minimizes frequency biasing and maintains a high frequency resolution. The method should also be statistically consistent and robust in the presence of small departures from stationarity.

The optimal method for calculating the spectral estimate uses discrete prolate spheroidal wavefunctions (DPSW) as the time weighting functions (Slepian and Pollak, 1961; Slepian, 1978; and Thompson, 1982). Slepian (1978) has shown that

the Fourier transform of the zeroth order DPSW contains the most inner bandwidth energy of any Fourier transform of a time limited sequence. This means that very little of the spectral energy computed for a particular inner bandwidth is biased into outside bands. The inner bandwidth of the DPSW is determined by the chosen time-bandwidth number (TBW). This number divided by the time series length determines the spectral resolution of the estimate. The frequency bias within the inner bandwidth is corrected by averaging several eigenspectra from different DPSW weighted time series while adaptively down-weighting the biased spectral energy from higher order windows. The weights are chosen to minimize broad band bias. These wavefunctions were particularly useful for analyzing LFASE data below 1.0 Hz because of the low frequency cutoff filter used in SEABASS.

Data chosen from the LFASE experiment came from twelve 8 minute OBS files, and eight 20 minute and seventy-four 6 minute SEABASS files. Table (3.1) lists the ROSE window index for file time for all of these events. Index numbers for the OBS files are the WHOI conversion of SIO index numbers and show that eight individual 1 minute files were spliced together to make a single continuous file. Similarly, two 10 minute SEABASS files were spliced to make a continuous 20 minute file. All times series were demeaned and the "turn on" transients on the OBS time series were skipped. Spectra from the LFASE time series data were computed by the multiple window method using DPSWs. The spectral analysis code was authored by Alan Chave, (Chave, personal communication, 1993) and was modified to correct for the transfer functions of the LFASE instruments by this author.

The multi-taper method involves weighting the entire time series with a known order DPSW, computing the discrete Fourier transform and averaging the resultant spectrum with other spectra computed using DPSWs of different order. Averaging decreases the variance and improves the spectral estimate.

The spectra in this thesis were calculated in two ways, both involving spherical prolate tapers as the time weighting function. The first and less computationally intensive uses a single $4\pi$-prolate taper averaged over eight overlapping time windows. The eight windows overlap by 15% and are averaged to provide a single spectral es-

timate. The single $4\pi$-prolate taper width provides a spectral resolution of 0.05 $Hz$. A second method of computing spectra employed the use of eight individually calculated eigenspectra using successively higher order prolate tapers. Each of these tapers is applied to the entire time series before the spectra are calculated. These spectra are then averaged to provide an accurate spectral estimate.

One advantage of employing multiple windows and eigenfunction analysis is the ability to exactly characterize the error statistics behind the spectral estimate. The chosen TBW controls the variance estimate of the spectrum. It is useful and occasionally necessary to provide an estimate of the variance of the spectrum in order to give credibility to spectral peaks in a data set. Figure (3.8) shows an example of a SEABASS spectrum (August 19th 12:00 GMT) from the 100 m vertical geophone along with the error estimate. The spectrum was computed with a TBW of 4 (implying, $\frac{4}{360\ sec\ record} = \pm 0.011\ Hz$ resolution) and 8 eigenspectra. We see from Figure (3.8) that the error in the spectrum is not only a function of the frequency. This is due to the frequency dependent adaptive weights of the individual eigenspectra.

### 3.4.3 System Limits

Farrell et al. (1991) and Stephen et al. (1993) have computed transfer functions for the LFASE OBS and SEABASS systems respectively. The amplitude and phase response of both of these instruments is shown in Figure (3.2). The OBS seismometer, which is resonant at 1.0 $Hz$, is much more sensitive to low frequency information than the SEABASS seismometers. For this reason, the SEABASS seismometers and amplifiers are the limiting factors on the low frequency range of the experiment. We now consider the lower frequency limits of the LFASE system sensitivity.

The spectral levels measured by the OBS are reliable below 0.2 $Hz$ but cannot measure absolute power within the noise notch ($0.03 - 0.1\ Hz$) because the power levels in the notch fall below the sensitivity of the instrument in this band. The ability of an instrument to record useful data in a frequency band is a function of

the dynamic range and transfer function of the instrument and the actual level of the "signal" (in our case "microseisms") in that band.

Stephen et al. (1993) give a complete review of the SEABASS technical specifications and number representation. They find that the maximum field values and least significant bit (LSB) recordable by SEABASS are $3.83X10^4$ $nm/s$ and $0.915X10^{-2}$ $nm/s$ respectively (for an assigned 16 bit word). Using this information and the known transfer function of the SEABASS system we can find the low frequency limit of the calculated spectra. The LSB spectral level is calculated by first assuming a fixed gain (the SEABASS system employed a variable gain recording system and we will discuss the effect of this below) and assuming round off errors are uniformly distributed around $\pm$ 1/2 digital count. We further assume the mean is zero and has a variance of 1/12 (see Adair, 1985, page 71). The geophone measures velocity directly and we assume the LSB spectral level is constant in velocity across all frequencies as defined by the equation:

$$S_{LSB} = \frac{\Delta t}{6}(LSB)^2 \tag{3.1}$$

where $\Delta t$ is the time sampling (1/125 sec). $S_{LSB}$ is approximately -69.5 dB rel 1 $(nm/s)^2/Hz$ in velocity (power). The uniform LSB noise in velocity will have a 6 $dB/octave$ slope in acceleration (both velocity and acceleration spectral levels are the same at $f = 1/2\pi$ for a given estimate, so the 6 $dB/octave$ slope pivots around this point).

The SEABASS filters were designed for a passband of 2-50 $Hz$ with a low-frequency filter roll-off at -18 $dB/octave$ below 3.0 $Hz$ in acceleration. The inverse transfer function is applied to LSB noise (i.e. dividing the LSB spectra by the transfer function) resulting in an LSB noise level slope of 18 $db/octave$ below 3.0 $Hz$. This slope is shown in Figure (3.3) as the dash-dot line sloping up between 2.1 and 0.11 $Hz$. This sloping line is plotted for a SEABASS internal gain of 44 $dB$ which is within the gain range of SEABASS of 0 to 66 $dB$. An estimate of the lowest meaningful frequency can be made by assuming that SEABASS levels should not exceed the maximum energy measured by the OBS. This assumption is reasonable

at low frequencies because wavelengths are long enough to be insensitive to small scale heterogeneities near the sea floor.

In Figure (3.3) the OBS and SEABASS 100 $m$ satellite power spectra taken during a relatively quiet period are compared. (Note that the SEABASS spectrum is, on average, 10 $dB$ below the OBS spectrum and that system noise is $\geq$ 10 $dB$ below the SEABASS spectra.) The slope of the SEABASS spectral parallels the LSB noise slope below 0.3 $Hz$ indicating that the SEABASS amplifier is operating on LSB noise. The actual ground acceleration at 0.2 $Hz$ at the sea floor is less than 60 $dB\ rel\ 1\ (nm/s^2)^2/Hz$ (indicated on the OBS Karen spectrum by a "+"). Where the two spectra separate (around 0.3 $Hz$ in Figure 3.3) marks a rough low frequency resolution limit. The lowest frequency of true ambient noise observation must lie between 0.2 and 0.3 $Hz$ for the vertical geophones in SEABASS (assuming the SEABASS gain remains below 44 $dB$).

The coherence and phase relation between vertical channels on SEABASS confirm this resolution limit. In Figure (3.4) the coherence between the SEABASS vertical seismometers at 70 and 100 meters (channels 7 and 10) is shown for a 6 minute noise window on 21 Aug. 02:00:00 GMT. Between 0.2 and 1.0 $Hz$ the coherence is greater than 0.8 and declines rapidly below 0.2 $Hz$ due to the introduction of system noise. Because the coherency calculation is also a biased process, a "zero-significance" line is also included in Figure (3.4). At the 95% confidence level, any coherence lying below this line has no greater significance than a coherence of zero.

Figure (3.5) shows the relative phase between the 10 $m$ and 100 $m$ vertical seismometers. If we assume a shear propagation velocity greater than 50 $m/s$ (a reasonable assumption for the upper 100 $m$ of oceanic sediment at 534B), then the wavelength of ambient noise below 0.5 $Hz$ is greater than the length of the array. Coherent energy below this frequency (and above 0.2 $Hz$) uniformly excites the entire array, making the relative phase between the $10m$ and $100m$ vertical geophones zero degrees. Between 0.7 and 1.0 $Hz$ the signal is less coherent, probably because of higher mode interface waves (Dorman and Schreiner, submitted). At higher frequencies both the vertical coherency and phase do not show evidence of

coherent energy and above 1.0 $Hz$ there seems little relationship between the energy seen at 10 $m$ and that seen at 100 $m$ until approximately 12 $Hz$.

Figures (3.6) and (3.7) show the coherence and phase between two adjacent transverse horizontal geophones at 10 $m$ and 70 $m$ (channels 2 and 8). Like channels 1 and 10, a similar coherency and phase relation is seen. First motion studies for explosive shots show that the orientations of the two horizontals are aligned along the same azimuth (Stephen et al., 1993). The coherency and phase indicates coherent energy between 0.2 and 0.7 $Hz$. Above 0.7 $Hz$, the coherency decreases, indicating the arrival of less coherent and possibly scattered omnidirectional noise. There is a $\pi$ degree phase difference between the two horizontal geophones from 0.7 to 2.0 $Hz$ indicating that the noise seen on the lower satellite is oppositely polarized from the upper satellite.

The presence of a strongly coherent signal and comparison with OBS Karen data show that SEABASS faithfully recorded ambient noise above 0.2 $Hz$ (Bradley and Stephen, 1992). Figure (3.8) shows an example spectrum from the 100 $m$ vertical geophone including the standard error curves. We find for the vertical spectra computed for the SEABASS data, the meaningful band lies between 0.3 and 64 $Hz$. Because of higher ambient noise levels on the horizontal components at low frequencies, the range of meaningful spectral is extended down to 0.2 $Hz$.

### 3.4.4 Particle Motion Analysis

A particle motion polarization algorithm following the methods of Sampson (1977) and Sampson and Olsen (1981) is used to observe the changes in particle motion. The spectral matrix,

$$S(\omega) = \begin{bmatrix} Z_{11} & Z_{12} & Z_{13} \\ Z_{21} & Z_{22} & Z_{23} \\ Z_{31} & Z_{32} & Z_{33} \end{bmatrix} \tag{3.2}$$

is computed where the cross-spectral density $Z_{ij}$ is defined as

$$Z_{ij} = [spectrum(X_i)] \cdot conj[spectrum(X_j)], \tag{3.3}$$

and $X_i$ and $X_j$ are the time series of the $i$ and $j$ component of displacement. Equation ( 3.3) is also known as the Fourier Transform of the cross-covariance function. The degree of coupling between components at a node is dependent on the polarization which can be measured in terms of the trace of $S$ and trace($S^2$) (Samson and Olson, 1981; equation 17):

$$P^2 = \frac{n(trS^2) - (trS)^2}{(n-1)\,(trS)^2}. \tag{3.4}$$

The matrix $S$ has $n$ scalar invariants where $n = 3$ for our three component problem. Equation ( 3.4) is an expression of the linear polarization. The degree of ellipticity or planar nature of the wave is:

$$P_2{}^2 = 1 - \frac{\left[(trS^3) - (\frac{3}{2}trS)(trS^2) + \frac{1}{2}(trS)^3\right]}{(n^{-2} - \frac{3}{2}n^{-1} + \frac{1}{2})\,(trS)^3}. \tag{3.5}$$

A spectral matrix is computed for all of the channels in SEABASS exclusive of the hydrophone channel in satellite 1. The relative orientations of the borehole receivers are computed using explosives and airgun arrivals from the active phase of LFASE (Stephen et al., 1993) in the frequency band 5 to 50 Hz. The computed azimuths of the transverse horizontals are 321°, 156°, 335° and 147° for depths 10m, 40m, 70m and 100m respectively with a standard deviation of less than 5°. (Farrell et al., 1991, reports slightly different azimuths with a maximum discrepancy of 10° in the 100m satellite). Corrections based on these azimuths are applied to align the transverse horizontal components to true North. Polarization versus azimuth is computed for the three satellites that monitor all three axes of motion. The 10m and 100m nodes are well coupled to the well casing. We also compute the polarizations at the 40m node even though the clamping is poor.

## 3.5 Frequency and Particle Motion: Results

The "mean behavior" is the averaged spectra from the entire noise week. Transients and signals that are nonstationary over a period of a few hours are averaged out. Changes in the natural environment are quantified by retaining the individual spectra computed from each noise record. In this study, the temporal history of the noise field suggests that a storm passing through the experiment site was the source of the microseismic field. (The noise history during LFASE is shown in a plot from Stephen et al. (1993) in Figure (3.9). The broad band RMS power levels for the vertical channel in satellite 1 of SEABASS are computed using a 10 second subsample from every minute of the LFASE data set. From this figure, the evolution of LFASE from the active phase (air gun and explosive shots) to the passive phase is marked by the sudden decrease in RMS power (near the 18th of August). Teleseism times from WWSSN files are plotted as triangles near the abscissa; however, none of these events were recorded by the LFASE array.)

This section begins with an overview of the experimental data and then separates the results of the frequency and particle motion analysis into mean and temporal behavior.

### 3.5.1 Mean Noise Behavior with Depth

The mean power spectra and the standard deviation for the vertical acceleration at depths of $10m$, $70m$ and $100m$ were computed by averaging spectra from the seventy-four 360 *second* noise windows from SEABASS (Figure 3.10a,b,c). Each individual spectrum was computed using a single, order zero, $4\pi$ prolate time taper and then averaged over eight overlapping time windows. A single $4/pi$ taper was used to minimize the computation time and eight time windows were chosen to prevent the spectral variance from becoming to large. The spectral variance is shown as the dotted lines in each of the figures. In all three spectra the microseism peak is centered at 0.3 $Hz$.

The one-week OBS spectral mean was computed from twelve 480 *second* time

series using a time bandwidth of 4 and selecting 8 eigenspectra. The resulting spectral resolution is 0.01 $Hz$. The power spectrum and standard deviation for the vertical acceleration are shown in Figure (3.11). The lowest frequency microseism peak is located at 0.3 $Hz$, however higher frequency peaks are seen at 0.75, 1.2 and 2.1 $Hz$. Figure (3.11) also shows the noise notch below 0.2 $Hz$. This "hole" in the ambient noise spectrum marks the transition from infragravity waves whose wavelengths are long enough to directly force the crust ($<$ 0.05 $Hz$ this is Case 1 from Chapter 2) and the microseismic band ($>$ 0.1 $Hz$ i.e. Case 2 and 3 of Chapter 2) where nonlinear wave-wave interaction is acoustically interacting with the crust.

In all four spectra, the mean behavior of the LFASE noise naturally divides into three frequency bands: the microseismic band ($0.2 - 0.75$ $Hz$), a middle frequency band containing higher modes ($0.75 - 2.1$ $Hz$), and the Holu spectrum band ($1.0 - 5.0$ $Hz$). Each of these bands is defined and results from spectral and particle motion calculations discussed separately below.

**Frequency Band:** $0.2 - 0.75$ $Hz$

The noise week spectra from KAREN and SEABASS are plotted in Figure (3.12). In the upper plot are shown the RMS horizontal components at 0 $m$ (OBS), 10 $m$, 70 $m$ and 100 $m$ depth. The lower plot shows the vertical components from the same depths. The most significant low frequency feature is the microseism peak at 0.3 $Hz$. The horizontal spectra ($MS \approx$ 75 $dB$ $rel$ 1 $(nm/s^2)^2/Hz$) are 10 $dB$ "louder" than the vertical spectra ($MS \approx$ 65 $dB$ $rel$ 1 $(nm/s^2)^2/Hz$). For this reason the microseism peak is much better defined by the horizontal spectra. Over the $100m$ length of the array, the power level of this peak varies less than 2 $dB$ in the horizontal component and less than 1 $dB$ in the vertical component spectra. Above the microseism peak the spectra begin to show depth dependence. In this band, the OBS and $10m$ node show similar levels on both the horizontal and vertical components. The horizontal spectra at 70 and $100m$ are up to 15 dB quieter below 0.75 $Hz$. In contrast, the vertical spectra in this band show about a 5 $dB$ decrease in the upper $100m$. Both plots in Figure (3.12) show increasing complexity at higher

frequencies. We will return to the spectra on this figure repeatedly in this section.

**Frequency Band:** 0.75 – 2.1 $Hz$

A group of peaks located near 0.75 $Hz$, 1.2 $Hz$, and 2.1 $Hz$ are clearly observed in the vertical spectra. These peaks seem to rise above the mean spectral level in this frequency band as narrow band "humps" or broad peaks. They are different in character from the line sources, such as ship prop noise, that occur at higher frequencies. We identify these peaks as higher modes.

The frequency peaks seen in the spectral analysis behave differently than the microseism peak. On the horizontal channels, the OBS and 10 $m$ SEABASS satellite have similar spectral energy up to 1.0 $Hz$ and the lower SEABASS satellites show very little evidence of the mode humps at 100$m$ depth. On the vertical spectra the noise humps do not appear at 70 or 100$m$ depth. One other feature of the higher modes is the frequency shift of the peaks with depth. As an example, the cluster of peaks near 2.0 $Hz$ seen on the OBS horizontal data shift upward to near 2.5 $Hz$ at 10$m$ depth.

The background noise level in this band above 1.0 $Hz$ and beyond this band up to 5.0 $Hz$ commonly reaches a saturation state during high seas. This band is discussed below.

**Frequency Band** 1.0 – 5.0 $Hz$

The OBS and SEABASS spectra (Figures 3.10a,b,c and 3.11) decrease by -14 $dB$/octave between 1.0 $Hz$ and 5.0 $Hz$. This slope is consistent with previous measurements from the OSS IV (-17 $dB$/octave) by Duennebier et al. (1986) and from the MSS (-15 $dB$/octave) reported by Adair (1985). This frequency band has recently been coined the "Holu spectrum" (from the Hawaiian word for deep ocean) by McCreery et al. (1993). They argue that within this band the spectrum is often saturated. Surface gravity waves at $\approx$ 1 $Hz$ have a phase velocity of 1.6 $m/s$. Winds over most of the ocean, where the fetch is long and the seas have a chance to build, travel

at this velocity or greater (Phillips, 1977). As a result the gravity wave spectrum in this band is usually over driven or saturated by the wind and the measured ambient noise in water column is also commonly saturated.

Within the Holu band the spectral slope is determined by sea state directly over the instrument. In the following section the behavior of the Holu spectrum is correlated with the local sea state.

### 3.5.2 Temporal Trends in the Noise over One Week

Figure (3.13) (from Stephen, et al., 1993) shows the response of the vertical, transverse and radial horizontals at 100 m depth during the passive recording period of LFASE. The spectra are computed on 5 minutes of data taken from the seventy-four 360 $s$ and eight 1200 $s$ windows. An average is then computed in one third octave bands around discrete frequencies (at 1, 2, 4, 8, 16, and 32 $Hz$). From the spectra we see that horizontal components contain more energy than vertical components by about 5-10 $dB$. There is also a hump in the 1.0 and 2.0 $Hz$ RMS power of $\approx$10 dB that begins on the 19th of August, peaks on the 21st, then decays to previous levels by the 23rd. Shipping noise is apparent as isolated line spectra only above 4.0 Hz and is therefore not of primary interest in this study.

A time history of spectra for the transverse horizontal component from OBS Karen is shown in Figure (3.14) between 0.05 and 4.0 $Hz$ for the noise week. The colors indicate power spectral density in $dB\ rel\ 1(nm/s^2)^2/Hz$ from $\sim$ 52 $dB$ (below 0.3 $Hz$ - green) to $\sim$ 80 $dB$ (between Aug 21 - 22 at 0.7 $Hz$ - pink). The data show the resolution of the noise notch at 0.1 $Hz$ and the presence of a high noise band between August 20th and August 22nd (with a maximum of 79 $dB$ at 1 $Hz$ on the 21st). (The absolute levels within the notch may fall below the resolution of the instrument and we observed a rapid rise in power below 0.1 $Hz$ due to the amplification of system noise when deconvolving the instrument transfer function (see section 3.4.3)).

The color meshplots shown in Figures (3.15) - (3.17) show time histories of

spectra for the SEABASS data. The spectra were computed on the transverse horizontal geophones using a zero order $4\pi$ prolate taper and an 80 *sec* time window. The horizontal components were chosen for display because they have a greater dynamic range and will more easily resolve low frequency information above the system noise.

These figures show the temporal change of the 74 noise windows from August 17th to August 25th between 0.16 and 4.0 $Hz$ for nodes at 10, 70 and 100$m$ depth. On August 21, the microseism energy reaches a maximum of 75 $dB$, at a frequency of 0.3 $Hz$ on all the horizontal channels at 70 and 100$m$ depth. At 10$m$, higher modes above 0.6 $Hz$ exceeds the energy at 0.3 $Hz$ as for the OBS. Below 2.0 $Hz$, there is a broad rise in power leading up to the peak on the 21st of August. In the 10 $m$ satellite (Figure 3.15), the average noise levels between 0.2 and 0.3 Hz are great enough to be sensed above system noise, thereby defining the lower frequency limit of the microseism peak in the borehole. The peak is well resolved in the borehole as a band of high energy at 0.3 $Hz$.

Between 0.5 and 1.0 Hz noise levels also peak between the 19nd and 23th of August. This "hump" is believed to be short wavelength higher mode Stoneley wave energy and will be discussed later.

All four meshplots for KAREN and SEABASS nodes at 10, 70 and 100$m$ show a several day rise and fall in power below 4.0 $Hz$ between the 19th and 23th of August. The most significant peak in the 70 and 100 m transverse horizontals is the 0.3 Hz microseism peak. The most significant peak on KAREN and the 10$m$ satellite is between 0.5 and 1.0 $Hz$. Throughout the noise phase the microseism peak remained a consistent peak near 65 $dB$ (for vertical components) and 75 $dB$ (for horizontal components). Above the microseism peak the spectra show a preferential excitation of different higher modes with depth. This is most easily seen in the meshplots at 1.2 and 2.0 $Hz$.

### Correlation with Buoy and GSOWM (0.2 – 4.0 $Hz$)

The temporal behavior of the LFASE spectra is correlated with the sea state at the site. Below we present and analyze buoy and ocean wave modeling data collected near the experiment site.

Wave spectral energy during LFASE was computed from data obtained at a NOAA waverider Buoy (41006). The buoy is moored in 1000 $m$ of water and is located within 180 $km$ of the LFASE site (see Figure 3.1). The buoy wave spectral energy measurements are plotted in Figure (3.18) at 48 discrete frequencies ranging from 0.03 $Hz$ to 0.5 $Hz$. A very strong wave set, consisting of both locally generated wind waves and distant swell, occurs in the region beginning on the 20th of August. Local growth of wave energy is evident in the buoy data (Figure 3.18). Initially the peak wave energy is near 0.15 $Hz$ on 19 August. As the wave set establishes itself, the process of local growth shows the peak energy increasing and shifting downward below 0.1 $Hz$ by mid-day on the 20th.

In addition to local growth, there is distant swell arriving at the buoy. The swell's energy dispersion across the buoy is used to computed the distance from the oceanic swell source. A rough distance calculation can be made as follows. The group velocity of oceanic gravity waves in deep water is:

$$c_g = \frac{g}{2\sigma}, \tag{3.6}$$

where $g$ is the acceleration of gravity and $\sigma$ the wave frequency. The distance from the source can be computed from the relation, $\frac{\partial \sigma}{\partial t} = \frac{\sigma c_g}{L}$, where $L$ is the propagation distance. Substituting the measured change in time $\Delta t$ and shift in dominant frequency, $\Delta\sigma$, the source distance is defined as

$$L = \frac{\Delta t\, g}{2\Delta\sigma}. \tag{3.7}$$

A positive spectral slope ($\frac{\Delta t}{\Delta \sigma} > 0$) in the buoy data prior to the large wave set arrival on August 18th and the frequency and time shift was graphically measured on a subset of the data shown in Figure (3.18). Measuring $\Delta\sigma$ to be 0.2 $Hz$ over a time period, $\Delta t$, of 86400 $s$ (one day), the source distance for the swell is approximately

2100 $km$. This distant swell observed at Site 534 may originate from a storm that was observed in the Eastern Atlantic that generated 0.1 $Hz$ to 0.06 $Hz$ waves (storm information from the National Hurricane Center). Although energy can propagate from the storm to the LFASE site as swell (long period surface gravity waves) or seismo-acoustically (modes coupled to the storm at the storm site), our observations are consistent with the former propagation mechanism. In general, the LFASE seismometers did not register changes in noise level that correlate with changes in the distant swell.

Figure (3.19a) is a graytone plot of the wave spectral energy shown in Figure (3.18). Companion graytone plots of the SEABASS transverse horizontal at 10 $m$ and 70 $m$ between 0.1 $Hz$ and 1.0 $Hz$ are shown in Figures (3.19b,c). The SEABASS spectra are plotted to twice the frequency range of the buoy spectra in order to detect evidence of the frequency doubling effect from nonlinear wave-wave interaction at the ocean surface. For each plot, the lightest shades indicate the maximum spectral energy and the darkest shades the minimum. The range in amplitudes is different for each graytone plot (3.19a: range = dark→light [0 - 8 $m^2/Hz$]; 3.19b: range = dark→light [60 - 85 $dB\ rel\ 1\ (nm/s^2)^2/Hz$]; 3.19c: range = dark→light [55 - 80 $dB\ rel\ 1\ (nm/s^2)^2/Hz$]). In each data set there is an initial onset of band-limited energy rising from the 19th of August to peak on the 21st. Buoy 41006 recorded the greatest wave energy between 0.1 and 0.2 $Hz$ through the entire noise window from the 18th through the 26th of August. During the rise in oceanic gravity wave energy, SEABASS records a similar rise in the band around 0.3 $Hz$ and at higher modes between 0.5 and 0.8 $Hz$. Closer analysis of the correlation of maximum energy between the buoy and borehole array shows the peak energy arrives at the borehole 2 to 4 hours before it arrives at the buoy. The lag time between the LFASE site and the buoy is partially explained by the travel time for ocean gravity waves at 30-20 km/hr (for $0.1 - 0.15\ Hz$ waves) traveling eastward between the site and the buoy (which is approximately 150 $km$ East and 100 $km$ North of the borehole).

The development of the storm center arriving on August 21st was also tracked by the GSOWM wind and wave height model data. Comparing the numerical modeling

data with the buoy data, we find the significant wave height estimates are within 0.1 meters of the buoy observations. Figures (3.20a,b) show contours of the wave height and frequency from the GSOWM model computed at the five closest grid points to the experiment (see Figure 3.1) from August 17th through the 26th. In addition to the contours, the relative wind vectors are shown; these wind vectors give a first order estimate of the wave direction (Clancy, 1986). At the latitude of the borehole (28.4° N) the wind velocity increases beginning on the 19th of August and continues to grow until the 21st. Commensurate with the change in wind velocity is an increase in the wave height and a decrease in wave frequency.

Since the microseism peak maintains a uniform energy whether measured at the sea floor or 100 $m$ below, the modes exciting it must have wavelengths greater than the array length. In Figure (3.20b) the frequency of the dominant swell is plotted from the GSOWM data. The wave energy is greatest at $0.1 - 0.15$ $Hz$ and given the deep water dispersion relation, $\sigma^2 = g\ k$, the gravity wavelength is between 156 and 69 $m$. These wavelengths are far too small to be sensed in deep water and this argues against direct loading as a source for the microseisms. The correlation of sea wave spectral energy near 0.15 $Hz$ within 200 $km$ of Hole 534B and the seismic energy at 0.3 $Hz$ observed within the borehole agrees with Longuet-Higgins theory. The microseisms are due to nonlinearly interacting gravity waves at a frequency of $\sigma$ which generate a second order acoustic force on the ocean crust at a frequency of $2\sigma$. Because the buoy, GSOWM and the borehole data have nearly synchronous behavior, we conclude that below 5.0 $Hz$, the crust is forced by the local sea state which rose due to the storm.

### The "Holu Spectrum" (1.5 – 5.0 $Hz$)

A subsampled and locally averaged version of the data shown in Figures (3.10) and (3.11) is displayed in Figures (3.21a,b,c). OBS windows taken from the peak noise period in the experiment (August 21st) and then from the three following days are plotted as different symbols. Local averaging over $\pm 5\ \Delta f$ around each plotted point is done to smooth frequency spikes.

The waning of the saturation spectrum or "Holu spectrum" can be traced as the spectral slope decreases from a maximum of -21 $dB$/octave on the 21st to average background levels of -12 $dB$/octave by the 24th of August. This saturation behavior is in agreement with that found by McCreery et al. (1993), using the Wake Island Hydrophone Array. They found a saturation spectrum of $\sim -20$ $dB$/octave and that lower frequencies saturate with increasing sea state. We also find that the saturation frequency limit moves down with increasing sea state. Above 5.0 $Hz$, a separate process is generating the noise since the daily spectra become widely separated again. Previous authors suggest that local wave breaking, shipping, biologic and industrial sources dominate in this band (Urick, 1986).

Figures (3.21b) - (3.21c) display spectra from the vertical geophones at 10 and 100$m$ depth. The data is subsampled and locally averaged as previously described. Below 1.0 Hz the daily spectra decay consistently with time away from the 21st of August. The spectrum is saturated for all the satellites between 1.0 and 5.0 Hz on the 21st and 22nd with a slope of -17 $dB$/octave. The spectral saturation slopes seen in the LFASE borehole data match those found by Duennebier et al., (1986) who found a -17 $dB$/octave spectral saturation slope on the OSS IV data from Hole 581C.

### 3.5.3 Particle Motion: Results and Discussion

The particle motion of the noise at Site 534B is not well aligned along any particular azimuth above 1.0 $Hz$. We conclude therefore that the energy above 1.0 $Hz$ is either scattered by local heterogeneities and/or generated by diffuse sources. However below 1.0 $Hz$ the microseismic noise is polarized and its polarization is affected by local sea state. The LFASE borehole polarization showed different behavior in two bands: 0.3 - 0.4 $Hz$ and 0.6 - 1.0 $Hz$. The first band contains the microseism peak and the second the first higher mode described earlier. The two frequency bands are analyzed separately using the method of Samson, (1980) (section 3.4.4). Finally, a dispersion curve for the LFASE data is computed based on a geophysical model of

the LFASE sediments.

The azimuths of the transverse horizontals are 321°, 156°, 335° and 147° for nodes at 10, 40, 70 and 100$m$ respectively. Corrections based on these azimuths are applied to align the transverse horizontal components to true North. Energy and polarization versus azimuth were computed for the three satellites that monitored all three axes of motion. On August 18th, before the storm, the time series shows omnidirectional energy (Figure 3.22a). In contrast, on the 21st of August during the local storm, the energy is maximized between 45 and 80 degrees. SEABASS particle motion during the noise peak is computed for a sagital plane striking 75 degrees and plotted in Figure (3.23). Most notable from the figure is the reversal of particle motion with depth. For a wave arriving from 75 degrees East of North, the rotation is retrograde elliptic at 10 $m$ and reverses to prograde elliptic at 100 $m$ for $\approx$ 0.8 $Hz$ energy. Models of interface wave modes over soft oceanic sediments (Schreiner and Dorman, 1993; Sauter et al., 1986) show that zero crossings occur at different depths for different surface wave modes. (We note here that although the node at 40$m$ depth was unclamped, it seems to have meaningful integrated displacement energy and polarization below 1.0 $Hz$).

Linear and elliptic polarizations were computed for the ambient noise from SEABASS after low pass filtering below 1.0 Hz. Nodes at 10 and 100$m$ depth are considered. Representative samples for the two frequency bands 0.3 - 0.4 and 0.6 - 0.8 $Hz$ are shown in Figures (3.24) and (3.25) for periods before, during and after the storm (a,b,c). The diagrams on the left illustrate the dominant azimuth of the sagital plane of polarization over a finite bandwidth. The vectors point in the direction from which energy is greatest. Their components are ($\omega$, $\theta$) where $\theta$ is the azimuthal angle with respect to East and $\omega$ is a discrete frequency. The polarization diagrams are weighted by the value of $P^2(\omega)$ (equation 3.4) which ranges from 0 to 1. The polar region is subdivided into 40 histogram bins and the rose diagrams on the right show the number of vectors falling within an azimuthal "pie-slice". Combined, the information in the left and right columns illustrates the degree of polarization and the directivity of noise in the two frequency bands.

Figures (3.24a,b,c) are polarizations computed near the microseism peak, 0.3 - 0.4 $Hz$, for noise records before, during and after the local storm. The polarization is strongly biased in the south east direction for the "PRE-STORM" and "POST-STORM" diagrams. During the storm peak the polarization is more varied with energy from the north and northeast. The 100 $m$ satellite appears to be less sensitive to the changes in sea state.

At higher frequency, the polarization results from 0.6 - 0.8 $Hz$ in Figure (3.25a,c) show a strong southeastern bias in the "PRE-" and "POST-STORM" diagrams similar too the 0.3 - 0.4 $Hz$ band. This bias is aligned with the dominant swell direction computed by the GSOWM model. Data from the storm peak period does not show this same alignment. Unlike the 0.3 - 0.4 $Hz$ band, the "STORM-PEAK" diagram indicates that most of the energy at the array is polarized northeast. Both the 100 $m$ and 10 $m$ satellites show this polarization.

This reaction to the local sea state could have two sources. The first is that the surface gravity wave spectrum becomes more omnidirectional as the sea state increases thus generating a more omnidirectional incident field. The second is that as the source field is increased, the potential for scattering from surface and volume heterogeneities in the crust is increased. If energy at 0.6 - 0.8 $Hz$ is short wavelength, as would be the case for Love and Stoneley waves at the interface, then scattering would explain the differences between the 10 and 100 $m$ satellites.

The particle motion polarization studies show the same division in the spectrum that the power spectral density analysis revealed. The ambient noise field between 0.2 $Hz$ and 1.0 $Hz$ responded directly to the presence of a storm in the vicinity of 534B. Higher amplitudes were recorded and strong polarizations were seen corresponding to the changing wind and wave direction. Dominant particle motion was elliptical and aligned in the direction of the swell between 0.3 and 0.4 $Hz$ and rotated with respect to the swell between 0.6 and 0.8 $Hz$. .

## 3.6 Conclusions

We have examined ambient noise spectra from LFASE in the band 0.2 - 5.0 $Hz$. Definite conclusions about the propagation and source of the observed LFASE noise were made by looking at 1) the one week average spectral levels seen on all components in both ocean bottom and sub-bottom instruments during the entire noise recording period of LFASE; and 2) by distinguishing the time dependent changes in the spectra. We conclude this chapter by reiterating the main points listed in the introduction and adding a few others:

- The low frequency noise system limits of the SEABASS borehole tool were determined to be 0.3 $Hz$ and 0.2 $Hz$ on the vertical and horizontal components respectively. This instrument is the first borehole array to simultaneously observe microseism behavior at several depths below the sea floor.

- The microseism peak at 0.3 $Hz$, has a nearly constant energy with depth, maintaining a vertical acceleration power level near 65 $dB\ rel\ 1\ (nm/s^2)^2/Hz$ and an RMS horizontal ($\sqrt{transverse^2 + radial^2}$) power level of 75 $dB\ \ rel\ 1\ (nm/s^2)^2/Hz$. The average value of the microseism peak over the "noise week" varied less than 2 $dB$ between the sea floor OBS and the SEABASS sensor 100 $m$ below the sea floor. The microseism energy rose 10 $dB$ during the passage of a local storm with some indication of a lowering of the microseism peak frequency with increased sea state.

- In general, there is a monotonic decrease in noise energy with depth between 0.8 and 15 $Hz$. In this band the average vertical and horizontal spectral energy drops 10 and 15 $dB$ respectively over the length of the array.

- In the band between 0.3 and 0.4 $Hz$, the ratio of the vertical/RMS-horizontal components remains fixed with depth, indicative of a single long wavelength mode. At higher frequencies the particle motion ratio is variable with depth, a feature consistent with the presence of higher order interface and wave guided

modes. We also find similar horizontal noise levels on both the sea floor OBS and the $10m$ SEABASS geophone. This indicates that high amplitudes commonly observed on the horizontal components of OBS's located on soft bottoms are real and not necessarily due to poor coupling.

- Several other narrow bandwidth "modes" or features in the LFASE data are also associated with the local sea state. These modes, which are not simple line spectra, have energy centered near 0.75, 1.2, and 2.1 $Hz$. Unlike the microseism peak, the modes are depth dependent. Vertical power levels of the 0.75 $Hz$ mode average 68 $dB$ at the sea floor and decay rapidly with depth to $<$ 60 $dB$ at 100 $m$ below the sea floor.

- Particle motion in the subsurface is dominantly elliptically polarized between 0.3 and 1.0 $Hz$ and is sub-parallel with the local surface gravity wave swell. Particle motion behavior with depth supports the theory of short wavelength Stoneley waves excited in the crust. Deep, soft sediments at the site limit the propagation mode to be Stoneley waves between 0.3 and 15 $Hz$.

- The Holu spectrum at the upper end of the microseism band seems to saturate at -15 to -17 $dB$/octave between 1.0 and 5.0 Hz. This spectral slope agrees with that found by Duennebier et al. (1986) for the OSS IV in DSDP Hole 581C.

- Mean noise levels at Hole 534B are comparable to those found at several oceanic sites. Figure (3.26) compares Karen and SEABASS power spectra with noise levels measured by a GURALP seismometer off the Oregon Coast in an ocean depth of 620 m ("The ULF/VLF Experiment" Duennebier, personal communication). The microseism peak for LFASE is around 0.3 Hz and peaks at 65 dB rel 1 $(nm/s^2)^2/Hz$ for the vertical component. The peak found by Duennebier is at 0.2 $Hz$ and the level is much higher at 90 $dB$. The differences between the two noise experiments may be due to the smaller fetch, and generally higher frequency lower energy swell in the North Atlantic. Anoth-

er possibility is that long wavelength normal mode Rayleigh waves are not excited in the Blake Bahama Basin due to the deep soft bottom sediments.

- Comparison of the SEABASS data with the surface gravity wave spectra show that the local swell is the primary noise source below 1.0 Hz down to the system resolution at 0.2 Hz. Detailed analysis of the spectra, particle motion and dispersion of the observed microseisms verify previous theories that propose interface wave Rayleigh/Stoneley modes as the propagation mechanism for microseisms.

- Perhaps the most significant conclusion from this chapter is the quantification of very low-frequency noise with depth below the sea floor. LFASE is the first experiment to measure VLF noise at several depths below the sea floor simultaneously. A strong monotonic decrease with depth was found for the average noise level over a one week period. These measurements suggest a quieter environment should exist in the borehole than on the sea floor for seismometers at frequencies from 0.3 - 5.0 $Hz$.

Table 3.1 Long Period Shot Files

| Instrument | ROSE window index | Time (GMT) dd:hh:mm:ss | Length (Min) | OBS/SEABASS overlap |
|---|---|---|---|---|
| OBS "KAREN" | 0071-079 | 18:00:00:00 | 8.0 | Y |
| | 0082-089 | 19:00:00:00 | 8.0 | Y |
| | 0092-099 | 19:12:00:00 | 8.0 | Y |
| | 0102-109 | 20:12:00:00 | 8.0 | Y |
| | 0112-119 | 21:00:00:00 | 8.0 | |
| | 0122-129 | 21:12:00:00 | 8.0 | Y |
| | 0132-139 | 22:00:00:00 | 8.0 | Y |
| | 0142-149 | 22:12:00:00 | 8.0 | Y |
| | 0152-159 | 23:00:00:00 | 8.0 | Y |
| | 0162-169 | 23:12:00:00 | 8.0 | Y |
| | 0172-179 | 24:00:00:00 | 8.0 | Y |
| | 0182-189 | 25:04:00:00 | 8.0 | Y |
| SEABASS | 4845-4846 | 18:02:00:02 | 20.0 | |
| | 4868-4869 | 18:04:00:02 | 20.0 | |
| | 4891-4892 | 18:06:00:02 | 20.0 | |
| | 4914-4915 | 18:08:00:02 | 20.0 | |
| | 4937-4938 | 18:10:00:02 | 20.0 | |
| | 4960-4961 | 18:12:00:02 | 20.0 | |
| | 4983-4984 | 18:14:00:02 | 20.0 | |
| | 5006-5007 | 18:16:00:02 | 20.0 | |

| Instrument | ROSE Shot | Time (GMT) dd:hh:mm:ss | Length (Min) | OBS/SEABASS overlap |
|---|---|---|---|---|
| SEABASS | 4801-4801 | 17:22:00:02 | 6.0 | |
| | 4823-4823 | 18:00:00:02 | 6.0 | Y |
| | 4857-4857 | 18:03:00:02 | 6.0 | |
| | 4880-4880 | 18:05:00:02 | 6.0 | |
| | 4903-4903 | 18:07:00:02 | 6.0 | |
| | 4926-4926 | 18:09:00:02 | 6.0 | |
| | 4949-4949 | 18:11:00:02 | 6.0 | |
| | 4972-4972 | 18:13:00:02 | 6.0 | |
| | 4995-4995 | 18:15:00:02 | 6.0 | |
| | 5018-5018 | 18:17:00:02 | 6.0 | |
| | 5029-5029 | 18:18:00:02 | 6.0 | |
| | 5051-5051 | 18:20:00:02 | 6.0 | |
| | 5073-5073 | 18:22:00:02 | 6.0 | |
| | 5095-5095 | 19:00:00:02 | 6.0 | Y |
| | 5117-5117 | 19:02:00:02 | 6.0 | |
| | 5139-5139 | 19:04:00:02 | 6.0 | |
| | 5161-5161 | 19:06:00:02 | 6.0 | |
| | 5183-5183 | 19:08:00:02 | 6.0 | |
| | 5205-5205 | 19:10:00:02 | 6.0 | |
| | 5227-5227 | 19:12:00:02 | 6.0 | Y |
| | 5249-5249 | 19:14:00:02 | 6.0 | |
| | 5271-5271 | 19:16:00:02 | 6.0 | |
| | 5293-5293 | 19:18:00:02 | 6.0 | |
| | 5315-5315 | 19:20:00:02 | 6.0 | |
| | 5348-5348 | 20:02:00:02 | 6.0 | |

| Instrument | ROSE Shot | Time (GMT) dd:hh:mm:ss | Length (Min) | OBS/SEABASS overlap |
|---|---|---|---|---|
| SEABASS | 5370-5370 | 20:04:00:02 | 6.0 | |
| | 5392-5392 | 20:06:00:02 | 6.0 | |
| | 5414-5414 | 20:08:00:02 | 6.0 | |
| | 5436-5436 | 20:10:00:02 | 6.0 | |
| | 5458-5458 | 20:12:00:02 | 6.0 | Y |
| | 5480-5480 | 20:14:00:02 | 6.0 | |
| | 5502-5502 | 20:16:00:02 | 6.0 | |
| | 5524-5524 | 20:18:00:02 | 6.0 | |
| | 5546-5546 | 20:20:00:02 | 6.0 | |
| | 5568-5568 | 20:22:00:02 | 6.0 | |
| | 5590-5590 | 21:02:00:02 | 6.0 | |
| | 5612-5612 | 21:04:00:02 | 6.0 | |
| | 5634-5634 | 21:06:00:02 | 6.0 | |
| | 5656-5656 | 21:08:00:02 | 6.0 | |
| | 5678-5678 | 21:10:00:02 | 6.0 | |
| | 5700-5700 | 21:12:00:02 | 6.0 | Y |
| | 5722-5722 | 21:14:00:02 | 6.0 | |
| | 5744-5744 | 21:16:00:02 | 6.0 | |
| | 5766-5766 | 21:18:00:02 | 6.0 | |
| | 5788-5788 | 21:20:00:02 | 6.0 | |
| | 5810-5810 | 21:22:00:02 | 6.0 | |
| | 5832-5832 | 22:00:00:02 | 6.0 | Y |
| | 5854-5854 | 22:02:00:02 | 6.0 | |
| | 5876-5876 | 22:04:00:02 | 6.0 | |
| | 5898-5898 | 22:06:00:02 | 6.0 | |

| Instrument | ROSE Shot | Time (GMT) dd:hh:mm:ss | Length (Min) | OBS/SEABASS overlap |
|---|---|---|---|---|
| SEABASS | 5920-5920 | 22:08:00:02 | 6.0 | |
| | 5942-5942 | 22:10:00:02 | 6.0 | |
| | 5964-5964 | 22:12:00:02 | 6.0 | Y |
| | 5986-5986 | 22:14:00:02 | 6.0 | |
| | 6008-6008 | 22:16:00:02 | 6.0 | |
| | 6030-6030 | 22:18:00:02 | 6.0 | |
| | 6052-6052 | 22:20:00:02 | 6.0 | |
| | 6074-6074 | 22:22:00:02 | 6.0 | |
| | 6096-6096 | 23:00:00:02 | 6.0 | Y |
| | 6118-6118 | 23:02:00:02 | 6.0 | |
| | 6140-6140 | 23:04:00:02 | 6.0 | |
| | 6162-6162 | 23:06:00:02 | 6.0 | |
| | 6184-6184 | 23:08:00:02 | 6.0 | |
| | 6206-6206 | 23:10:00:02 | 6.0 | |
| | 6228-6228 | 23:12:00:02 | 6.0 | Y |
| | 6250-6250 | 23:14:00:02 | 6.0 | |
| | 6272-6272 | 23:16:00:02 | 6.0 | |
| | 6294-6294 | 23:18:00:02 | 6.0 | |
| | 6316-6316 | 23:20:00:02 | 6.0 | |
| | 6338-6338 | 23:22:00:02 | 6.0 | |
| | 6360-6360 | 24:00:00:02 | 6.0 | Y |
| | 6382-6382 | 24:02:00:02 | 6.0 | |
| | 6404-6404 | 24:04:00:02 | 6.0 | |
| | 6437-6437 | 25:04:00:02 | 6.0 | Y |

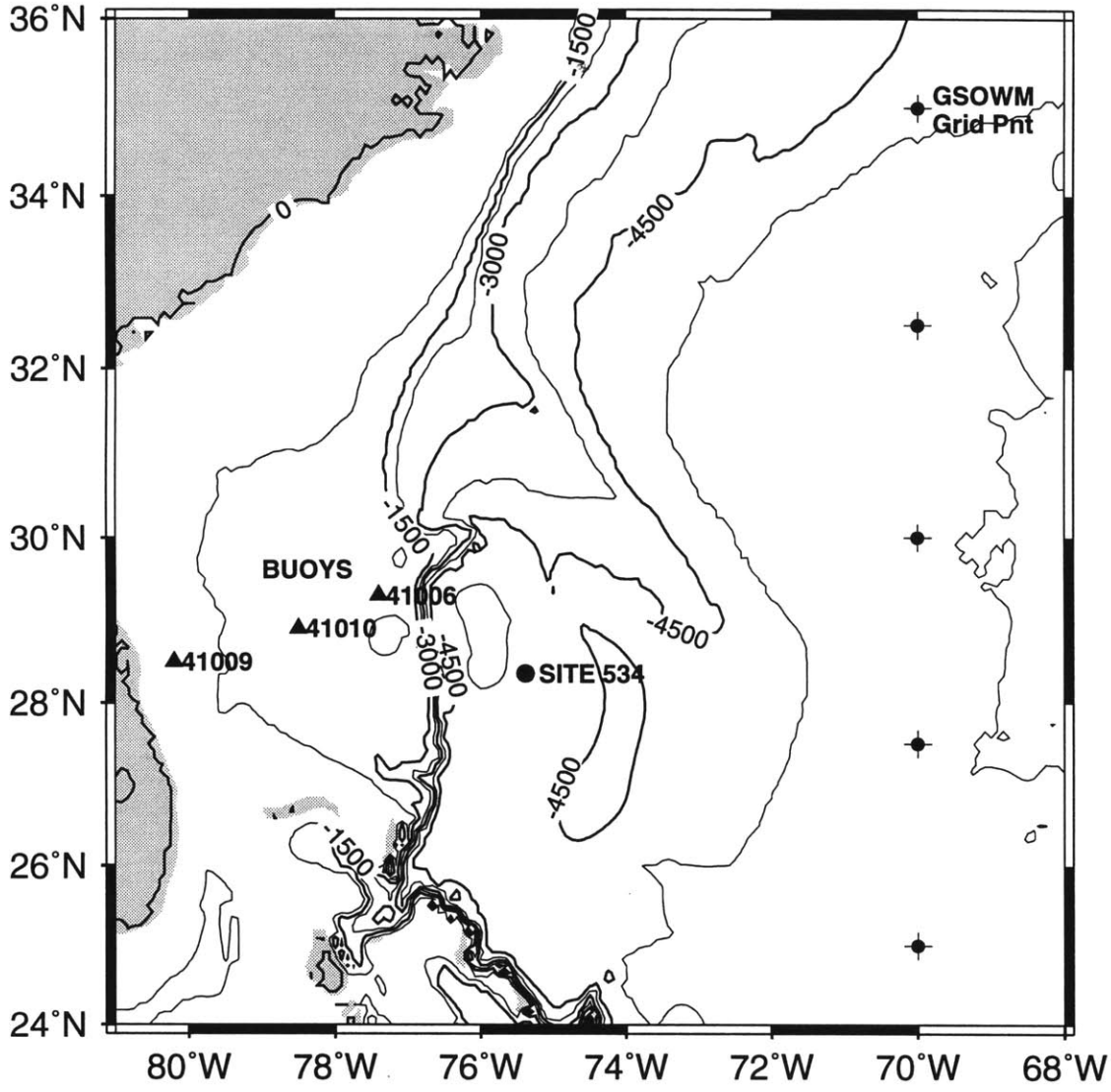


Figure 3-1: Location map of Sites 534. The NOAA wave-rider buoy locations are labeled as black triangles and GSOWM grid point locations nearest to the experiment are marked as crosses with black centers.

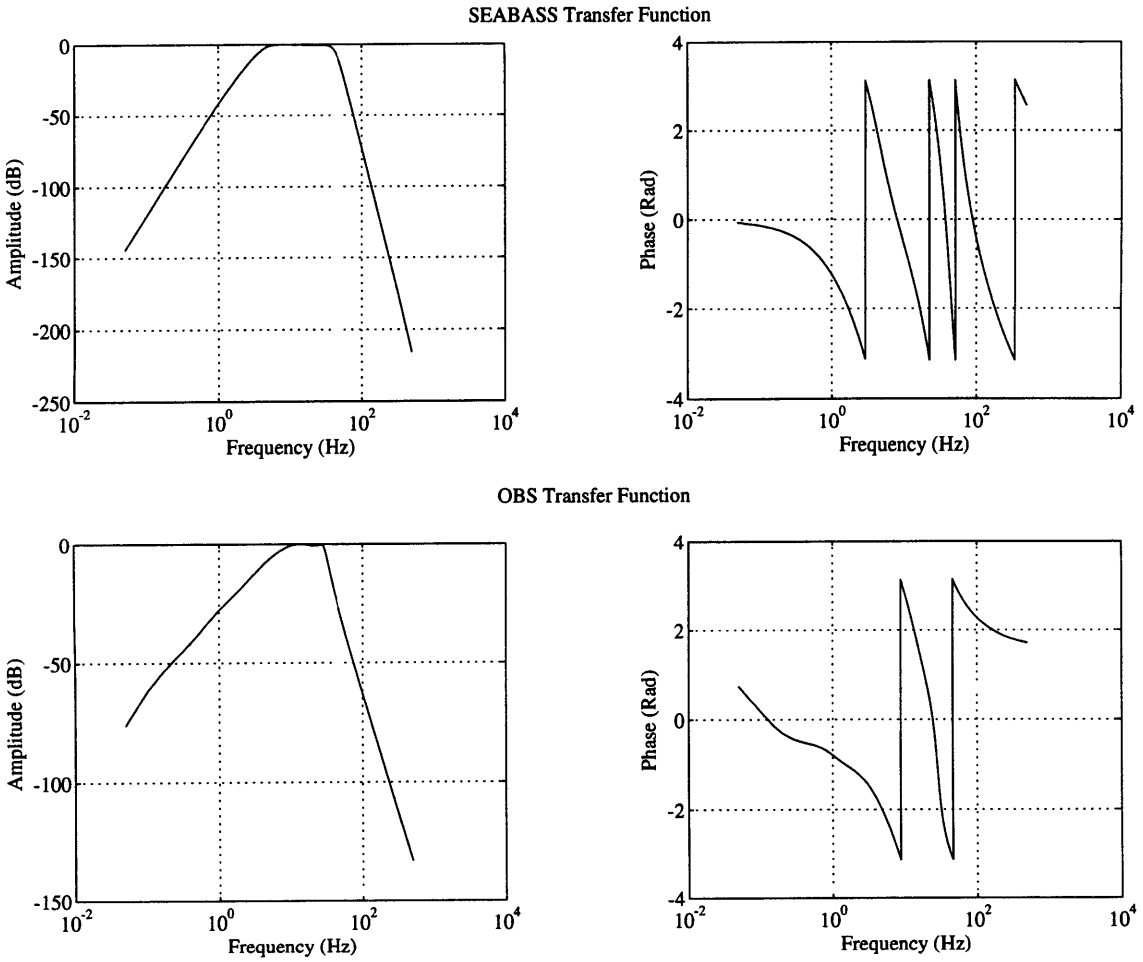


Figure 3-2: SEABASS and OBS amplitude and phase response curves. Note that the amplitude scales differ between the two transfer function plots.

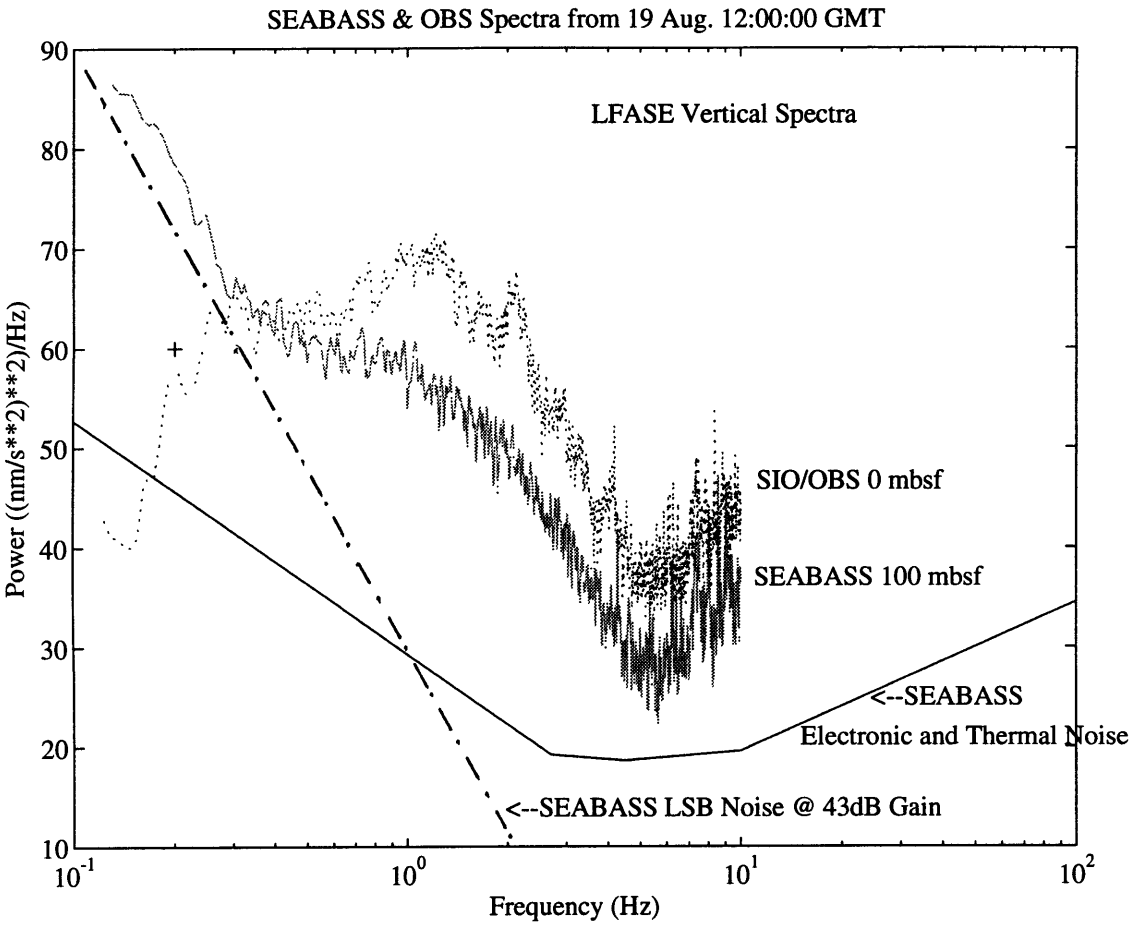


Figure 3-3: LFASE acceleration spectra from OBS "KAREN" and SEABASS. OBS spectrum plotted as a dotted line. Theoretical thermal and electronic noise for SEABASS plotted as solid line segments. The inverse transfer function curve for SEABASS is plotted as the dash-dot line and an example SEABASS spectrum calculation is the solid spectrum. Both spectra are computed using a TBW of 4 with eight eigenfunction spectra windows. 360 and 420 seconds of data were used to compute the SEABASS and OBS spectra respectively.

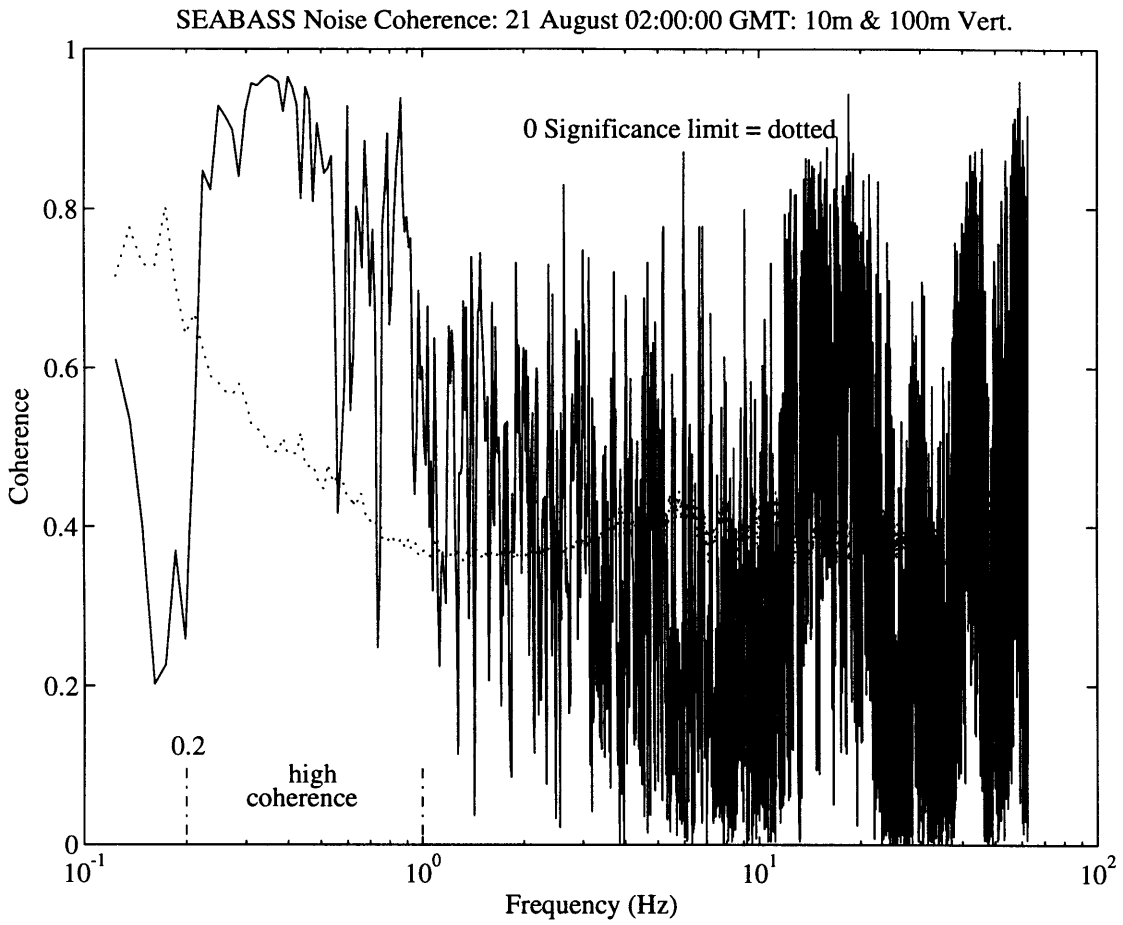


Figure 3-4: LFASE SEABASS coherency spectrum computed with a TBW of 4 and eight eigenspectra. Noise window taken 19 August 12:00:02 GMT. Coherency was computed for the 10 m and 100 m vertical channels. The 95% significance level is indicated as the dotted line.

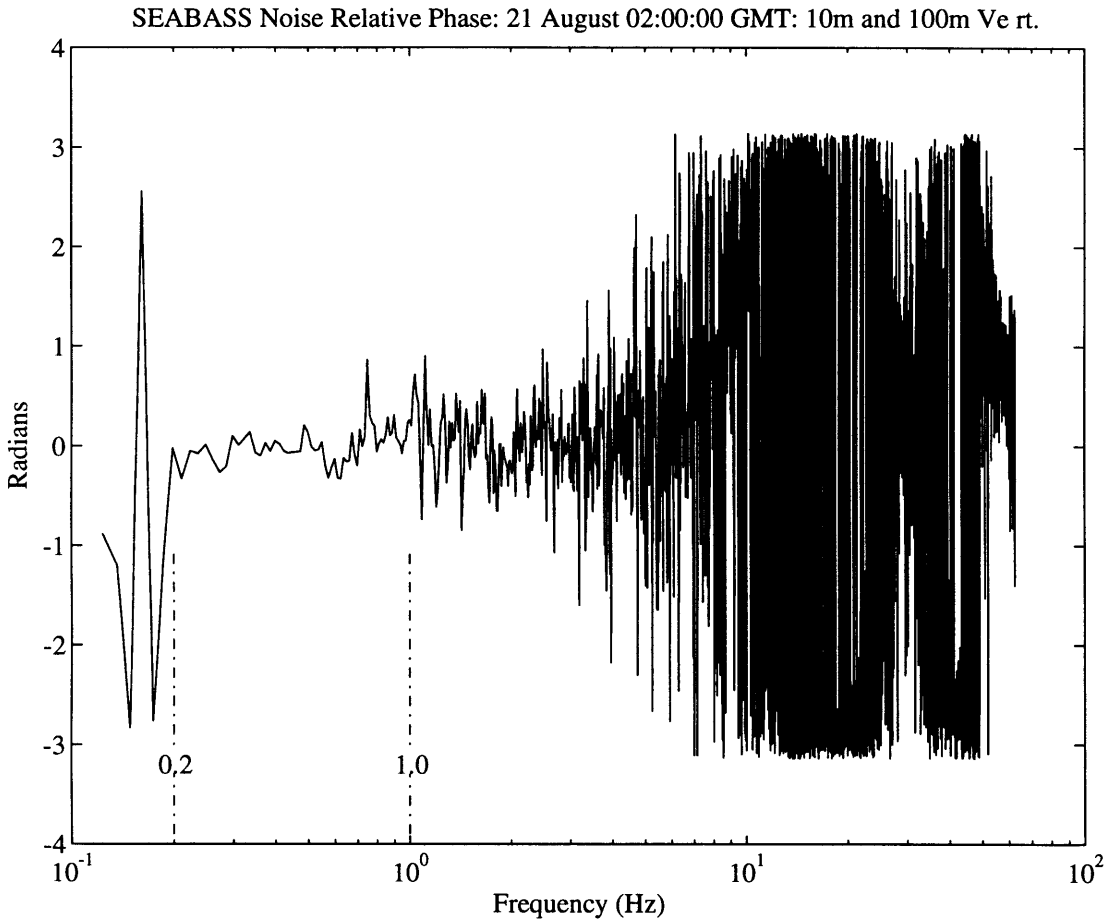


Figure 3-5: SEABASS relative phase plot between the 10 and 100 m vertical geophones.

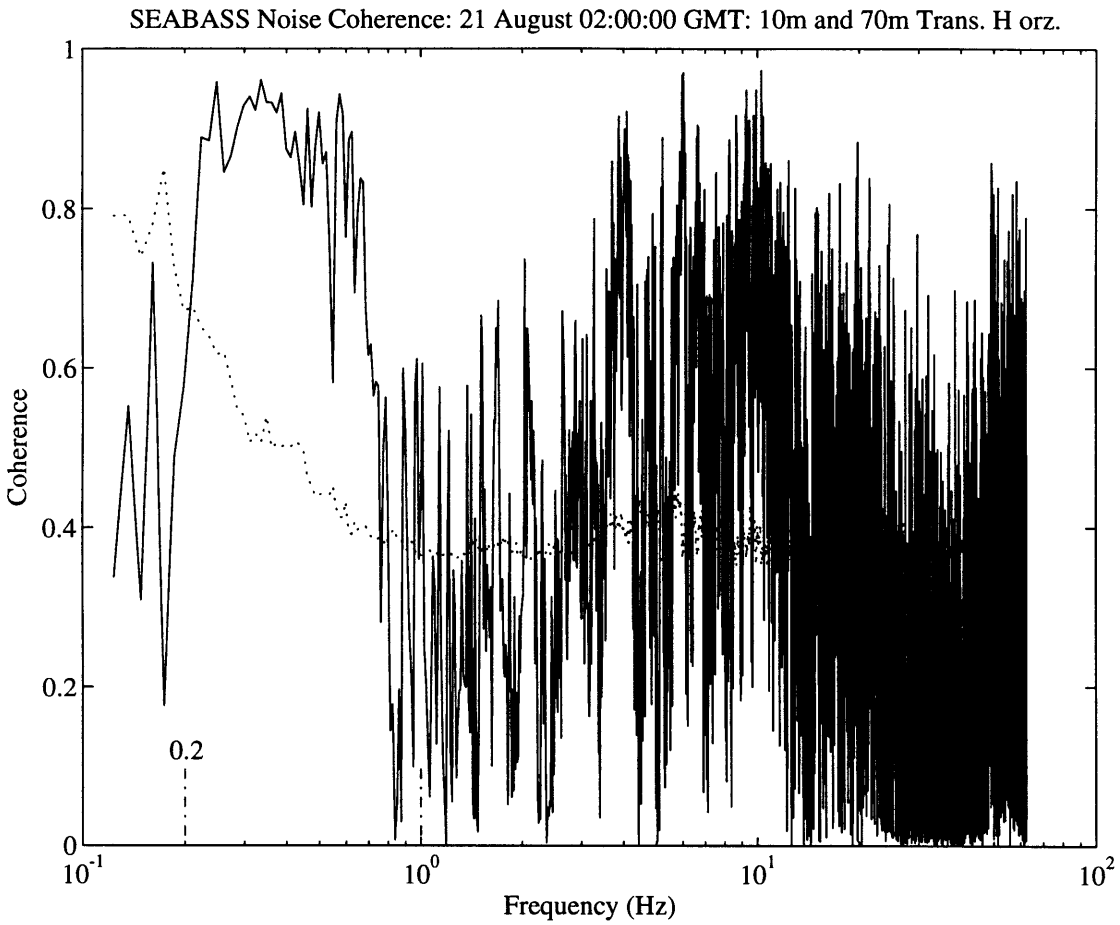


Figure 3-6: Coherency plot between the 10 and 70 m transverse horizontal geophones (channels 2 and 8). The 95% significance level is indicated as the dotted line.

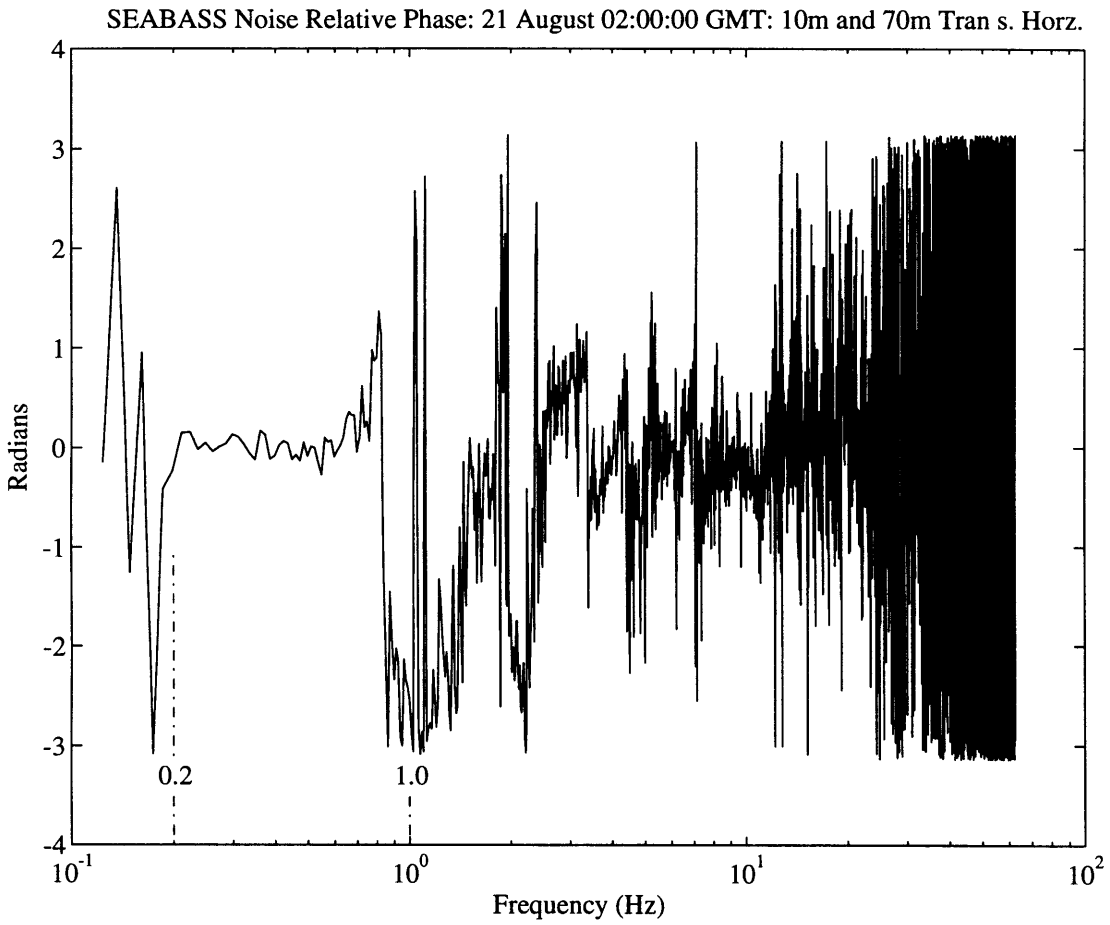


Figure 3-7: SEABASS relative phase plot between channels 2 and 8.

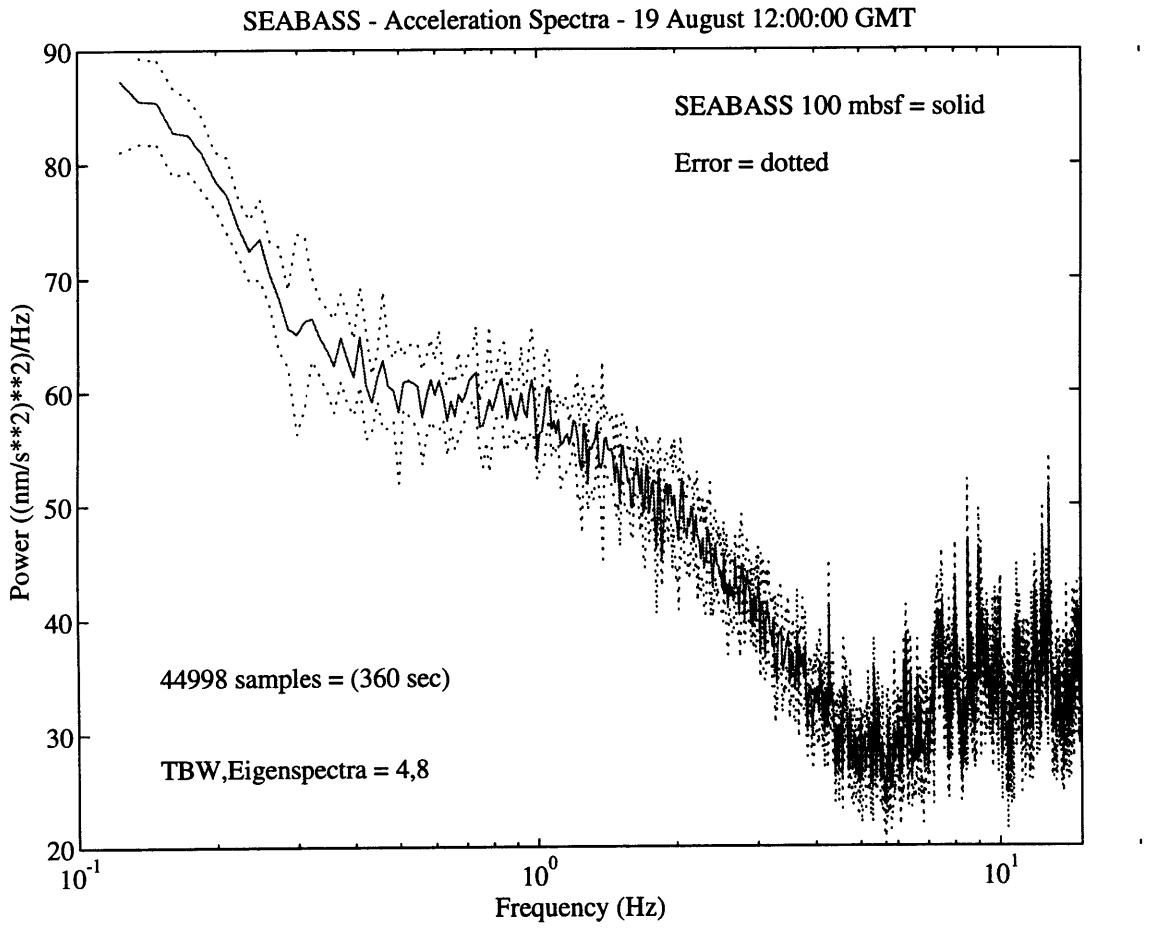


Figure 3-8: SEABASS spectrum (solid) with error estimate (dotted) computed using eigenspectra analysis. Time band width is 4 and 8 eigenspectra were averaged. Spectrum computed on 360 seconds of data from the 100 m vertical geophone.

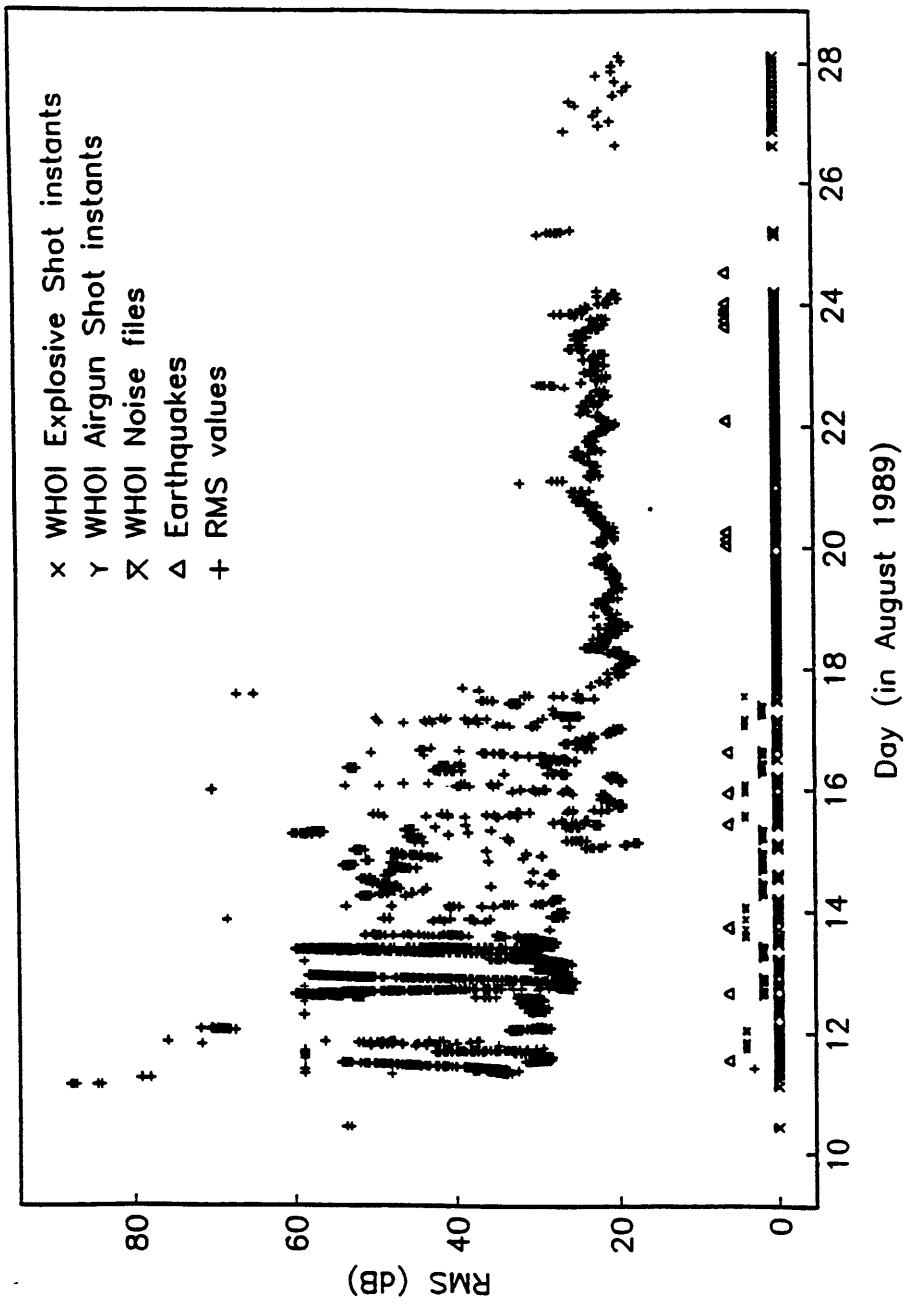


Figure 3-9: Short time series RMS power summary of LFASE experiment. Power was computed on 10 seconds from every minute recorded during the experiment. The RMS values are computed for the vertical channel in satellite 1. The peak levels on days 10-18 are from the shooting phase of the experiment. Before the 18th both USNS Lynch and R/V Melville are on site. After the 18th transient ships in the vicinity show up as peaks. The symbols at the bottom of the plot show the location of the explosives and airgun shots ($X$, $Y$), teleseisms ($\Delta$) and SEABASS noise files ($\vec{X}$) (from Stephen et al., 1993.).

Figure (10a)

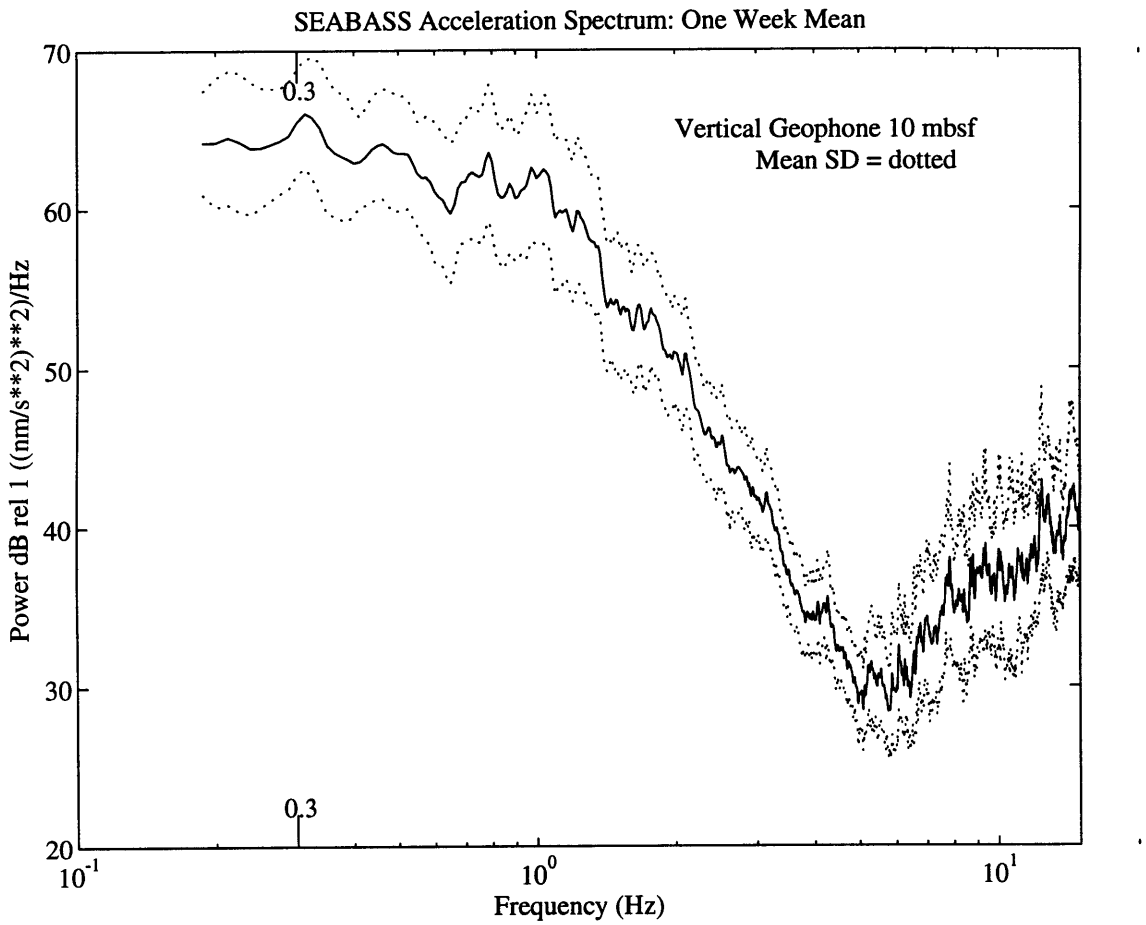


Figure 3-10: The one week spectral average from all spectra computed from seventy-four 6 and 20 minute SEABASS vertical channels. Figure (3.10a) is from the 10 $m$ satellite. Figure (3.10b) is from the 70 $m$ satellite. Figure (3.10b) is from the 100 $m$ satellite. Dotted lines indicate the standard deviation of the average. The microseism peak is at 0.3 Hz.

Figure (10b)

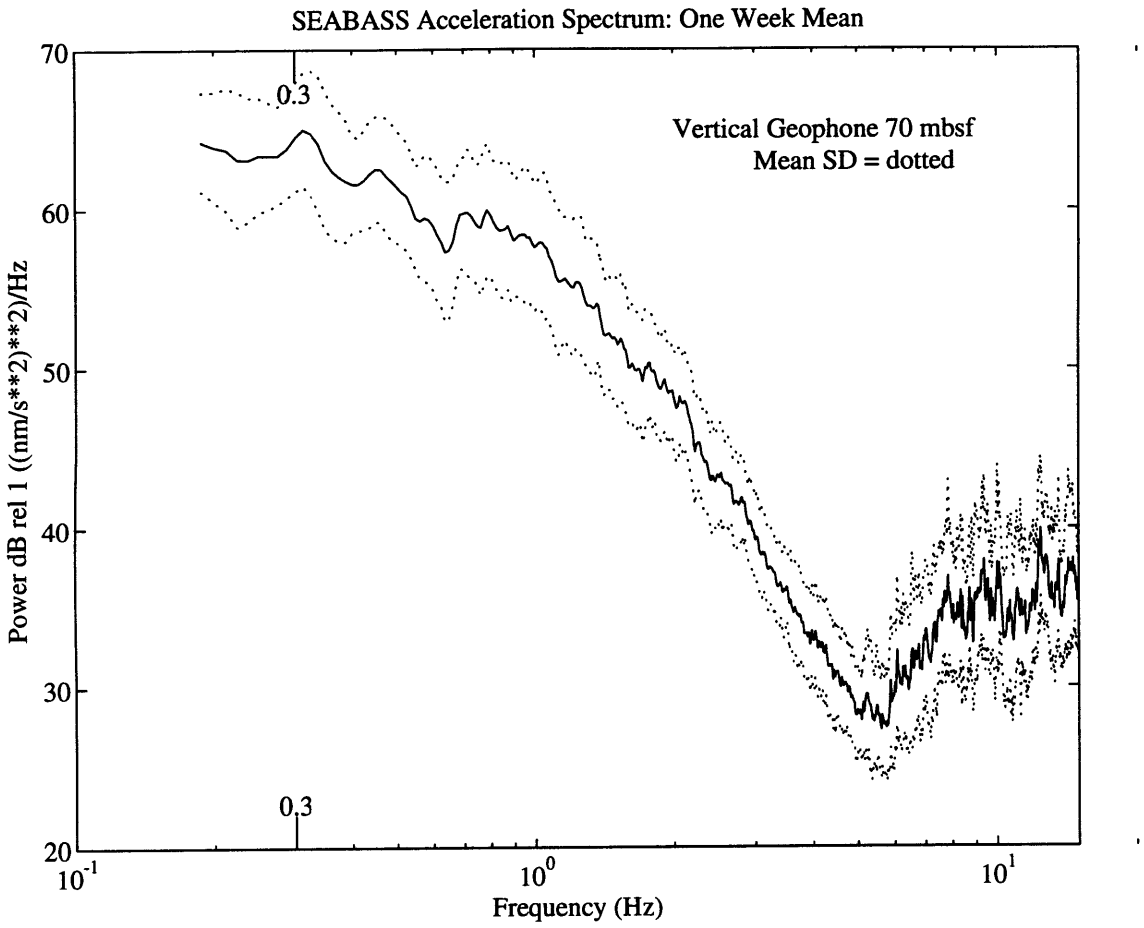
SEABASS Acceleration Spectrum: One Week Mean
Vertical Geophone 70 mbsf
Mean SD = dotted
0.3
0.3
Power dB rel 1 ((nm/s**2)**2)/Hz
Frequency (Hz)
70
60
50
40
30
20
$10^{-1}$
$10^{0}$
$10^{1}$

Figure (10c)

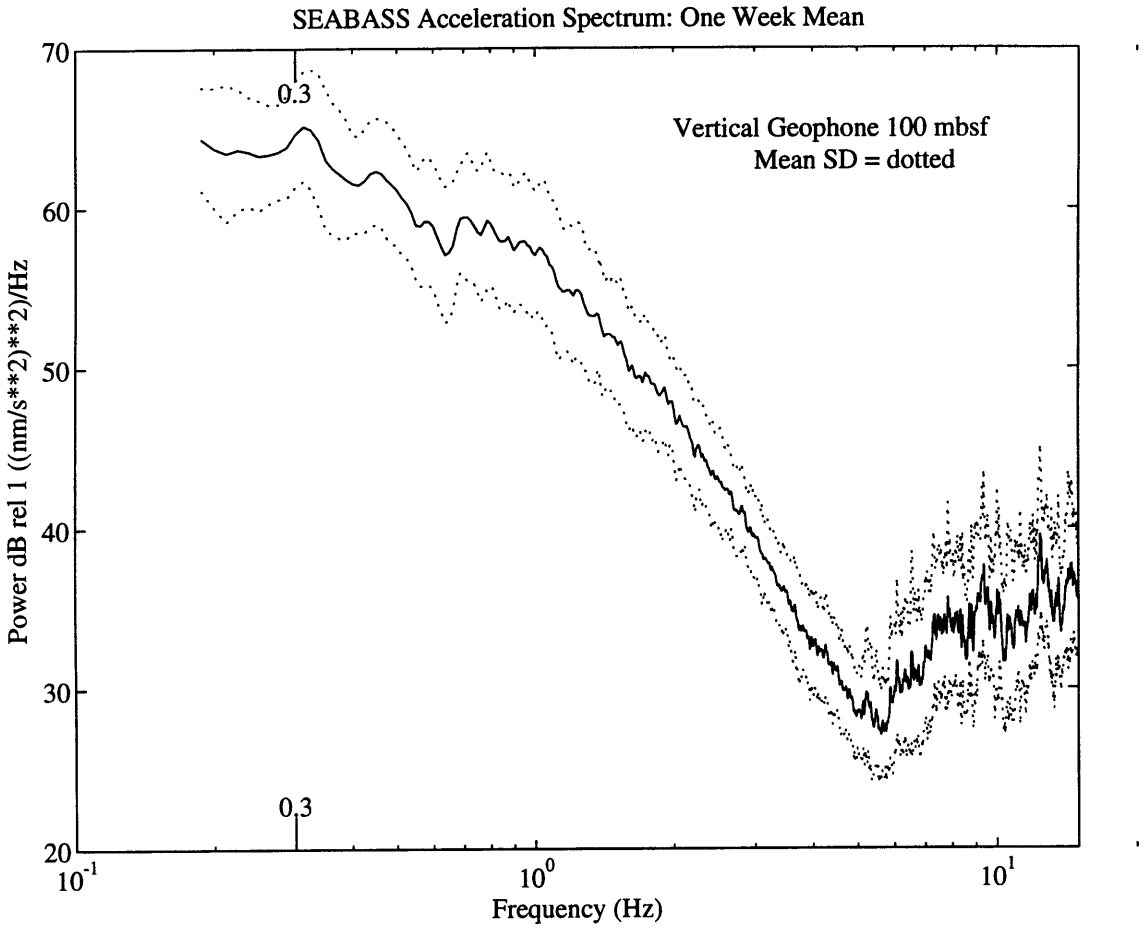
SEABASS Acceleration Spectrum: One Week Mean
Vertical Geophone 100 mbsf
Mean SD = dotted
0.3
0.3
70
60
50
40
30
20
$10^{-1}$
$10^{0}$
$10^{1}$
Power dB rel 1 ((nm/s**2)**2)/Hz
Frequency (Hz)

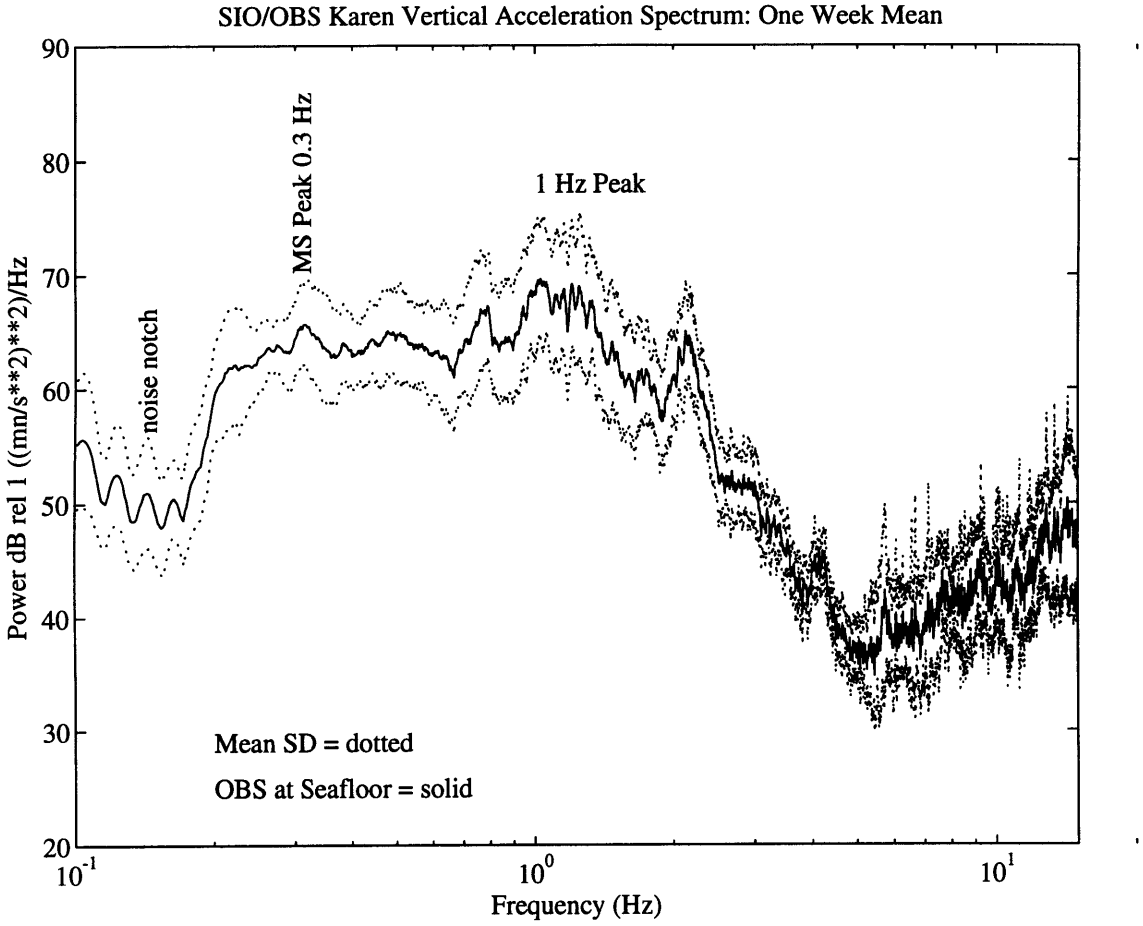


Figure 3-11: The one week spectral average of all twelve 8 minute OBS spectra vertical channel. Dotted lines indicate the standard deviation of the average. The location of the noise notch is well resolved below 0.2 Hz, bu the floor of the noise notch is system noise. In addition to the microseism peak at 0.3 $Hz$ there are peaks in the spectrum at 0.75, 1.2 and 2.1 $Hz$.

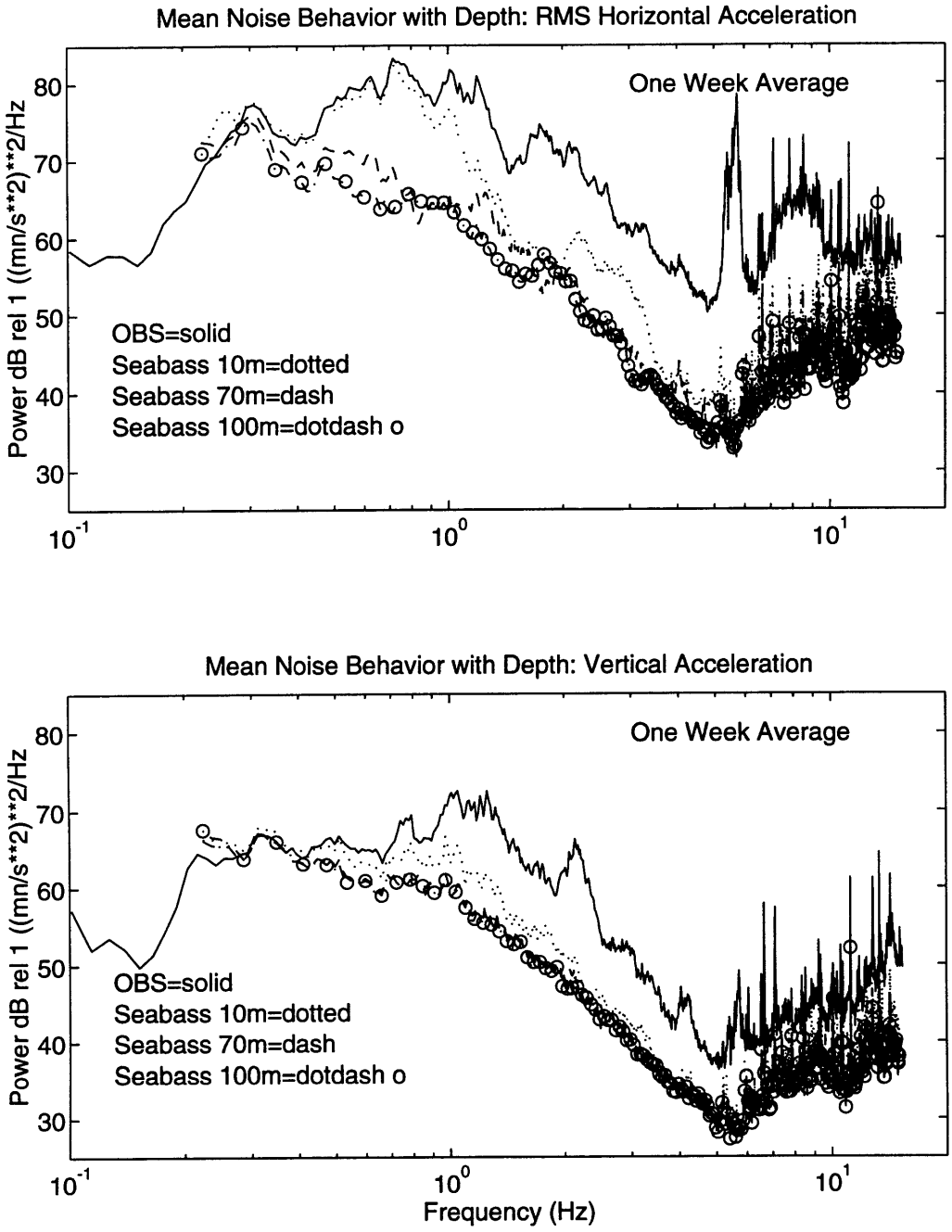


Figure 3-12: The vertical and RMS horizontal spectra from the OBS and SEABASS. Notice the almost identical level of the microseism peak at 0.3 Hz. Above 0.3 Hz the SEABASS levels are 10-15 dB lower than the OBS. The RMS-horizontal components show the largest decrease in levels with depth. Below 0.2 Hz the SEABASS channels are subject to numerical noise.

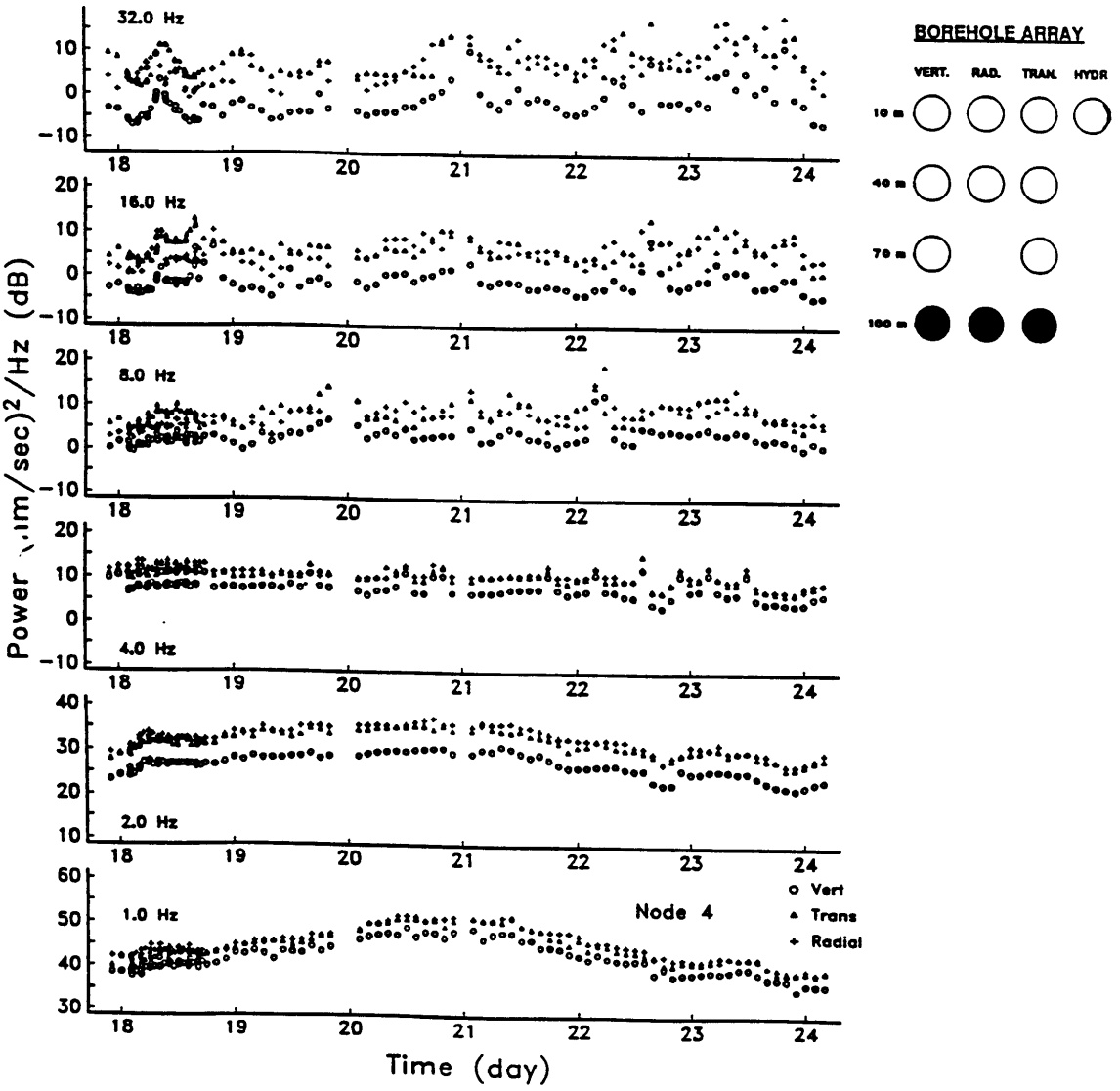


Figure 3-13: Time evolution of the spectra on the three components at $100m$ depth. Spectra were calculated on 300 second windows taken from the 6 and 20 minute times series. The data points indicate averages in one third octave bands around 1, 2, 4, 8, 16 and 32 Hz for the window at the indicated time. Shipping is seen above 4.0 Hz as isolated peaks in the spectra. There is a marked difference between the horizontal and vertical geophone responses at all frequencies with the vertical response generally 5 - 10 $dB$ quieter. A broad spectra hump rising over 10 dB is displayed in the 2.0 and 1.0 Hz data beginning on the 19th and ending on the 23rd of August (from Stephen et al., 1993).

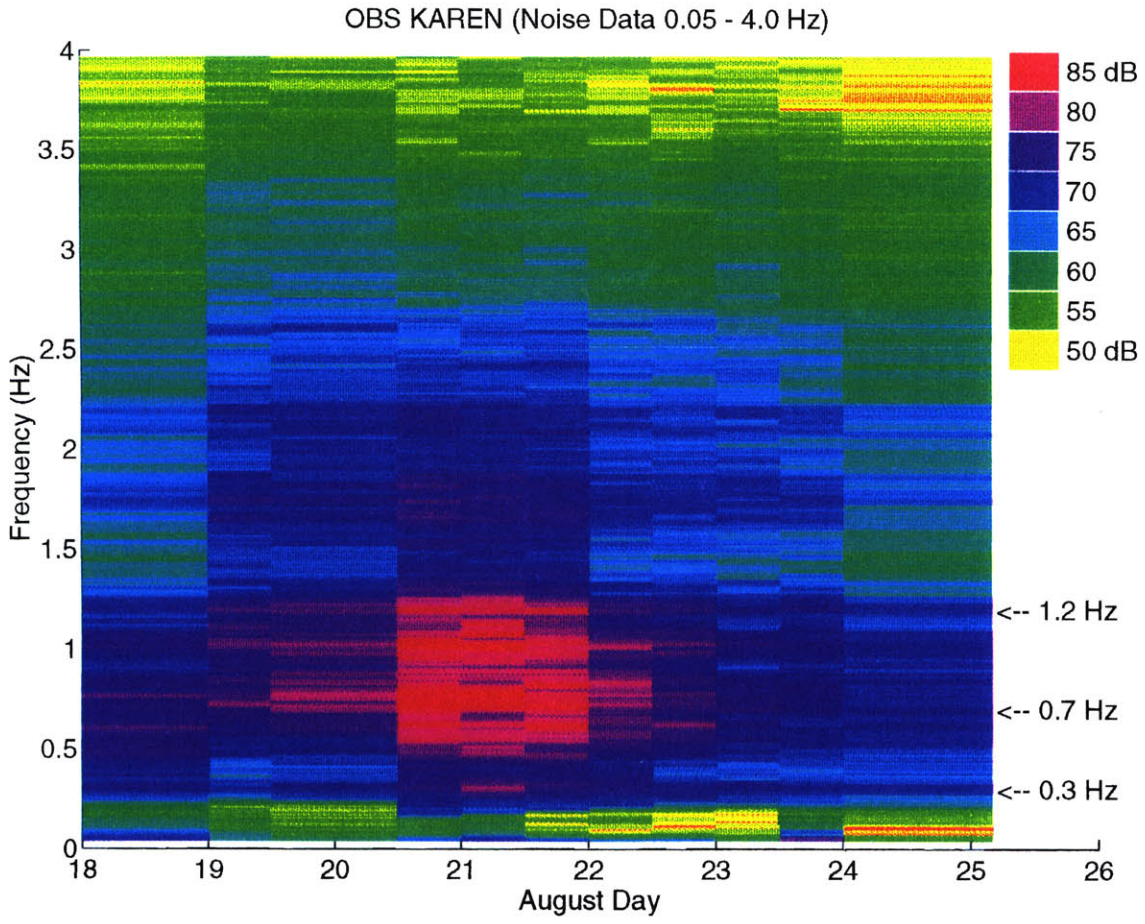


Figure 3-14: Time history of spectra for the transverse horizontal acceleration power for OBS "KAREN" from 0.05 to 3.8 Hz. The 1 Hz peak during August 21 - 22 is associated with a local storm. The upper edge of the "noise notch" is lies near 0.2 Hz. The twelve OBS spectra were computed from 420 *seconds* of data.

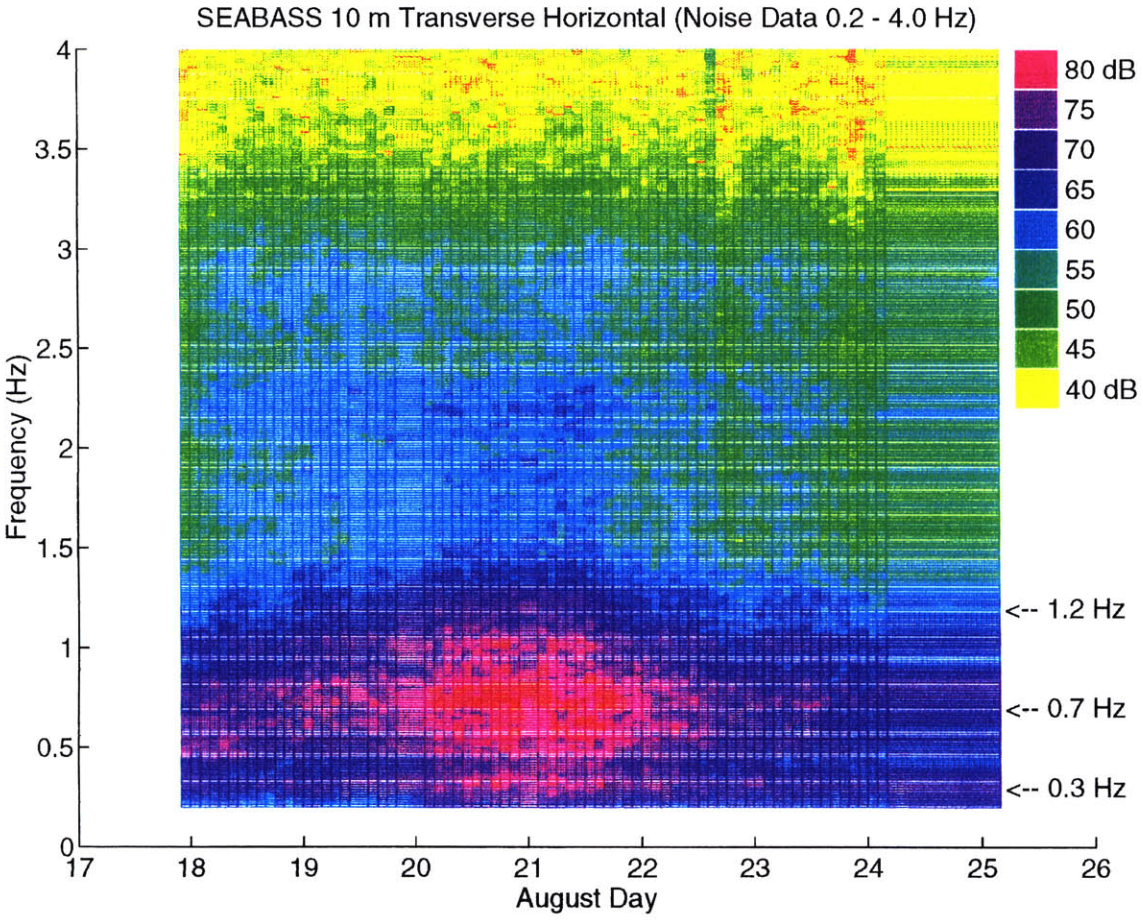


Figure 3-15: Spectral plot showing the evolution of the 10 m SEABASS transverse horizontal geophone between 0.2 and 4.0 Hz. The rise in energy between the 20th and 21st of August is associated with a local storm. Higher modes are generated in the spectra during the local storm period near 0.7 $Hz$. Spectra from seventy-four SEABASS files are shown. Each spectrum is computed using a $4\pi$ prolate taper on an 80 *second* time window. Eight windows overlapping by 15% were averaged. The range in the power spectral values is $\approx$ 75 $dB$ (at the microseism peak, 0.3 $Hz$ - pink) to $\approx$ 35 $dB$ (near 4.0 $Hz$ - yellow) $rel$ 1 $(nm/s^2)^2/Hz$.

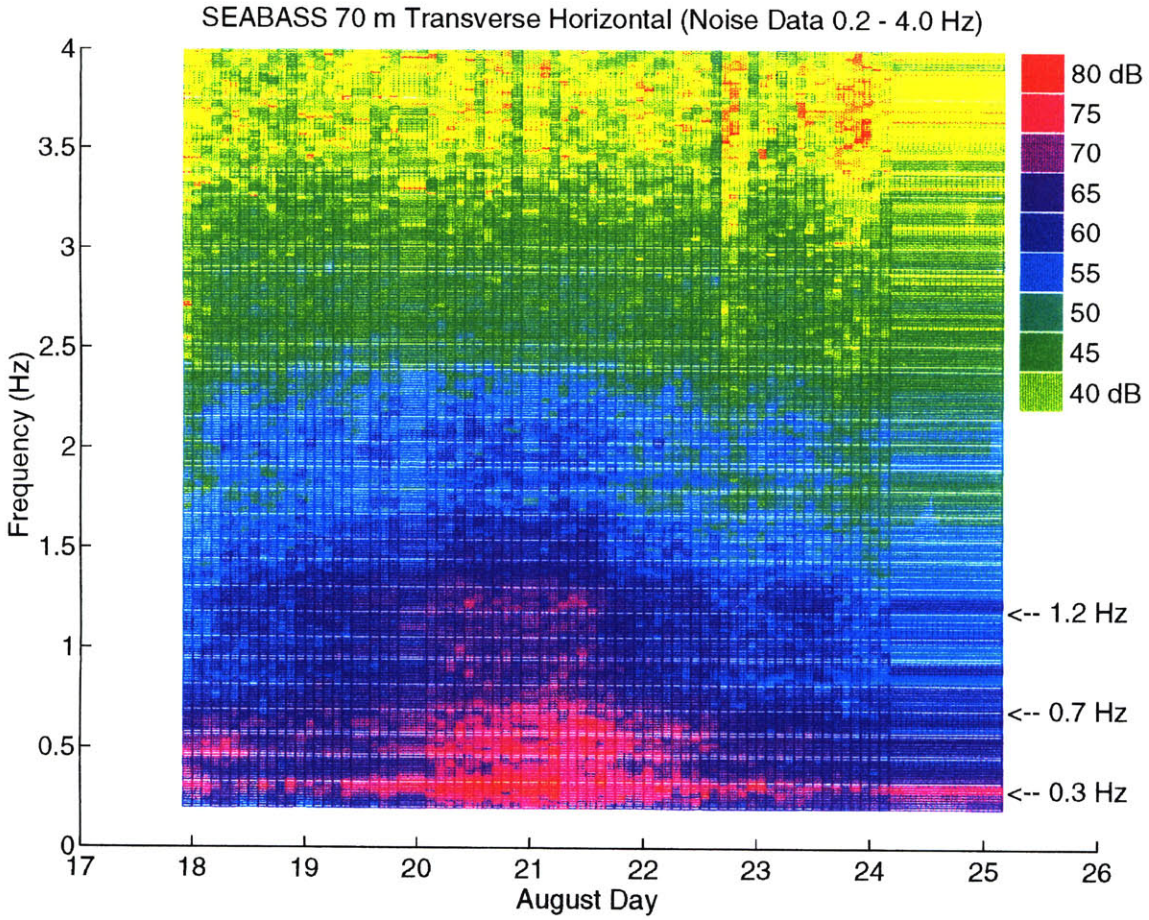


Figure 3-16: Spectral plot showing the evolution of the 70 m SEABASS transverse horizontal geophone between 0.2 and 4.0 Hz. The microseism frequency at 0.3 Hz is well defined throughout the experiment. Each spectrum is computed using a $4\pi$ prolate taper on an 80 *second* time window. Eight windows overlapping by 15% were averaged. The range in the power spectra is $\approx$ 75 $dB$ (at the microseism peak, 0.3 $Hz$ - pink) to $\approx$ 35 $dB$ (near 4.0 $Hz$ - yellow) *rel* 1 $(nm/s^2)^2/Hz$.

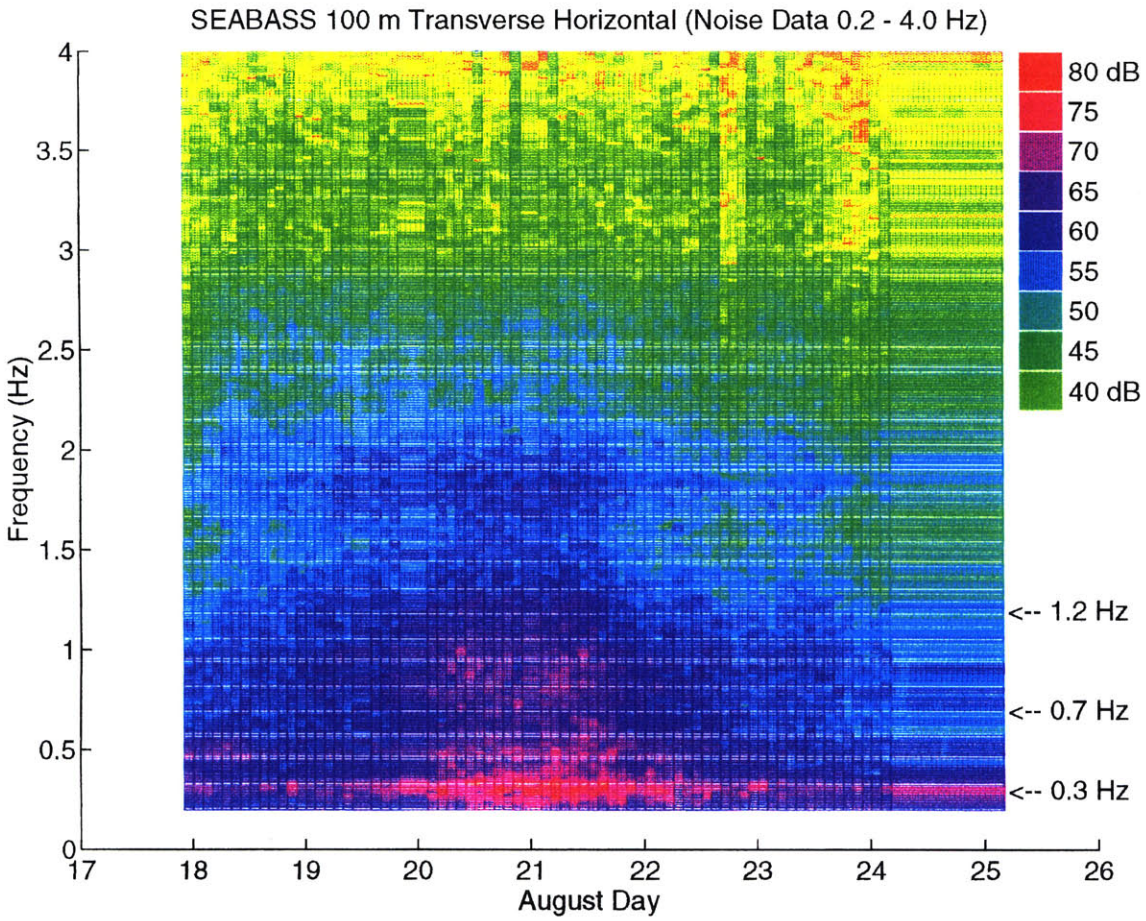


Figure 3-17: Spectral plot showing the time evolution of the 100 m SEABASS transverse horizontal geophone between 0.2 and 4.0 Hz. The 0.3 Hz peak is the microseism peak. Higher mode energy is evident near 0.5 1.0 and 2.0 Hz. Eight windows overlapping by 15% were averaged. The range in the power spectra is $\approx$ 75 $dB$ (at the microseism peak, 0.3 $Hz$ - pink) to $\approx$ 35 $dB$ (near 4.0 $Hz$ - yellow) $rel$ 1 $(nm/s^2)^2/Hz$.

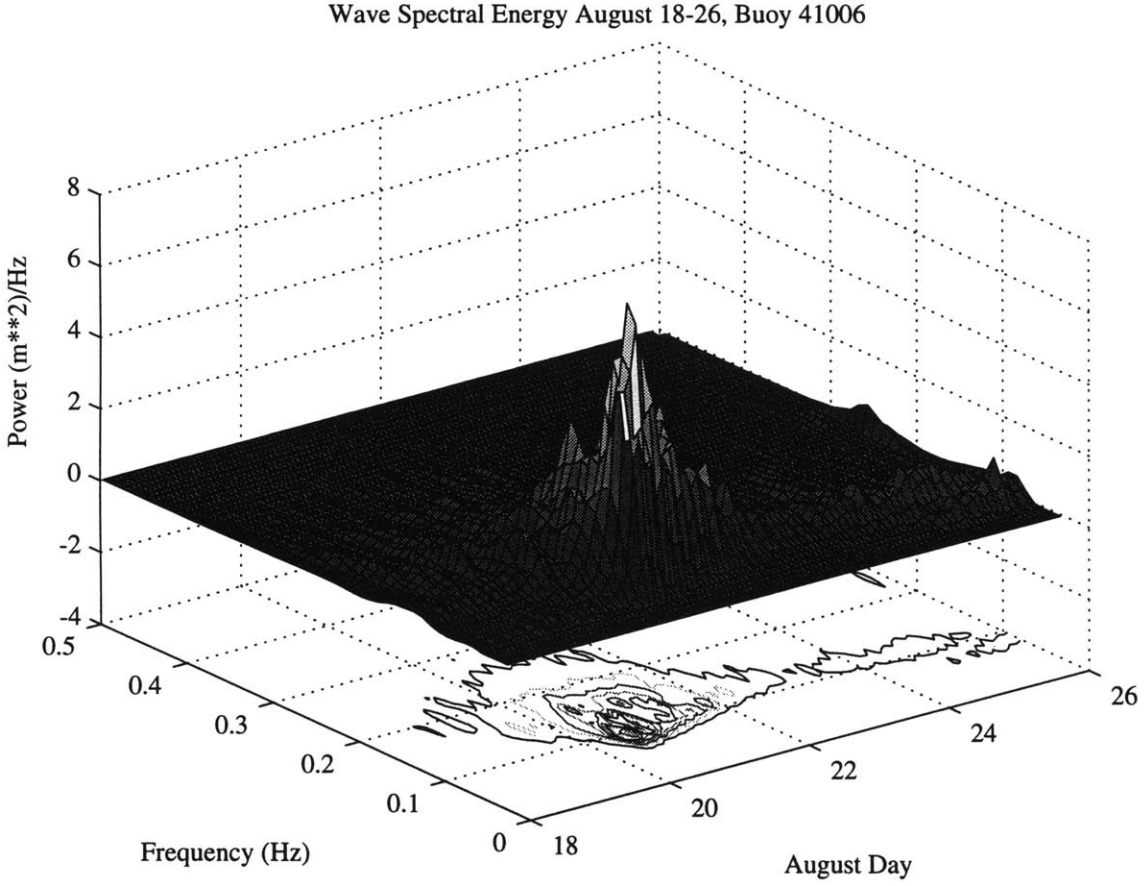


Figure 3-18: Wave spectral energy for Buoy 41006 moored at 29.3°N 77.4° W. The mesh shows the onset of high wave energy peaking midday on the 20th of August. The contour plot below shows the growth of high amplitude, low frequency wave energy, a process indicative of a local storm.

Figure (3.19a)

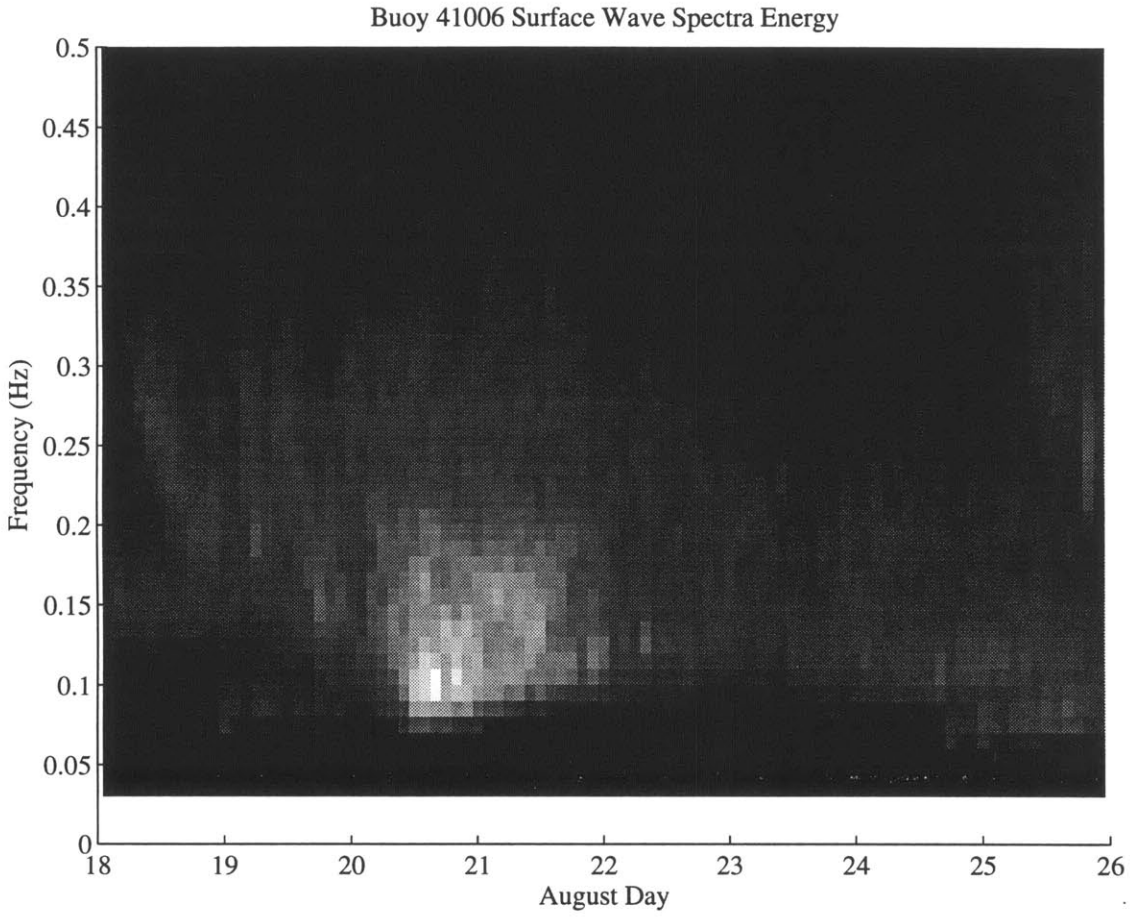


Figure 3-19: Graytone plot showing the relative power spectral density seen at the Buoy 41006 (3.19a), satellite 1 (3.19b) and satellite 3 (3.19c) from the 18 through the 26th of August 1989. Figure (3.19a) shows the wave onset beginning on August 20th and local wave growth from higher frequency to lower frequency between the 20th and 21st. Figures (3.19b,c) show the onset of high microseism and broad band noise levels on the 20th. Maximum and minimum values in these figures are given in Figures (3.18), (3.15) and (3.16).

Figure (3.19b)

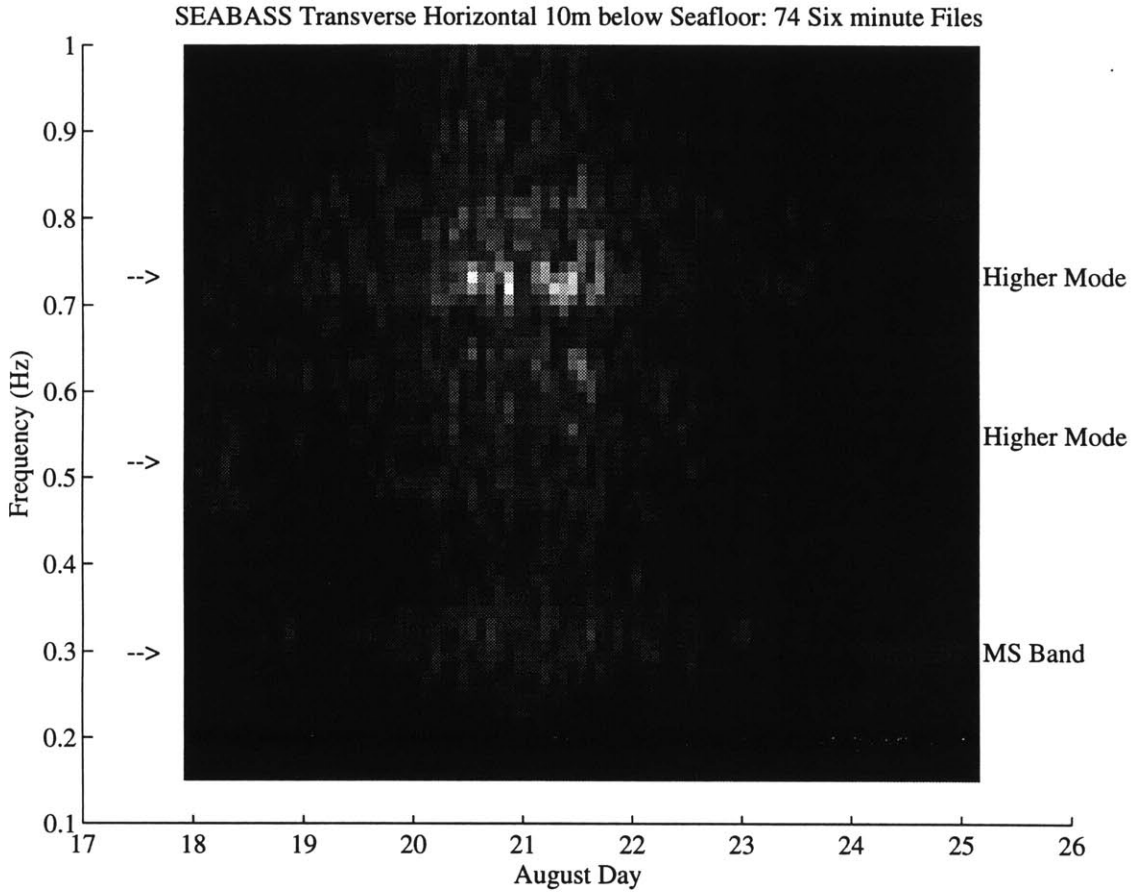
SEABASS Transverse Horizontal 10m below Seafloor: 74 Six minute Files
Frequency (Hz)
1
0.9
0.8
0.7
0.6
0.5
0.4
0.3
0.2
0.1
-->
-->
-->
Higher Mode
Higher Mode
MS Band
17
18
19
20
21
22
23
24
25
26
August Day

Figure (3.19c)

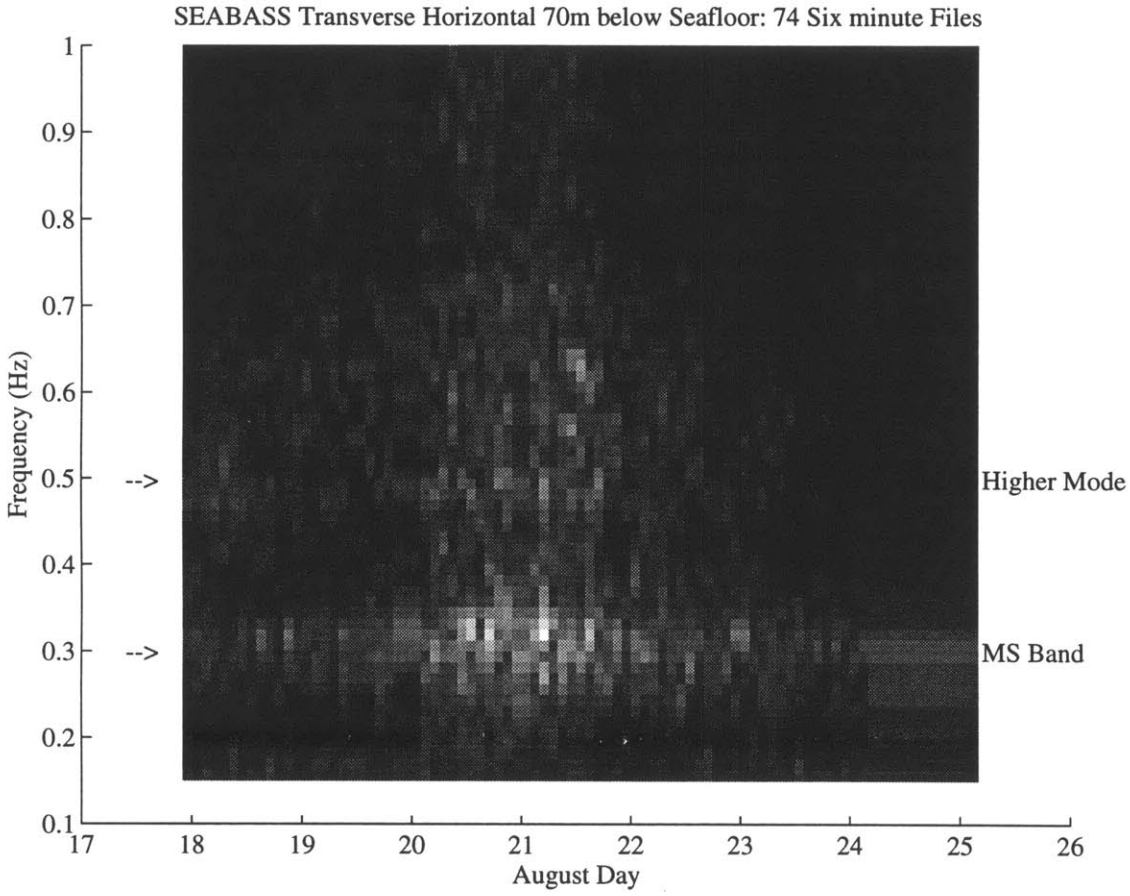
SEABASS Transverse Horizontal 70m below Seafloor: 74 Six minute Files
Frequency (Hz)
1
0.9
0.8
0.7
0.6
0.5
0.4
0.3
0.2
0.1
-->
-->
Higher Mode
MS Band
17
18
19
20
21
22
23
24
25
26
August Day

Figure (3.20a)

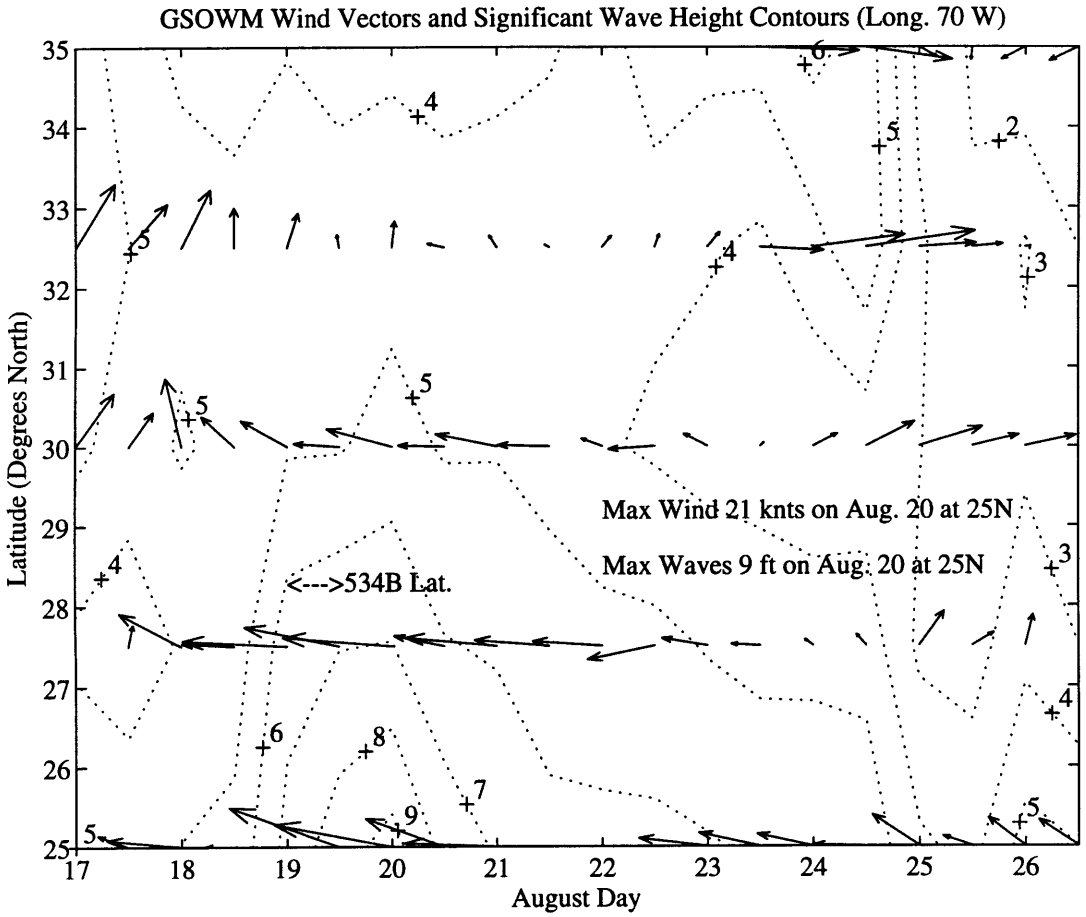


Figure 3-20: Model output from the five nearest GSOWM grid points to Hole 534B located between 25 and 35 North latitude. Figure (3.20a) shows the wind direction as vectors and the significant swell height as dotted contours. The maximum swell height is 9 ft and maximum winds are 21 knots (scale: 5/8" = 20 knts). Figure (3.20b) plots the change in wind direction with time as vectors and the significant wave frequency as dotted contours.

Figure (3.20b)

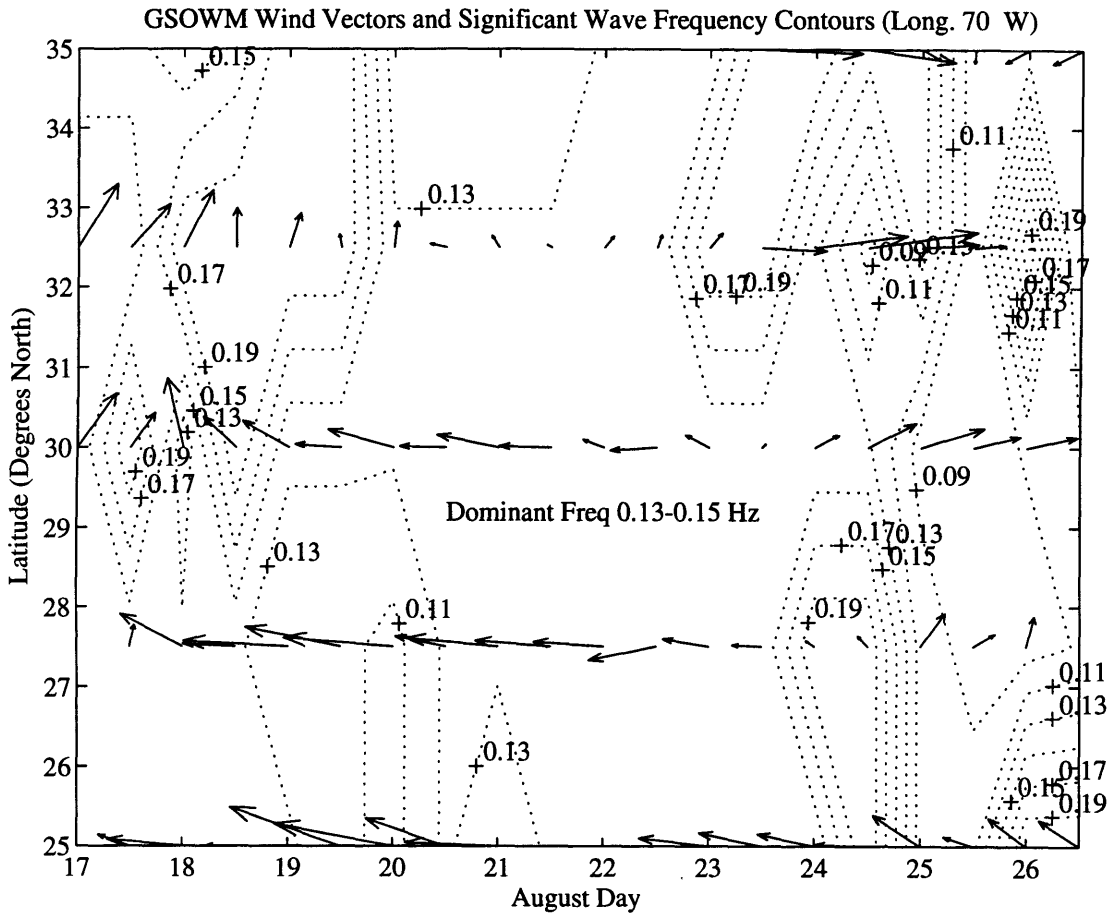
GSOWM Wind Vectors and Significant Wave Frequency Contours (Long. 70 W)
Latitude (Degrees North)
August Day
Dominant Freq 0.13-0.15 Hz
35
34
33
32
31
30
29
28
27
26
25
17
18
19
20
21
22
23
24
25
26

Figure (3.21a)

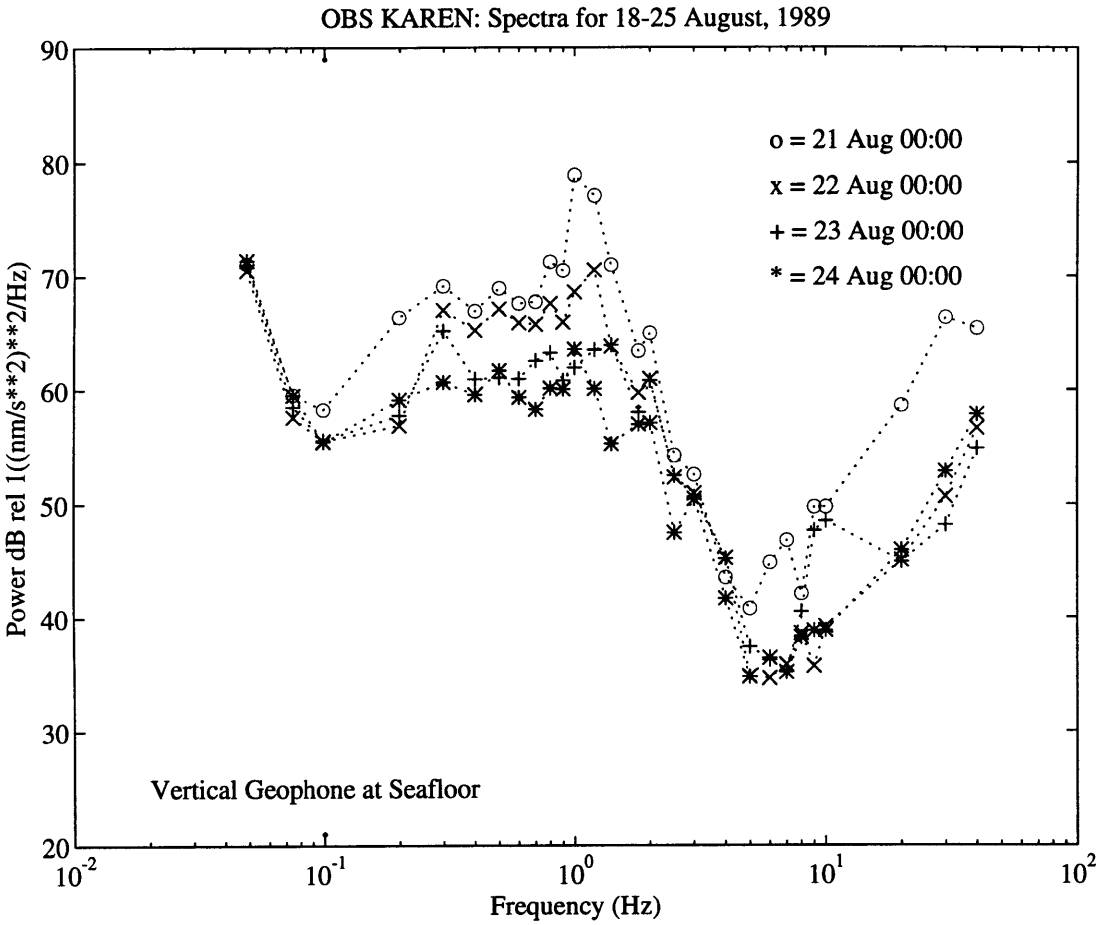


Figure 3-21: Subsampled and averaged OBS "KAREN" (Figure 3.21a), SEABASS 10 $m$ (Figure 3.21b) and 100 $m$ (Figure 3.21c) vertical acceleration spectra from the 21st to the 24th of August 1989. Complete spectra were computed for four noise windows and averaged power were computed at 28 discrete frequencies by averaging $\pm 5\ \Delta f$ around each discrete frequency. The comparative spectra show the evolution of the Holu spectrum ($1\ -\ 5\ Hz$). The three sensors have saturation slopes of -21, -17 and -15 $dB/octave$ respectively.

Figure (3.21b)

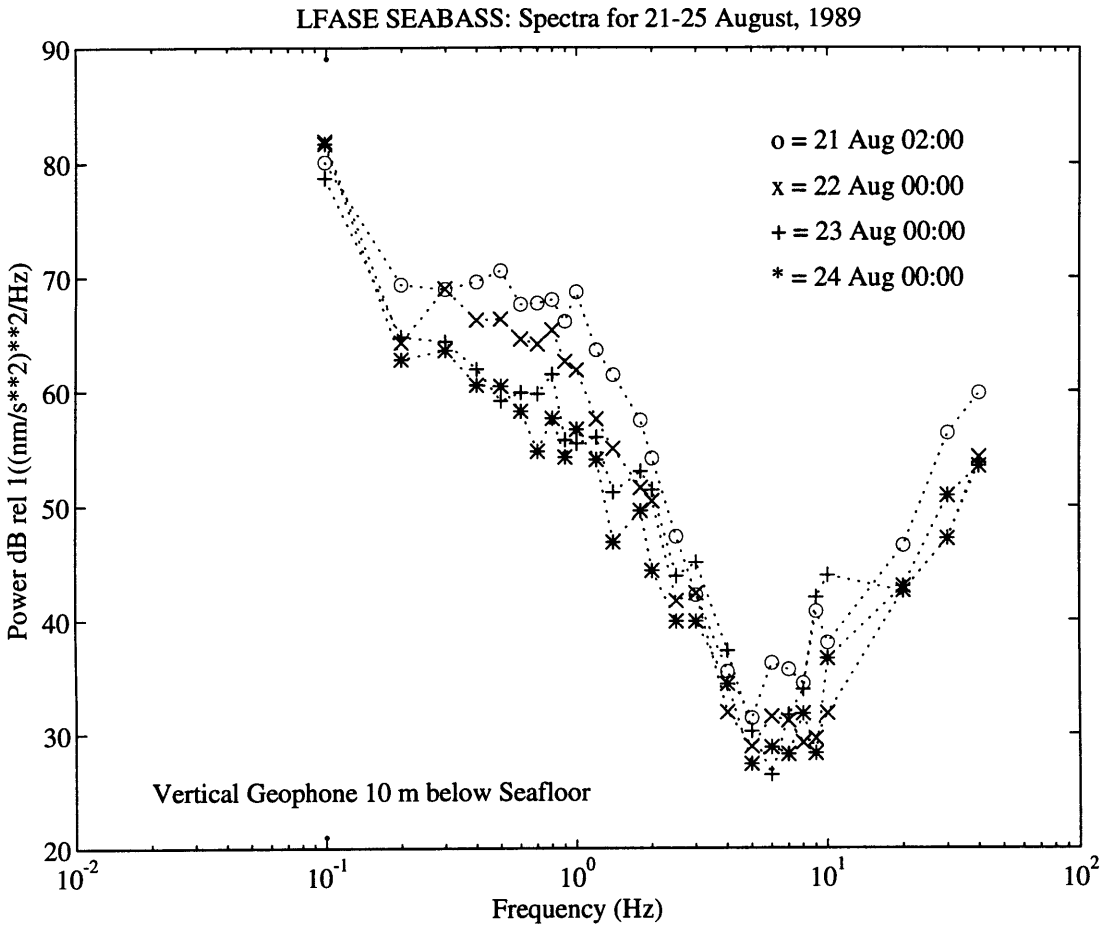
LFASE SEABASS: Spectra for 21-25 August, 1989
o = 21 Aug 02:00
x = 22 Aug 00:00
+ = 23 Aug 00:00
* = 24 Aug 00:00
Vertical Geophone 10 m below Seafloor
Power dB rel 1((nm/s**2)**2/Hz)
Frequency (Hz)
90
80
70
60
50
40
30
20
10^-2
10^-1
10^0
10^1
10^2

Figure (3.21c)

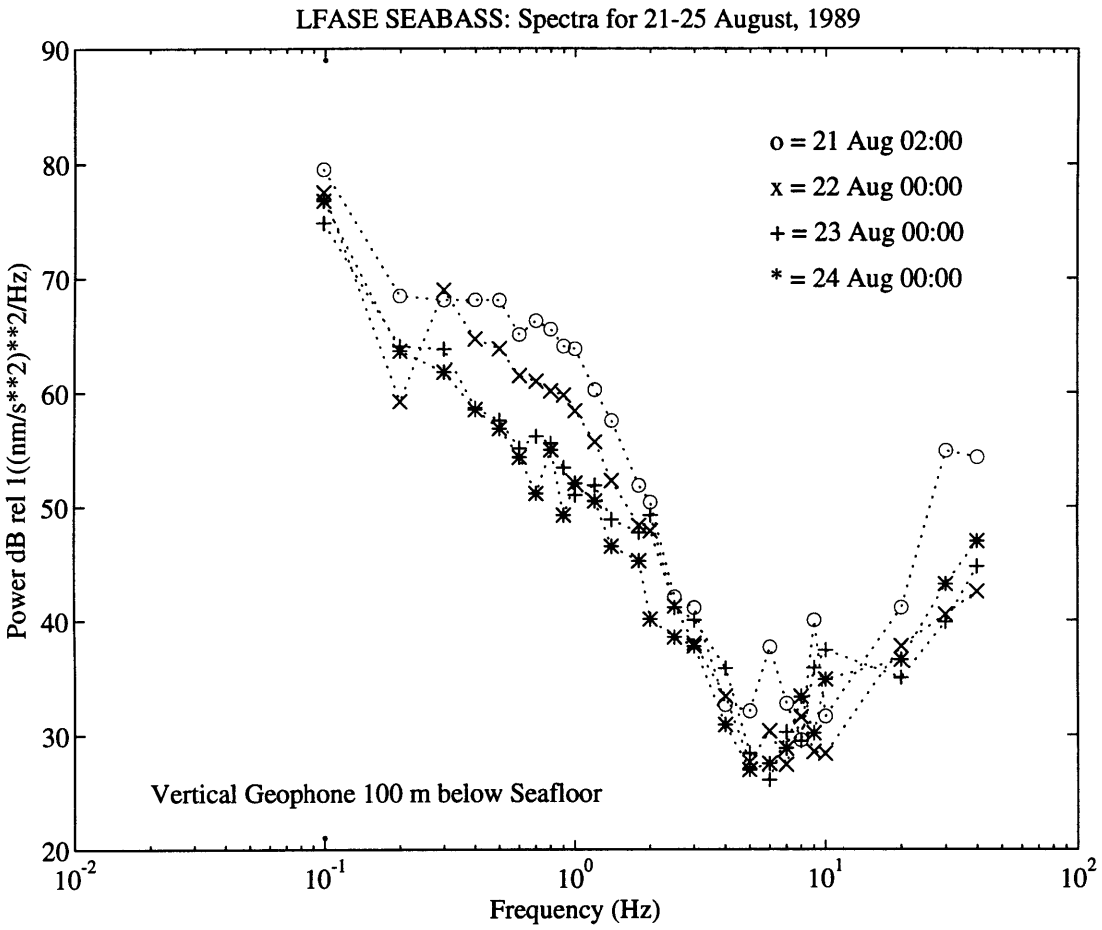
LFASE SEABASS: Spectra for 21-25 August, 1989
o = 21 Aug 02:00
x = 22 Aug 00:00
+ = 23 Aug 00:00
* = 24 Aug 00:00
Vertical Geophone 100 m below Seafloor
Power dB rel 1((nm/s**2)**2/Hz)
Frequency (Hz)
90
80
70
60
50
40
30
20
10^-2
10^-1
10^0
10^1
10^2

Figure (3.22a)

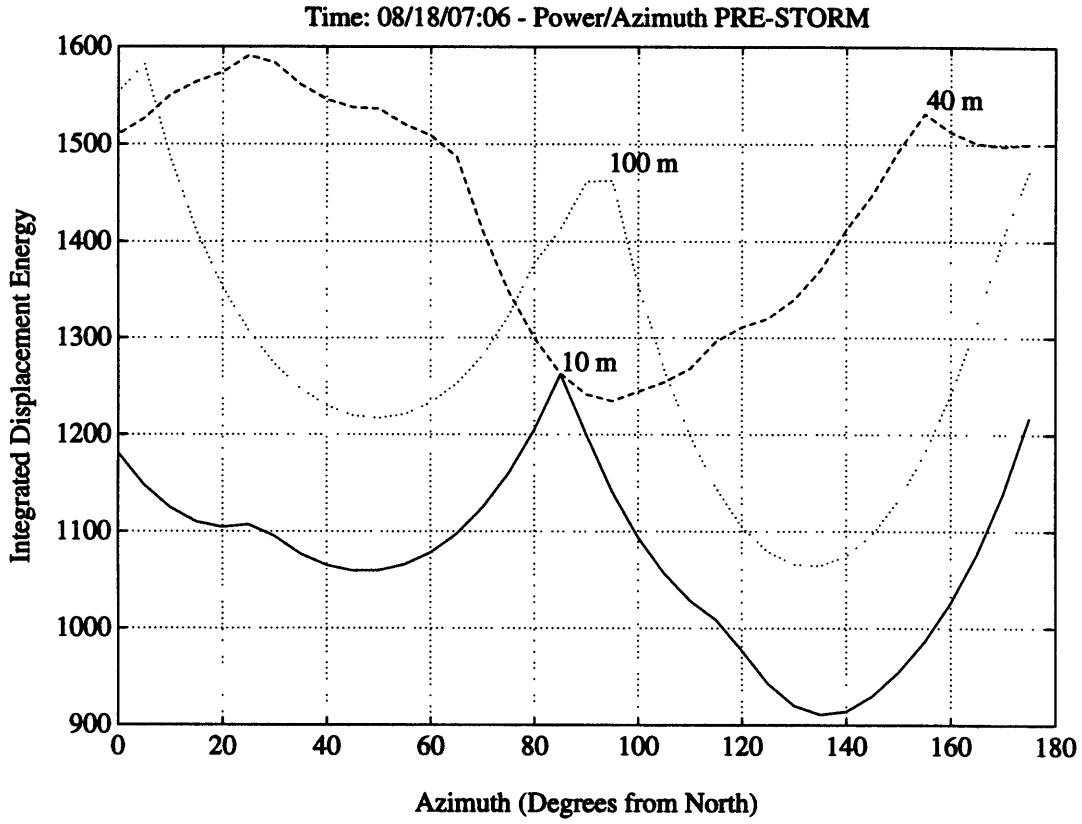


Figure 3-22: The integrated displacement energy versus azimuth for 1.0 Hz low-pass filtered time series before the storm (Figure 3.22a) and during the storm (Figure 3.22b). Satellite 1 energy is shown as the solid line, satellite 2 plotted as the dashed and satellite 4 is plotted as the dotted line.

Figure (3.22b)

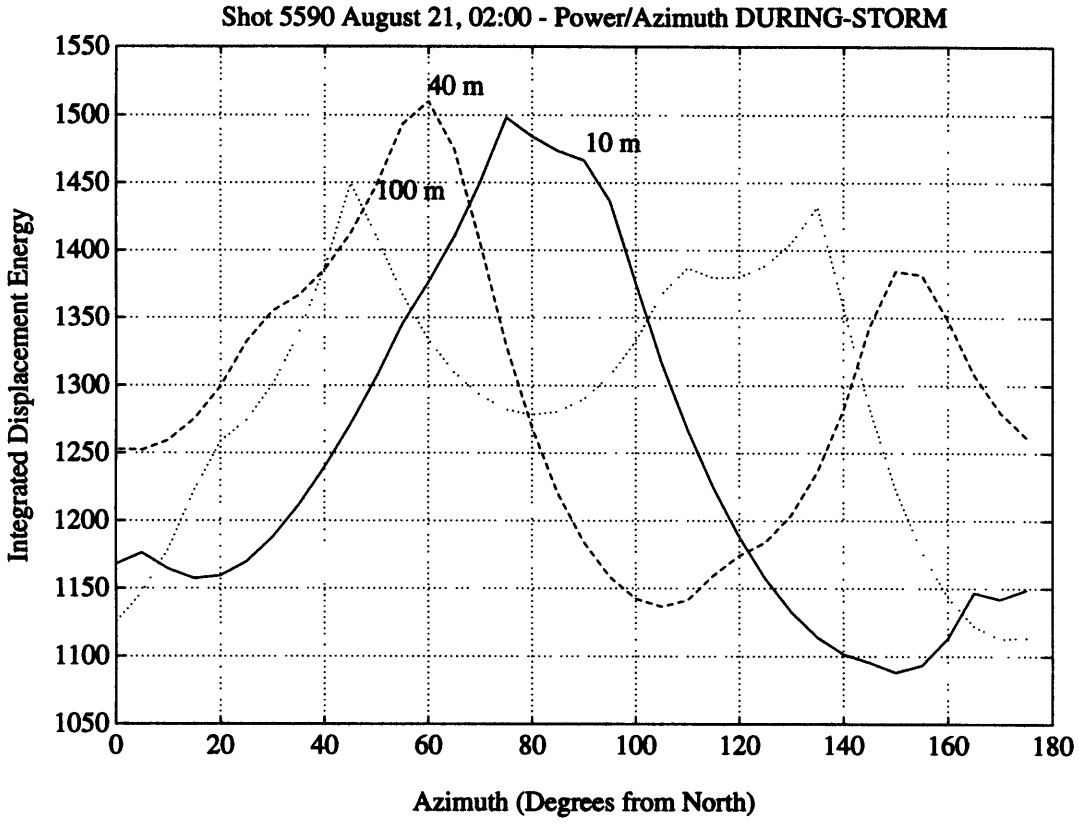
Shot 5590 August 21, 02:00 - Power/Azimuth DURING-STORM
Integrated Displacement Energy
Azimuth (Degrees from North)
40 m
10 m
100 m
1550
1500
1450
1400
1350
1300
1250
1200
1150
1100
1050
0
20
40
60
80
100
120
140
160
180

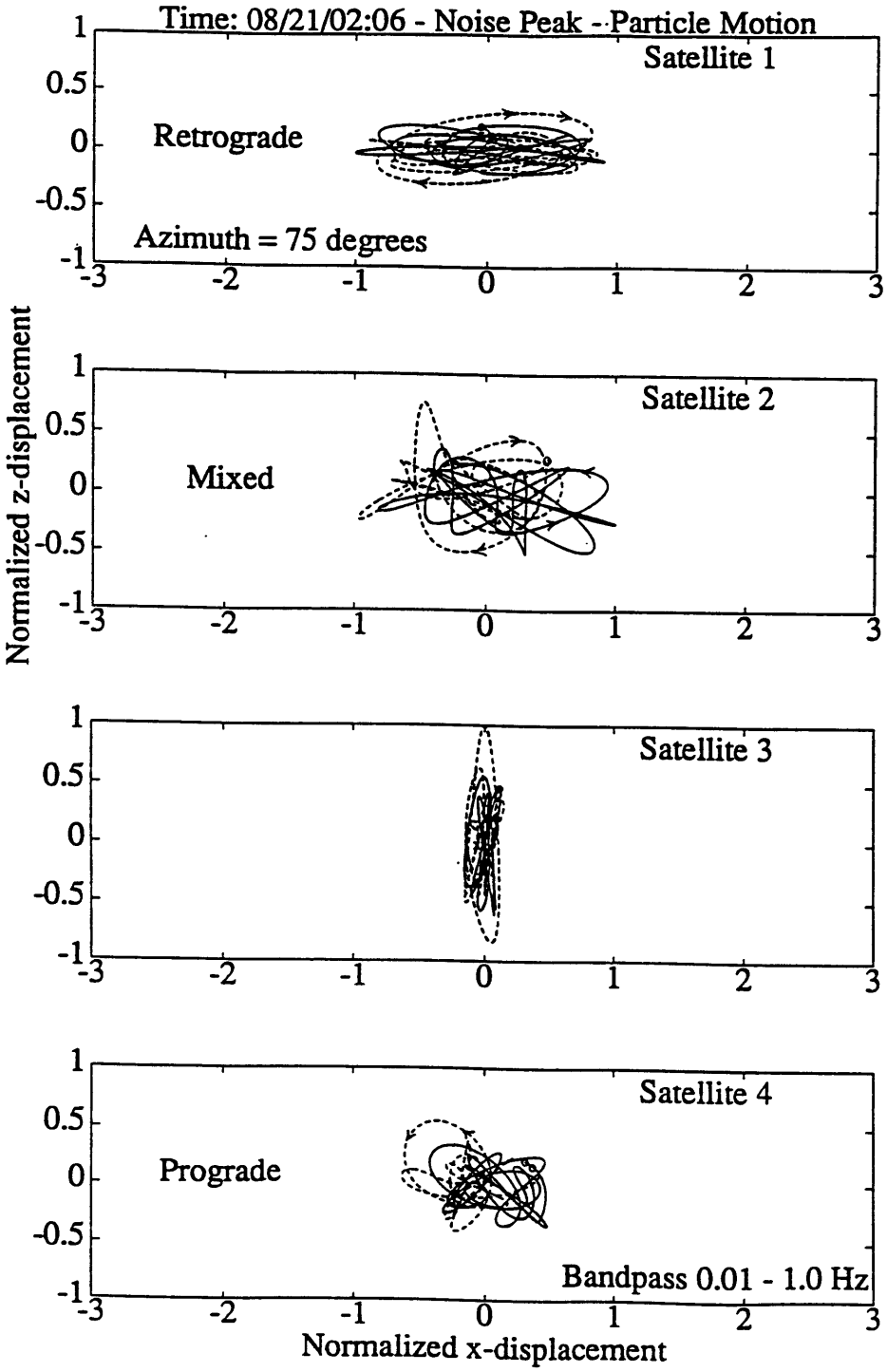


Figure 3-23: Particle motion with depth along the SEABASS instrument projected onto a plane striking $N75°E$. Assuming the event is traveling from right to left, the motion in satellite 1 is retrograde elliptic, satellite 2 has mixed motion and satellite 4 shows prograde elliptic motion. The particle motion is normalized to unit maximum displacement. Motion on satellite 3 is artificially projected onto the $N75°E$ plane since there is no radial horizontal component.

Figure (3.24a)

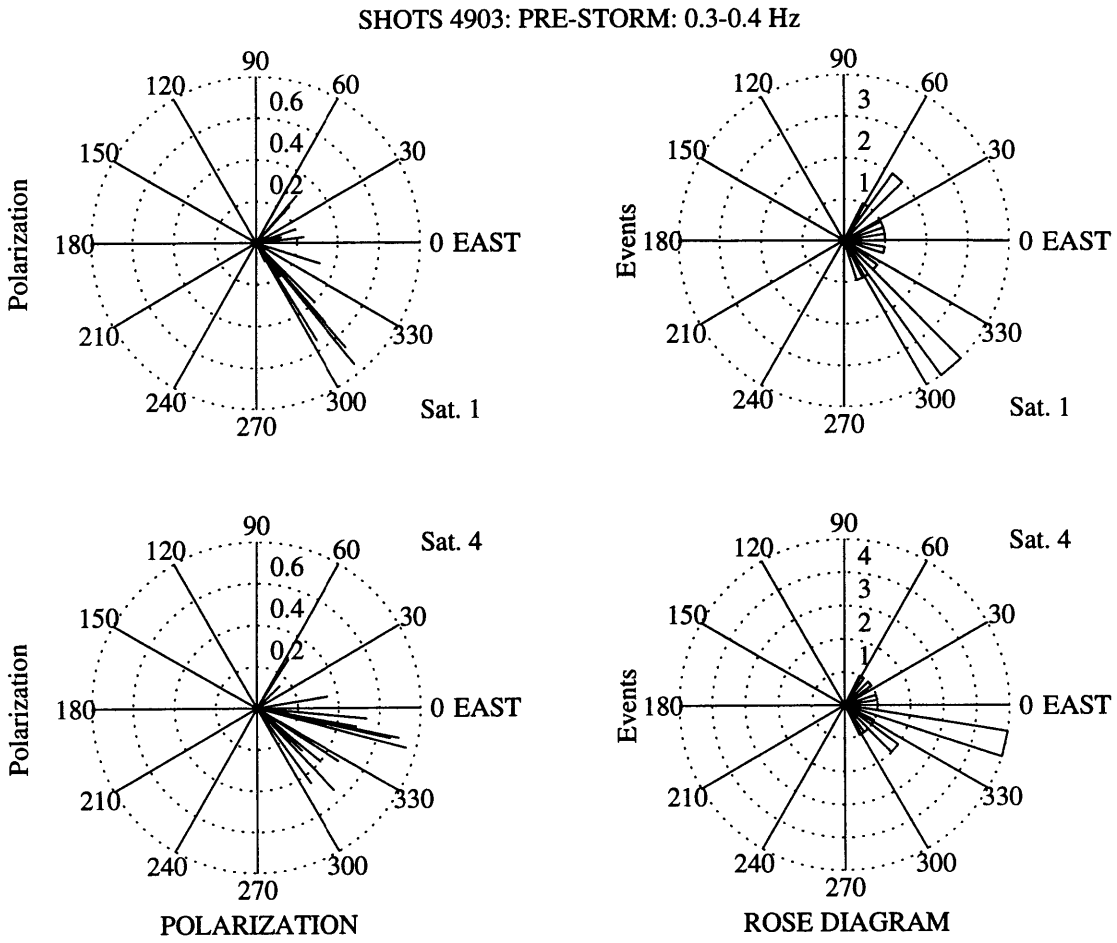


Figure 3-24: Polarization azimuth and rose plots for energy near the microseism peak (0.3-0.4 Hz) for pre-storm (3.24a), syn-storm (3.24b) and post-storm (3.24c) representative shot files. The polarization azimuth magnitudes are weighted by the degree of polarization computed. The rose diagram shows the respective density of azimuth falling within a directional "pie-slice". Each azimuth represents the direction of a particular frequency. The bandwidth from 0.3 to 0.4 Hz was divided into 14 discrete frequencies.

Figure (3.24b)

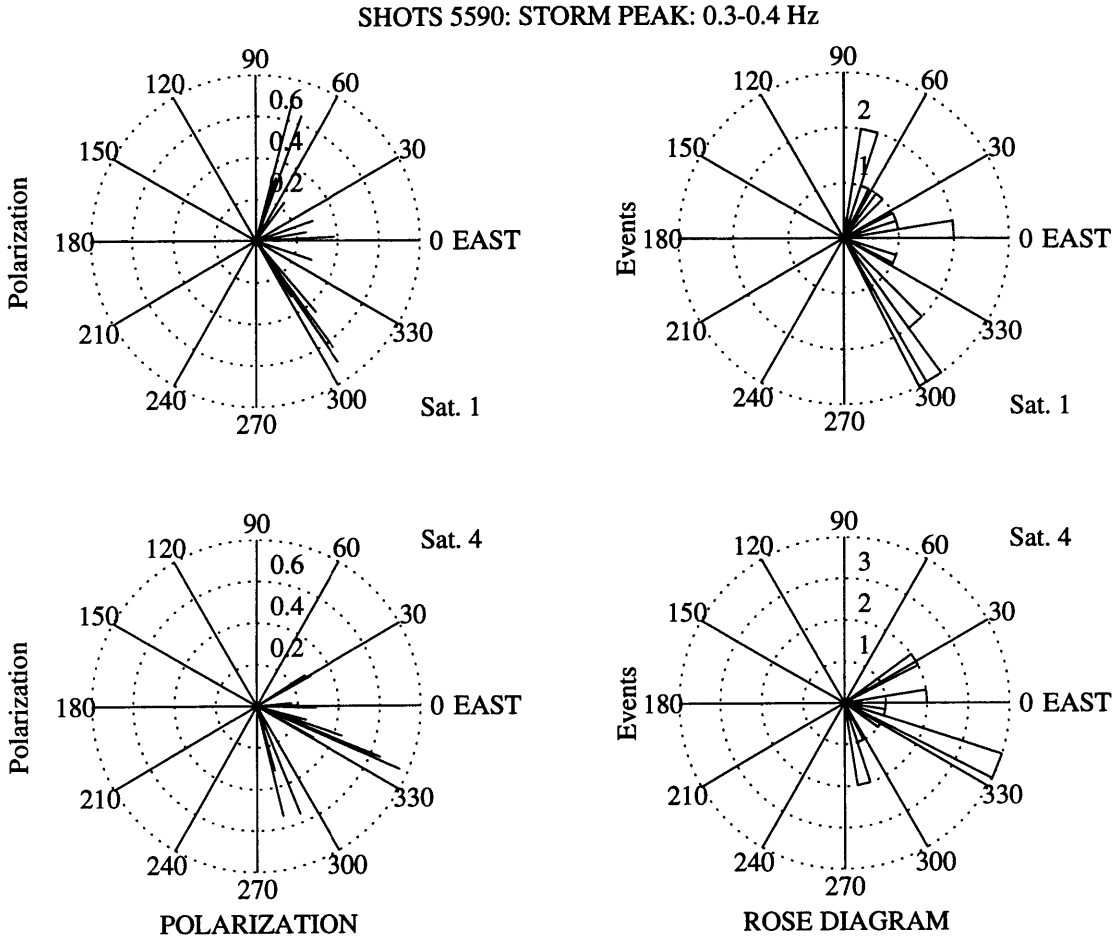
SHOTS 5590: STORM PEAK: 0.3-0.4 Hz
Polarization
Events
Sat. 1
Sat. 4
0 EAST
90
120
60
150
30
180
210
330
240
300
270
0.6
0.4
0.2
1
2
3
POLARIZATION
ROSE DIAGRAM

Figure (3.24c)

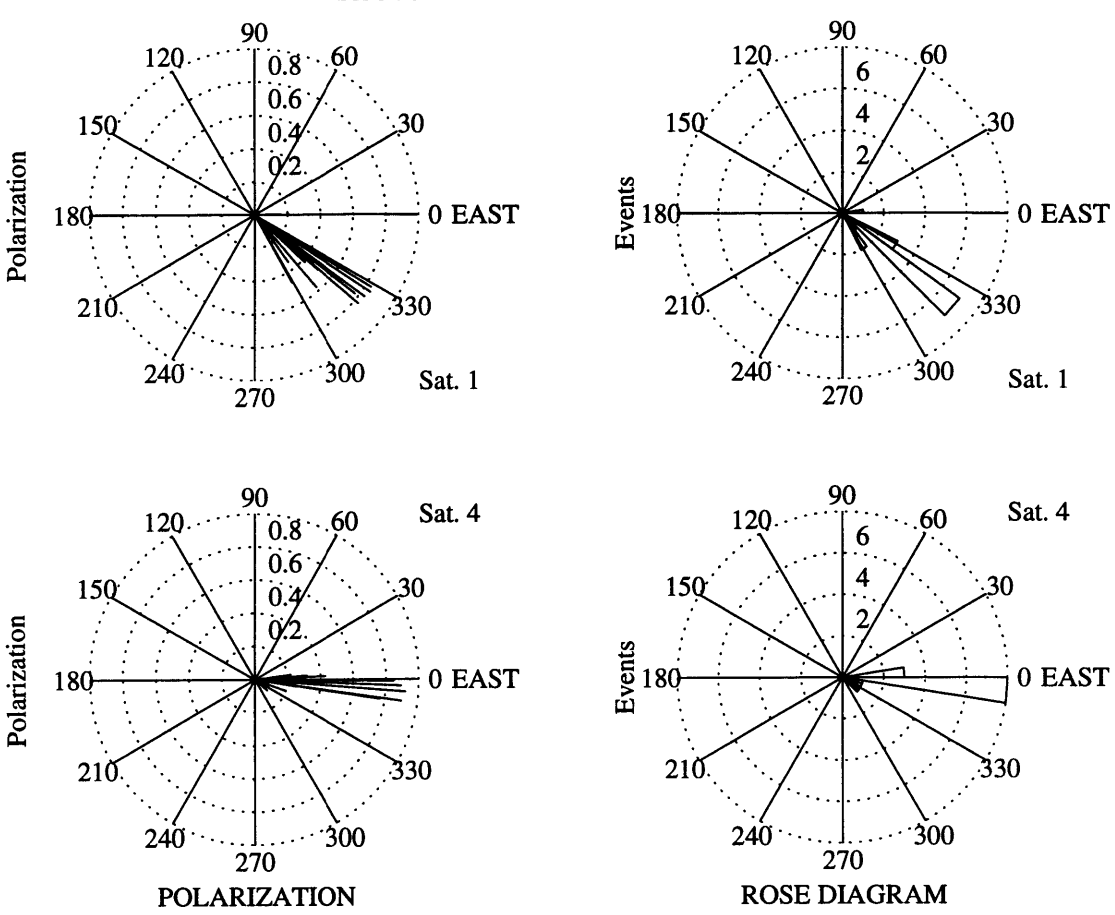
SHOTS 6437: POST-STORM: 0.3-0.4 Hz
Polarization
Events
90
120
60
150
30
180
0 EAST
210
330
240
300
270
0.8
0.6
0.4
0.2
6
4
2
Sat. 1
Sat. 4
POLARIZATION
ROSE DIAGRAM

Figure (3.25a)

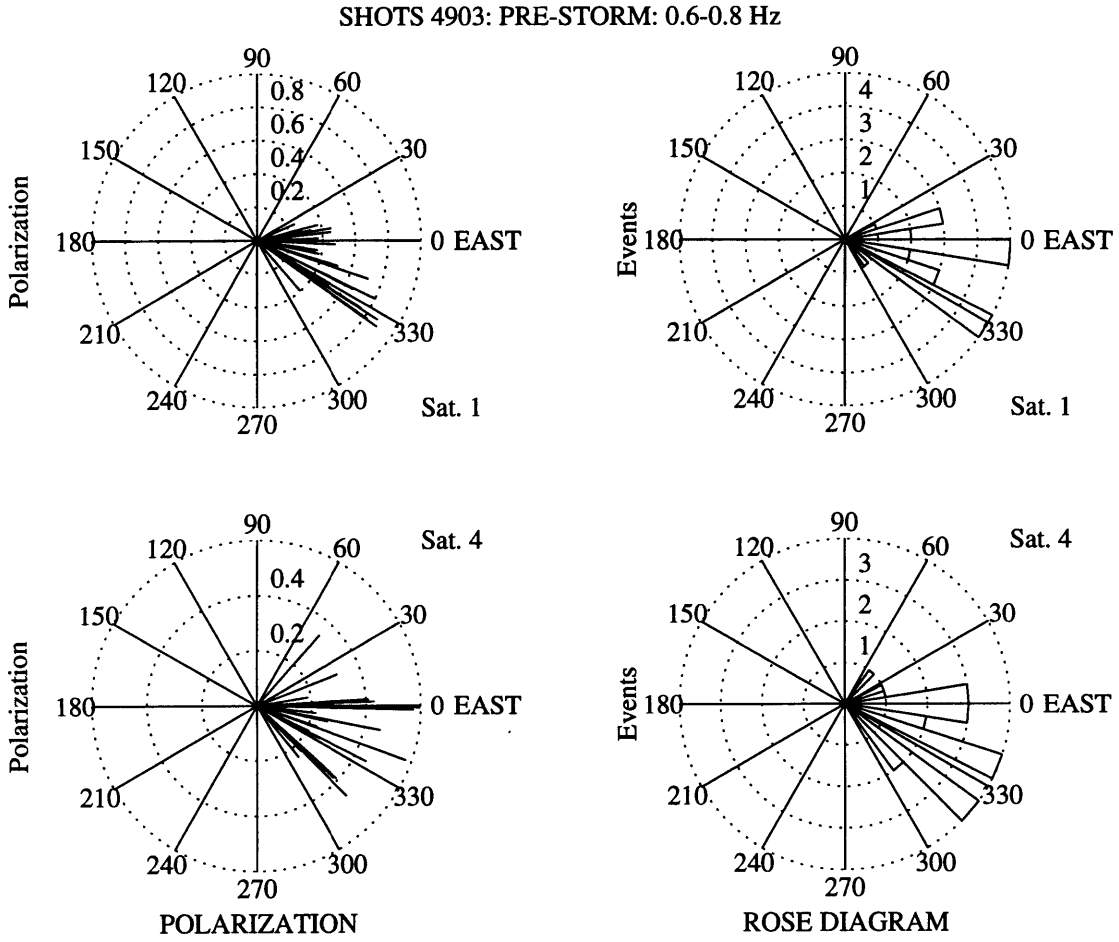


Figure 3-25: Polarization azimuth and rose plots for energy near the broad band peak (0.6-0.8 Hz) for pre-storm (3.25a), syn-storm (3.25b) and post-storm (3.25c) representative shot files. The polarization azimuth magnitudes are weighted by the degree of polarization computed. The rose diagram shows the respective density of azimuth falling within a directional "pie-slice". Each azimuth represents the direction of a particular frequency. The bandwidth from 0.6 to 0.8 Hz was divided into 28 discrete frequencies.

Figure (3.25b)

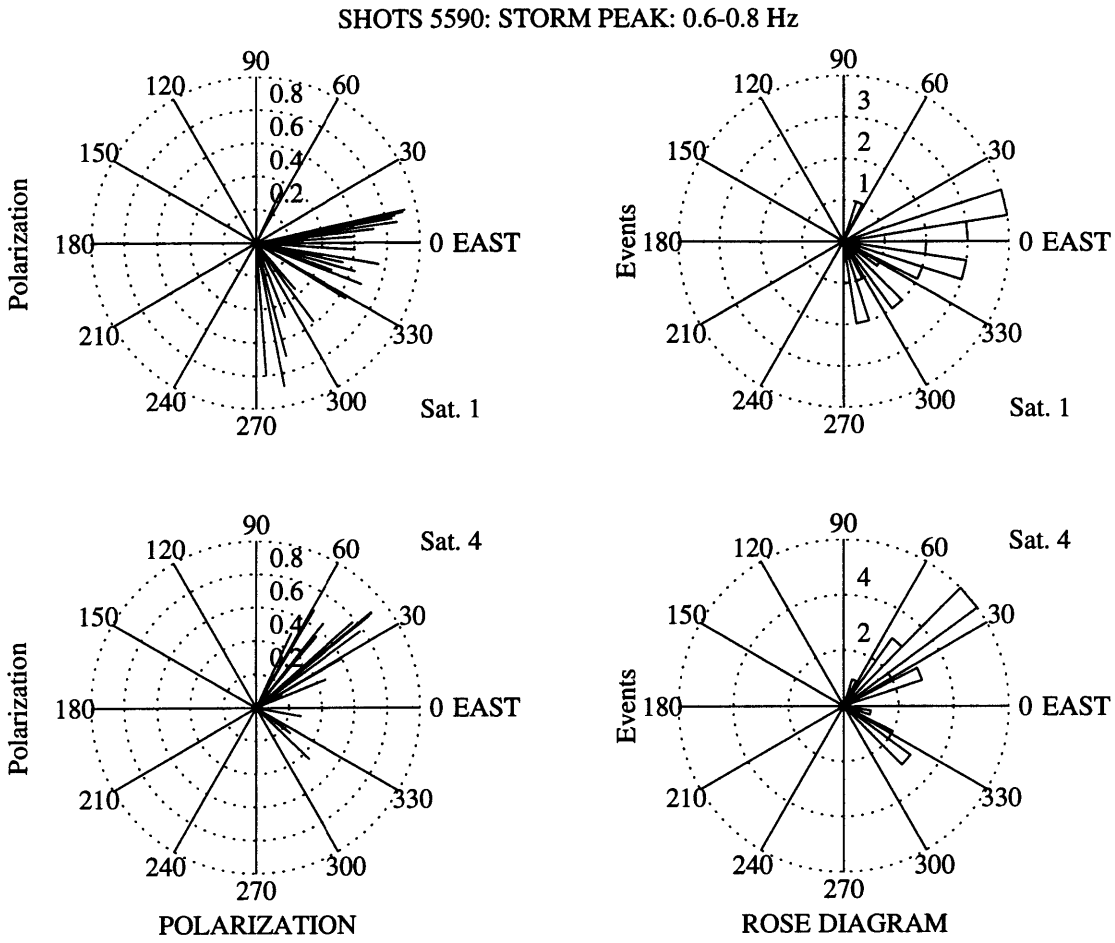
SHOTS 5590: STORM PEAK: 0.6-0.8 Hz
Polarization
Events
90
120
60
150
30
180
0 EAST
210
330
240
300
270
0.8
0.6
0.4
0.2
3
2
1
4
Sat. 1
Sat. 4
POLARIZATION
ROSE DIAGRAM

Figure (3.25c)

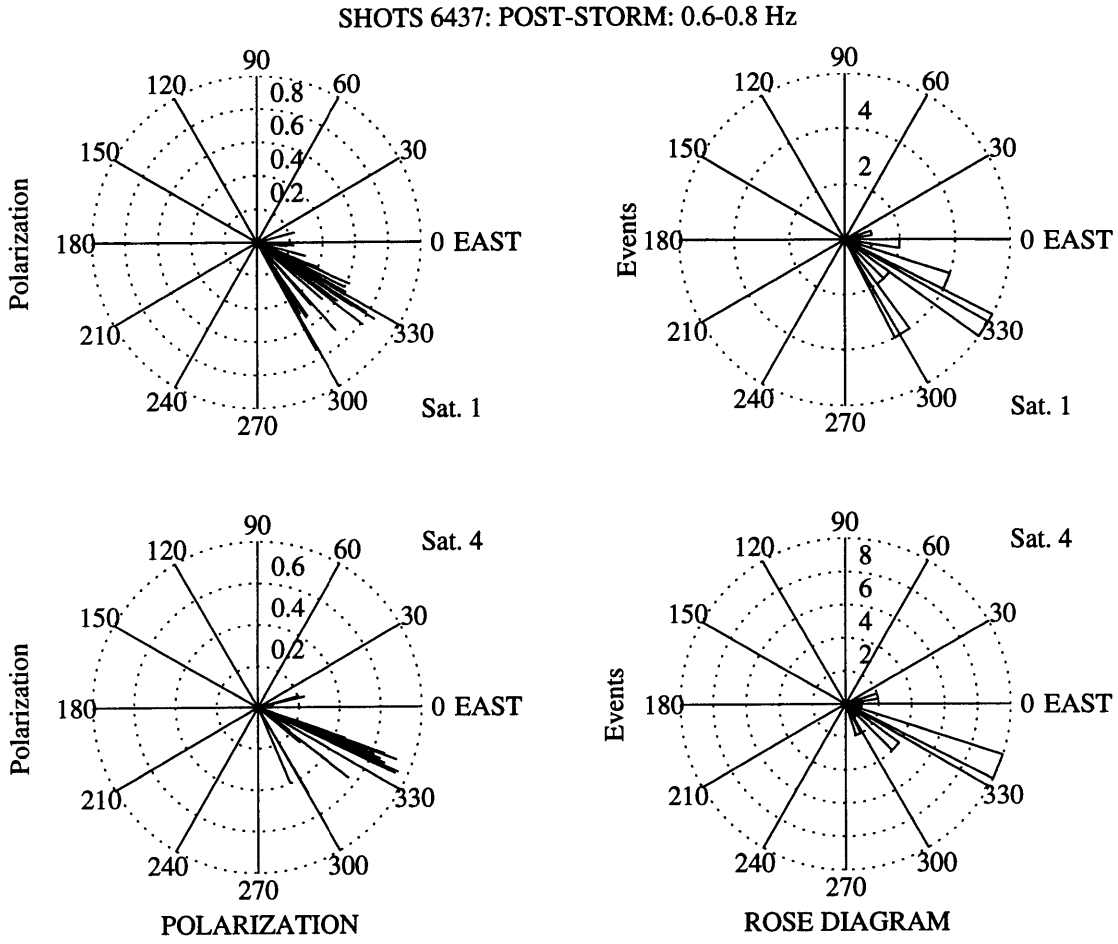
SHOTS 6437: POST-STORM: 0.6-0.8 Hz
Polarization
Events
Sat. 1
Sat. 4
0 EAST
90
120
60
150
30
180
210
330
240
300
270
0.8
0.6
0.4
0.2
4
2
8
6
POLARIZATION
ROSE DIAGRAM

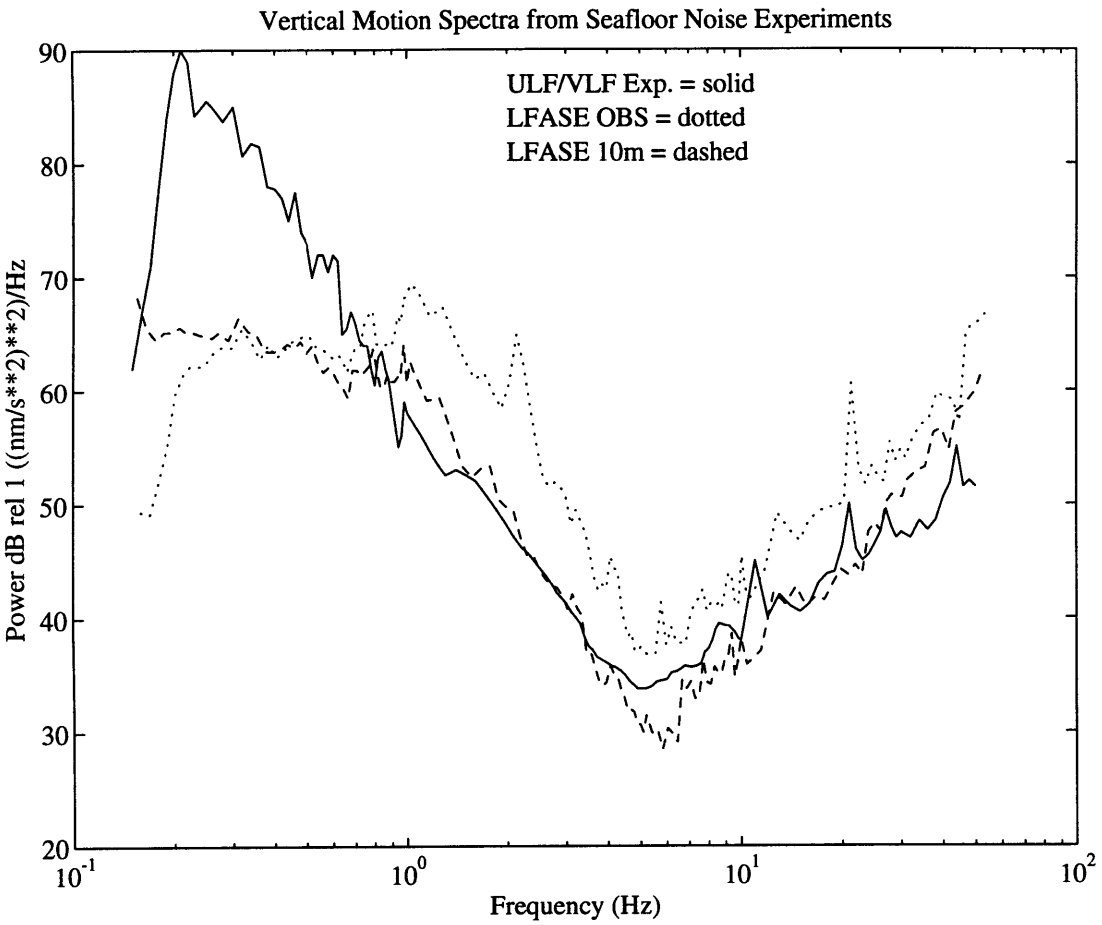


Figure 3-26: A comparison of different oceanic noise spectra (vertical acceleration). The solid line is from a GURALP long period instrument off the coast of Oregon (ULF/VLF Experiment, Duennebier, personal communication), the dotted line from the LFASE OBS, dashed line from the SEABASS 10 m satellite and dash-dot line is data from the 100 m SEABASS satellite.

# Chapter 4

# Wave Propagation and Scattering in 3-D Heterogeneous Media

## 4.1 Introduction

Several questions about ambient noise arise from the theory and data presented in Chapters 2 and 3. There are three fundamental questions pertaining to the seismic observations:

- What is the **source** of the noise?
- How is the source energy **coupled** to the sea floor?
- How does the energy **propagate** through the crust?

We can draw several conclusions about the ambient noise source from the data analysis in Chapter 3. We observe in this thesis that groups of similar period ocean gravity waves interact nonlinearly at the sea surface to generate a second order acoustic wave at twice their frequency. Data from the LFASE experiment show that the noise field is strongly correlated with local sea state and that the primary **source** of the ambient noise is directly linked to the sea surface conditions. In Chapter 2 elastic wave theory for an acoustic source in the water column is presented and the process by which acoustic waves are coupled to the sea floor is looked at in detail. Elastic body and interface waves are produced by an acoustic source interacting with a flat, infinite, homogeneous sea floor. These interface waves along with acoustic normal modes of the ocean/sea floor waveguide represent the

probable **coupling** mechanisms between noise in the ocean and seismicity in the oceanic crust. Kuperman and Schmidt (1989) estimate that there is no direct coupling of acoustic normal modes above 1.0 $Hz$ but that at lower frequencies normal modes can directly couple energy into the sea floor. But what are the **propagation** mechanisms of noise in the upper oceanic crust? In this chapter we investigate the propagation of noise in a heterogeneous crust using the method of finite differences.

Experience tells us that the ocean crust is not a simple flat homogeneous body. The ocean crust is (over a broad range of scales) rough and laterally heterogeneous at the water-crust interface (Menard, 1964; Goff and Jordan, 1988) and within its volume (Christensen and Salisbury, 1982; Collins et al., 1986). These lateral heterogeneities scatter seismic energy and affect the nature of the noise field in an area. Even low order lateral heterogeneities such as a shoaling bottom can have a profound effect on the ambient noise. Hasselmann (1962) states that microseismic energy in higher Rayleigh modes of a fluid-solid system necessarily convert to scattered energy as the ocean shallows and the energy propagates onto continental shelves.

This chapter is motivated by the evidence of scattering in the LFASE data. Particle motion behavior in the explosive shot data from LFASE (Stephen et al., 1993) shows that direct arrivals are well polarized in the direction of the shot, however the shot coda (often defined as signal generated noise) are scattered in all directions. During high sea states, the LFASE noise data show highly polarized energy below 1.0 Hz but more omnidirectional scattered noise at higher frequencies. Volume scattering seems unlikely in this region considering the laterally homogeneous appearance of the subsurface sediments (Bryan et al., 1980) and the thickness of the sediments. However, the shot and ambient noise energy may be scattered by surface roughness (observed by Hollister et al., 1974). This roughness consists of 1-100 m wide abyssal furrows superimposed on 2-4 km wide mud waves at the LFASE site. These surface heterogeneities have length scales near the Stoneley wavelength of the noise which makes them ideal scatterers (Aki and Richards, 1982). Considering the scattered energy observed in the data and the topographic roughness at the LFASE site it seems that a study of the three dimensional scattering processes is warranted in the treatment of ambient noise.

Most numerical seismo-acoustic models of the ocean crust are two dimensional or pseudo-three dimensional (e.g. radially symmetric). For practical arguments these are

reasonable models of the ocean/sea floor system considering memory and computational limitations. But propagation and scattering is a three dimensional process in the ocean crust. Out-of-plane energy such as diffracted acoustic waves, SH body waves and guided Love waves are not considered by these two dimensional schemes even though this energy may comprise a significant portion of the seismo-acoustic field. We address this limitation by studying small scale (20 $\lambda$ per side) three dimensional models of the ocean sea floor environment. Liu (1992) has developed a method for modeling the scattered field from a statistically rough interface generated by a statistically distributed source at the sea surface. His method involves only single scattering from random heterogeneities which may under-estimate the scattered field. (Wavelength ($\lambda$) is taken in water at the dominant source frequency. The symbol $\lambda$ is now used to indicate wavelength where previously it has been used as a Lamé parameter).

The results from modeling wave propagation through a three dimensional heterogeneous oceanic crust are shown in this chapter. We will look in detail at the results from wave scattering off volume and surface heterogeneities in the ocean crust. In particular, scattering differences between two and three dimensional approximations of bottom topography are compared. These models start simply with a flat homogeneous sea floor model. The models become more complex first by including volume heterogeneities, then single facets and finally rough sea floor approximations.

## 4.2 Background

The finite difference approximation to the elastic wave equation has proven to be an effective computational method for modeling the sharp contrast in Poisson's ratio that exists at the ocean/sea floor interface (Stephen, 1983). The method is preferred over others because arbitrarily complex media (i.e. media whose heterogeneities in elastic paramenters exist on scale lengths ranging from much less than a wavelength to several wavelengths) can be modeled. The resulting seismograms are a complete solution to the elastic wave equation including all converted phases, diffractions, multiple scattering and caustics. Frankel and Clayton (1984, 1986) have used this method to compute seismograms for random elastic media. For them, the finite difference method was the most versatile, allowing a much more finely described media and an arbitrary placement of source and

receiver.

The ability of this technique to accurately model deterministic sea floor features such as faults scarps, valleys and hills is reported by Stephen (1983), Stephen (1984) and Dougherty and Stephen (1991). Using a 2-D second order algorithm Dougherty and Stephen find that sea floor topography with scale lengths greater than the water acoustic wavelength will convert a significant amount of the incident energy into subsurface shear and interface waves. They also find that steep topography allows compressional and especially shear energy to enter the sea floor even at great ranges where incident angles exceed the critical angle. A fully 3-D second order finite difference code was developed by Burns and Stephen (1990) and used to model idealized fault scarps, sea floor channels and seamounts. Their results show that out of plane scattering is significant for even simple sea floor features.

Dougherty and Stephen (1988) used the finite difference technique to model laterally heterogeneous media beneath a flat sea floor. One of their results show that there are significant differences in the scattered field between Gaussian and self-similar realizations of a heterogeneous sea floor. For Gaussian models, random scatter increased as the product of the spatial wavenumber, k, and the correlation length of the media heterogeneities, a, approaches 1. When ka = 1 scattering is greatest. Because, by definition, self-similar models contain some heterogeneity uniformly across a range of scale lengths their seismograms show scattering effects over a range of scales.

This study presents the results from a fully 3-D finite difference model of the heterogeneous elastic wave equation. With this method we are able to quantify the contribution of out-of-plane energy contributing to the scattered field. These include 3-D diffractions, multiple scattering and perhaps most importantly Love and SH wave propagation. The models presented represent both deterministic and random sea floor roughness and lateral volume heterogeneities. The next sections begin with an overview of the numerical methodology used and then present the modeling results. The final section summarizes the modeling. We find in hard bottom environments that surface roughness has a more important effect on both acoustic backscatter and sub-bottom scattering than volume heterogeneities. The majority of the reverberant energy in rough hard bottom models appears to be converted SH and SV energy. In contrast, soft bottoms with similar scale volume heterogeneities can scatter significant amounts of energy back into the water column.

## 4.3 The Elastic Wave Equation and the Finite Difference Method

The system of equations we wish to solve are the elastodynamic equations of motion written below:

$$\begin{aligned}
\rho\frac{\partial^2 u_x}{\partial t^2} &= \frac{\partial \tau_{xx}}{\partial x} + \frac{\partial \tau_{xy}}{\partial y} + \frac{\partial \tau_{xz}}{\partial z}, \\
\rho\frac{\partial^2 u_y}{\partial t^2} &= \frac{\partial \tau_{xy}}{\partial x} + \frac{\partial \tau_{yy}}{\partial y} + \frac{\partial \tau_{yz}}{\partial z}, \\
\rho\frac{\partial^2 u_z}{\partial t^2} &= \frac{\partial \tau_{xz}}{\partial x} + \frac{\partial \tau_{yz}}{\partial y} + \frac{\partial \tau_{zz}}{\partial z},
\end{aligned} \tag{4.1}$$

with the symmetric stress tensor $\tau_{ij}$ (where $\tau_{ij} = \tau_{ji}$) defined by,

$$\begin{aligned}
\tau_{xx} &= (\lambda+2\mu)\frac{\partial u_x}{\partial x} + \lambda\frac{\partial u_y}{\partial y} + \lambda\frac{\partial u_z}{\partial z}, \\
\tau_{yy} &= \lambda\frac{\partial u_x}{\partial x} + (\lambda+2\mu)\frac{\partial u_y}{\partial y} + \lambda\frac{\partial u_z}{\partial z}, \\
\tau_{zz} &= \lambda\frac{\partial u_x}{\partial x} + \lambda\frac{\partial u_y}{\partial y} + (\lambda+2\mu)\frac{\partial u_z}{\partial z}, \\
\tau_{xy} &= \mu(\frac{\partial u_y}{\partial x} + \frac{\partial u_x}{\partial y}), \\
\tau_{xz} &= \mu(\frac{\partial u_z}{\partial x} + \frac{\partial u_x}{\partial z}), \\
\tau_{yz} &= \mu(\frac{\partial u_z}{\partial y} + \frac{\partial u_y}{\partial z}),
\end{aligned} \tag{4.2}$$

In equations ( 4.1) and ( 4.2), $u_x$, $u_y$, $u_z$ are the displacements in the $x$, $y$ and $z$ direction, $\rho$ is the local material density, $\lambda$ and $\mu$ are Lamé elastic parameters and $t$ is time. This system of equations represents the propagation of elastic waves in a three-dimensional heterogeneous isotropic body.

The finite difference method involves the spatial and temporal discretization of partial or ordinary differential equations on a regular grid. The wave equation is a second order, homogeneous linear differential equation which may be discretize in many ways (see Fornberg, 1987, for a comparison of different methods). Burns and Stephen (1990) have coded the method outlined in Virieux (1984; 1986). We have used their code and method in this thesis. The wave equation is discretized using a "staggered grid" scheme with centered differences. In Virieux (1986) the wave equation is differenced as a first order system in terms of velocity $\frac{\partial u_x}{\partial t}$, $\frac{\partial u_y}{\partial t}$, and $\frac{\partial u_z}{\partial t}$ and stress $\tau_{ij}$. The method was modified in two

dimensions into a second order system of particle displacements and stresses by Stephen (1988) and then in three dimensions by Burns and Stephen (1990).

Figure (4.1) (from Burns and Stephen, 1990) shows a schematic of the three dimensional staggered discretization grid and is a direct extension of the two dimensional grid given by Virieux . Note that the vertical and horizontal displacements are defined at different points within the grid and each has its own subgrid staggered in space with respect to one another. Additionally, the stresses and stiffness constants are defined at another set of subgrids staggered by 1/2 grid spacing. The seismograms produced by this method are accurate to second order for sea floor modeling (Virieux, 1986; Dougherty and Stephen, 1988). The major advantage to using staggered grids is the improvement of the stability condition. Prior to Virieux (1986) the common finite difference schemes were unstable for rough fluid/solid boundaries (Stephen, 1988). Assuming the solution of the wave equation has the form $e^{(i\vec{k}x - i\omega t)}$ (i.e. using the Fourier mode method) the stability condition becomes:

$$V_p \cdot \Delta t \sqrt{\frac{1}{\Delta x^2} + \frac{1}{\Delta y^2} + \frac{1}{\Delta z^2}} < 1 \tag{4.3}$$

where $V_p$ is the P-wave velocity. From equation ( 4.3) we see that stability of the system relies on the P-wave velocity only, making the staggered grid method most appropriate for modeling fluid-solid boundaries where the contrast in shear wave velocity is infinite. If $\Delta x = \Delta y = \Delta z$ then the time step size is limited by the maximum P-wave velocity:

$$\Delta t \leq \frac{\Delta x}{\sqrt{3} V_{p_{max}}}. \tag{4.4}$$

Given a stable scheme, grid dispersion becomes the most serious source of numerical noise. To minimize the effects of grid dispersion the media must be sampled at between 8 and 30 grid points per smallest wavelength within the model (Kelly et al., 1976; Dablain, 1986). For a two-dimensional staggered grid scheme, Prange (1989) (from the expressions for stability, phase and group velocity) computed the velocity error which arises when the medium is too coarsely sampled. His expressions show that for our reference model of the ocean sea floor system ($\frac{V_{p_{water}} = 1.5\ km/s}{V_{p_{seafloor}} = 4.0\ km/s}$) we must have at least 12 points/wavelength to keep phase velocity errors below 1.0 % and group velocity errors below 4.0 %. We have chosen a minimum sampling of 12.5 points/(acoustic wavelength) in the results presented below. (Note that for the soft bottom models the sampling is only 3.75 points/(shear wavelength) but the model remains stable due to the stability of the staggered grid scheme).

### 4.3.1 The Algorithm

The model is divided into three zones in order to minimize the storage and computational requirements. In all the subsequent model runs, the medium has both a homogeneous fluid zone and a homogeneous solid zone, each with some finite thickness. Between these two zones lies a transitional heterogeneous zone within which the elastic parameters can be varied spatially (for heterogeneity). With some modification and considerable increase in storage requirements a directionally dependent stiffness matrix can be assigned to each grid location (for anisotropic media) (Winterstein, 1990). Figure (4.2) is an illustration of the modeling zones. There is no need to treat the boundaries between zones explicitly because the equations for homogeneous and heterogeneous media (Equations 4.1 and 4.2) are identical. The difference between homogeneous and heterogeneous regions in the code is only the storage of the wave velocities and density in the heterogeneous case. Within the heterogeneous zone any interface or velocity distribution can be implicitly modeled subject to time step and discretization restrictions. (Errors due to the inaccurate discretization of rough interfaces was explored by Dougherty and Stephen (1991). They found that microroughness created by discretizing a curvilinear horizon on a rectangular grid created backscatter and generation of interface waves.)

The displacement and velocity are set to zero for the grid initial conditions. A point dilatational source is then introduced by analytically calculating the displacement field throughout a rectangular prism and applying this displacement field to the grid. The source field is computed for a small time after $t = 0$. This avoids singularities at the source point. The point source method is developed in Nicoletis (1981) and used in two dimensional Cartesian sea floor models by Dougherty and Stephen (1988; 1991) and in radial coordinates for borehole acoustic modeling by Stephen et al., (1985). Burns and Stephen (1990) have extended the technique to three dimensional Cartesian sea floor models. The source function is derived from the solution to the wave equation for a compressional displacement potential:

$$\phi(\mathbf{R},t) \;=\; \frac{A}{4\pi\rho {V_p}^2 \mathbf{R}}\, g(t \;-\; \frac{\mathbf{R}}{V_p}) \tag{4.5}$$

where $\mathbf{R} = \|\sqrt{x^2 + y^2 + z^2}\|$ is the distance from source to receiver, $A$ is a unit constant

with dimensions of (mass x length$^2$/time) and $g(t)$ is chosen as a Gaussian time function:

$$g(t) \;=\; -2\xi T\, e^{-\xi\, T^2} \tag{4.6}$$

where $T \;=\; t - t_s$ is the time shift function. The vector displacement field ($\vec{u}$) due to a point compressional potential is the gradient of the potential where

$$\vec{u}(x,y,z,t) \;=\; (\partial\phi/\partial x, \partial\phi/\partial y, \partial\phi/\partial z)$$

and from equations ( 4.5) and ( 4.6):

$$\vec{u}(x,y,z,t) \;=\; \begin{pmatrix} x \\ y \\ z \end{pmatrix} \frac{-A}{4\pi\rho {V_p}^2\, \mathbf{R}} \left( \frac{g(t \,-\, \frac{\mathbf{R}}{V_p})}{\mathbf{R}^2} \;+\; \frac{g'(t \,-\, \frac{\mathbf{R}}{V_p})}{\mathbf{R}\, V_p} \right), \tag{4.7}$$

where $g'(t \,-\, \frac{\mathbf{R}}{V_p}) \;=\; -2\xi(1 \,-\, 2\xi T^2)\, e^{-\xi T^2}$. These displacements are then applied to the grid using a spatial scaling function (Nicoletis, 1981).

The boundary conditions are designed to take advantage of natural symmetries in the model sea floors. The source is introduced along the $z - axis$ ($x \;=\; y \;=\; 0$) (Figure (4.3)). The vertical $xz$- and $yz$-planes through the source are planes of symmetry. A simple flat ocean floor is shown as the shaded horizontal $xy$-plane. Absorbing boundaries are applied along the planes defining the maximum edges of the model (i.e. $x \;=\; x_{max}$; $y \;=\; y_{max}$; $z \;=\; z_{max}$ are absorbing boundaries) and the $z \;=\; 0$ plane at the top of the model. In the four absorbing boundary regions we use the telegraph equation over a 25 node absorbing region near the boundary (Emerman and Stephen, 1982; Levander, 1985; Cerjan et al., 1985). In this region a damping term is applied to the wave equation whose damping coefficient is increased using a cosine weighting toward the boundary. The damping coefficient is empirically balanced to minimize reflections from the front edge of the damping region and to effectively absorb most of the energy within the damping zone. In three dimensions, there is a great sacrifice of usable model space due to these absorbing boundaries so models are constructed carefully to take advantage of the symmetry planes.

Finite difference algorithms compute the displacement of an individual node based on displacements from neighboring nodes. The complete solution of the problem can be seen in "snapshot" form for any time step at any plane in the model. These snapshots are

referred to as numerical Schlieren diagrams. In the results that follow Schlieren diagrams of the compressional and shear amplitude densities ($-\sqrt{\lambda + 2\mu}\ \nabla \cdot \vec{u}$ and $-\sqrt{\mu}\ \nabla \times \vec{u}$ respectively) are shown to display particular features of the wave field. The divergence and curl of the displacements are computed along cross-sections through the model and are related to the compressional and shear wave energies by (Morse and Feshbach, 1953):

$$E_c = (\lambda + 2\mu)\,(\nabla \cdot \vec{u})^2 \tag{4.8}$$

$$E_s = \mu\,(\nabla \times \vec{u})^2. \tag{4.9}$$

Time series data at individual grid points can also be stored as output from the finite difference code. The pressure and/or displacement response is recorded along lines of computational nodes in the model in order to simulate the response of seismic arrays (see Figure 4.3).

## 4.4 Post Processing: Calculations in $\tau - p$ Space

The time series records or seismograms mentioned above are used to estimate the scattered field by transforming them into $\tau - p$ space. The $\tau - p$ transform is a method of transforming the seismic data, $\vec{u}(\vec{x}, t)$ (recorded in offset and time) into its plane wave representation, in slowness and independent time intercept $\tilde{u}(p, \tau)$. This transform is commonly referred to as a "slant-stack" or Radon transform. We use this method to compute the angular scattering strength for all of the test models.

Though we model the data in three dimensions, memory restrictions make it impractical to collect the time series over the entire 3-D space. We have chosen to compute the scattered field along linear arrays limited to the $XZ$-midplane of the model. Our justification for this is not only memory considerations but the desire to directly compare scattering from two- and three-dimensional realizations of a particular model. The two dimensional Radon transform is defined (Chapman, 1978, 1981):

$$\tilde{u}(\tau, p) = \int_{-\infty}^{\infty} \vec{u}(\tau + px, x)dx. \tag{4.10}$$

For a 2-D geometry the field $\tilde{u}(\tau, p)$ is the exact plane wave decomposition of the data. Mathematically, the $\tau - p$, Radon transform is a linear invertible transform and its properties and applications for seismic interpretation have been thoroughly studied (Durrani

and Bisset, 1984; for oceanographic data applications see Stoffa et al., 1981 and Kappus et al., 1990).

Fricke (1991, 1993) outlines a method for calculating the Radon transform on "serpentine" arrays (i.e. linear arrays lying in a plane but not necessarily aligned in a single direction). His method is an extension of the normal Radon transform which allows corrections due to the different phase alignment of linear array segments aligned along different azimuths. The serpentine Radon transform reduces up-down hemispheric ambiguity in the stack by discriminating wave propagation direction as well as phase angle across the array (Fricke, 1991). Using Fricke's equation (4.46) we find equation ( 4.10) becomes:

$$\tilde{u}(\tau, p) = \int_{\vec{x}_s} A(\vec{x}, p)\vec{u}(\tau + p\vec{x}, \vec{x})dS \tag{4.11}$$

where $\vec{x}_s$ is the location along the integration path $S$. $A(\vec{x}, p)$ is a normalization factor which compensates for the addition of different array segments. Equation ( 4.11) is the Radon transform used in this thesis.

Figure (4.4) is an illustration of the model array locations (upper diagram). The definition of $\theta$ for a single plane wave measured by an 'L'-shaped portion of the serpentine array is illustrated in the figure (lower diagram). Here horizontal ray-parameter, $p = \frac{sin\theta}{c}$, remains constant along a given ray path. In the water column we will assume, $c$, the phase velocity is a constant and $\theta$ is the wave field propagation angle (defined with respect to the horizontal). We can see from the figure that the phase speed across the horizontal array is $\frac{c}{sin(\theta)}$ or $\frac{1}{p}$ and phase propagation along the vertical array is $\frac{c}{cos(\theta)}$ or $\frac{1}{(\frac{1}{c^2} - p^2)^{\frac{1}{2}}}$. The vector representation of $p$ in the $XZ$-plane is:

$$p = \begin{pmatrix} p \\ \pm(\frac{1}{c^2} - p^2)^{1/2} \end{pmatrix} = \frac{1}{c}\begin{pmatrix} sin(\theta) \\ cos(\theta) \end{pmatrix}. \tag{4.12}$$

The complete serpentine array (i.e. the two vertical segments joined by a horizontal segment) is orthogonally projected element by element onto a "virtual" array at a specified angle $\theta$ in the $XZ$-plane. The projection of the serpentine array onto 11 different angles is illustrated in Figure (4.5).

The $\tau - p$ stack is carried out by:

- Projecting the serpentine array elements onto a given propagation angle ($\theta$ or $p$).
- Sorting the projected elements into monotonic order in the $\theta$ direction.

- Delaying (or advancing) the time series for each point by the time corresponding to the shift to its new location.

- Integrating (summing) along the projected arrays. This step is a trapezoidal integration using the inter-element spacing of the projected elements.

- For each ray parameter, the RMS level is computed in time to give a single scattering coefficient.

This process taken as a whole is the same as "beam-forming" an arbitrary array of receiver nodes.

It should be noted here that because of the symmetry planes in the finite difference code the receiver array is placed near the model plane of symmetry. As a result, the out of plane energy calculated using the serpentine array will be under-estimated. For our computation of horizontally polarized (in the solid) and out of plane (in the water) energy we use a single vertical array placed off the symmetry axis (Figure 4.21).

## 4.5 Models and Results

As mentioned at the beginning of this chapter, a significant portion of the noise field above 1.0 $Hz$ in the Blake Bahama Basin contains scattered energy from many directions. We know that backscattering requires either volume or surface heterogeneities to scatter the incident wave field. The simplest heterogeneity to model is a step change in velocity and in the ocean basin this first order change in velocity is most strongly represented at the water-sea floor interface or at the interface between sea floor sediments and basaltic crust. Near this interface the sea floor can have buried heterogeneities or exposed surface roughness like that seen near mid ocean ridge axes. There is a great difference in propagation and scattering mechanisms between "soft" sea floors (i.e. those sea floors whose shear velocity is less than the pressure wave in the water column) and "hard" sea floors (i.e. sea floors with a shear velocity greater than the acoustic water wave) (Strick, 1959; see Chapter 2 of this thesis). This is primarily due to the degree of penetration (or transmission) of the direct wave into the subsurface, the differences in interface wave propagation and the scale of the volume heterogeneities in the sub-bottom.

We present a logical trend in complexity from (1) flat homogeneous sea floors to (2) simple facets to (3) statistically varied volume and surface heterogeneities. Both hard and soft bottom sea floors are modeled for each of these test cases.

### 4.5.1 Flat Sea Floor

#### Flat Hard Bottom

In Figure (4.3) the shaded horizontal plane indicates a uniformly flat sea floor with the source located along the $x = 0, y = 0$ edge of the model. Synthetic seismograms were collected along the diagonal array shown in the figure as well as along the serpentine array shown in Figure (4.4). The dimensions of the model are scaled in terms of ($\lambda$) the wavelength at peak frequency of the source in water. The water depth is 7.6 $\lambda$ and the crustal depth is 2.4 $\lambda$. Water velocity is 1.5 $km/s$ and the crust has P- and S-wave velocities of 4.0 and 2.3 $km/s$ respectively. The density for the water and crust are 1.0 and 2.3 $gm/cc$. This model identified further as the "Flat Hard Bottom" model (FHB), is used as a control against which the subsequent scattering models are compared.

A point source is introduced 3.6 $\lambda$ above the sea floor and numerically propagated in time through the model; snapshots and time series were collected as the wave propagated. Figure (4.6) is a snapshot 12 periods after the source initiation for the wave field in the $XZ$- and $XY$-plane. The top diagram shows the P-wave field in the $XZ$-plane and energy partitioning occurs as the direct wave interacts with the sea floor in the model. Table (4.1) summarizes the numbering scheme for the various wave types. For this model in the P-wave field one can identify (1) the direct wave, (2) the sea floor reflection, (3) the P-head wave, (4) the direct wave root, (5) numerical dispersion and boundary reflections and (6) the S-head wave (see Dougherty and Stephen, 1988 for a discussion of these wave types). The transmitted P-wave (7) in the bottom is not visible in the top snapshot because it has propagated out of the frame. The middle snapshot in Figure (4.6) shows the S-wave field in the $XZ$-plane. Displayed amplitudes are multiplied 10 fold to show the wave types present. In this figure the converted S-wave from the direct wave root (4) is shown along with the transmitted S-wave (8) and a series of shear converted direct wave roots excited by the dispersive waves (5). The lower snapshot shows the P-wave amplitude in a horizontal plane (i.e. map-view) approximately 1/2 $\lambda$ above the sea floor. The direct

(1) and reflected (2) waves are clearly seen with some numerical dispersion (5). The head wave (3) should be present at about 20 /*lambda* but is not discernible at this gray scale.

In order to approximate a plane wave at a high angle of incidence, the experiment is designed to minimize the energy directly propagated by the crust. This is made possible by placing the source at least 10 $\lambda$ (a minimum far field approximation) from the seismic arrays. For a source height of 3.5 $\lambda$ this gives an incidence angle at the base of the near array of 18°. The steeply diving transmitted energy is absorbed within the damping region at $z = z_{max}$.

The pressure response of the nearest vertical array of seismometers is shown in Figure (4.7). Clearly we see the direct wave (1), sea floor reflection (2), and a low amplitude P-head wave (3) above the sea floor. Below the sea floor both the transmitted P-wave (7) and direct wave root (4) are very low amplitude relative to the water born arrivals. Arriving behind the sea floor reflection, high frequency grid dispersion "ripples" and a boundary reflection from the $y = y_{max}$ plane (5) disturb the seismogram.

All of these direct and converted waves are present to varying degrees in the subsequent models. A scattering diagram computed via the $\tau - p$ method shows plane wave energy in dB (unnormalized) versus propagation angle ($\theta$) in degrees (Figure 4.8) at the array. The three major components of the seismogram are seen: (1) the direct wave near 10°, the sea floor reflection at 30° and P-head wave between 60° and 70° (The particular angle is $\sim 68°$). The direct wave is not well represented as a discrete plane wave. This appears in the energy-propagation angle plot as a smearing of energy between 0° and 20°. The aliased arrival from the sea floor reflection is labeled (2*) and arrives at 170° (i.e. the backscattered compliment to (2)). This aliased arrival provides a rough measure in the reduction of hemispheric ambiguity. Comparing the aliased and true sea floor reflection peaks, there is a 15 $dB$ improvement over the single array scattering estimate. Scattering diagrams from more complicated models are referenced to these values to determine forward and backward scatter relative to the FHB model.

## Flat Soft Bottom

The material properties of the model crust were changed to mimic the soft sediment bottom commonly observed in abyssal plains, sediment ponds and continental margins.

Very low shear modulus sediments along the ocean bottom have shear velocities much slower than the compressional wave velocity of the water and are defined as "soft bottom" sediments. The consequences of a soft bottom are several: the pseudo-Rayleigh interface wave cannot exist, the incident wave is always pre-critical for the transmitted S-wave and the sea floor reflection is weaker due to the smaller contrast in Poisson's ratio.

Figure (4.9) shows the $XZ$- and $XY$-plane wave field snapshots for a flat soft bottom model (FSB) with P- and S-wave velocities of 1.70 and 0.45 $km/s$ respectively. As before, the snapshots are taken 12 periods after the source initiation. Because of the lower velocity contrast between the water and crust, there is a discernible transmitted P-wave (7) in the upper snapshot and a transmitted shear wave (8) observable in the S-wave snapshot. The seismogram in Figure (4.10) is the pressure response of the nearest vertical array. It shows a smaller sea floor reflection and a strong transmitted P-wave. The scattering diagram in Figure (4.11) summarizes the difference between forward and backscattered levels relative to the hard sea floor. In this figure the hard flat bottom scattered field is subtracted out before plotting. From Figure (4.11) we see the scattered field for the SFB model falls below the hard bottom model. The relative forward scatter of acoustic energy into the water column is $3 - 7\ dB$ below than the FHB model due primarily to the weak bottom reflection.

### 4.5.2 Faceted Sea Floor

The next level of sea floor complexity invokes surface roughness. The main purpose of the following models is to estimate the difference in scattering from a $\lambda$ sized object that is constructed in two or three dimensions. The first model is a step in a flat hard bottom sea floor. The step, or 2D facet, has a relief of one $\lambda$ in $Z$ and extends "to infinity" in $Y$. The second model is a 3D facet in which the facet is limited in the $Z$ and $Y$ direction to one $\lambda$. In Figure (4.4) a schematic of the two models is shown. Notice in Figure (4.4) that the model 3D facet is made only $1/2\ \lambda$ thick because of the $y = 0$ symmetry plane.

#### 2D versus 3D Facets

A series of snapshots of the P-wave field is shown at increments of 6 periods in Figure (4.12). This view of the $XZ$-plane shows the same direct and converted phases as the

FHB model until the direct wave reaches the facet. A diffracted P-wave in the bottom (9) is generated at the facet face along with interface waves initiated at the facet edges (10). After 24 periods a diffracted P-wave in the water (11) is well established with the highest intensity normal to the facet face. The backscattered wave travels primarily as a diffraction off the corners of the facet. Stoneley waves (10) travel along the interface at a velocity just under the water wave velocity (1.42 $km/s$) and a backscattered P-head wave (12) is generated. The pressure measured across the vertical array is shown in Figure (4.13) and the relative strength of the backscatter can be directly compared to the direct and converted phases. The diffracted P-wave in the water (11) from the facet is a prominent arrival at 23 periods.

The 2D facet model was created to analyze the scattered field from a two dimensional continuous object while allowing the wave field to have correct three dimensional spreading. A truly three dimensional wavelength scale object is discontinuous in $y$. So in order to relate facet scattering in two and three dimensions a 3D facet model was tested to compare to the 2D results. Figure (4.14) shows incremental time snapshots for the 3D model. The major differences between the 2D and 3D model are that the backscattered head wave and facet reflection are much smaller. Comparison of the 2D and 3D vertical array seismograms show nearly identical direct and sea floor reflections but weaker diffractions from the facet (Figures 4.13 and 4.15). The facet diffractions in both models exhibit two out of phase high amplitude arrivals across the array which correspond to diffractions from the upper and lower facet corners.

It is easier to understand the differences in the 2D and 3D facets if scattering in the third dimension is observed. Figure (4.16) shows the P-wave field for both the 2D and 3D facets in a horizontal snapshot 18 periods after the source is introduced in the upper left hand corner. The snapshot is a slice in the $XY$-plane through the facet and shows the diffracted wave (11) traveling left away from the facet face. In addition to the lower amplitude backscatter, the 3D facet shows interface waves along the edges of the facet that are continually excited by the direct wave (1). Both the 2D and 3D facets show strong backscatter, however the location of the seismic arrays near the $XZ$ symmetry plane will not detect the full scattered field in the 3D case, however the array will detect the variation of vertically polarized energy due to out of plane scattering.

A scattering diagram in Figure (4.17a) summarizes the differences in forward and

backscatter between the two facet models. There is a 3.5 $dB$ stronger backscattered head wave for the 2D facet and the diffracted wave and the specular reflection are $1 - 2$ $dB$ greater. Overall both the forward and backscattered field are $1 - 4$ $dB$ greater for the 2D single facet model.

### 4.5.3 Volume Heterogeneities

Models were run to compare flat sea floors with volume heterogeneities for both hard and soft bottoms Figure (4.18a - b). The soft bottom models having volume velocity heterogeneities with a correlation length of approximately 0.3 $\lambda$ (corresponding to a $ka \approx 2$) and a standard deviation of 10% show the largest backscatter potential of the models tested (four models were tested: $ka = 6$, $\Delta V_p = 5\%$; $ka = 2$, $\Delta V_p = 5\%$; $ka = 6$; $\Delta V_p = 10\%$, $ka = 2$; $\Delta V_p = 10\%$). The snapshots in Figure (4.19) display the P-wave field for the two 3D models. Penetration of the direct wave into the soft bottom model can scatter a significant amount of energy back into the water column. This is primarily due to focusing of the transmitted P-wave (7) by the volume heterogeneities and then scattering (9). The snapshots also show a diffracted diving wave (15) generated as the transmitted wave enters the heterogeneous region (10 $\lambda$ to the right of the source) and then reradiates into the water column.

Tau-p analysis shows that forward scattered diffractions exceed the surface facet levels for both the hard and soft heterogeneous bottoms (4.17b).

#### 2D versus 3D Volume Heterogeneities

A two dimensional version of the 3D heterogeneous hard bottom model was created to compare with the 3D model. The 2D and 3D models show no discernible difference in backscatter into the water column. Figure (4.20) displays two snapshots (amplified 10 fold over those in Figure (4.19) 12 periods into the numerical run for a 2D and 3D hard bottom model with 10% volume heterogeneities. The scattered field from the flat hard bottom model is subtracted from the computed scattered field of the heterogeneous models (resultant fields shown in Figure 4.17). Because the incident energy fails to penetrate into the crust, the heterogeneities have little effect, however, Figure (4.17b) shows a relatively large scattering component from the diffracted P-wave (forward scatter between $40 - 60°$).

To address the accuracy of using 2D or 3D modeling for heterogeneous crust, an estimate of the amount of energy arriving from outside the source-receiver plane was made. A calculation of the "in-plane" versus "out-of-plane" scattering is made for the vertical arrays shown in Figure (4.21) for both the HHB and SHB models. This calculation is a ratio of the transverse component to the radial plus vertical component of displacement in an azimuthal plane containing both source and receiver. The results of this calculation for the "near axis" (i.e. near the model symmetry axis) vertical array (Figure 4.21) show that both HHB or SHB scatter less than 1% of the incident energy in the transverse direction above the sea floor. This result is expected from the forced symmetry of the model and because the direct wave contains the greatest amount of energy in the radial and vertical directions, a second calculation excluding the direct arrival is made by summing the component energies after the direct arrival has passed through the model. This estimate reveals that $\sim$ 6% of the reverberation is out of plane energy for the SHB and $\ll$ 1% of the reverberation is out of plane for the HHB. For the "off axis" array (Figure 4.22) the out of plane scattering for the SHB model is about 10% and the HHB model shows less than 5% out of plane scattering.

These estimates suggest that 2D modeling is probably 90% accurate (i.e. in estimating the total scattered field) for soft and hard bottom sea floors with wavelength sized heterogeneities and velocity variations of 10%.

### 4.5.4 Rough Sea Floor

The water-sea floor an sediment-basalt interfaces represent the strongest contrast in elastic parameters in the ocean crust. At mid ocean ridges sea floor roughness is extreme and it is an important source of scattering of seismo-acoustic signals. In the previous section it was determined that 2D models could reasonably estimate backscatter from a flat sea floor with smoothly varying velocity heterogeneities. In this section a statistically rough sea floor is modeled and its backscattering properties quantified in two and three dimensions.

Goff and Jordan (1988) developed a method for characterizing a rough sea floor using statistical methods to invert for a roughness covariance function from SEA BEAM data. The sea floor relief is assumed to be a zero mean Gaussian distributed process defined by an anisotropic two point covariance function. The covariance function has five free

parameters; the amplitude, orientation, characteristic width and length and the fractal dimension of the model sea floor. For the study presented below we use model parameters inverted from a "typical" region of the sea floor near the Mid Atlantic Ridge. The RMS amplitude of the topography is 0.43 $\lambda$, a characteristic width is 0.3 $\lambda$, the characteristic length is 0.9 $\lambda$ and the fractal dimension is 0.85. The orientation of the topography is elongated in the $Y$-direction so that the elongated ridges are in some sense the realization of the previously modeled facets.

As before, the model consists of a 10 $\lambda$ flat and homogeneous "spreading zone" before the wavefront enters the rough sea floor region. A detail of the Goff-Jordan (GJ) sea floor is shown in Figure (4.23) and its total relief is approximately 1.0 $\lambda$. We computed the sub-bottom scattering of P-, SV- and SH-waves on the horizontal plane illustrated in Figure (4.23).

### 2D versus 3D Rough Sea Floors

Two models were chosen to compare the effects of scattering in two and three dimensions. The first is a 2D realization of the GJ sea floor. This model was created by first generating a complete GJ sea floor (i.e. a 2D surface) and then selecting a cross-section in the $X-$direction (across the short dimension of the topographic ridges). This cross-section is then repeated in the $Y$-direction to form a model which varies only in $X$ and $Z$. The second model is the complete GJ sea floor described above.

A comparison between the 2D and 3D GJ models is made by observing the snapshot diagrams in Figures (4.24) and (4.25). These diagrams were made 18 periods after the source initiation and show the P- and S-wave field in the $XZ$-plane and the P-wave field in a horizontal plane cutting through the topography in the $XY$-plane.

In the 2D GJ model the backscattered field (11) in the upper P-wave snapshot (Figure 4.24) is stronger and more complex than the 2D facet model (Figure 4.12). Several discrete radiation points are seen on the rough interface. These act as sources (line sources in $y$) of diffracted energy into the water column. In the S-wave snapshot, forward and backward propagating Stoneley waves (10) correlate with the source points and also spawn scattered S-wave energy (14). A converted S-wave (8) is now visible in the bottom initiated by the P-diving wave. The lower snapshot shows the direct wave (1) at the point the snapshot

plane enters the topography. Scattered energy is seen as linear wavefronts both in front of and behind the direct wave.

The 3D GJ model (Figure 4.25) shows a larger scattered field than the 2D model. The $XZ$-plane snapshots look similar to the 2D model. However the reradiated diffracted energy (11) shows higher amplitude wavefronts and interference patterns in the 3D model. The scattered S-wave (14) is less coherent than the 2D model because the wave is initiated from irregular features that exist both in- and out-of-plane.

The reason for the strong backscatter is seen in the $XY$-plane snapshot. This snapshot plane cuts across the topography along the 0.5 $\lambda$ relief contour. Many discrete sources are identified in the snapshot. As interface waves propagate along the sea floor they excite acoustic waves in the water column, which then in turn rescatter off adjacent features in the surface relief. These features are numerous both in and out of the $XZ$-plane.

The scattered fields from the two models are shown in Figure (4.17c). Both models show a strong specular reflection from small scale facets in the surface relief (see specular backscatter peak in Figure 4.17b). Out of plane scattering is $3 - 5\ dB$ greater in the 3D GJ sea floor.

Figures (4.26) and (4.27) show the P-wave field across a vertical array in the 2D and 3D GJ model respectively. Scattering in both seismograms is large but the reverberation measure from the 3D GJ model is much greater. The reason for this increase in reverberation is discussed in the summary below.

## 4.6 Summary and Conclusions

The study of oceanic noise requires knowledge of the propagation and scattering of waves in the ocean crust. This chapter has been undertaken in order to understand mechanisms of scattering and their relative contribution to the propagation of seismo-acoustic noise. The previous models all show differences in their scattered fields. By breaking down the models to examine individual scattering parameters, the effects of these parameters on the scattering potential and propagation phases are determined.

The flat homogeneous sea floor models provide a reference against which the volume and surface heterogeneity models were compared. Relative to the Hard Flat Bottom (HFB) model the Soft Flat Bottom (SFB) sea floor was the only model to show a lower scattered

field. However, the SFB model did show penetration of energy into the subsurface which could then propagate as body and secondary head waves.

In order to quantify and summarize the sub-bottom scattering mechanisms for the heterogeneous volume and surface models, the SV-, SH- and P-wave energies were computed on a subsurface horizontal plane (Figure 4.23) for each of the model runs. This was done by calculating the SV- and P-wave component energies in the sagital plane containing the source and a receiver on the subsurface plane. Each grid point on the subsurface plane was considered a receiver. The SH-wave component energy was also calculated on the subsurface plane and the resultant SV-, SH-, and P-wave energies were then summed over the entire plane. The results of this calculation over model run time are shown in Figure (4.28). The curves are for the SHB, HḢB and the GJ 3D models and plot the ratio of the SH/P wave energy in dB. After the direct wave leaves the model (approximately 8 periods) the converted SH-wave energy exceeds the P-wave energy for the heterogeneous hard bottom and rough sea floor models.

Each model tested had a unique behavior both above the sea floor and below it. Below is a summary of the water column and sub-bottom scattering conclusions.

### 4.6.1 Scattering into the Water

The following conclusions are drawn from the models about the forward and backward scattered acoustic field in the water:

- Forward scattered energy from soft flat bottom models is weaker than hard flat bottom models because of the decreased reflection coefficient and the transmission of energy into the sub-bottom (the critical incidence angle is $22^o$ for the hard bottom model whereas the critical angle is $68^o$ for the soft bottom model, allowing much more energy to penetrate into the soft bottom from the point source).

- Single 2D facets show that most of the scattering back into the water column is in the form of diffractions off the facet edges. Interface waves (dominantly Stoneley waves) are initiated at the facet edges and propagate in the forward and backward direction away from the facet. Within the facet, it is postulated that interface waves can reverberate between the facet edges, resulting in a long reverberation wave train.

- Single 3D facets show similar features to the 2D facets, but the scattering strength is 3 dB below the 2D facet. Much less of the incident wave is reflected by the facet face and interface waves generated along the $Y$-coordinate facet edge are not excited (see Figure 4.16 lower diagram).

- The soft heterogeneous sea floor showed a scattering strength within 2 dB of the 3D facet model and scatters nearly 1% of the incident field. This is due to the penetration of the direct wave energy into the sediments and scattering between the volume heterogeneities back into the water column. 10 to 15% of the acoustic scattered field is out of plane energy and therefore can not be modeled by 2D seismic propagation algorithms.

- Both 2D and 3D heterogeneous hard bottom models show a small scattered acoustic field other than the sea floor reflection. Most of the incident wave is post critical and the direct wave root excites only weak scattering from the heterogeneities.

- The most significant scattering feature on the sea floor is topographic roughness. The 2D Goff-Jordan model reveals that wavelength scale features can act as point diffraction sources. Stoneley wave energy at the sea floor interacts with the surface roughness to be reradiated as acoustic reverberation.

- The 3D GJ model is a much more effective scattering surface than the 2D GJ surface. This may seem counter intuitive considering the 2D and 3D facet results, however, the dominant length scale of the 3D GJ model is $ka \approx 1.9$. The value of $ka$ determines the scattering regime for the medium. For $0.01 < ka \ll 1.0$ this is the low frequency scattering regime or Rayleigh scattering. Scattering in this regime is of order $k^4$. For the scale of the features modeled here, $ka \approx 1.9$, scattering is practically isotropic with backscattering comparable to forward scattering. This is sometimes called Mie scattering. As a result, scattering from features out of the plane containing the source and receiver can be large.

### 4.6.2 Scattering Below the Sea Floor

Scattering of incident energy back into the water column is necessarily paired with the transmission and conversion of energy down into the ocean crust. For this thesis, the

observed ambient seismo-acoustic noise (microseism) corresponds to the acoustic energy from ocean gravity waves that is scattered in the crust. The model results show the many wave types that an acoustic source in the water column can generate within the crust. In particular we observe those ocean floor properties that can scatter significant energy. A summary of the sub-bottom propagation findings is given below:

- The Hard Flat Bottom (HFB) model shows that little of the incident energy is transmitted into the sea floor via the direct wave root.

- The Soft Flat Bottom (SFB) model allows penetration of converted S wave into the low velocity sediments. The transmitted P- and converted S-waves can scatter into interface Stoneley waves if a heterogeneity is encountered. Between 0.3 and 1.0 Hz, the LFASE data shows a strong polarization during a high sea state and evidence that the wave energy is a Stoneley mode. Large scale regional topography may be responsible for this "directional" scattering near the LFASE site.

- The facet and rough GJ sea floor models show that much of the sub-bottom energy can be scattered out of plane by localized topography. It is possible that the scattering seen at the LFASE site could be scattered by abyssal furrows and mud waves that have been observed along the surface of the sea floor.

The finite difference method allows the exact modeling of the wave equation in complex environments. Previous methods (e.g. Liu, 1992; Cato, 1991a) have been able to model the total scattered field from rough interfaces and are arguably the best method for estimating the ambient noise field. However, these methods do not provide a mechanism to observe the differences between two vs. three dimensional multiple scattering. Our deterministic method provides a way to exactly model the observed topography and with improvements in the source function can model statistically distributed sources. Additionally, the finite difference method is ideal for observing the scattered field both in the water column and within the ocean crust simultaneously.

Table 4.1 Wave Types in Numerical Schlieren (snapshot) Diagrams

| # Identifier | Wave Type |
|---|---|
| 0 | Source Location |
| 1 | Direct Wave |
| 2 | Sea Floor Reflection |
| 3 | P-Headwave |
| 4 | Direct Wave Root |
| 5 | Numerical Dispersion and Boundary Reflections |
| 6 | Converted S-Headwave |
| 7 | Transmitted P-Wave |
| 8 | Transmitted S-Wave (converted) |
| 9 | Diffracted P-Wave in the Bottom |
| 10 | Stoneley Wave |
| 11 | Diffracted P-Wave in the Water |
| 12 | Backscattered P-Headwave |
| 13 | Scattered S to P Transmitted Wave |
| 14 | Scattered Stoneley to S-Wave |
| 15 | Edge Diffracted Transmitted P-Wave |

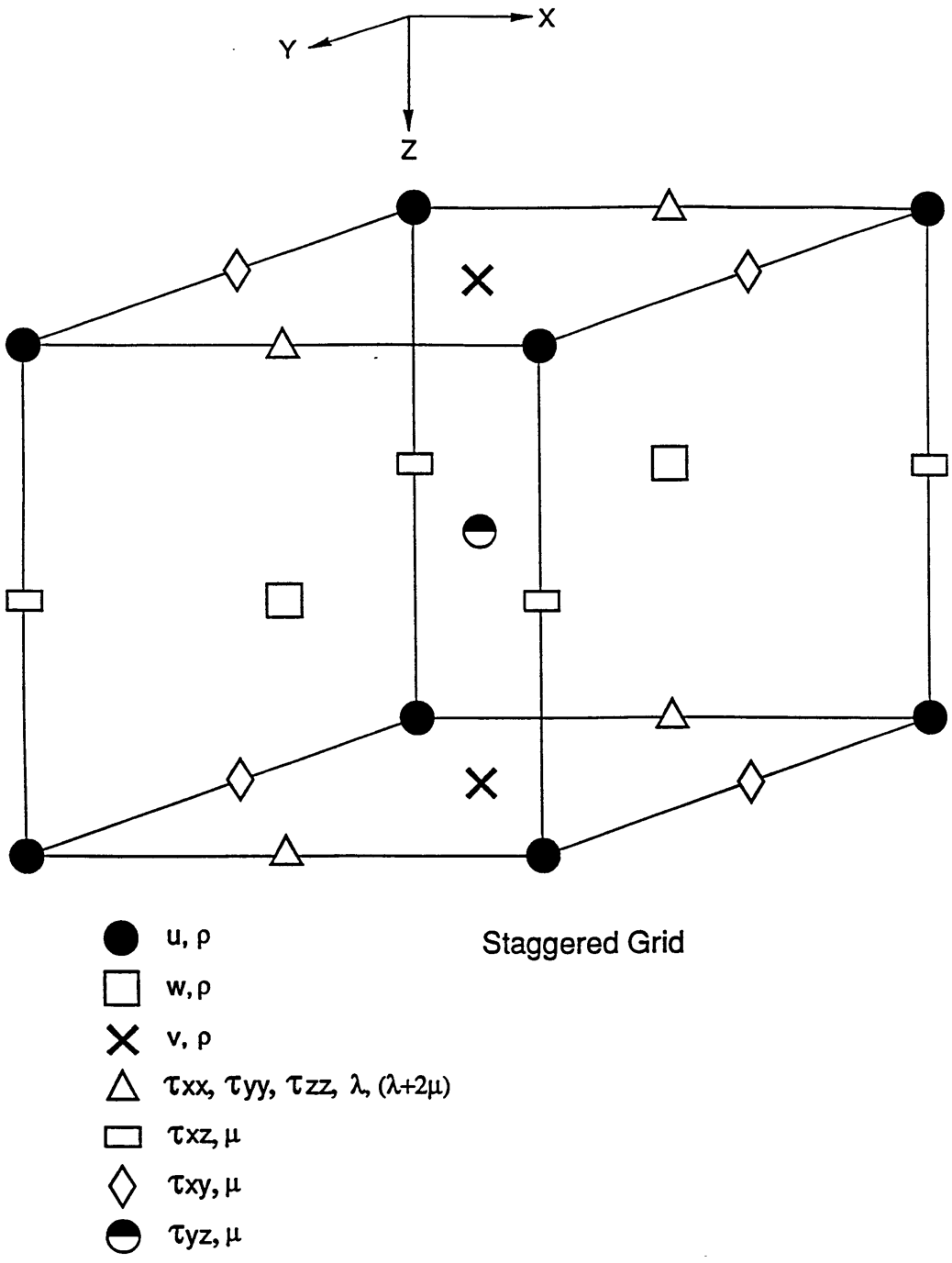


Figure 4-1: Schematic of the three dimensional staggered grid structure used for the displacement-stress formulation for the finite difference approximation of the heterogeneous elastic wave equation. The displacements, $u$, $w$, and $v$, and stresses, $\tau_{ij}$, are computed on separate grids and displacements are stored for the previous time step. The elastic parameters, $\rho$, $(\lambda + 2\mu)$, and $\mu$, are defined on three separate grids (from Burns and Stephen, 1990).

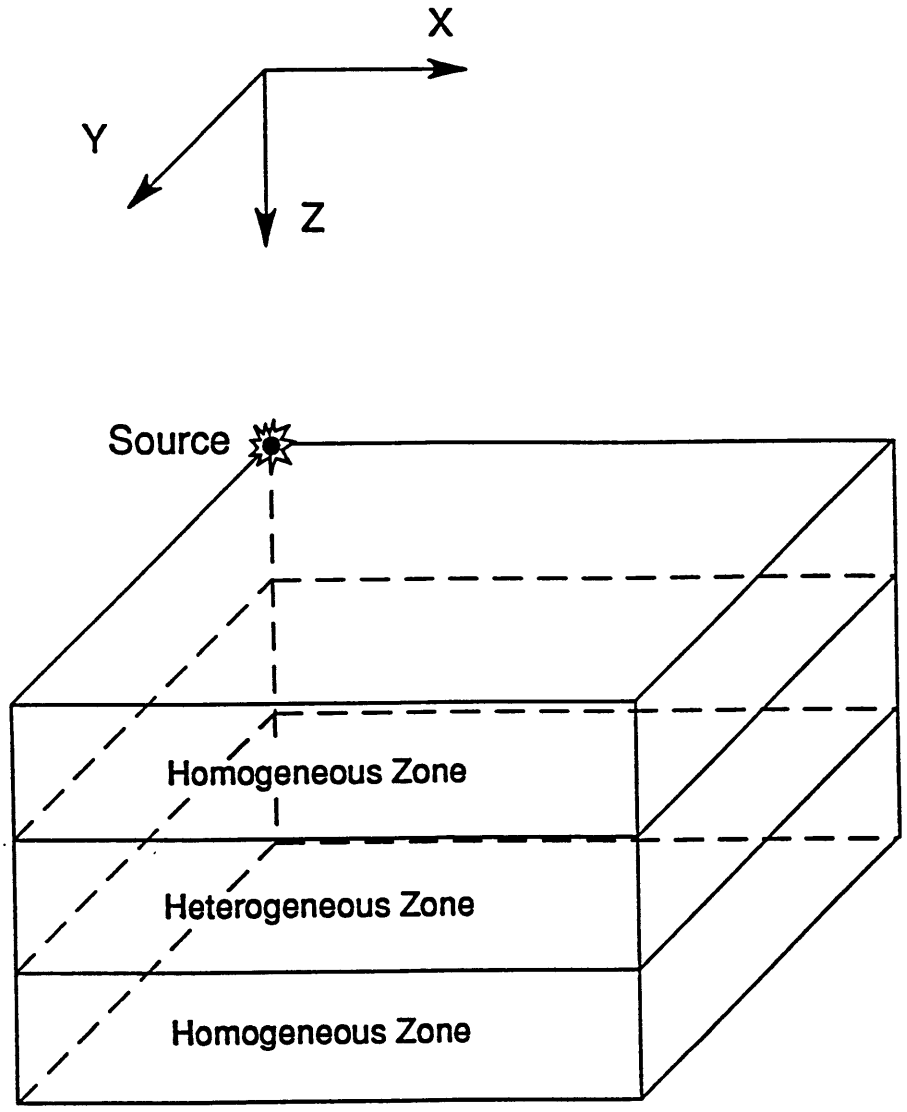


Figure 4-2: Model zones for the finite difference equation. The upper zone is usually defined as a homogeneous liquid whose depth corresponds to the modeled ocean depth. The center zone is a transition zone between the homogeneous fluid and the homogeneous solid and can include generally heterogeneous fluid/solid media. (from Burns and Stephen, 1990).

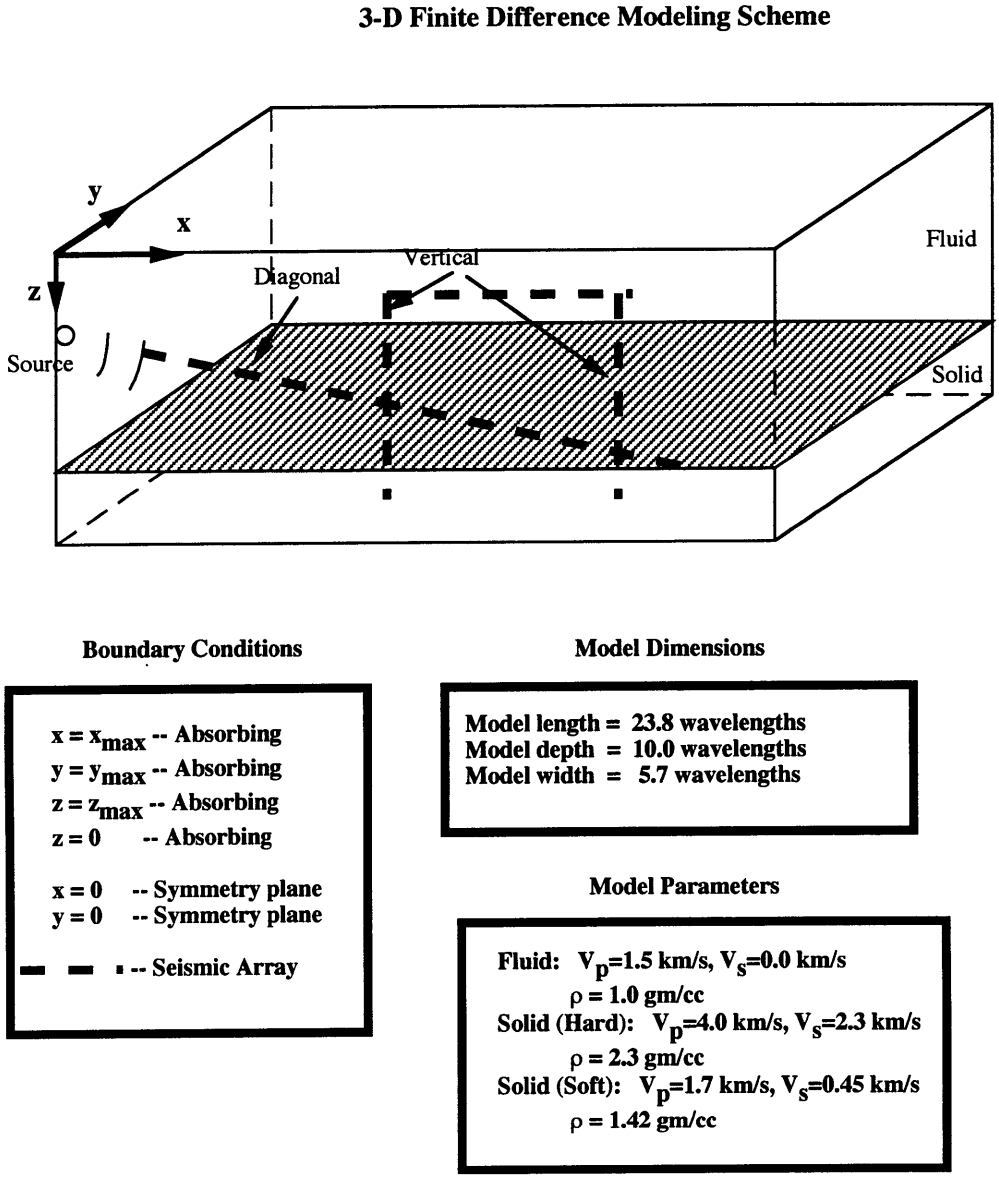


Figure 4-3: Example schematic of a simple flat bottom 3D finite difference model. Model boundary conditions and dimensions are summarized in the figure tables. Heavy dashed lines indicate seismic array locations. One advantage of the finite difference method is the ability to model elastic wave propagation in a medium with arbitrary source and receiver positions.

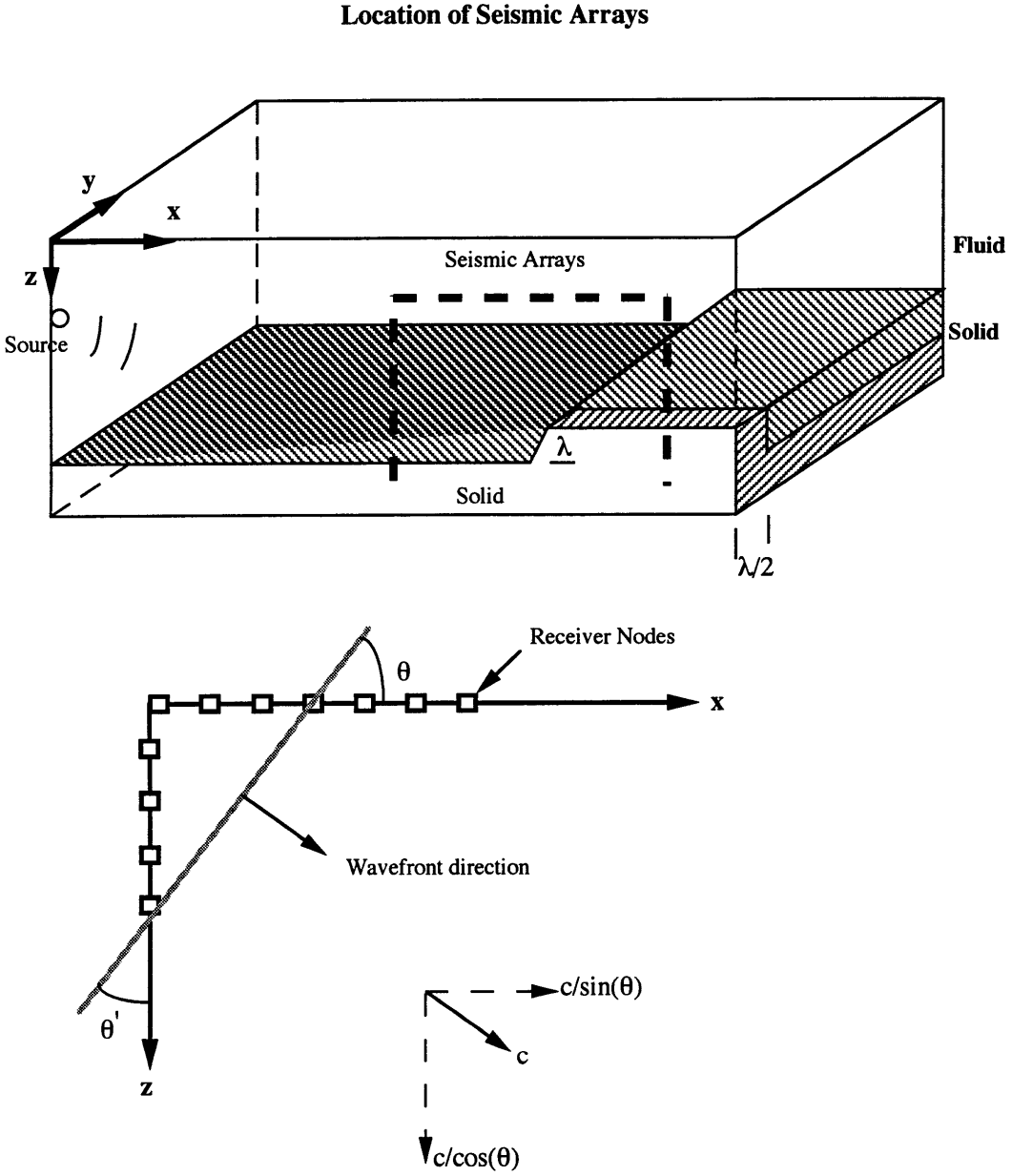


Figure 4-4: Diagram of the synthetic seismogram arrays in a faceted bottom model. The upper diagram shows the rectangular array used to measure scattering from the sea floor. Two synthetic models are illustrated: a 2D (or infinite) facet one wavelength ($\lambda$) high and extending across the model, and a 3D facet one wavelength high and 1/2 wavelength wide (the symmetry plane at $y = 0$ makes this an equivalent $\lambda \times \lambda$ facet). The lower diagrams show the relationship of a single plane wave (propagating at $-45°$) to two segments of the rectangular array. The angle $\theta$ is defined with respect to the positive $x - axis$ (i.e. grazing angle).

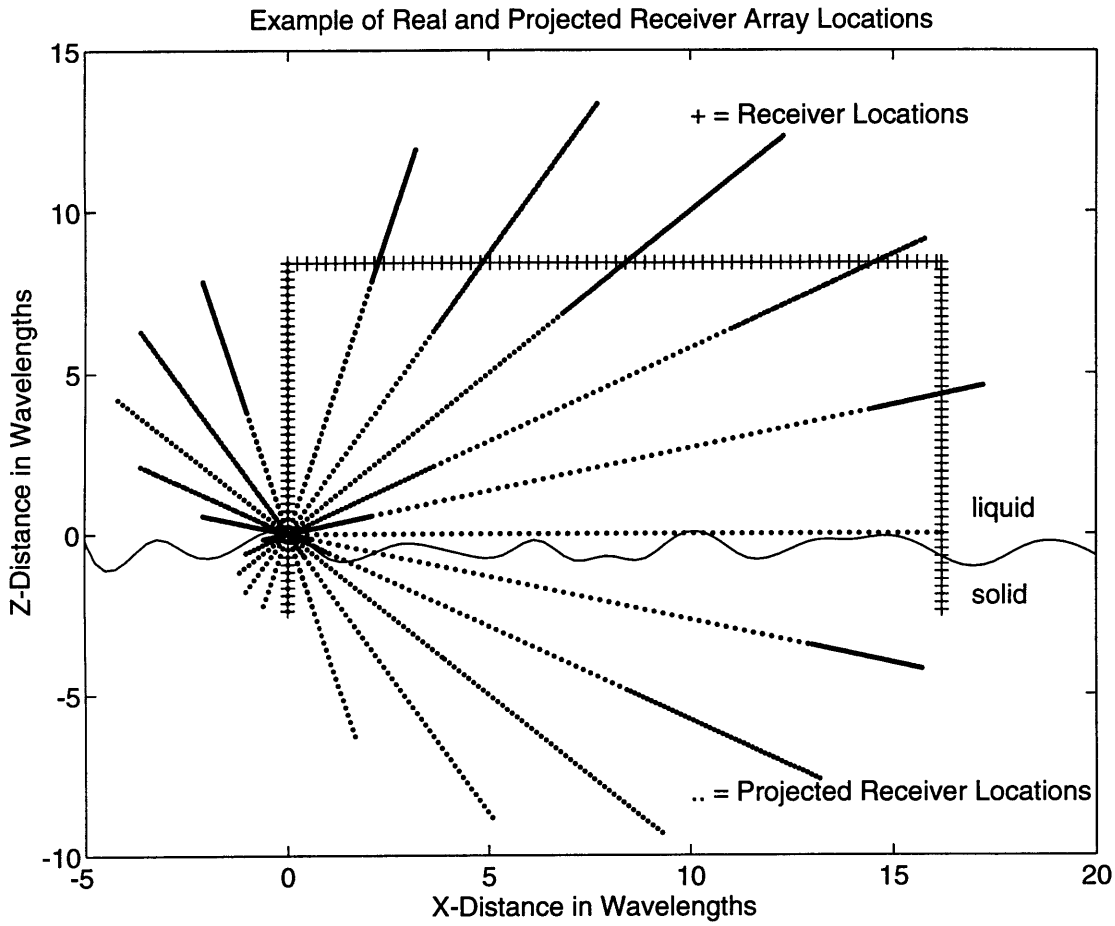


Figure 4-5: The projection step of the serpentine Radon transform. This is a diagram in the $XZ$-plane of the rectangular synthetic seismogram array and their projected receiver positions along 11 different angles from $-70^{o}$ to $+70^{o}$. The receiver nodes are labeled "+" and the projected locations are labeled "•". There are 160 receivers ("+") in the rectangular array. Each receiver is normally projected onto a line and the plane wave energy traveling along that line is computed. (An example rough water-sea floor interface is illustrated as a solid line).

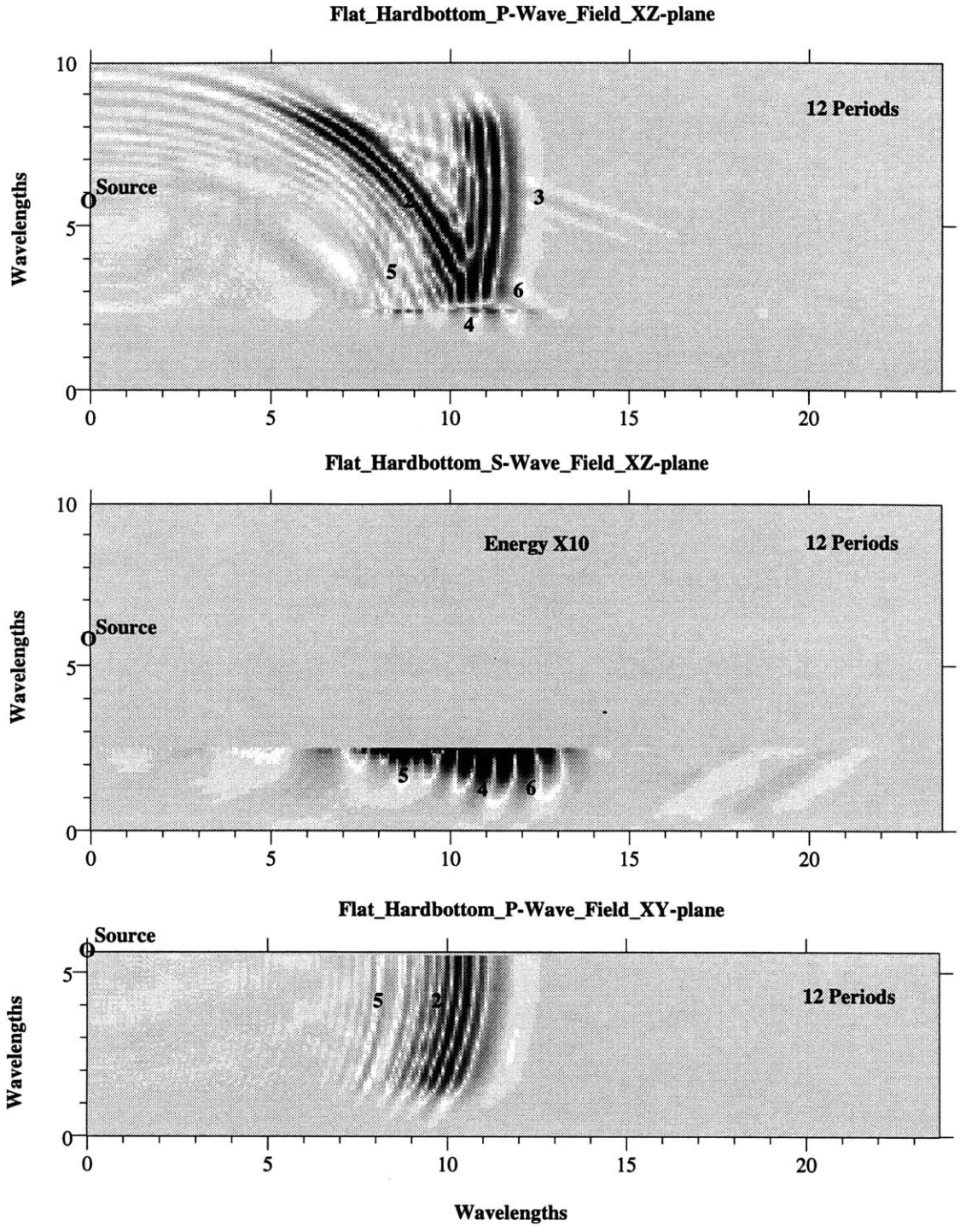


Figure 4-6: Schlieren diagram of a flat hard bottom sea floor. $\rho_2 = 2.3\ gm/cc$, $V_p = 4.0\ km/s$, $V_s = 2.3\ km/s$. The dimensions of the model are scaled in source wavelengths of the peak frequency in water. Wave types are identified in Table (4.1).

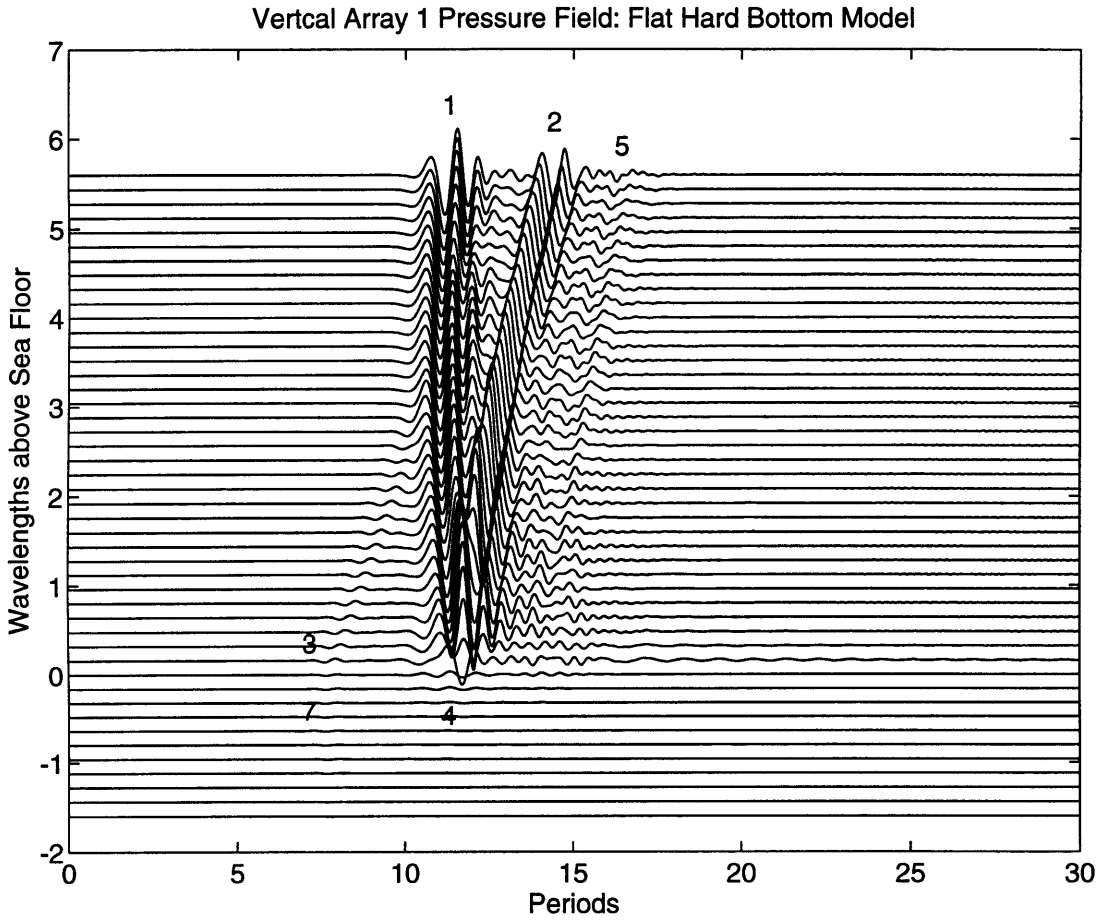


Figure 4-7: Calculated pressure along a vertical array in the flat hard bottom model. The horizontal axis is in periods with respect to the peak frequency of the source and the vertical axis is in wavelengths above the sea floor. The vertical array has 11 elements below the sea floor and 35 elements above the sea floor in the water column. The arrivals are identified in Table (4.1).

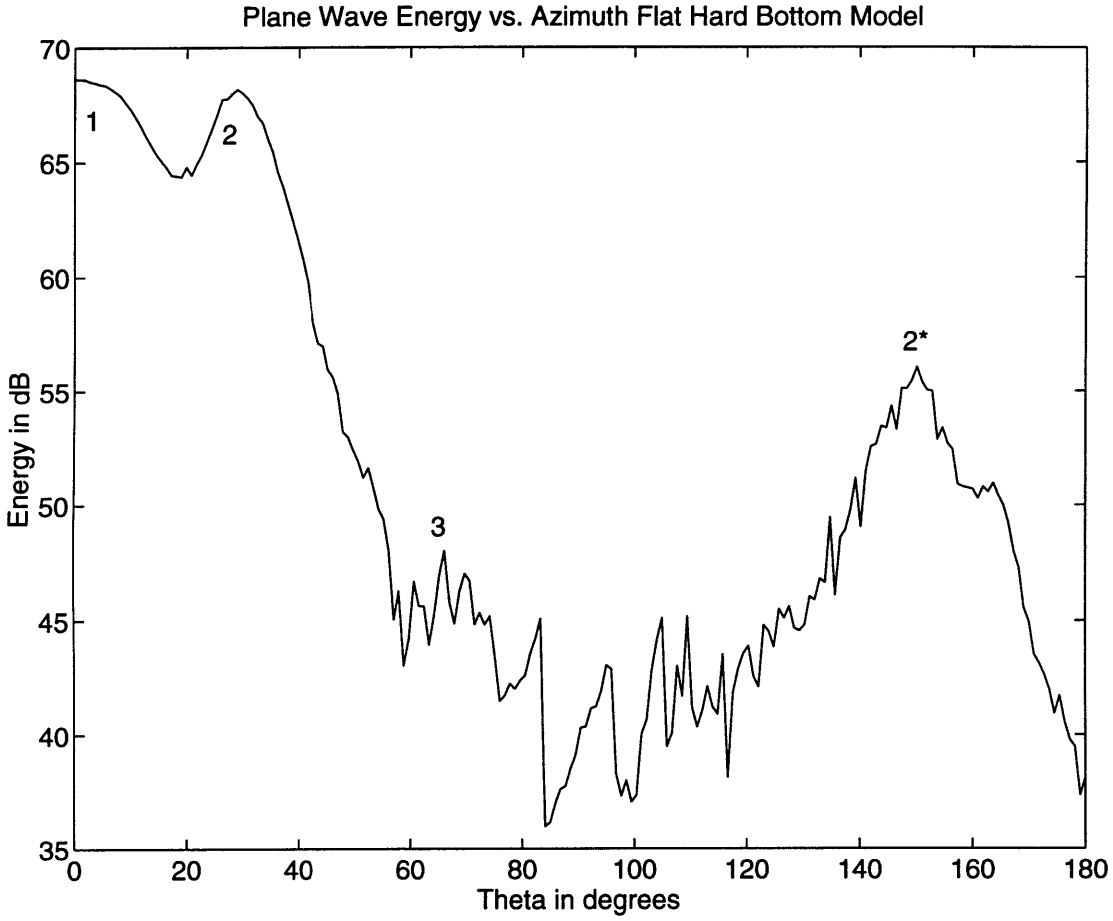


Figure 4-8: Plane wave energy versus propagation angle for the Hard Flat Bottom (HFB) model. The direct wave (1) and sea floor reflection (2) energies are shown at $10^o$ and $30^o$ respectively. The low amplitude P-head wave energy is indicated by (3) and the aliased sea floor reflection from the $\tau - p$ stack is labeled (2*). This scattered field is used as a reference field and all subsequent energy-propagation angle figures have had this field subtracted out (i.e. all scattering diagrams show energy relative to the HFB model).

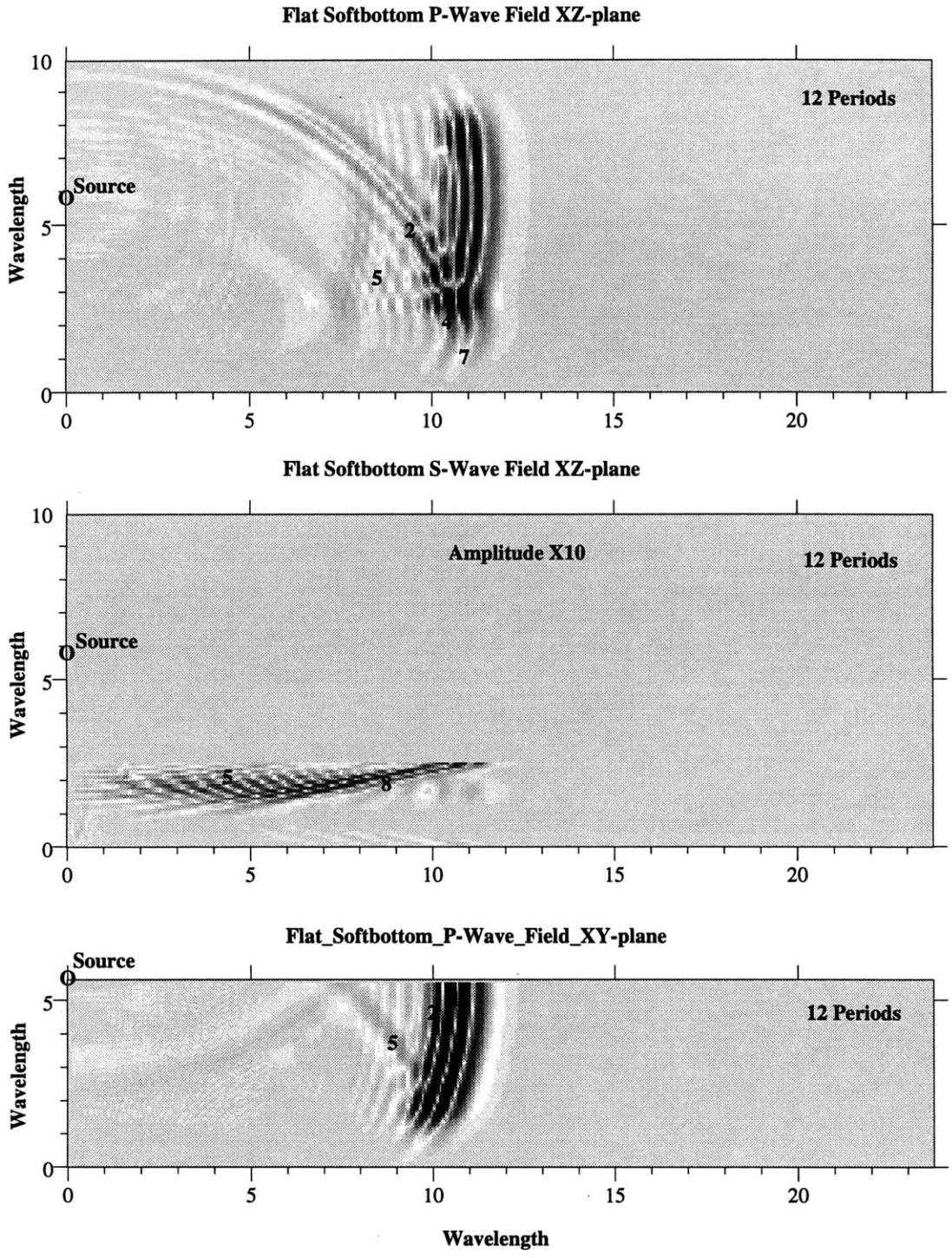


Figure 4-9: Schlieren diagram from the flat soft bottom model. $\rho_2 = 1.42\ gm/cc$, $V_p = 1.7\ km/s$, $V_s = 0.45\ km/s$. The dimensions of the model are scaled in source wavelengths of the peak frequency in water ($V_p = 1.5\ km/s$). Wave types are identified in Table (4.1).

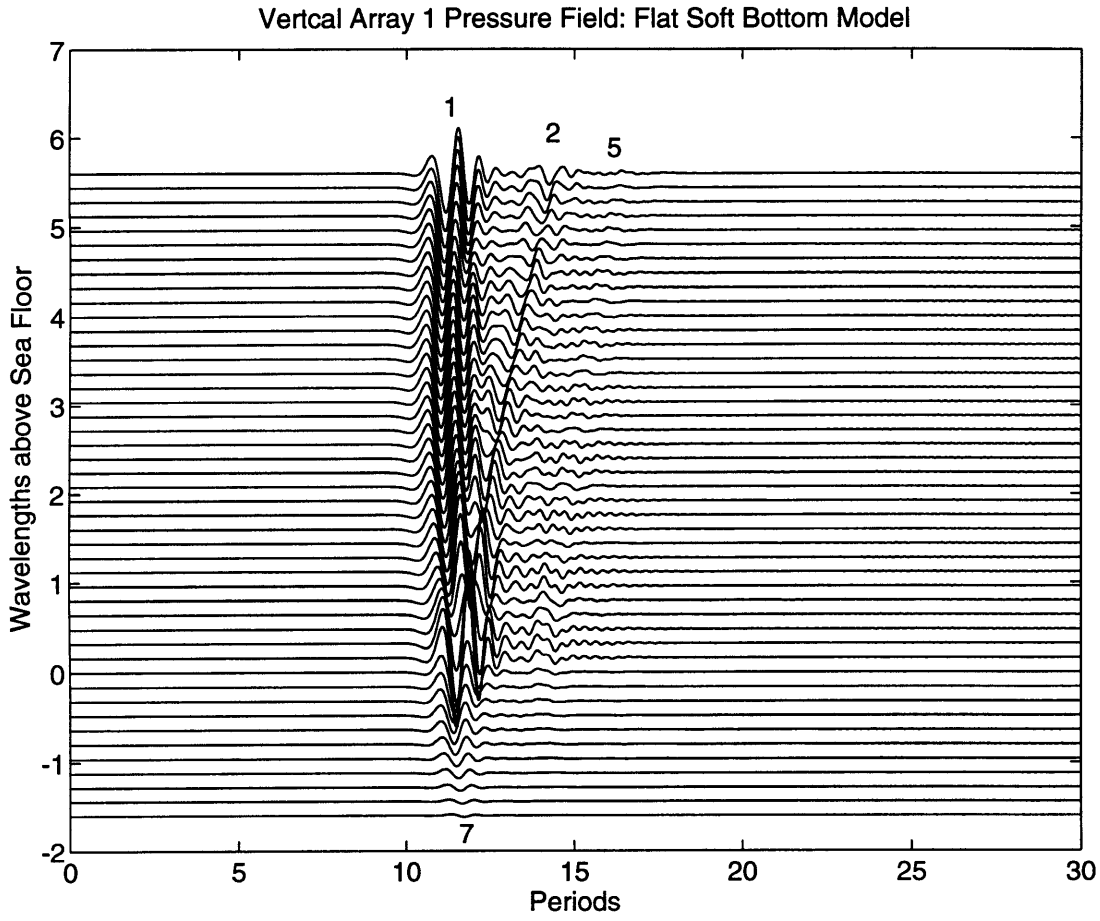


Figure 4-10: Calculated pressure along a vertical array in the flat soft bottom model. The horizontal axis is in periods with respect to the peak frequency of the source and the vertical axis is in wavelengths above the sea floor. The vertical array has 11 elements below the sea floor and 35 elements above the sea floor in the water column. The arrivals are identified in Table (4.1).

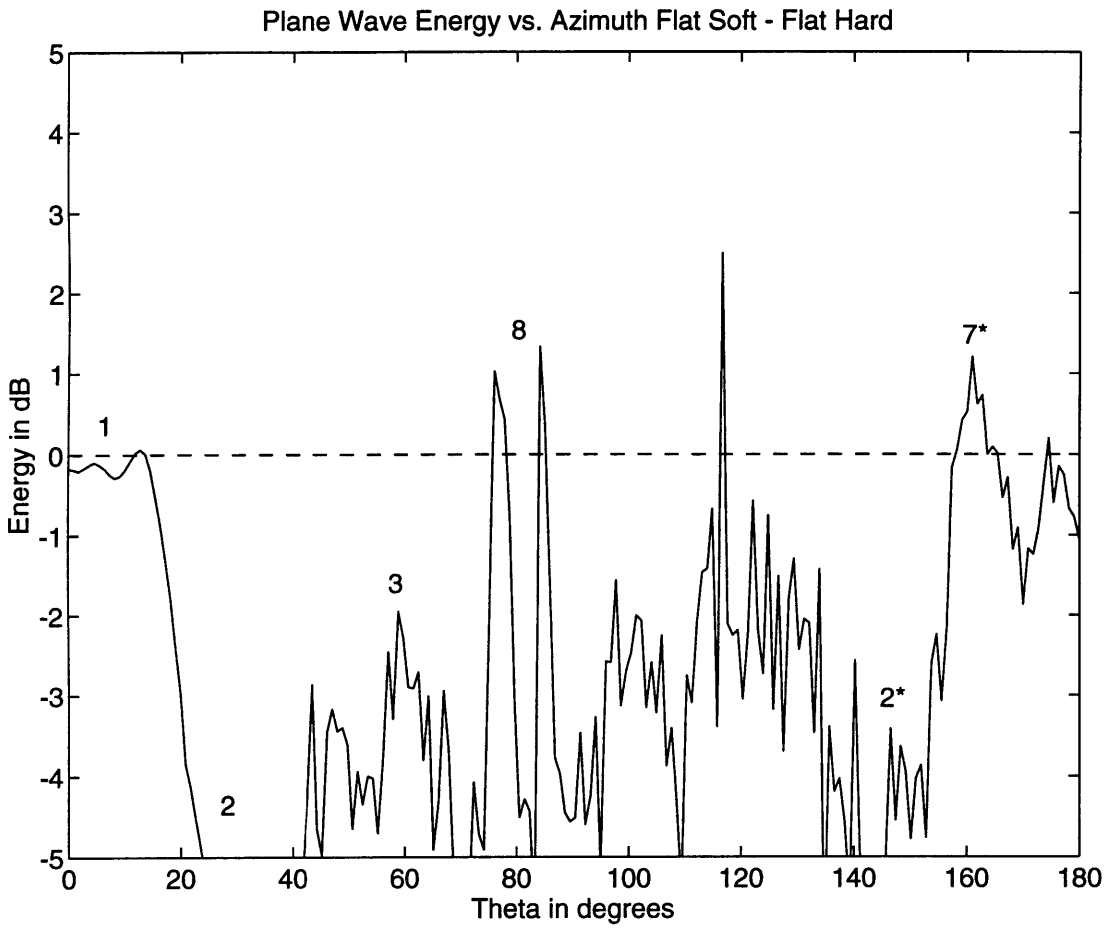


Figure 4-11: Tau-p scattering diagram for the flat soft bottom model. Field is computed using a serpentine Radon transform calculation over the arrays shown in Figure (4.4) and then subtracting the computed tau-p field from the flat hard bottom model.

**2D Facet Hardbottom P-Wave XZ-plane**

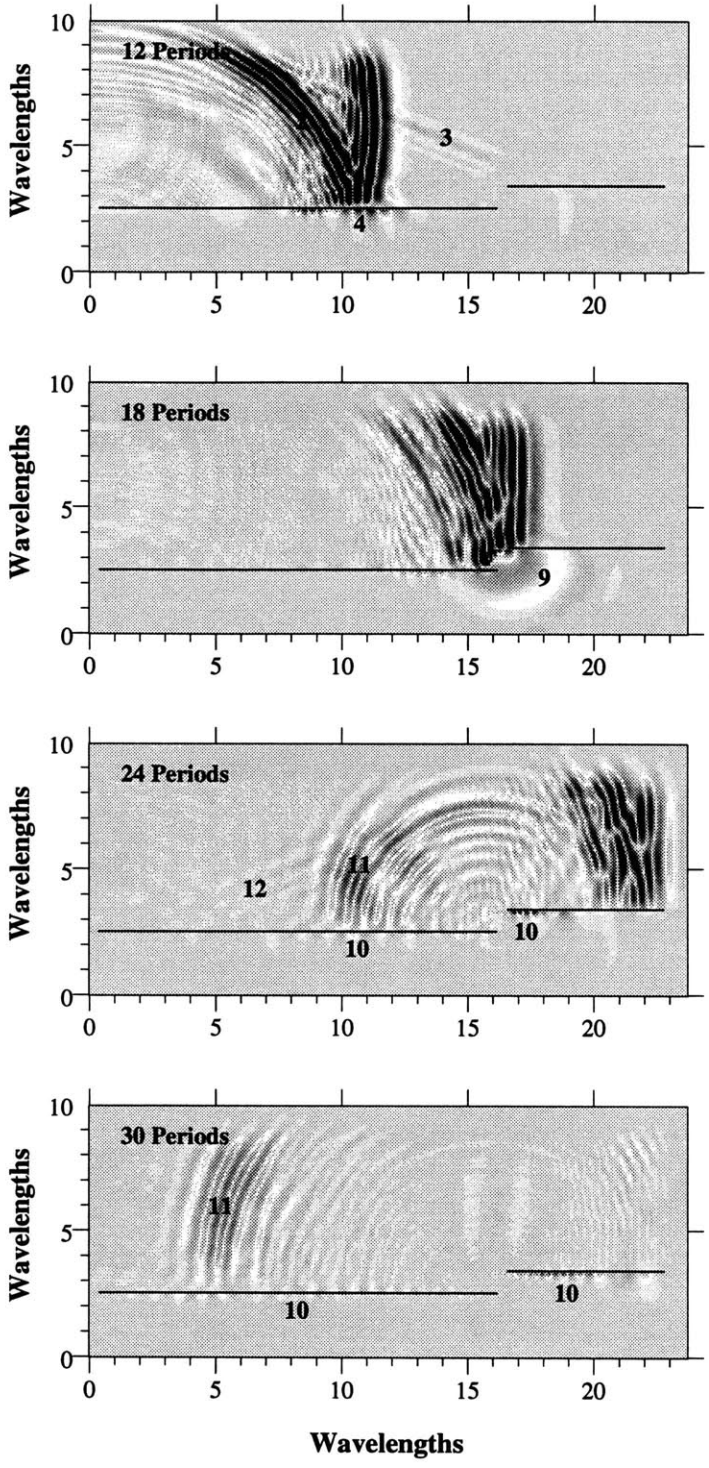

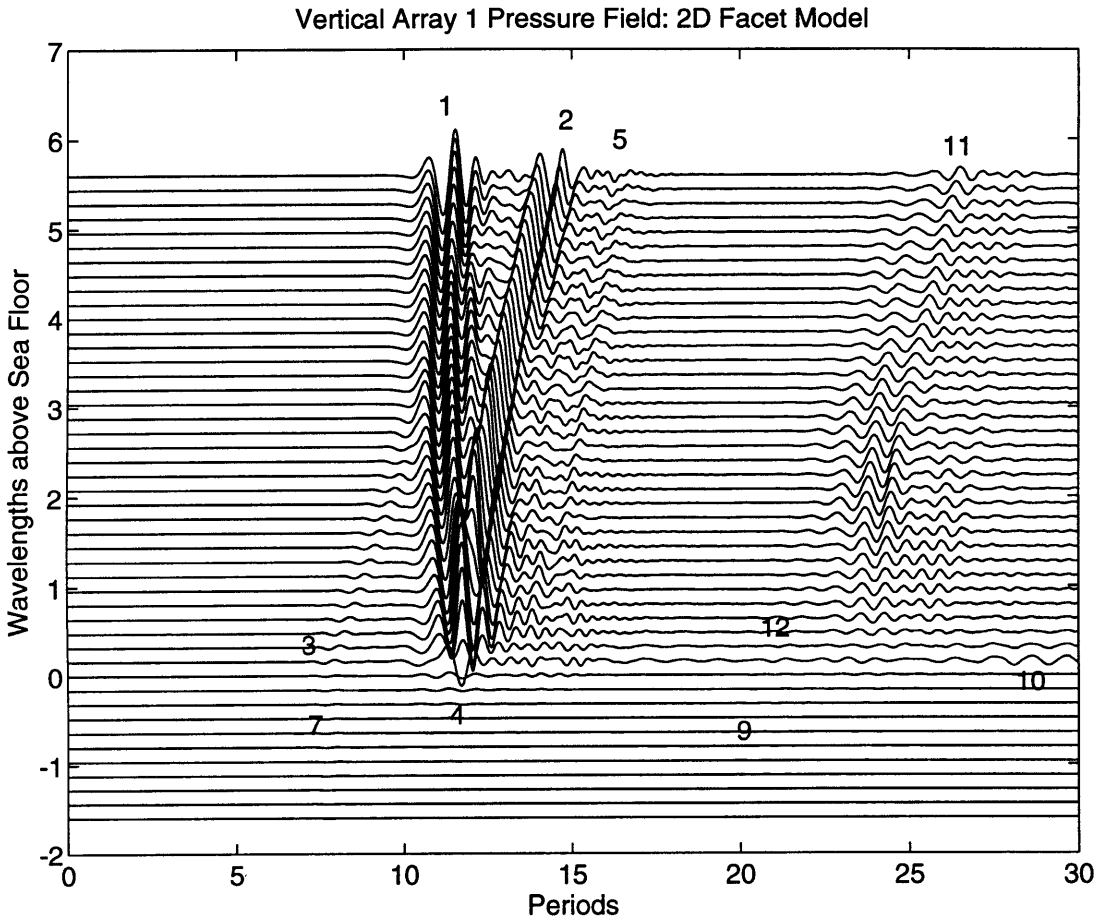


Figure 4-13: Calculated pressure along a vertical array in the 2D facet hard bottom model. The horizontal axis is in periods with respect to the peak frequency of the source and the vertical axis is in wavelengths above the sea floor. The vertical array has 11 elements below the sea floor and 35 elements above the sea floor in the water column. The arrivals are identified in Table (4.1).

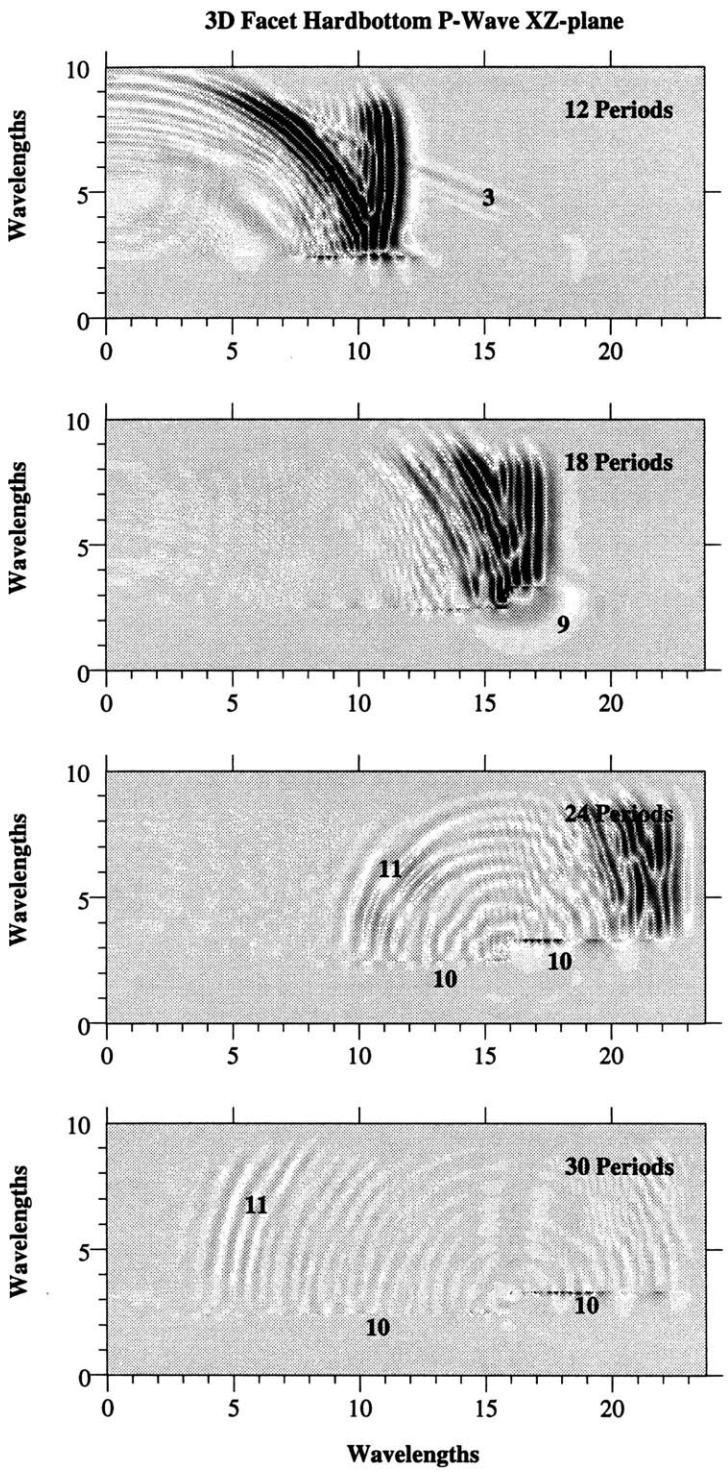


Figure 4-14: Schlieren diagrams for the 3D facet model. The snapshots are taken at 6 period intervals and show the interaction of a point source with a 3D single facet in the sea floor. The facet is one $\lambda$ in relief and one $\lambda$ wide. The facet reflection is smaller relative to 2D facet reflection in Figure (4.12). Wave types are identified in Table (4.1).

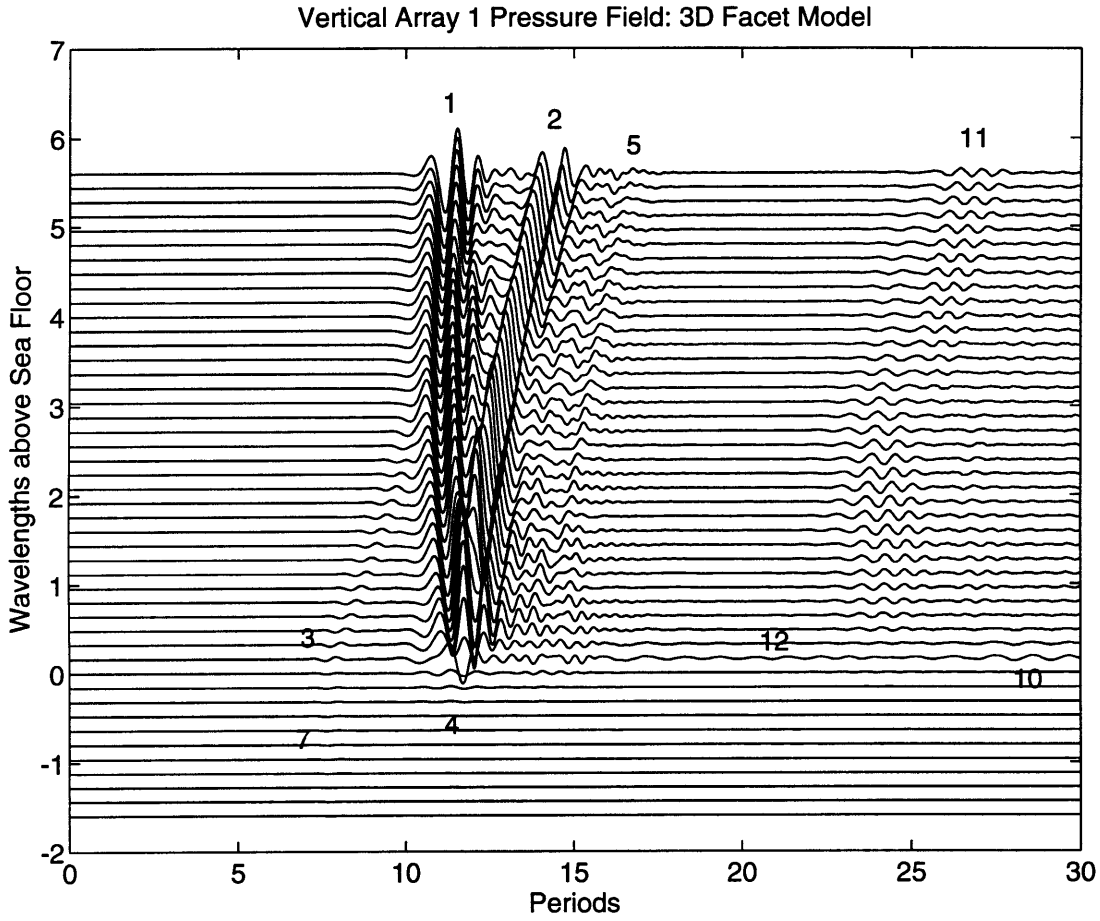


Figure 4-15: Calculated pressure along a vertical array in the 3D faceted hard bottom model. The horizontal axis is in periods with respect to the peak frequency of the source and the vertical axis is in wavelengths above the sea floor. The vertical array has 11 elements below the sea floor and 35 elements above the sea floor in the water column. The arrivals are identified in Table (4.1).

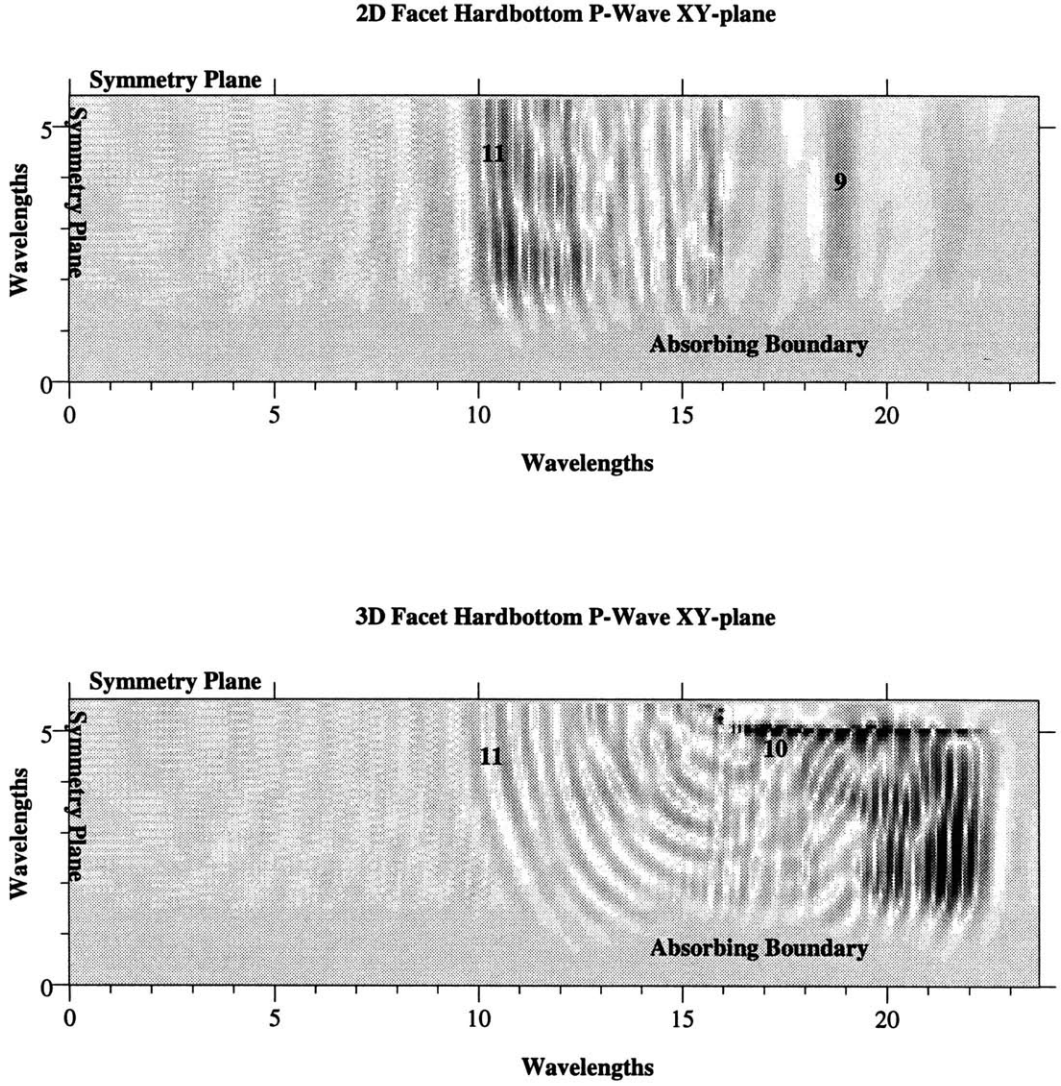


Figure 4-16: P-wave Schlieren diagram computed at 18 periods on a horizontal ($XY$) plane approximately 1/2 $\lambda$ above the sea floor for the 2D facet (upper diagram) and 3D facet (lower diagram). Facet edges are outlined in black. Wave arrivals are identified in Table (4.1).

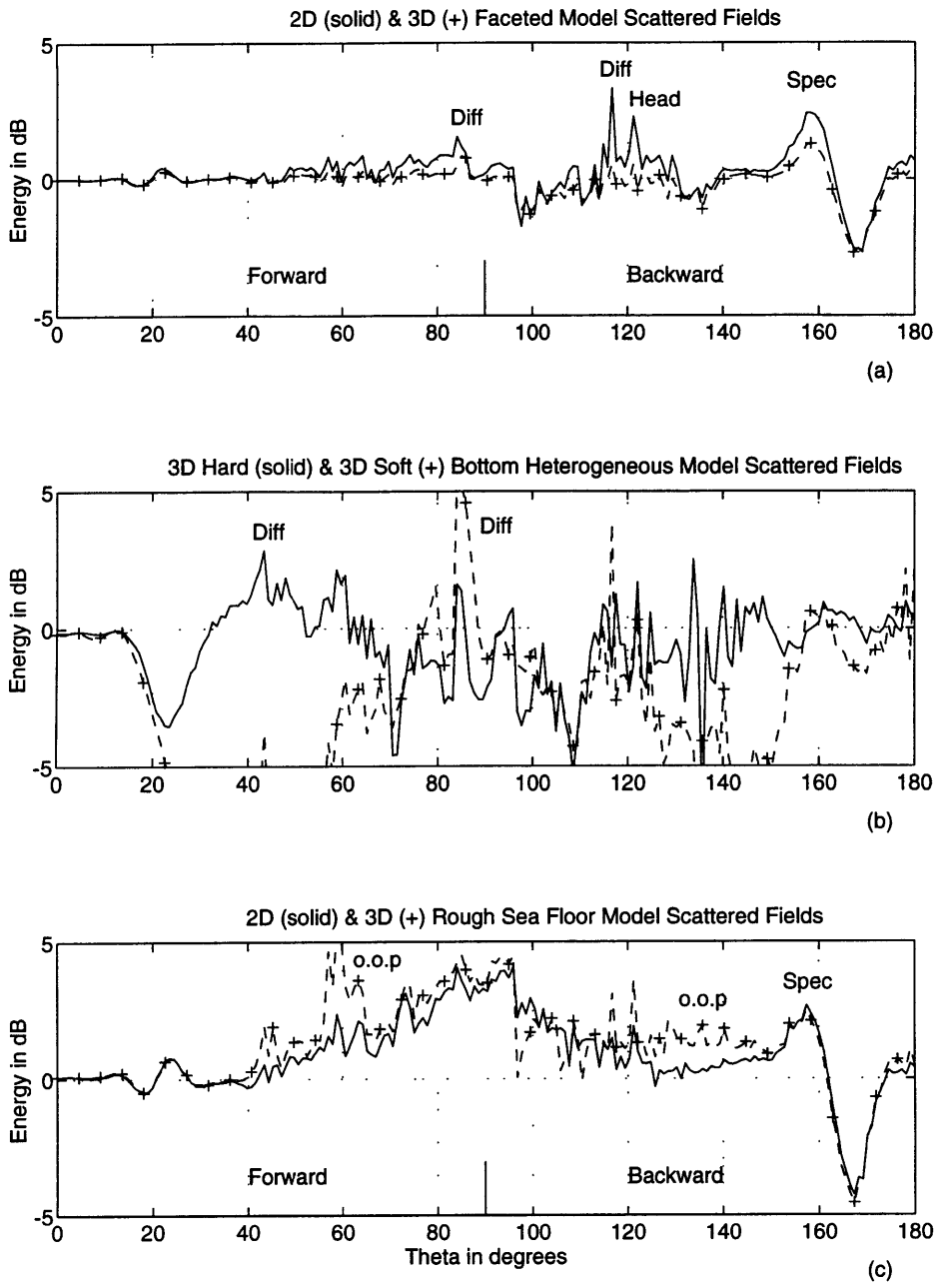


Figure 4-17: Scattered energy relative to the flat hard bottom model (i.e. after subtraction of the HFB field). (a) Scattered field from the 2D (solid) and 3D (dashed +) facet models. Scattered head wave (Head), diffracted (Diff) and backscattered specular (Spec) waves are indicated. (b) Scattered field from the 3D hard (solid) and 3D soft (dashed +) heterogeneous bottom models. (c) Scattered field from the 2D (solid) and 3D (dashed +) Goff-Jordan sea floor models. Note that the 3D surface has stronger scattering from out-of-plane (o.o.p) events. (Note that these data were acquired near the model plane of symmetry so out of plane energy is under-estimated)

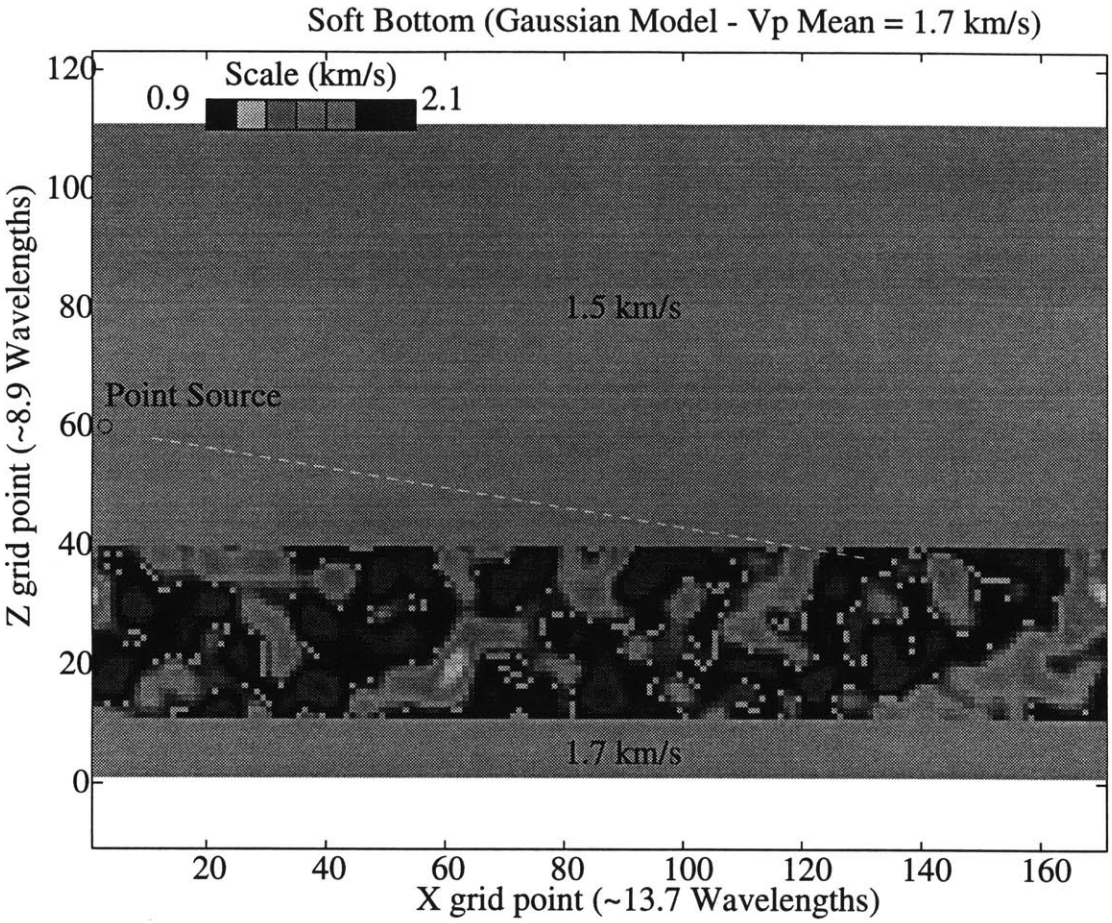


Figure 4-18: $XZ$-cross section graytone plot of the heterogeneous velocity models. (a) Soft bottom model. Mean P-wave velocity is 1.7 $km/s$ with a standard deviation of 10% and correlation length $ka \sim 2$. (b) Hard bottom model. Mean P-wave velocity is 3.0 $km/s$ with a standard deviation of 10% and correlation length $ka \sim 2$.

Figure (4.18b)

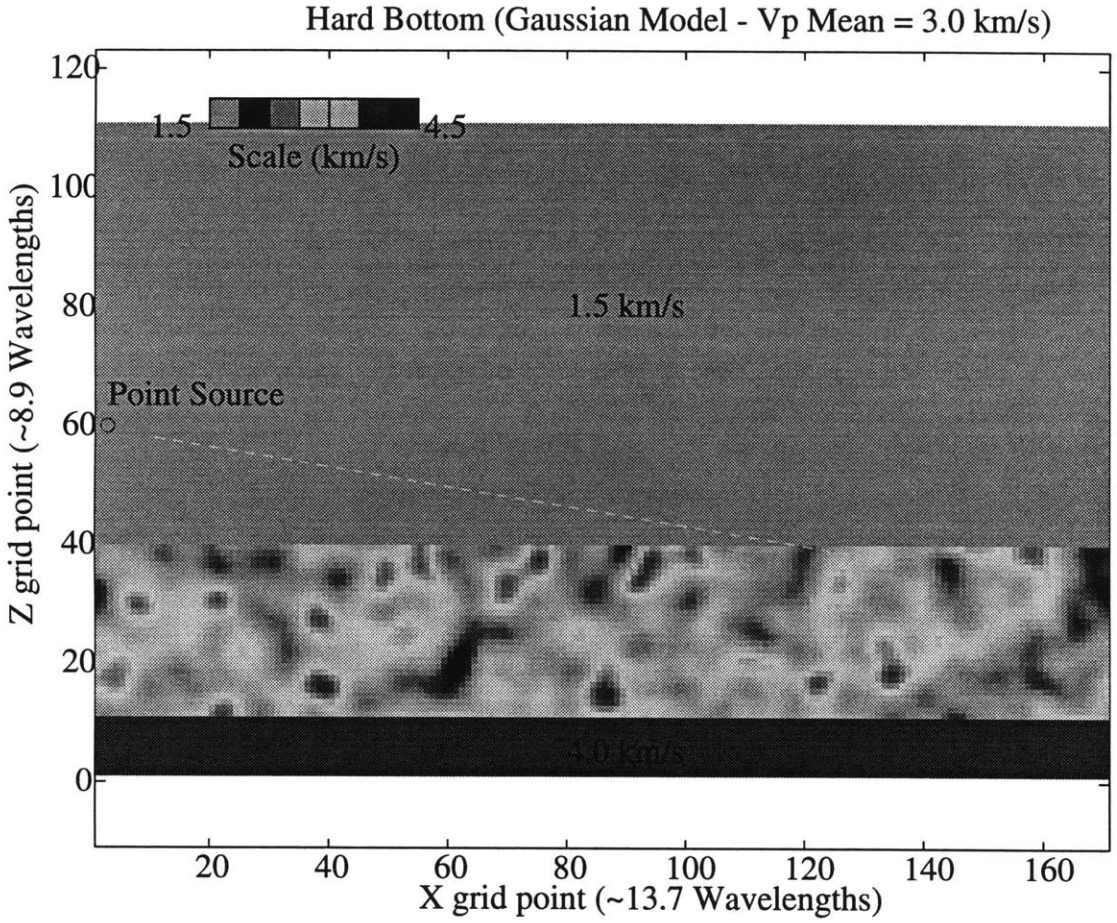
Hard Bottom (Gaussian Model - Vp Mean = 3.0 km/s)
1.5
4.5
Scale (km/s)
1.5 km/s
Point Source
4.0 km/s
Z grid point (~8.9 Wavelengths)
X grid point (~13.7 Wavelengths)
0
20
40
60
80
100
120
140
160

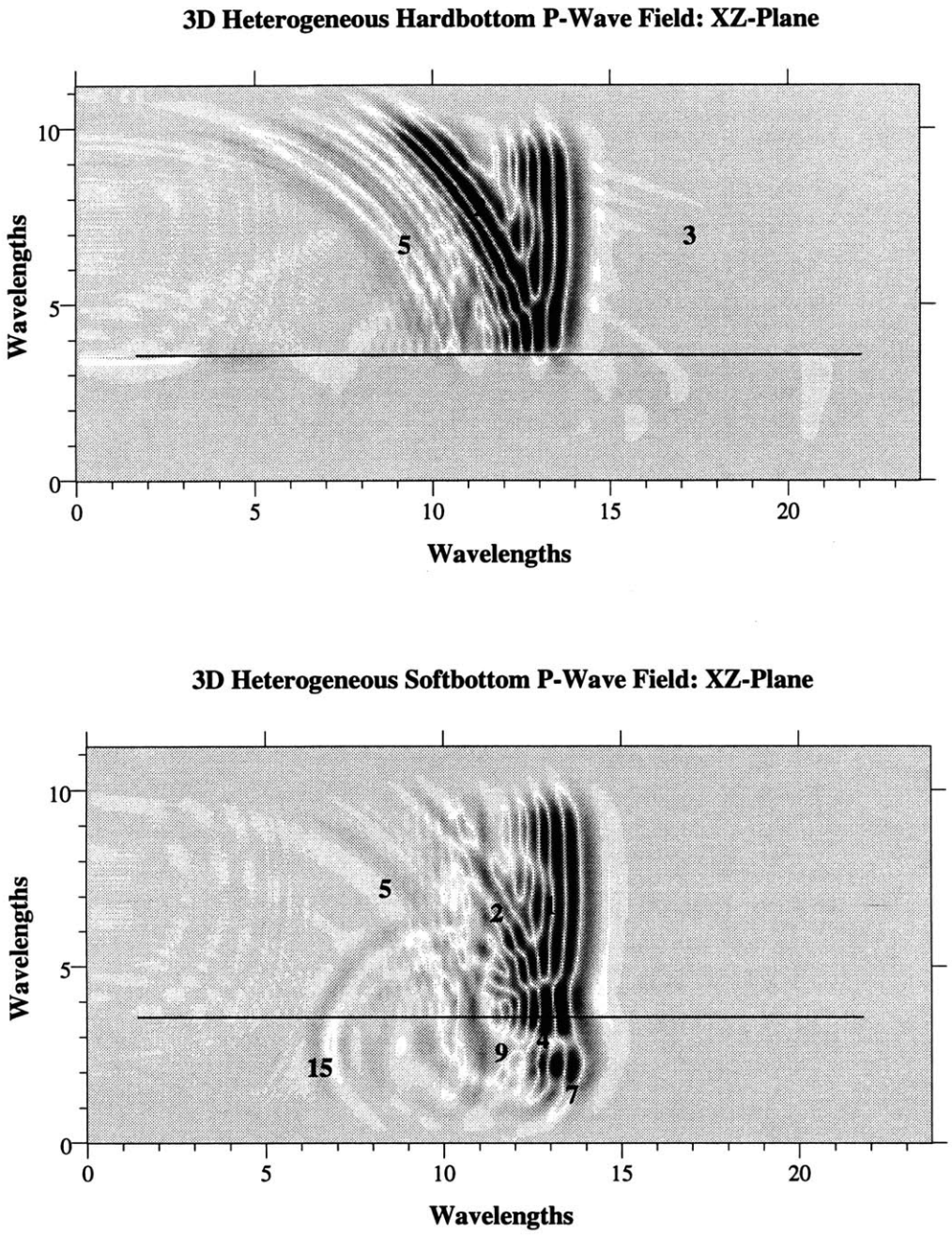


Figure 4-19: P-wave Schlieren diagram computed at 16 periods on the vertical ($XZ$) plane for the 3D heterogeneous hard bottom (upper diagram) and 3D heterogeneous soft bottom (lower diagram). Sea floor is outlined in black. Note the backscattered diffraction from a diving P-wave striking a volume heterogeneity (15); other wave arrivals are identified in Table (4.1).

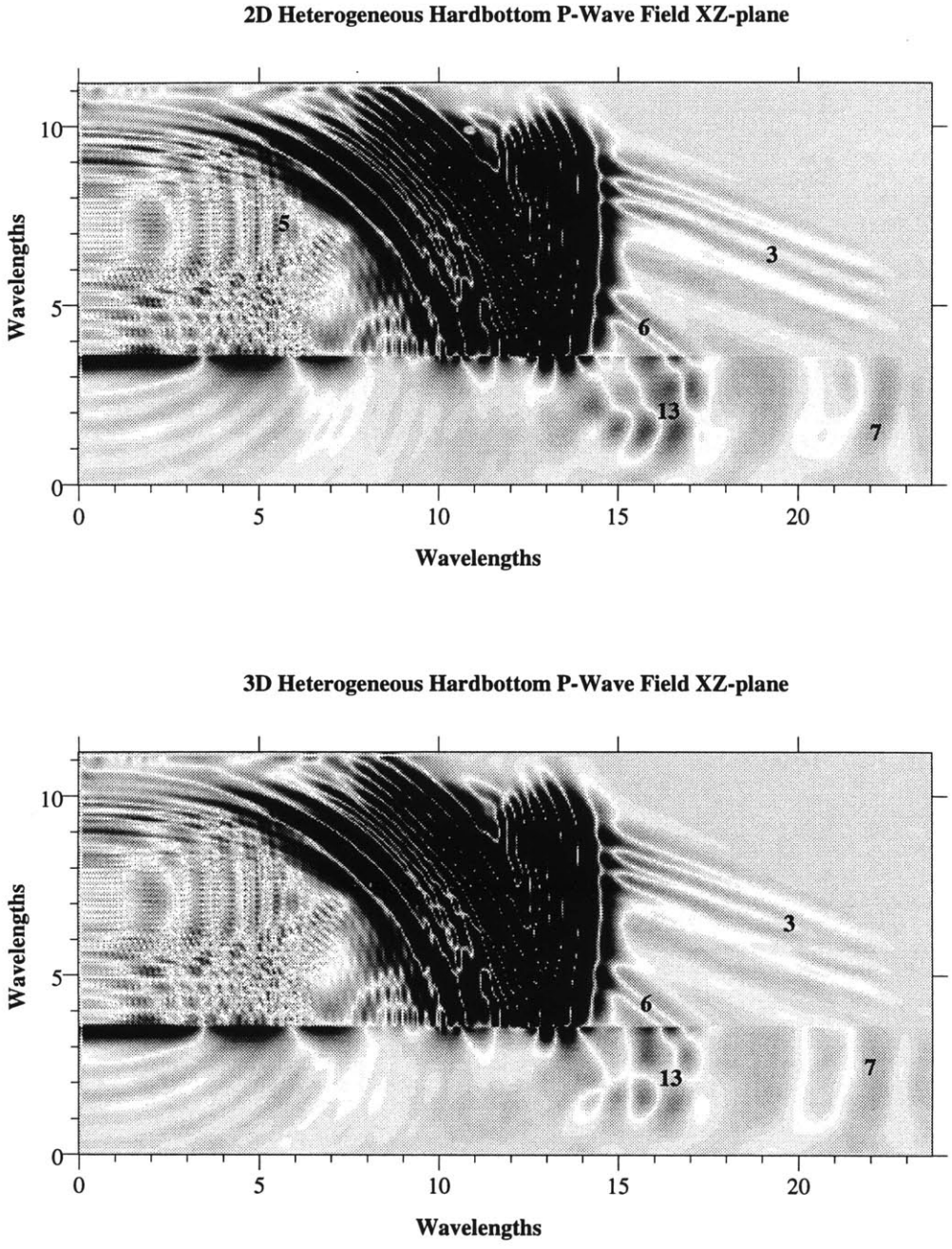


Figure 4-20: P-wave Schlieren diagram computed at 16 periods on the vertical ($XZ$) plane for the 2D heterogeneous hard bottom (upper diagram) and 3D heterogeneous hard bottom (lower diagram). A scattered S- to P-diving wave is labeled (13); other wave arrivals are identified in Table (4.1).

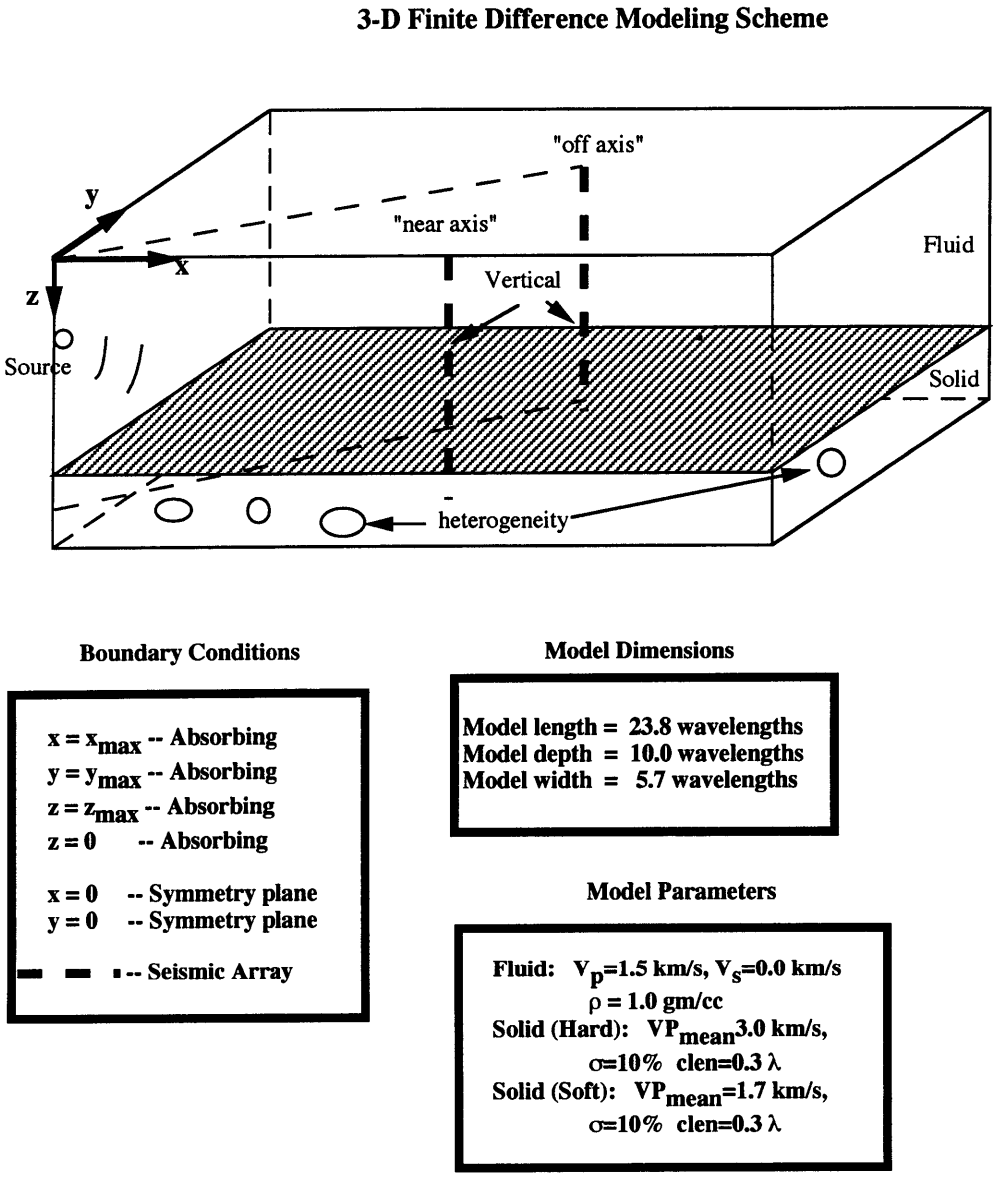


Figure 4-21: Model schematic showing the relative location of the "near axis" and "off axis" arrays. An azimuthal plane containing both source and "off axis" receivers is shown dashed.

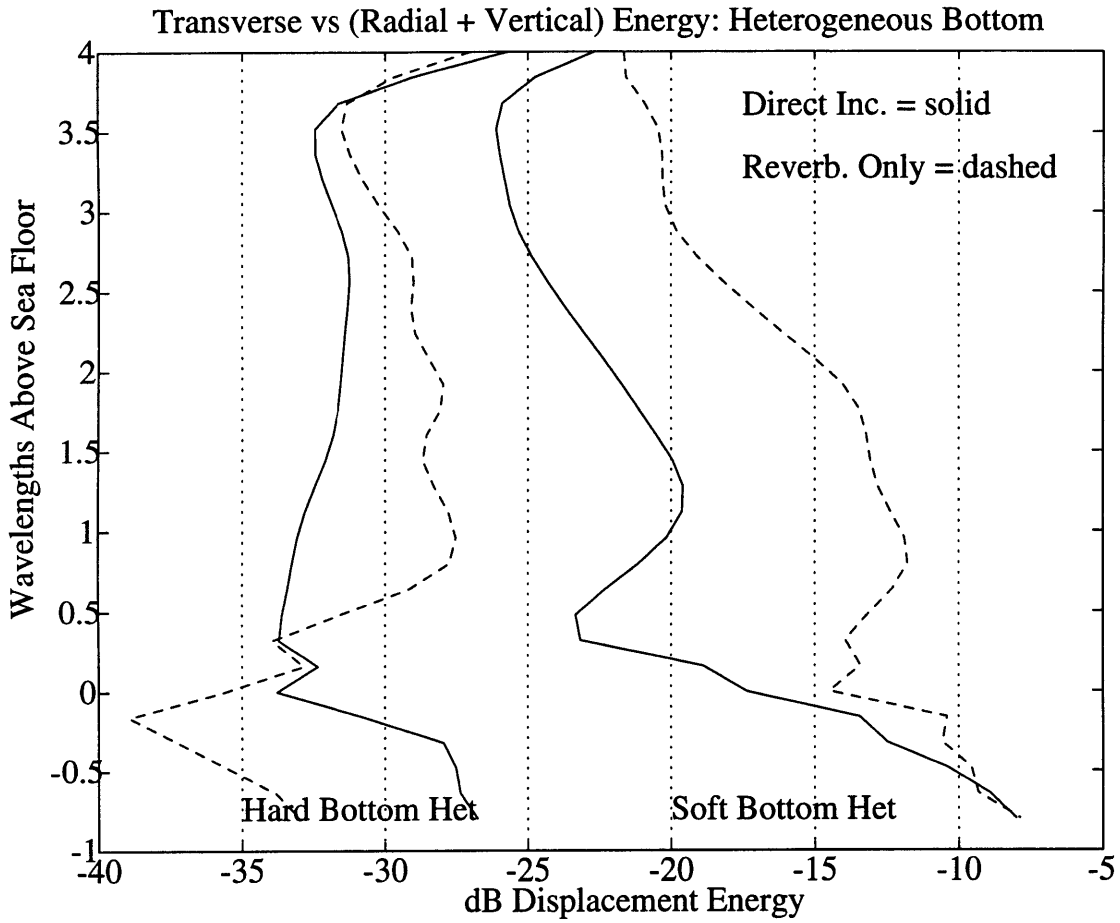


Figure 4-22: Transverse versus sagital (radial + vertical) energy for the "off axis" array in the 2D and 3D heterogeneous volume models. The solid lines include the contribution of the direct and sea floor reflected waves; dashed lines are computed after the direct and sea floor reflected waves have left the model. Note that up to 10% of the Soft Flat Bottom energy is transversely polarized.

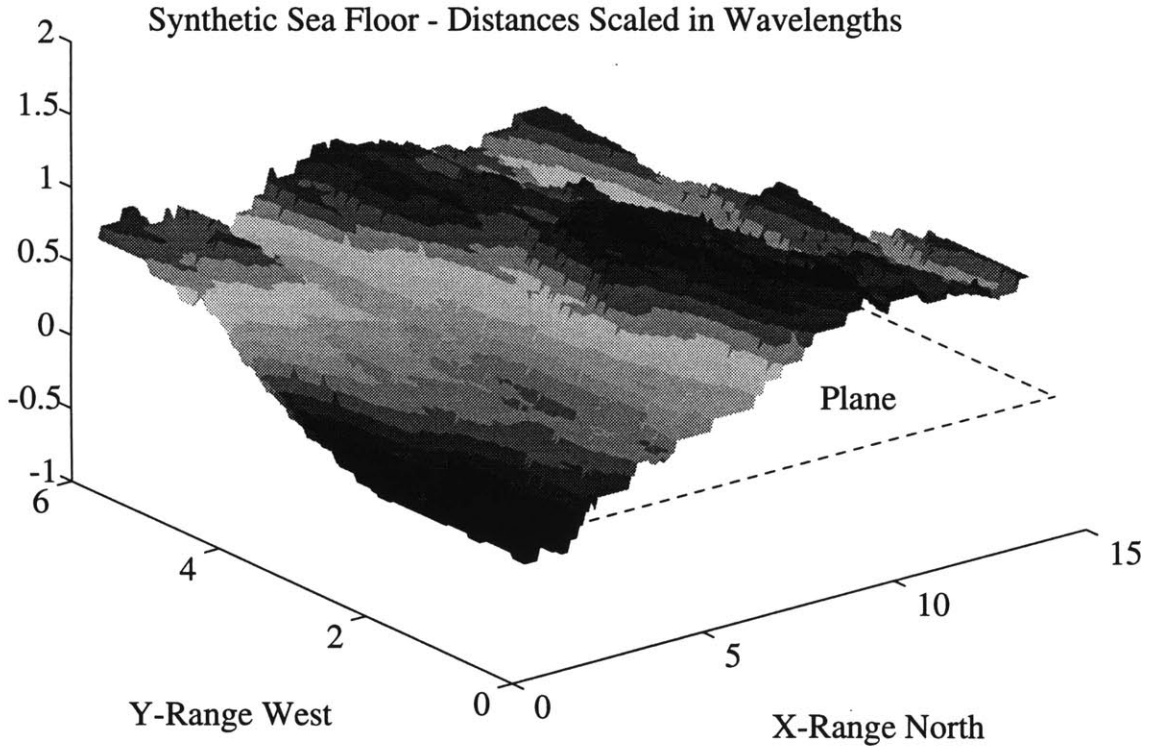


Figure 4-23: Synthetic sea floor based on Goff-Jordan covariance function computed for a portion of the Mid Atlantic sea floor. Total relief is approximately $\sim$ 1.5 $\lambda$. A sub-bottom $XY$-plane is indicated by the dashed lines. P-, SV-, and SH-wave energy were computed along this plane and similar planes in the heterogeneous bottom models.

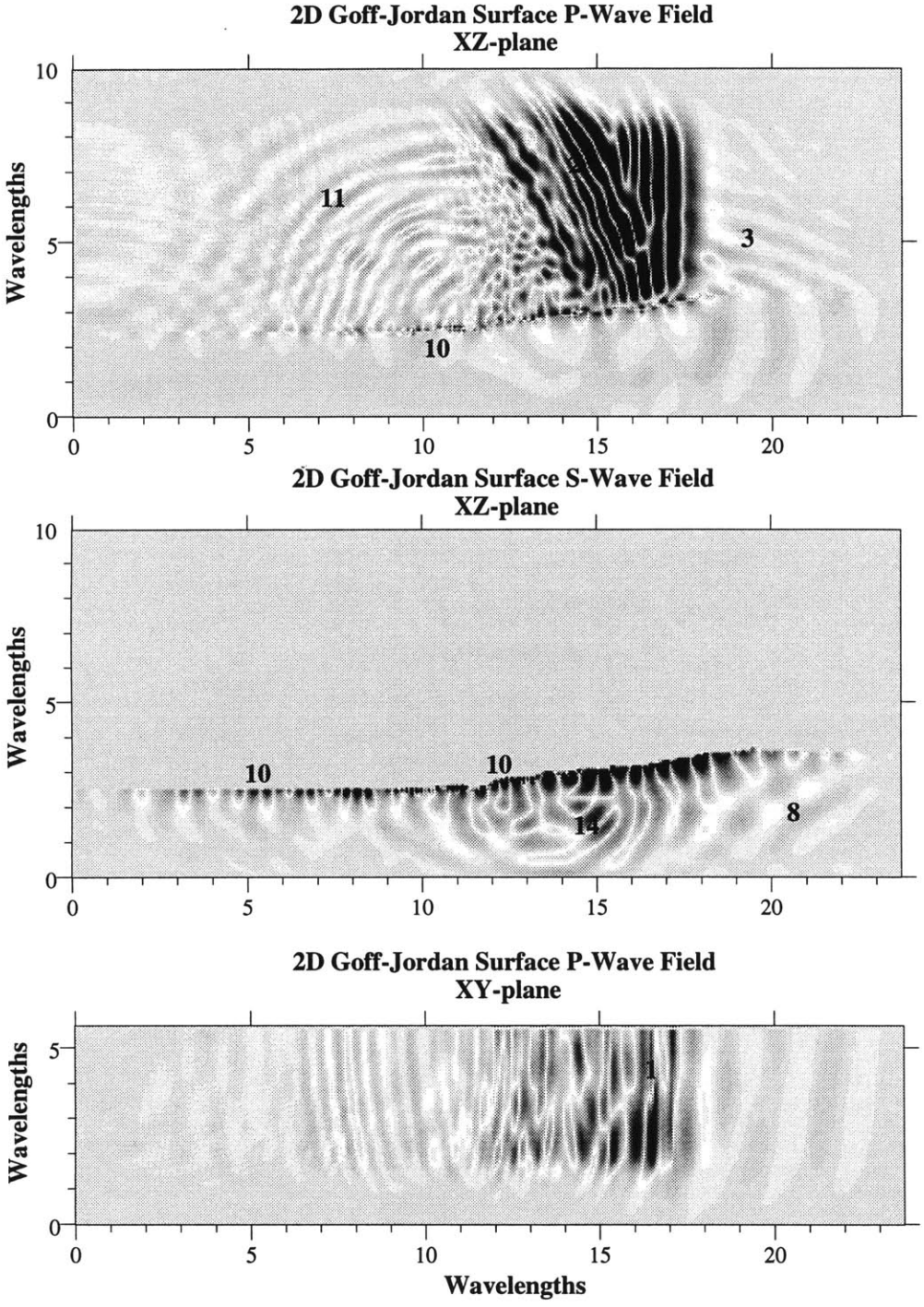


Figure 4-24: Schlieren diagrams computed at 18 periods for the 2D Goff-Jordan rough sea floor. Wave arrivals are identified in Table (4.1).

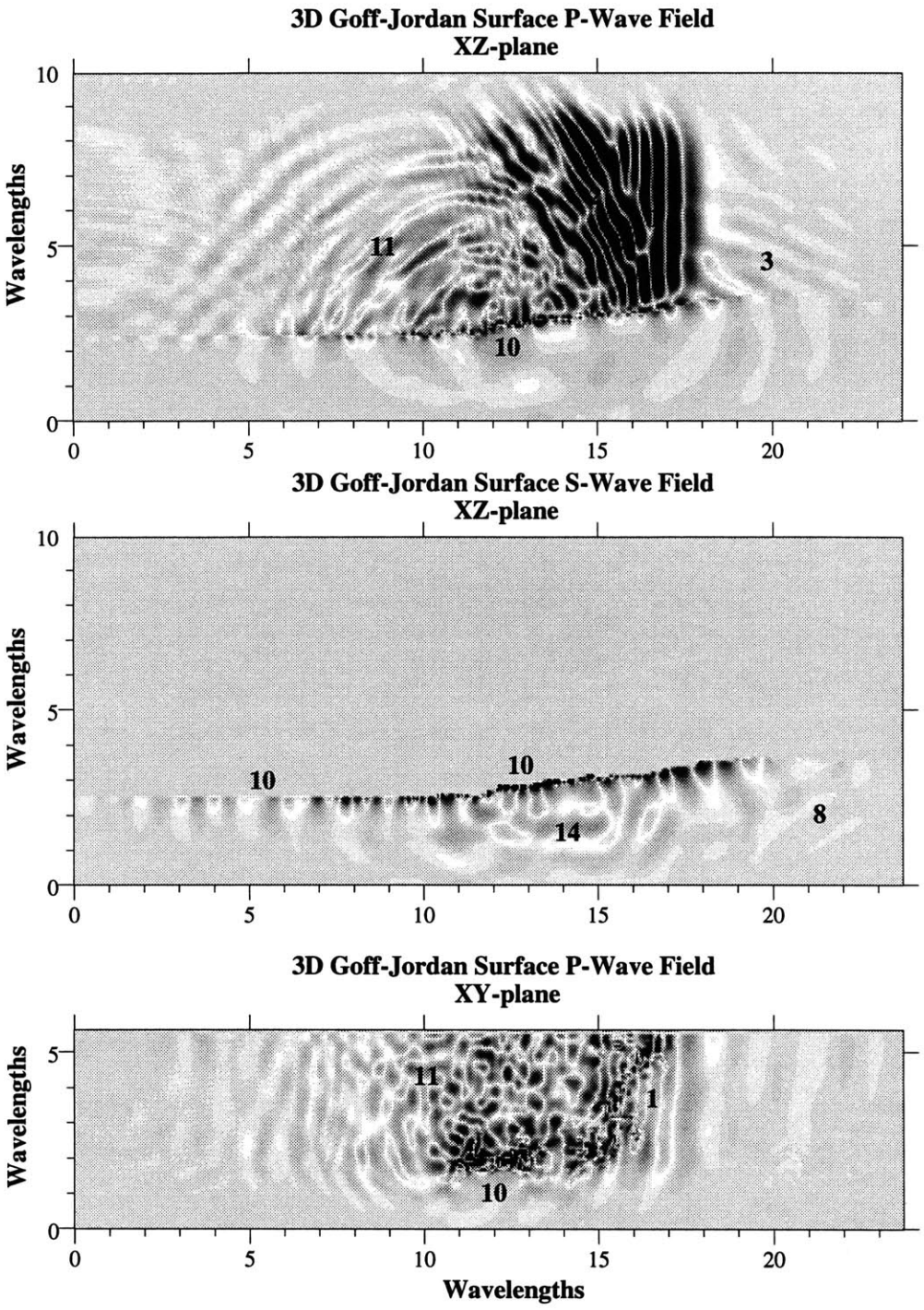


Figure 4-25: Schlieren diagrams computed at 18 periods for the 3D Goff-Jordan rough sea floor. Wave arrivals are identified in Table (4.1).

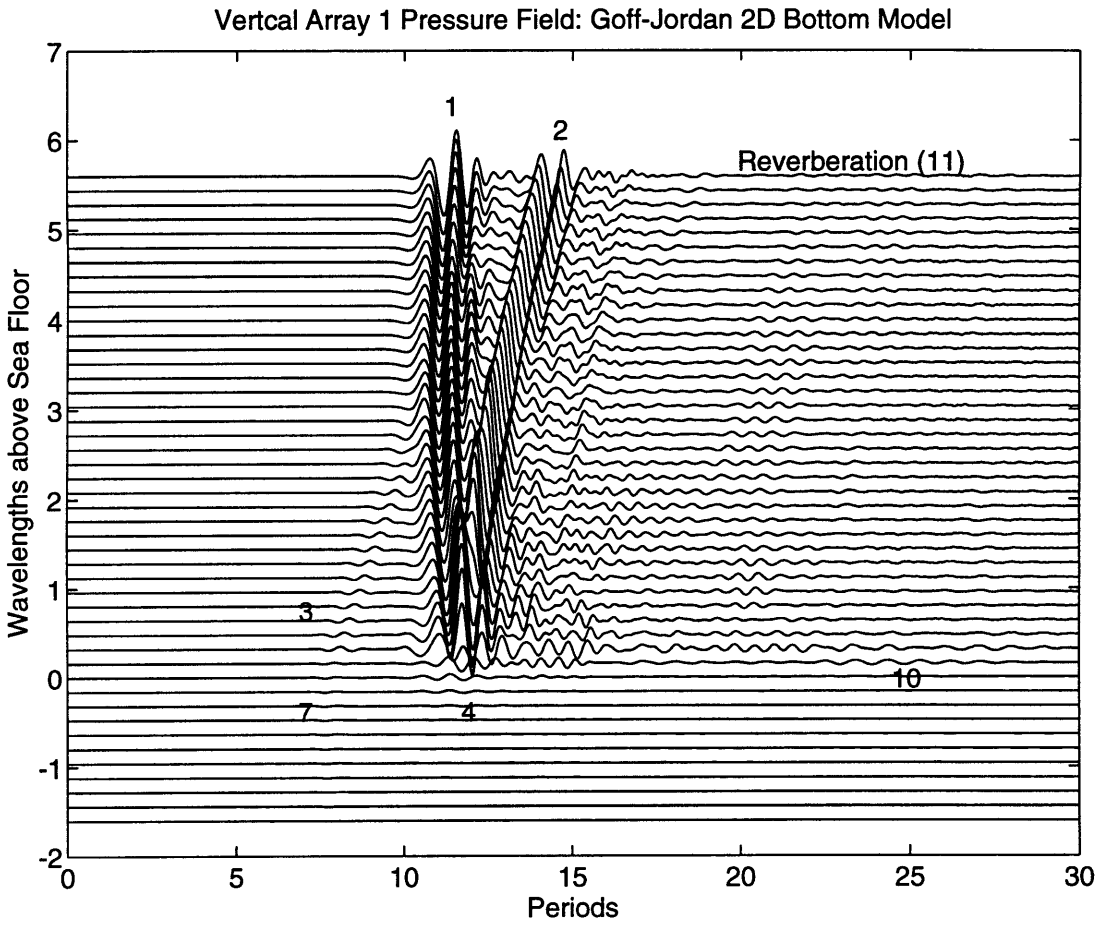


Figure 4-26: Calculated pressure along a vertical array in the 2D Goff-Jordan model. The horizontal axis is in periods with respect to the peak frequency of the source and the vertical axis is in wavelengths above the sea floor. The vertical array has 11 elements below the sea floor and 35 elements above the sea floor in the water column. The arrivals are identified in Table (4.1).

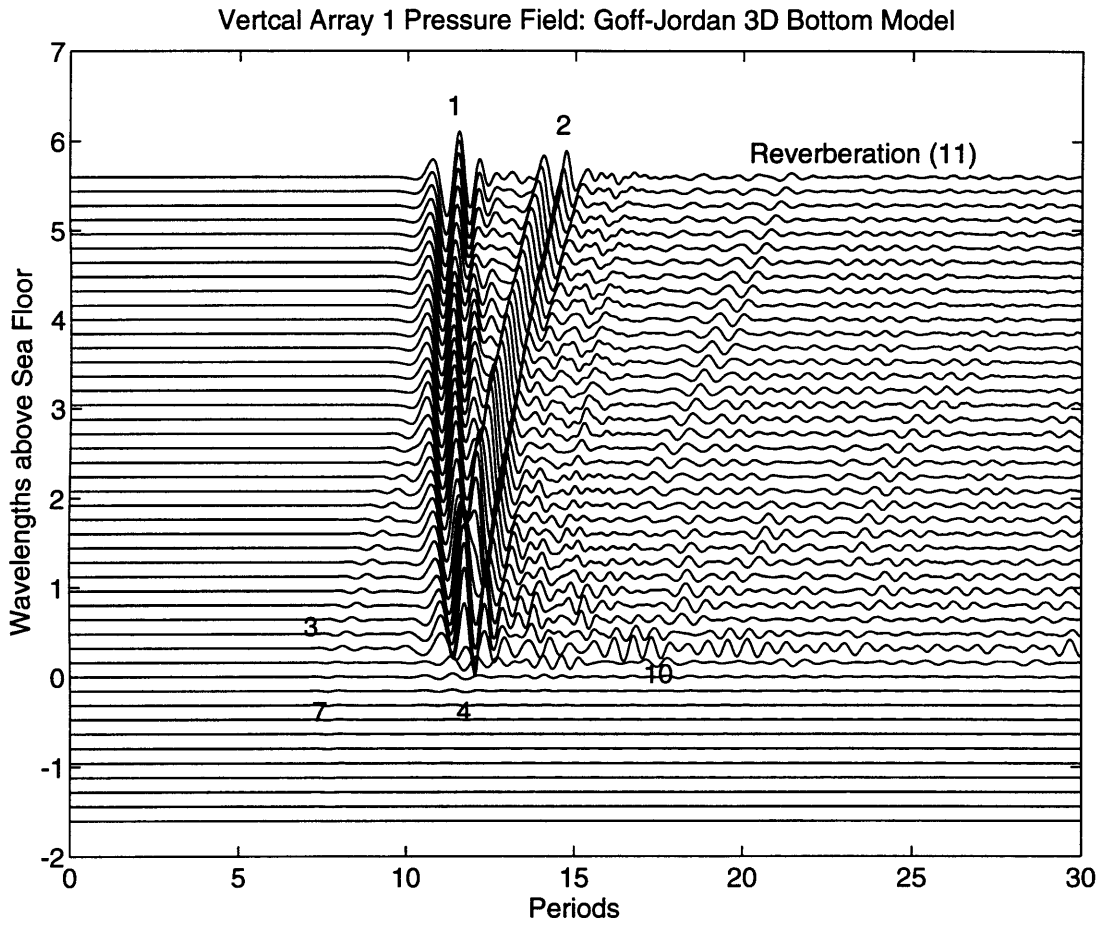


Figure 4-27: Calculated pressure along a vertical array in the 3D Goff-Jordan model. The horizontal axis is in periods with respect to the peak frequency of the source and the vertical axis is in wavelengths above the sea floor. The vertical array has 11 elements below the sea floor and 35 elements above the sea floor in the water column. The arrivals are identified in Table (4.1).

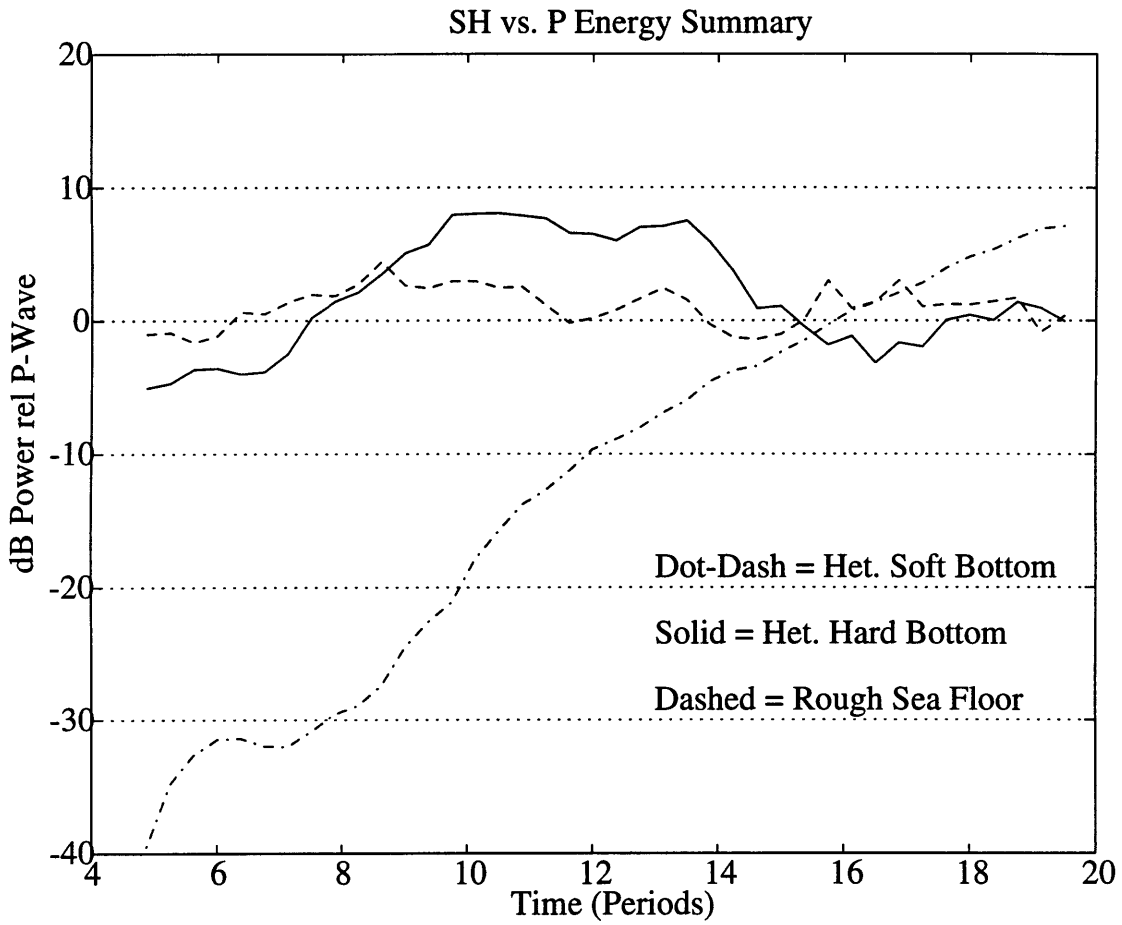


Figure 4-28: SH- versus P-wave summary for sub-bottom reverberation in the soft and hard bottom containing volume heterogeneities and the Goff-Jordan rough sea floor. The direct wave leaves the models after 8.25 periods and the SH-wave component of the sub-bottom reverberation becomes greater than the P-wave component for both the heterogeneous hard bottom and rough sea floor models. The heterogeneous soft bottom shows a dominant SH-wave only after 16 periods.

# Chapter 5

# Discussion and Conclusions

## 5.1 Overview

This thesis is an investigation into the behavior of oceanic seismo-acoustic noise in the microseism band $0.1 - 5.0\ Hz$. Below the microseism band (the infragravity wave band) the oceanic crust is excited directly by long wavelength ($> 1\ km$) gravity waves, and above this band (exclusive of industrial, shipping and biologic sources) the effects of wind and white capping are the largest contributions to the spectrum. Within the microseism band crustal noise is primarily generated by the nonlinear interaction of opposing sea surface gravity waves.

The microseism band is sub-divided into two frequency bands, each controlled by different environmental processes. Between 0.1 and 1.0 $Hz$ (the longer wavelengths) microseisms correspond to modes of the waveguide created by the ocean+crust+upper-mantle system. The magnitude of the noise is controlled by the amplitude of the surface gravity waves and attenuation in the upper mantle (Webb, 1992). Between 1.0 and 5.0 $Hz$ wind generated ocean gravity waves are often driven to their maximum amplitudes. As a result the microseism spectrum is often saturated. In this band (the "Holu" spectrum) there appears to be a world wide maximum spectral level ($\sim 60\ dB\ rel\ 1\ (nm/s^2)^2/Hz$ at $1.0\ Hz$) with a frequency dependence of 15 - 17 $dB$/octave. The following observations reported in this thesis support the hypothesis that the source of microseism noise is wave-wave interaction local to the site. Given this overview of the *source* of noise in the ocean the natural questions are how is the source *coupled* to the crust? and how does it *propagate*?

## 5.2 Contributions

The primary accomplishment of this thesis is an increased understanding of the *coupling* of acoustic energy in the water column to the sea floor and the *propagation* of microseismic noise **on** and **within** the ocean crust. The three core chapters of this thesis follow a logical order toward understanding the interaction of an acoustic noise source in the water column with the oceanic crust. In this thesis I first examine the theoretical coupling of an acoustic source with the sea floor (Chapter 2). Knowledge gained from this chapter was used to investigate a sea floor data set collected on and below the sea floor (Chapter 3). Finally, the scattering features seen in the data set prompted a numerical study of low frequency scattering in three dimensional media (Chapter 4).

### 5.2.1 Asymptotic Analysis of the Sommerfeld Integral

Asymptotic analysis of the Sommerfeld integral was carried out in Chapter 2 of this thesis using modern nomenclature and basing the analysis in the complex ray parameter plane. The primary goals were to understand the coupling of a point acoustic source in the water column with an elastic medium. We were particularly interested in the interface wave modes of the fluid/solid system because microseisms propagate at Rayleigh and Stoneley interface wave velocities. Both hard bottom ($V_{S_{solid}} > V_{P_{fluid}}$) and soft bottom ($V_{S_{solid}} < V_{P_{fluid}}$) models were analyzed for fluid depths of varying thickness. The following are findings and implications from the asymptotic analysis:

1. In deep water, longer wavelength microseisms (i.e. lower frequency) can propagate as the fundamental mode of the ocean/crust waveguide (as proposed by Webb, 1992). The phase velocity of these modes approaches the Rayleigh wave velocity of the crust at low frequencies (e.g. near the acoustic cut-off: 0.075 $Hz$ for 5.0 km deep water or for shallow water, 3.75 $Hz$ for 0.1 km deep water) (Tolstoy, 1954).

2. Shorter wavelength, higher mode Stoneley waves can be generated at the fluid/solid interface if the source point is near enough for inhomogeneous P- and S-waves to couple. These shorter wavelength modes can be excited by interface and volume heterogeneities near the water/crust interface or the sediment basalt interface. In shallow water the source field (gravity wave interaction at the ocean surface) can

directly couple energy to the sea floor and generate interface waves, but in deep water the vertical loading generated at the sea surface from wave-wave interaction can be converted into horizontally propagating interface wave energy via interaction of the acoustic wave with sea floor roughness.

3. The pseudo-Rayleigh wave (which only exists for hard bottom scenarios) has a complex velocity and lies on an unphysical Riemann sheet for the half-space fluid over half-space solid problem. This wave makes an important contribution to the wave field for post-critical incidence. We find that the pseudo-Rayleigh wave propagates like a true free surface Rayleigh wave in the crust but behaves more like a shear head wave in the water column. For the ocean/crust waveguide, the pseudo-Rayleigh wave becomes real and no longer attenuates exponentially with range. Fundamental and higher modes of the pseudo-Rayleigh wave dominate the noise spectrum.

In addition to the interface wave conclusions above, we found that the real component of the pseudo-Rayleigh pole underwent a continuous transition from a velocity less than $V_{S_{solid}}$ for a density ratio $\frac{\rho_{solid}}{\rho_{fluid}} > 1.0$ to a velocity greater than $V_{S_{solid}}$ as the density ratio was dropped below 1.0. This transition may have important consequences for scattering from sea ice where $\frac{\rho_{solid}}{\rho_{fluid}} < 1.0$ and $V_{S_{ice}} > V_{P_{fluid}}$.

One other contribution was the development of a fast, graphically interactive, root finding algorithm for locating poles on different Riemann sheets for media with arbitrary density and velocity contrasts.

### 5.2.2 Analysis of the LFASE Data

A unique data set collected off the eastern Florida coast in the Blake Bahama Basin was analyzed in Chapter 3 of this thesis. This data set was the first of its kind, employing the use of a seismic borehole array and ocean bottom seismometers. The borehole array (SEABASS) and the OBS's autonomously recorded the microseism field for a one week period during which a local storm passed through the area.

The multiple window power spectral (MWPS) analysis method (Chave et al., 1987) was used to find the lower spectral limits of the OBS and SEABASS instruments. The amplifier systems in the OBS (which contained 1.0 $Hz$ geophones) and SEABASS (which contained 4.5 $Hz$ geophones) were calibrated for a maximum pass band between 2 and 50

$Hz$. However using MWPS, the lower frequency limits of the OBS and SEABASS were extended to 0.1 $Hz$ and 0.2 $Hz$ respectively. Below these lower limits both instruments show contamination by system noise.

The mean behavior of the microseismic spectrum was analyzed first and the following conclusions were made:

- A 0.3 $Hz$ "microseism peak" was observed on all components of the sea floor OBS and all three clamped nodes of the SEABASS instrument. This peak was robust with depth, varying only 2 $dB$ over the 100 $m$ length of the array. The vertical component power spectral density was 65 $dB$ $rel$ 1 $(nm/s^2)^2/Hz$ and the horizontal component was 75 $dB$ $rel$ 1 $(nm/s^2)^2/Hz$. I believe that this represents long wavelength propagating microseisms like those mentioned in item (1) from the asymptotic analysis.

- Between 1.0 and 10 $Hz$ there is a monotonic decrease in the vertical and horizontal component of the microseism energy with depth. Over the 100 $m$ array length there is approximately a 10 $dB$ drop in the power spectral density level. On the averaged transverse and radial horizontal components the spectral energy decreases $15 - 20$ $dB$ over 100 $m$ depth. For both vertical and horizontal components most of the attenuation is in the upper 10 $m$ of sediment with the vertical component showing a slightly higher attenuation with depth.

- Higher order modes are evident in the borehole and OBS data. Narrow frequency band resonances in both the vertical and horizontal components show a more complex decay with depth below the sea floor. We propose these to be higher mode Stoneley waves trapped in the surface sediment layers.

Temporal variability in the LFASE data confirmed the source of the microseismic energy to be wave-wave interaction directly above the experiment site. Noise level closely followed the evolution of a local storm. Buoy data and global modeling data (GSOWM) show the passage of a local storm commensurate with an increase in the sea floor and sub-bottom noise levels. Specific observations made are itemized below:

- Temporal changes in the microseism peak are correlated with the local swell measured on a deep water buoy moored within 200 $km$ of the LFASE borehole. A rise

and fall of 10 $dB$ was seen in the microseismic data nearly synonymously with a change in swell amplitude.

- There is a preferential excitation of narrow band higher frequency modes (centered near 0.75, 1.2 and 2.1 $Hz$) during the storm's passage. These modes are not simple harmonics of the microseism peak. We propose they are Stoneley or Love wave modes within the sediments (mentioned in the mean behavior observations above).

- Particle motions during the storm are roughly aligned with the local swell conditions before the storm for frequencies between 0.3 and 0.4 $Hz$. During high sea states and at higher frequencies ($0.6 - 0.85\ Hz$) the data is less aligned with the swell. At frequencies above 1.0 $Hz$ the data shows no dominant polarization direction for either low or high sea states.

One of the most important conclusions from the LFASE analysis was the general monotonic energy attenuation with depth for frequencies above 0.3 $Hz$. This result has important implications for the emplacement of ocean bottom seismic stations for teleseismic monitoring. It argues for at least shallow burial of seismic stations and probably for burial $\geq$ 10 $m$ in soft bottom environments. Commonly, in ocean bottom seismic experiments the horizontal components of the OBS's are biased by tilting of the instrument, however in the horizontal components in SEABASS at 10 $m$ depth show displacements similar to those on the OBS leading to increased confidence in the OBS recordings and the overall noise estimates.

There is strong evidence for scattering at higher frequencies in the particle motion data. In an earlier study (Stephen et al., 1993) the active shot data from LFASE also showed strong scattering in its coda. Scattering can be generated at the source, from surface heterogeneities and volume heterogeneities. The fourth chapter in this thesis addressed both surface and volume scattering in two and three dimensions.

### 5.2.3 Numerical Modeling

Chapter 4 is a numerical investigation into surface and volume scattering from heterogeneous media. The method of finite differences is used for a staggered grid formulation of the heterogeneous elastic wave equation. The particular goals for this chapter were to

compare and contrast 2D and 3D realizations of deterministic and statistical scattering models. Results from the scattering tests can be grouped into two categories: scattering into the water column, and scattering below the sea floor. The most pertinent results from the numerical modeling are given below. Above the sea floor we find:

- Forward scatter is strongest for the hard bottom models in all test cases because of the sea floor reflection. Soft bottom models allow penetration of the direct wave and energy leakage into converted S-waves into the sub-bottom.
- Wavelength scale facets are not simple mirror-like scattering faces. Initial scattering radiates as diffractions from the facet corners. Stoneley waves scatter from the facet corners and reradiate back into the water. This effect creates long duration acoustic reverberation.
- Of the models tested, sea floor roughness generates the highest scattered field. Three dimensional models show out of plane scattering is a large component of the scattered field.

For scattering below the sea floor:

- For hard bottom models, the direct wave root is the primary mechanism by which energy enters the sea floor when the incident energy is post critical.
- Soft bottom models never are post critical for the converted shear wave and although there is a small amplitude transmitted shear wave it accounts for a majority of the sub-bottom volume scattering.

The most important acoustic scattering feature in the ocean is the sea floor. Wavelength scale features on the ocean bottom can initiate converted body and interface waves which can create secondary scattering into the water column or continue as body waves in the crust. Surface roughness at the LFASE site may be the source of the scattering in the explosive shot coda and the noise records from the experiment.

## 5.3 Future Work

No thesis is ever completely finished. The purpose of a good thesis is to answer a few questions and to ask many more. There were several aspects that could not be adequately

covered in this research project but should be listed as a guide to further our understanding of the propagation of microseisms. Listed below are several topics that either fall beyond the scope of this thesis or require a separate research effort.

### 5.3.1 Improvements in Theory and Mode Modeling

More complicated analysis should be carried out for the fluid/solid problem. Analytic expressions for the interface wave modes created for a homogeneous ocean overlying a layered solid would improve our understanding of the higher order modes seen in the LFASE data. The root finding algorithm could be improved to include effects from a layered half-space. Normal mode or locked mode algorithms exist for modeling layered media with intrinsic attenuation (Gomberg and Masters, 1988) and could be used to model the LFASE sediments.

### 5.3.2 LFASE Data analysis

There are a few puzzling aspects of the LFASE data that still remain unanswered. The most important of these is the reason for the incoherent behavior of both the OBS and SEABASS hydrophones. Electronic failure is the most likely culprit for the OBS hydrophone but the SEABASS hydrophones behavior is not as easily dismissed. Usable signals were recorded on the SEABASS hydrophone channel but there was no regular correlation between the pressure and vertical or horizontal geophones. The best hypothesis to date is the presence of tube waves in the borehole disturbing the pressure spectrum. This hypothesis should be tested on the explosive shot data and noise data.

With the solution from a more realistic model of the LFASE site should come a more detailed dispersion curve calculation. Given this curve and comparing them with the dispersion curves computed in Chapter 3, the comparison should either verify present hypotheses or suggest further mechanisms for the microseism propagation. In addition, the higher mode narrow band peaks should be checked for any strong alignment exclusive of the surrounding frequencies. If they are created directly by sea surface swell and not a product of scattering at the sea floor they should be closely aligned with the swell.

### 5.3.3 Numerical Modeling

Chapter 2 raised many questions about the significance of the different interface waves to the solution of scattering from a plane interface. The 3D finite difference algorithm used in Chapter 4 should be used to test the solutions found in the asymptotic analysis. In particular, the pseudo-Rayleigh pole predicted an interface wave that propagates faster than the shear wave velocity of the solid for density and velocity conditions that are close to a sea ice/water model. This should be tested numerically and the attributes of this wave documented. (The pseudo-Rayleigh pole is complex and therefore travels with attenuation. For the sea ice/water model the pseudo-Rayleigh pole may be insignificant due to down range attenuation.)

As memory on mainframe computers becomes more available, larger, more realistic models of the three dimensional environment near the LFASE site could be run. Presently we are limited to 20 $\lambda/side$ models which only roughly model the geologic complexity in the Blake Bahama Basin. The real surface of the sea floor is scoured by furrows and mud waves which may guide or bias the particle direction of the microseismic field. The observed trend of the furrows in the Blake Bahama Basin (Hollister et al., 1974) sub-parallel with the particle motion seen in the low frequency noise spectrum. The importance of these furrows and nature of the sea floor at any ocean bottom seismic station could and should be modeled. Figure (5.1) is a bathymetric map of the abyssal mud waves (contoured large scale features) and furrows (thin lines) within the Blake Bahama Basin (Figure 1 from Hollister et al., 1974). The particle motion discussed in Chapter 3 shows a rough alignment with the furrows during low sea states and an orthogonal alignment during high sea states. This behavior is predicted by Liu (1992) for interaction of the microseismic field with a statistically rough sea floor.

In a more practical sense, the following improvements should be made to the finite difference code:

1. New absorbing boundaries should be added. The current scheme employs the telegraph equation over a 20 – 25 point skin sacrificing much of the model space. Higdon (1991) presents a method based on simple first order differential operators which requires only 2 or 3 point absorbing skin.

2. Introduce a time dependent boundary condition allowing the introduction of a plane

wave or Gaussian beam to the model space. This would more accurately approximate the incidence energy from a distant source. In addition to these sources, more complicated source functions such as a statistical distribution of dipoles (to emulate nonlinear wave-wave interaction) or a simple continuous wave (CW) source could be coded.

3. In the future, changes should be made to the algorithm to allow for fully or transverse anisotropic models and intrinsic attenuation.

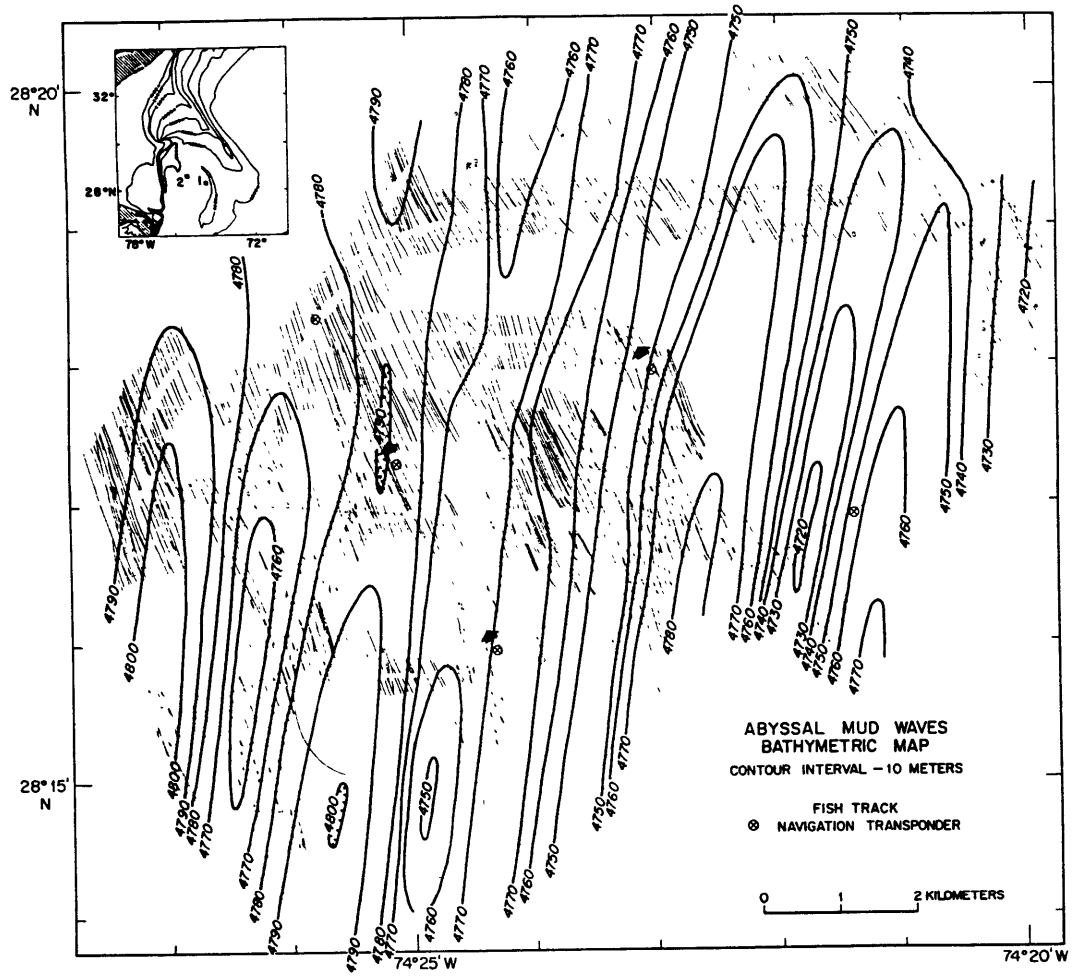


Figure 5-1: Index map from Hollister et al., 1974 showing the location of abyssal mud waves (heavy bathymetric contours) and furrows (thin lineations). Current direction is indicated by the black arrows. The noise data measured by SEABASS show particle motion is sub-parallel to the furrows during low sea states and nearly orthogonal during high sea states.

# References


Adair, R. G. , J. A. Orcutt, and T. H. Jordan, Analysis of ambient seismic noise recorded by downhole and ocean-bottom seismometers on Deep Sea Drilling Project Leg 78B, in *Initial Reports of the Deep Sea Drilling Project,* edited by Orlofsy, S. , vol. 78B, pp. 767–781, Washington (U.S. Govt. Printing Office), 1984.

Adair, R. G. , J. Orcutt, and T. H. Jordan, Low-frequency noise observations in the deep ocean, *J. Acoust. Soc. Am., 80,* 633–645, 1986.

Adair, R. G. , *Microseisms in the deep ocean: Observation and theory,* PhD thesis, University of California, San Diego, 1985.

Aki, K. and P. Richards, *Quantitative Seismology – Theory and Methods,* W. H. Freeman, San Francisco, 1980.

Bender, C. and S. M. Orszag, *Advanced methods for scientists and engineers,* McGraw-Hill, New York, 1978.

Bertelli, I. , Atti. accad. pontif. nuovi. lincei, *Comptes Rendus, Anno XXI, sess. 2a,* –, 1875.

Biot, M. A. , The interaction of Rayleigh and Stoneley waves in the ocean bottom, *Bull. Seismol. Soc. Am., 42,* 81–93, 1952.

Bolmer, S. T. , S. A. Swift, and R. A. Stephen, LFASE borehole array data acquisition and reduction summary, Technical Report No. 04-91, Woods Hole Ocean. Inst., 1991.

Bradley, C. R. and R. A. Stephen, Very low frequency seismo-acoustic noise below the seafloor, in *Prog. of the 123rd Mtg. of ASA ,vol. 91,* p. 2426, 1992.

Bradley, C. R. and R. A. Stephen, Three-dimensional modeling of low-angle seismo-acoustic backscatter, in *Prog. of the 125rd Mtg. of ASA, vol. 93,* p. 2322, 1993.

Brekhovskikh, L. M. , *Waves in Layered Media,* Academic Press, San Francisco, 1960.

Bryan, G. M. , R. G. Markl, and R. E. Sheridan, IPOD site surveys in the Blake-Bahama Basin, *Marine Geology, 35,* 43–63, 1980.

Burns, D. and R. Stephen, Three-dimensional numerical modeling of geoacoustic scattering from seafloor topography, *J. Acoust. Soc. Am., 88,* 2338–2345, 1990.

Cagniard, L. , Réflexion et réfraction des ondes séismiques progressives, *Gauthier-Villars Paris,* 1939, trans. E. A. Flynn and C. H. Dix, McGraw-Hill, New York, 1962.

Carter, J. A. , F. K. Duennebier, and D. Hussong, A comparison between a downhole seismometer and a seismometer on the ocean floor, *Bull. Seismol. Soc. Am., 74,* 763–772, 1984.

Cato, D. H. , Sound generation in the vicinity of the sea surface: Source mechanisms and the coupling to the received sound field, *J. Acoust. Soc. Am., 89,* 1076–1095, 1991a.

Cato, D. H. , Theoretical and measured underwater noise from surface wave orbital motion, *J. Acoust. Soc. Am., 89,* 1096–1112, 1991b.

Cerjan, C. , D. Kosloff, R. Kosloff, and M. Reshef, A nonreflecting boundary condition for discrete acoustic and elastic wave equations, *Geophysics, 50,* 705–708, 1985.

Chapman, C. H. , A new method for computing synthetic seismograms, *Geophys. J. R. astr. Soc., 54,* 481–518, 1978.

Chapman, C. H. , Generalized Radon transforms and slant-stacks, *Geophys. J. R. astr. Soc., 66,* 445–453, 1981.

Chave, A. D. , D. J. Thompson, and M. E. Ander, On the robust estimation of power spectra, coherences and transfer functions, *J. Geophys. Res., 92,* 633–648, 1987.

Chave, A. D. , 1993, personal communication.

Christensen, N. I. and M. H. Salisbury, Lateral heterogeneity in the seismic structure of the oceanic crust inferred form velocity studies in the bay of islands ophiolite, newfoundland, *Geophys. J. R. astr. Soc., 68,* 675–688, 1982.

Clancy, R. M. , J. E. Kaitala, and L. F. Zambresky, The Fleet Numerical Oceanography Center Global Spectral Ocean Wave Model, *Bull. Am. Meteor. Soc., 67,* 498–512, 1986.

Collins, J. A. , T. M. Brocher, and J. A. Karson, Two-dimensional seismic reflection modeling of the inferred fossil ocean crust/mantle transition in the Bay of Islands ophiolite, *J. Geophys. Res., 91,* 12520–12538, 1986.

Dablain, M. A. , The application of high-order differencing to the scalar wave equation, *Geophysics, 51,* 54–66, 1986.

Darbyshire, J. , Identification of microseismic activity with sea waves, *Proc. Roy. Soc., London, 202,* 439–448, 1950.

Darbyshire, J. , *Microseisms,* pp. 700–719, Wiley-Interscience, 1960.

Deacon, G. E. R. , Relation between sea waves and microseisms, *Nature, 160,* 419–421, 1947.

Dorman, L. M. and A. E. Schreiner, The depth dependence of seismic background noise within the seafloor, *submitted,* pp. –, 1993.

Dougherty, M. E. and R. A. Stephen, Seismic energy partitioning ans scattering in laterally heterogeneous oceanic crust, *PAGEOPH, 128,* 195–229, 1988.

Dougherty, M. E. and R. A. Stephen, Seismo/acoustic propagation through rough seafloors, *J. Acoust. Soc. Am., 90,* 2637–2651, 1991.

Dougherty, M. E. , *Ocean Bottom Seismic Scattering,* PhD thesis, MIT/WHOI Joint Program Oceanography, 1989.

Duennebier, F. , R. Cessaro, and P. Anderson, Geo-acoustic noise levels in a deep ocean borehole, in *Ocean seismo-acoustics: low-frequency underwater acoustics,* edited by Akal, T. and J. M. Berkson, pp. 743–751, NATO conference series, 1986.

Duennebier, F. K. , C. S. McCreery, D. Harris, R. K. Cessaro, C. Fisher, and P. Anderson, OSS IV: Noise levels, signal-to-noise ratios, and noise sources, Deep Sea Drilling Project Leg 88, in *Initial Reports of the Deep Sea Drilling Project,* edited by Turner, K. L. , vol. 88, pp. 89–103, Washington (U.S. Govt. Printing Office), 1987.

Durrani, T. S. and D. Bisset, The Radon transforms and its properties, *Geophysics, 49,* 1180–1187, 1984.

Emerman, S. H. and R. A. Stephen, Comment on: Absorbing boundary conditions for acoustic and elastic wave equations, by R. Clayton and B. Enquist, *Bull. Seismol. Soc. Am., 73,* 661–665, 1982.

Ewing, W. M. , W. S. Jardetzky, and F. Press, *Elastic Waves in Layered Media,* McGraw Hill Book Co, New York, NY, 1957.

Farrell, W. E. , T. J. Sereno, and D. J. Williams, LFASE instrument transfer functions, Technical report, Science Applications International Corporation, San Diego, CA, 1991.

Frankel, A. and R. Clayton, Finite difference simulations of wave propagation in two dimensional random media, *Bull. Seismol. Soc. Am., 74,* 2167–2186, 1984.

Frankel, A. and R. Clayton, Finite difference simulations of seismic scattering: Implications for the propagation of short-period seismic waves in the crust and models of crustal heterogeneity, *J. Geophys. Res., 91,* 6465–6489, 1986.

Fricke, J. R. , *Acoustic Scattering from Elastic Ice: A Finite Difference Solution,* PhD thesis, MIT/WHOI Joint Program Oceanography, 1991.

Fricke, J. R. , Acoustic scattering from elemental Arctic ice features: Numerical modeling results, *J. Acoust. Soc. Am., 93,* 1784–1796, 1993.

Frisk, G. V. , J. A. Doutt, and E. E. Hays, Bottom interaction of low-frequency acoustic signals at small grazing angles in the deep ocean, *J. Acoust. Soc. Am., 69,* 84–94, 1980.

Gilbert, F. and S. J. Laster, Experimental investigation of PL modes in a single layer, *Bull. Seismol. Soc. Am., 52,* 59–66, 1962.

Gilmore, M. H. , Microseisms and ocean storms, *Bull. Seismol. Soc. Am., 36,* 89–119, 1946.

Goff, J. A. and T. H. Jordan, Stochastic modeling of seafloor morphology: Inversion of Sea Beam data for second order statistics, *J. Geophys. Res., 93,* 13589–13608, 1988.

Gomberg, J. S. and T. G. Masters, Waveform modeling using locked-mode synthetic and differential sesimograms: application to determination of the structure of Mexico, *Geophys. Journ., 94,* 193–218, 1988.

Gutenburg, B. , Die seismiche bodenruhe, *Inaugural Dissertation, Goettingen,* –, 1910.

Hasselmann, K. , On the non-linear energy transfer in a gravity wave spectrum, 2, Conservation theorems; wave-particle analogy; irreversibility, *J. Fluid Mech., 15,* 273–281, 1962.

Hasselmann, K. , A statistical analysis of the generation of microseisms, *Rev. Geophys., 1,* 177–210, 1963.

Haubrich, R. A. , W. H. Munk, and F. E. Snodgrass, Comparative spectra of microseisms and swell, *Bull. Seismol. Soc. Am., 53,* 27–37, 1963.

Hildebrand, F. B. , *Advanced Calculus for Applications,* Prentice Hall, Englewood Cliffs, New Jersey, 1976.

Hollister, C. D. , R. D. Flood, D. A. Johnson, P. Lonsdale, and J. B. Southard, Abyssal furrows and hyperbolic echo traces on the Bahama Outer Ridge, *Geology, 2,* 395–400, 1974.

Hughes, B. , Estimates of underwater sound (and infrasound) produced by nonlinearly interacting ocean waves, *J. Acoust. Soc. Am., 60,* 1032–1039, 1976.

Hyndman, R. D. and M. H. Salisbury, in *Initial Reports of the Deep Sea Drilling Project,* edited by Orlofsky, S. , vol. 78B, pp. 623–848, Washington (U.S. Govt. Printing Office), 1984.

Imbo, G. , Agitazione del mare e microsismika a Cantania, *Bull. Seismol. Soc. Italy, 29,* 165–169, 1931.

Kadota, T. T. and F. M. Labianca, Gravity-wave-induced pressure fluctuations in the deep ocean, *IEEE J. of Ocean Eng., OE-6,* 50–58, 1981.

Kappus, M. E. , A. J. Harding, and J. A. Orcutt, A comparison of tau-p transforms methods, *Geophysics, 55,* 1202–1215, 1990.

Kawahara, H. , *Asymptotic Analysis of Ocean Bottom Reflected Acoustic Fields,* PhD thesis, MIT/WHOI Joint Program Oceanography, 1984.

Kelly, K. R. , R. W. Ward, S. Treitel, and R. M. Alford, Synthetic seismograms: A finite-difference approach, *Geophysics, 41,* 2–27, 1976.

Kibblewhite, A. C. and K. C. Ewans, Wave-wave interactions, microseisms and infrasonic ambient noise in the ocean, *J. Acoust. Soc. Am., 78,* 981–994, 1985.

Kibblewhite, A. C. and C. Y. Wu, The generation of infrasonic ambient noise in the ocean by nonlinear interaction of ocean surface waves, *J. Acoust. Soc. Am., 85,* 1935–1945, 1989.

Kibblewhite, A. C. and C. Y. Wu, The theoretical description of wave-wave interactions as a noise source in the ocean, *J. Acoust. Soc. Am., 89,* 2141–2252, 1991.

Kuperman, W. A. and H. Schmidt, Self-consistent pertubation approach to rough surface scattering in stratified elastic media, *J. Acoust. Soc. Am., 86,* 1511–1522, 1989.

Lamb, K. , On the propagation of tremors over the surface of an elastic solid, *Phil. Trans. Roy. Soc. London A, 203,* 1–42, 1904.

Laska, W. , Ueber pendelanruhe, *Verhandl. der 1. Intern. Seism. Konf. Strassburg 1901, Gerlands Beiter. z. Geoph., Ergaenzungsband 1,* 209–235, 1902.

Latham, G. V. and A. A. Nowroozi, Waves, weather, and ocean bottom microseisms, *J. Geophys. Res., 73,* 3945–3956, 1968.

Latham, G. V. and G. H. Sutton, Seismic measurements on the ocean floor, *J. Geophys. Res., 71,* 2545–2573, 1966.

Lavoie, D. and S. O'Hara, LSAP test site: Geoacoustic environment, Prepared for the Seismic Sensor Program, 1989.

LeMehaute, B. , *An Introduction to Hydrodynamics and Water Waves,* Springer-Verlag, New York, New York, 1976.

Levander, A. R. , Use of the telegraphy equation to improve absorbing boundary efficiency for fourth-order acoustic wave finite difference schemes, *Bull. Seismol. Soc. Am., 75,* 1847–1852, 1985.

Lighthill, M. J. , On sound generated aerodynamically: I. General theory, *Proc. of the Roy. Soc., A211,* 564–578, 1952.

Lindstrom, T. E. , Predictions and observations of seafloor infrasonic noise generated by sea surface orbital motion, Master's thesis, MIT/WHOI Joint Program Oceanography, 1991.

Liu, J. Y. , *Seismo-acoustic rough interface scattering of surface-generated ambient noise in a stratified ocean,* PhD thesis, Massachusetts Institute of Technology, 1992.

Longuet-Higgins, M. , A theory of the origin of microseisms, *Phil. Trans. Roy. Soc. A., 243,* 1–35, 1950.

Macelwane, J. B. , Sketch of the history of microseismology, *In: Symposium on Microseisms, Harriman, NY,* 1–125, 1952.

McCreery, C. S. , F. K. Duennebier, and G. H. Sutton, Correlation of deep ocean noise (0.4-30 hz) with wind, and the Holu spectrum - A worldwide constant, *J. Acoust. Soc. Am., 93,* 2639–2648, 1993.

Melton, B. S. , The sensitivity and dynamic range of inertial seismographs, *Rews. Geophys. Space Phys., 14,* 93–116, 1976.

Menard, H. W. , *Marine geology of the Pacific,* McGraw-Hill, San Francisco, CA, 1964.

Miche, M. , Mouvements ondulatoires de la mer en profonder constante ou décroissante, *Ann. ponts et chaussées, 114,* 25–87,131–164,270–292, 396–404, 1944.

Milne, J. , Earth pulsations, *Trans. Sesimol. Soc. of Japan, VI,* 1–12, 1883.

Morse, P. M. and H. Feshbach, *Methods of Theoretical Physics,* McGraw-Hill, New York, 1953.

Nicoletis, L. , *Simulation numerique de la propagation d'ondes sismiques dans les miliuex stratifies a deux et trois dimensions: contributions a la construction et a l'interpretation des sismogrammes synthetique,* PhD thesis, Universite Pierre et Marie Curie, Paris, France, 1981.

Orcutt, J. A. , R. D. Moore, and T. H. Jordan, Description and performance of the Scripps ocean bottom seismographs during the Ngendei experiment, Deep Sea Drilling Project Leg 88, in *Initial Reports of the Deep Sea Drilling Project,* edited by Turner, K. L. , vol. 91, pp. 347–356, Washington (U.S. Govt. Printing Office), 1987.

Orcutt, J. A. , C. S. Cox, A. C. Kibblewhite, W. A. Kuperman, and H. Schmidt, Observations and causes of ocean and seafloor noise at ultra-low and very-low frequencies, *unpublished,* 1992.

Pekeris, C. L. , Theory and propagation of explosive sound in water, *Geol. Soc. Am., Mem. 27,* –, 1948.

Phillips, O. M. , *The Dynamic of the Upper Ocean,* Cambridge University Press, Cambridge, England, 1977.

Press, F. and M. Ewing, A theory of microseisms with geologic applications, *Trans. Amer. Geophys. Union, 29,* 163–174, 1948.

Ramirez, J. , An Experimental investigation of the nature and origin of microseisms at St. Louis, Missouri, *Bull. Seism. Soc. Amer., 30,* 35–84; 139–178, 1944.

Rayleigh, L. , On waves propagated along the plane surface of an elastic solid, *Proc. London Math. Soc., 17,* 4–11, 1887.

Riedesel, M. A. , R. D. Moore, and J. A. Orcutt, Limits of sensitivity of inertial seismometers with velocity transducers and electronic amplifiers, *Bull. Seismol. Soc. Am., 80,* 1725–1752, 1990.

Roever, W. L. and T. F. Vining, Propagation of elastic wave motion from an impulsive source along a fluid/solid interface: Part I. the experimental pressure response, *Philos. Trans. Roy. Soc. Lond., A. 251,* 455–523, 1959.

Samson, J. C. and J. V. Olsen, Some comments on the descriptions of the polarization state of waves, *Geophys. J. R. astr. Soc., 61,* 115–129, 1981.

Samson, J. C. , Matrix and Stokes vector representations of detectors for polarized waveforms: theory, with some applications to teleseismic waves, *Geophys. J. R. astr. Soc., 51,* 583–603, 1977.

Sauter, A. W. , L. M. Dorman, and A. E. Schreiner, A study of seafloor structure using ocean bottom shots and receivers, in *Ocean seismo-acoustics: low-frequency underwater acoustics,* edited by Akal, T. and J. M. Berkson, pp. 673–681, NATO conference series, 1986.

Schmidt, H. and F. B. Jensen, A full wave solution for propagation in multilayered viscoelastic media with application to Gaussian beam reflection at fluid solid interfaces, *J. Acoust. Soc. Am., 77,* 813–825, 1984.

Schmidt, H. and W. A. Kuperman, Estimation of surface noise source levels from low-frequency seismoacoustic ambient noise measurements, *J. Acoust. Soc. Am., 84,* 2153–2162, 1988.

Scholte, J. , On the propagation of seismic waves, *Proc. Kon. Ned. Akad. v. Wetensch., 45,* 380–387; 449–457; 515–524, 1942.

Scholte, J. , On the large displacements commonly regarded as caused by Love waves and similar dispersive surface waves, *Proc. Kon. Ned. Akad. v. Wetensch., 51,* 533–543; 642–649; 828–835; 969–976, 1948.

Scholte, J. , On true and pseudo Rayleigh waves, *Proc. Kon. Ned. Akad. v. Wetensch, 52,* 652–653, 1949.

Schreiner, A. E. and L. M. Dorman, Coherence lengths of seafloor noise: Effect of ocean bottom structure, *J. Acoust. Soc. Am., 88,* 1503–1514, 1990.

Sereno, T. J. , W. E. Farrell, and D. J. Williams, Notes for: LFASE data analysis workshop, *Science Applications International Corporation, San Diego, CA,* 1–92, 1989.

Slepian, D. and H. O. Pollak, Prolate spheroidal wave functions, Fourier analysis and uncertainty, *Bell Syst. Tech. J., 40,* 43–64, 1961.

Slepian, D. , Prolate spheroidal wave functions, Fourier analysis and uncertainty: The discrete case, *Bell Syst. Tech. J., 57,* 1371–1429, 1978.

Stephen, R. A. , F. Cardo-Casas, and C. H. Cheng, Finite-difference synthetic acoustic logs, *Geophysics, 50,* 1588–1609, 1985.

Stephen, R. , H. Berteaux, D. Koelsch, R. Turpening, A. Bocconcelli, S. Bolmer, J. Cretin, N. Etourmy, A. Fabre, R. Goldsborough, M. Gould, S. Kery, J. Laurent, G. Omnes, K. Peal, S. Swift, and C. Zani, The seafloor borehole array seismic system (SEABASS), *W.H.O.I. Technical Memorandum., 1,* 1–135, 1993.

Stephen, R. A. , A comparison of finite difference and reflectivity seismograms for marine models, *Geophys. J. R. astr. Soc., 72,* 39–57, 1983.

Stephen, R. A. , Finite difference seismograms for laterally varying marine models, *Geophys. J. R. astr. Soc., 79,* 185–198, 1984.

Stephen, R. A. , A review of finite difference methods for seismo-acoustics problems at the seafloor, *Review of Geophysics, 26,* 445–458, 1988.

Stoffa, P. L. , P. Buhl, J. B. Diebold, and F. Wenzel, Direct mapping of seismic data to the domain of intercept time and ray parameter - a plane-wave decomposition, *Geophysics, 46,* 255–267, 1981.

Strick, E. , Propagation of elastic wave motion from an impulsive source along a fluid/solid interface: Part III. The pseudo-Rayleigh wave, *Philos. Trans. Roy. Soc. Lond., A. 251,* 488–523, 1959.

Sutton, G. H. and N. Barstow, Ocean-bottom ultralow-frequency (ulf) seismo-acoustic ambient noise: 0.002 to 0.4 hz, *J. Acoust. Soc. Am., 87,* 2005–2012, 1990.

Sutton, G. H. , W. G. McDonald, D. D. Prentiss, and S. N. Thanos, Ocean-bottom seismic observatories, *Proc. IEEE, 53,* 1909–1921, 1965.

Sutton, G. H. , Ulf/vlf (0.001 to 50 hz) seismo-acoustic noise in the ocean, *Proceedings of a workshop at the Institute for Geophysics, University of Texas, Austin,* 1–48, 1990.

Thompson, D. J. , Spectrum estimation and harmonic analysis, *Proc. of IEEE, 9,* 1055–1096, 1982.

Tolstoy, I. and C. S. Clay, *Ocean Acoustics: Theory and experiment in underwater sound,* American Institute of Physics, New York, NY, 1987.

Tolstoy, I. , Dispersive properties of a fluid overlying a semi-infinite elastic solid, *Bull. Seismol. Soc. Am., 44,* 493–512, 1954.

Trehu, A. M. , K. D. Klitgord, D. S. Sawyer, and R. T. Buffler, Atlantic and Gulf of Mexico continental margins, *Geological Soc. of America, Memoir 172,* 349–381, 1989.

Tuthill, J. D. , B. T. R. Lewis, and J. D. Garmany, Stoneley waves, Lopez Island noise and deep sea noise from 1 to 5 hz, *Mar. Geophys. Res., 5,* 95–108, 1981.

Urick, R. J. , *Ambient Noise in the Sea,* Peninsula Publishing, Los Altos, California, 1986.

Virieux, J. , Sh-wave propagation in hetereogeneous media: Velocity-stress finite-difference method, *Geophysics, 49,* 1933–1942, 1984.

Virieux, J. , P-SV wave propagation in heterogeneous media: Velocity-stress finite - difference method, *Geophysics, 51,* 889–901, 1986.

Webb, S. C. , X. Zhang, and W. Crawford, Infragravity waves in the deep ocean, *J. Geophys. Res., 96,* 2723–2736, 1991.

Webb, S. C. , Long-period acoustic and seismic measurements and ocean floor currents, *IEEE Journal of Ocean Engineering, 13,* 263–270, 1988.

Webb, S. C. , The equilibrium microseism spectrum, *J. Acoust. Soc. Am., 92,* 2141–2158, 1992.

Wiechert, E. , Verhandlung der zweiten internationalen seismologischen konferenz, *Suppl. 2,* pp. 41–44, 1905.

Wilson, J. T. and F. P. (ed), Symposium on microseisms, *Nat. Acad. Sciences, NRC, Washington, D.C.,* 1–125, 1952.

Winterstein, D. F. , Velocity anisotropy terminology for geophysicists, *Geophysics, 55,* 1070–1088, 1990.